



DISSERTATION

**Bifurcation Analysis for Systems with
Piecewise Smooth Nonlinearity and
Applications**

Miriam Steinherr Zazo

Dissertation
zur Erlangung des Grades
Dr. rer. nat.

Vorgelegt im
Fachbereich Mathematik und Informatik
der Universität Bremen
im Oktober 2021

Gutachter:

Prof. Dr. Jens D. M. Rademacher (University of Bremen)

Prof. Dr. Alan R. Champneys (University of Bristol)

Promotionskolloquium am 17.12.2021

*In memory of Kira,
who will always shine in my heart.*



“Measure not the work until the day’s out and the labor done.”

Elizabeth Barrett Browning

“The greatest mistake you can make in life is continually fearing that you will make one.”

Elbert Hubbard

“Rest and be kind, you don’t have to prove anything.”

Jack Kerouac

Acknowledgments

In the first place, I owe an immense debt of gratitude to Jens Rademacher for giving me the opportunity to start my PhD with him, accompanying me during these years of research filled with exciting moments of breakthrough. This thesis would not have been possible without all his support, consideration and time.

I would like to extend my sincere thanks to Alan Champneys, Ivan Ovsyannikov, and Kathrin Flasskamp for their assistance, inspiration and valuable discussions, and who also formed part of my PhD advisory committee. In addition, I am truly grateful to Alan for hosting me at the University of Bristol and the chance to perform a research stay there.

I would also like to warmly thank Martin Rasmussen and Thor I. Fossen for fruitful discussions, productive critic and stimulating remarks.

I may pay thanks to Ed van Daalen for initiating the corresponding ship maneuvering analysis and sharing reports along with supporting the initial implementation in `AUTO` together with the intern Antoine Anceau. I also thank Mathias Temmen for contributing to the starting implementation and linear stability study in the context of his Msc thesis.

Furthermore, I am very thankful to the Applied Analysis working group, in particular, to Artur, Luby and the former member Jichen, for their interesting meetings with profitable exchanges, welcomed feedback, and friendly critic. I would also like to thank Dörte and Katie for all their help regarding bureaucratic and organizational procedures during my PhD, as well as Ingo for his technical assistance.

On a personal note, I would like to thank all my friends for their love, support and motivation throughout this whole time, either here by my side in Germany or from far away showing that friendship overcomes all distance. Finally, I would like to express my deepest gratitude to my family, Kira, and specially Pascal, for their endless encouragement, love and understanding.

This research has been funded by the Deutsche Forschungsgemeinschaft (DFG, German Research Foundation) within the framework of the Research Training Group (RTG) 2224 “ π^3 : Parameter Identification - Analysis, Algorithms, Applications”, with project number 281474342/GRK2224/1.

Abstract

Bifurcation Analysis for Systems with Piecewise Smooth Nonlinearity and Applications

by Miriam Steinherr Zazo

In the first part of this thesis, Andronov–Hopf bifurcations in systems with piecewise smooth nonlinearity are analyzed, which are motivated by models that arise in controlled ship maneuvering. In particular, within this nonsmooth setting, we derive explicit formulas for the generalization of the first Lyapunov coefficient, which generically determines the direction of branching (super- versus subcriticality). In addition, we show that, in general, this differs from any fixed smoothing of the vector field. Specifically, we focus on nonsmooth nonlinearities of the form $u_i|u_j|$, i.e., the product of one variable of the system times the absolute value of another variable. However, our results are formulated in broader generality for systems in any dimension with piecewise smooth nonlinear part. Moreover, we discuss some codimension-one degeneracies and apply the results to a model of a shimmying wheel.

Furthermore, other bifurcations occur in systems with the aforementioned nonsmooth nonlinearity. In particular, we perform an analysis of normal forms with piecewise smooth nonlinear part for coefficients for Bogdanov–Takens points, and compare these results with the corresponding smooth version. We show how these two kinds of models differ from each other in terms of the criticality of the Hopf bifurcation and its scaling law. Homoclinic and heteroclinic orbits are briefly studied via an example.

After the most theoretical part of this manuscript, we consider a particular ship maneuvering model, and show that the previously developed outcomes really apply in actual systems. Specifically, nonlinear terms in standard models of ship maneuvering entail continuous nonsmooth terms so that bifurcations of straight motion are not amenable to standard center manifold reduction. In the second part of this dissertation, and using an approach based on the results developed in the first part, we determine the criticality of Hopf bifurcations that arises in stabilizing the straight motion of a marine craft model. For such a 3 degree of freedom system of ship motion with yaw damping and yaw restoring control, we present a detailed study of the possibilities for stabilizing the straight motion and the resulting nonlinear effects. To facilitate the analysis, we consider a combination of rudder and propeller forces into an effective thruster force. We identify the existence, location and geometry of the stability boundary in terms of the controls, including the dependence on the propeller diameter and the thruster position. We find numerically that “safe” supercritical Hopf bifurcations are typical and, by means of numerical continuation, we provide a global bifurcation analysis, which identifies the arrangement and relative location of stable and unstable equilibria and periodic orbits. We illustrate the resulting stable ship motions in Earth-fixed coordinates and present some direct numerical simulations.

Zusammenfassung

Verzweigungsanalyse von Systemen mit stückweise glatten Nichtlinearitäten und deren Anwendungen

von Miriam Steinherr Zazo

Im ersten Teil dieser Doktorarbeit analysieren wir die Andronov–Hopf-Verzweigung in Systemen mit stückweise glatten Nichtlinearitäten, die durch Modelle aus der gesteuerten Schiffsmanövrierung motiviert sind. Vor allem leiten wir in diesem nichtglatten Rahmen explizite Formeln für die Verallgemeinerung des ersten Lyapunov-Koeffizienten her, der im Allgemeinen die Richtung der Verzweigung bestimmt (super- oder subkritische Verzweigung). Zusätzlich zeigen wir, dass sie sich im Allgemeinen von festen Glättungen des Vektorfeldes unterscheiden. Wir konzentrieren uns besonders auf nichtglatte Nichtlinearitäten in der Form $u_i|u_j|$, das heißt also das Produkt aus einer Variablen aus dem System und dem Betrag einer anderen Variablen. Wir formulieren die Ergebnisse dennoch allgemeiner für Systeme in beliebiger Dimension mit stückweise glatten Nichtlinearitäten. Zudem behandeln wir einige Degeneriertheiten mit Kodimension eins und wenden die Ergebnisse auf ein Modell an, das ein taumelndes/flutterndes Rad beschreibt.

Darüber hinaus entstehen auch andere Verzweigungen in Systemen mit den oben genannten nichtglatten Nichtlinearitäten. Wir führen insbesondere eine Analyse in Normalform durch, mit stückweise glatten Nichtlinearitäten, um die Koeffizienten für Bogdanov–Takens Punkte zu untersuchen, und vergleichen diese Ergebnisse mit den entsprechenden glatten Varianten. Wir zeigen, wie sich die zwei Arten von Modellen bezüglich des kritischen Zustandes der Hopf-Verzweigung und dessen Skalierungsgesetz voneinander unterscheiden. Homokline und heterokline Orbits werden kurz anhand eines Beispiels untersucht.

Nach dem theoretischen Teil dieser Doktorarbeit betrachten wir ein bestimmtes Modell zur Schiffsmanövrierung und zeigen, dass die zuvor hergeleiteten Resultate auch anwendbar sind auf reale Systeme. Nichtlineare Terme in Standardmodellen der Schiffsmanövrierung bringen stetige, nichtglatte Terme mit sich, wodurch Verzweigungen von geraden Bewegungen nicht zugänglich ist für eine gewöhnliche Reduktion auf Zentrumsmannigfaltigkeiten. Im zweiten Teil dieser Arbeit bestimmen wir, mit Hilfe der Resultate im ersten Teil, den kritischen Zustand von Hopf-Verzweigungen, der durch das Stabilisieren der geraden Bewegung in einem Wasserfahrzeugmodell entsteht. Für solch ein System, das die Bewegung eines Schiffes beschreibt, mit drei Freiheitsgraden und mit Dämpfungs- und Wiederherstellungssteuerung der Gierrichtung liefern wir eine ausführliche Analyse über die Möglichkeiten zur Stabilisierung der geraden Bewegung und die entstehenden nichtlinearen Effekte. Um die Untersuchungen zu erleichtern, betrachten wir eine Kombination aus Ruder- und Schiffschraubekraft zu einem effektiven Schubantrieb. Wir stellen fest, dass überwiegend “sichere” superkritische Hopf-Verzweigungen vorherrschen und mittels Numerischer Kontinuierung liefern wir eine globale Verzweigungsanalyse, die die Anordnung und relative Lage der

stabilen und instabilen Gleichgewichtszustände und periodischen Orbits ermittelt. Wir veranschaulichen die stabilen Schiffsbewegungen, die sich ergeben, in einem erdfesten Koordinatensystem und präsentieren einige direkte numerische Simulationen.

Contents

Acknowledgments	ix
Abstract	xi
Zusammenfassung	xiii
List of Figures	xviii
List of Tables	xix
List of Acronyms and Symbols	xxiii
1 Introduction and Background	1
1.1 Basic ideas of dynamical systems	1
1.1.1 Fixed points and stability	2
1.1.2 Bifurcation theory	3
1.2 Bifurcations for systems with nonsmooth nonlinearities	12
1.3 Marine craft modeling and control	19
1.4 Outline	23
2 Lyapunov Coefficients for Hopf Bifurcations	25
2.1 Abstract viewpoint	26
2.2 Planar normal form case with absolute values	33
2.2.1 Averaging	33
2.2.2 Smoothing and the first Lyapunov coefficient	37
2.2.3 Direct method	38
2.3 Generalizations	45
2.3.1 Generalization from the absolute value	45
2.3.2 3D system	47
2.3.3 n -dimensional system	52
2.3.4 General linear part	54
2.4 A 3D example: Shimmying wheel	57
3 Bogdanov–Takens Bifurcation	61
3.1 Planar normal form case with absolute value	62
3.1.1 Bifurcation analysis at the zero equilibrium	62
3.1.2 Bifurcation analysis at the nonzero equilibria	67

3.2	Generalized absolute value	73
3.3	Example for homoclinic and heteroclinic bifurcations	77
4	Stabilizing Nonsmooth Ship Models with P-Control	81
4.1	Governing equations and thruster model	83
4.2	Theoretical analysis	86
4.2.1	Equilibrium straight motion	87
4.2.2	Linear stability of the straight motion	87
4.2.2.1	Impact of changing the parameters n_p and D_p	92
4.2.2.2	Impact of changing the thruster position parameter x_T	93
4.2.3	Nonlinear stability and bifurcation analysis	99
4.2.3.1	Pitchfork bifurcation for $\varepsilon_\psi = 0$	100
4.2.3.2	Hopf bifurcation	102
4.3	Numerical bifurcation analysis	106
5	Conclusions and Outlook	113
5.1	Bifurcation and stability analysis	113
5.2	Partial differential equations	114
5.3	Analysis for marine craft models	117
5.4	Further applications	118
A	Detailed Calculations for Chapter 2	119
A.1	Averaging	119
A.2	Poincaré map	122
A.3	3D system	124
A.3.1	Computation of γ_{ij}, δ_{ij} of system (2.57)	124
A.3.2	Computation of δ_{03} of system (2.65)	126
B	Ship Characteristics	127
B.1	HTC Characteristics	127
B.2	Rudder forces	128
C	Implementations of Simulations	131
	Afterword	133

List of Figures

1.1	Stability and instability in a double-well	3
1.2	Exhibiting criticality by means of the double-well	5
1.3	Bifurcation diagrams for the pitchfork bifurcation	5
1.4	Phase portrait of a Lotka-Volterra model	7
1.5	Phase portraits showing homoclinic and heteroclinic orbits	9
1.6	Sketch of the phase portrait illustrating the supercritical Hopf bifurcation . . .	11
1.7	Sketch of the phase portrait illustrating the subcritical Hopf bifurcation	12
1.8	Bifurcation diagrams for the pitchfork bifurcation for the smooth and the nonsmooth case	13
1.9	Comparison of the absolute value function with smooth approximations of it .	17
1.10	Bifurcation diagrams showing hysteresis	18
1.11	Ship-fixed coordinates with 3 DOF	20
2.1	Bifurcation diagram for the nonsmooth Bautin situation	45
2.2	Degenerate supercritical pitchfork bifurcation	46
3.1	Σ and Σ_s values from the zero equilibrium case	65
3.2	Subcritical Hopf bifurcations from the zero equilibrium case	66
3.3	Periodic orbits of the nonsmooth system approaching heteroclinic trajectories.	66
3.4	Σ_2 and Σ_{s_2} values from the nonzero equilibria case	71
3.5	Supercritical Hopf bifurcations from the nonzero equilibria case	72
3.6	Periodic orbits of the nonsmooth system approaching homoclinic trajectories.	72
3.7	Subcritical pitchfork bifurcation, degenerate subcritical pitchfork and trans- critical bifurcation	74
3.8	Bifurcation diagrams affected by the generalization from the absolute value .	75
4.1	Different forms of the stability boundary depending on the value of x_T	82
4.2	Expressions u_0 and $\partial_u \tau(u_0)$ in terms of D_p	88
4.3	Stability boundary of the straight motion in the $(\varepsilon_r, \varepsilon_\psi)$ -plane.	92
4.4	Different behaviors of the curve $\varepsilon_\psi(\varepsilon_r)$	94
4.5	Relevant quantities as functions of x_T	95
4.6	Function $\varepsilon_\psi(\varepsilon_r)$ for different critical x_T values.	95
4.7	Nonsmooth pitchfork bifurcation diagrams in the 3D system for $\varepsilon_\psi = 0$	102
4.8	Function Σ for diverse D_p values.	105
4.9	Function Σ for diverse x_T values.	106

4.10	Stability boundary of the straight motion in the $(\varepsilon_r, \varepsilon_\psi)$ -plane indicating significant regions.	107
4.11	Nonsmooth Hopf bifurcation diagrams in the 4D system with $\varepsilon_r = 0$	108
4.12	Sample profiles of periodic orbits and solution for fixed $\varepsilon_r \approx 10.6$	109
4.13	Earth-fixed coordinate plots of periodic solutions from Figure 4.12 for $\varepsilon_\psi \geq 1$	110
4.14	Earth-fixed coordinate plots of periodic solutions from Figure 4.12 close to the termination point.	110
4.15	Thruster angles of distinct solutions.	111
4.16	Time simulation for $\varepsilon_\psi = 0, \varepsilon_r \approx 10.6$ from the straight motion.	111
4.17	Time simulation for $\varepsilon_\psi = 0.2, \varepsilon_r \approx 10.6$ from $t = 1050$ on.	111
4.18	Time simulation from a non-trivially perturbed initial condition.	112
A.1	Illustrations of the Poincaré map in the nonsmooth setting	123
0	Applied analysis logo.	133

List of Tables

B.1	Rescaled rigid-body's mass, added mass coefficients and moment of inertia.	127
B.2	Hydrodynamic bare hull coefficients, (4.2).	127
B.3	Propeller characteristics.	128
B.4	Further parameters from the HTC.	128

List of Acronyms and Symbols

BT	Bogdanov–Takens
DOF	Degrees of Freedom
HTC	Hamburg Test Case
ODE(s)	Ordinary Differential Equation(s)
P-control	Proportional control
PD-control	Proportional Derivative control
PI-control	Proportional Integral control
PID-control	Proportional Integral Derivative control

Symbol	Meaning
$ \cdot $	Euclidean norm
$[[\cdot]]$	$\cdot \cdot $
$[u]_{p_{\pm}}^{p_{\pm}}$	$p_{+}u$ for $u \geq 0$, and $p_{-}u$ for $u < 0$
sgn	sign function
Re	real part of a complex number
Im	imaginary part of a complex number
$\det(L)$	determinant of the matrix L
$\text{tr}(L)$	trace of the matrix L
\mathbb{N}	set of natural numbers $\{1, 2, 3, \dots\}$
\mathbb{R}^n	n -dimensional space of real numbers
\mathbb{R}_{+}	set of positive real numbers $(0, +\infty)$
\mathbb{C}	set of complex numbers
$\mathcal{O}(\mu)$	$\lim_{\mu \rightarrow 0} \mathcal{O}(\mu)/\mu \leq K < \infty$, for $K \in \mathbb{R}_{+}$
$o(a)$	$\lim_{a \rightarrow 0} o(a)/a = 0$
$\mathcal{O}(n)$	terms of at least n^{th} order in the corresponding variables, $n \geq 2$
C^k	continuous and k -times differentiable, $k \geq 0$
\dot{r}	$dr(t)/dt$
r'	$dr(\varphi)/d\varphi$
$\Psi_u(u, r, \varphi)$	$u' = du/d\varphi$
$\Psi_r(u, r, \varphi)$	$r' = dr/d\varphi$
$\partial_r^i \Psi(0, \varphi)$	$\partial^i \Psi(r, \varphi) / \partial r^i _{r=0}$, $i \in \mathbb{N}$

Symbol	Meaning
\mathbf{u}	vector $(u_1, \dots, u_n) \in \mathbb{R}^n$
s	$\sin \varphi$
c	$\cos \varphi$
$\sigma_{\#}$	degenerate first Lyapunov coefficient
σ_2	degenerate second Lyapunov coefficient
σ_s	first Lyapunov coefficient (smooth case)

The following list refers to the symbols in Chapter 4:

Symbol	Name	Units ¹
ε_r	control strength for yaw damping	s
$\bar{\varepsilon}_r$	rescaled control strength for yaw damping	s/m
ε_{ψ}	control strength for yaw restoring	—
$\bar{\varepsilon}_{\psi}$	rescaled control strength for yaw restoring	1/m
η	steering angle	—
ρ	water density	kg/m ³
τ	rescaled propeller force	m/s ²
ψ	yaw angle	—
$\bar{\psi}$	rescaled yaw angle	m
D_p	propeller diameter	m
I_z	moment of inertia in yawing	kg · m ²
\bar{I}_z	rescaled moment of inertia in yawing	—
L_{pp}	length between perpendiculars	m
m	mass of the rigid-body	kg
\bar{m}	rescaled mass of the rigid-body	—
m_{rr}	added mass in yaw mode due to yaw motion	kg · m ²
\bar{m}_{rr}	rescaled added mass in yaw mode due to yaw motion	—
m_{rv}	added mass in yaw mode due to sway motion	kg · m
\bar{m}_{rv}	rescaled added mass in yaw mode due to sway motion	—
m_{uu}	added mass in surge mode due to surge motion	kg
\bar{m}_{uu}	rescaled added mass in surge mode due to surge motion	—
m_{vr}	added mass in sway mode due to yaw motion	kg · m
\bar{m}_{vr}	rescaled added mass in sway mode due to yaw motion	—
m_{vv}	added mass in sway mode due to sway motion	kg
\bar{m}_{vv}	rescaled added mass in sway mode due to sway motion	—
n_p	propeller frequency	1/s
r	yaw velocity	1/s
\bar{r}	rescaled yaw velocity	m/s

¹For the units listed here, the radian (symbol rad), which is the measure of angles in the International System of Units, is omitted. Notice that since it is the ratio of arc length to radius length, the units of length cancel out.

Symbol	Name	Units
T	mean draft	m
t	thrust deduction fraction	—
u	surge velocity	m/s
v	sway velocity	m/s
w	wake fraction	—
X_P	propeller force	kg · m/s ²
x_T	longitudinal thruster position	m
\bar{x}_T	rescaled longitudinal thruster position	—
∂_*	partial derivative with respect to *	
$\langle \cdot, \cdot \rangle$	inner product	

Chapter 1

Introduction and Background

The world is nonlinear and it may be nonsmooth, even discontinuous sometimes. In the present thesis, we consider continuous systems with piecewise smooth nonlinearities; investigation of these has become a subject of current interest caused by the will and need for refined modelings.

The key contribution of this work is an exhaustive analysis regarding Hopf bifurcations for systems with piecewise smooth nonlinearities, not considered so far in the literature, which are motivated by applications along with general research interest. Specifically, modesty aside, we establish decisive results on the criticality of the degenerate Hopf bifurcation and apply these on a particular model for ship maneuvering.

Before opening the starting section, I want to point out that during the last few years, several friends and relatives (who are not into the topic of dynamical system, or not directly involved in maths), have asked me repeatedly about my PhD topic. Unfortunately (or luckily for them), the time and the place was never appropriate to explain the subject properly. Therefore, I would like to dedicate a few lines here, in the first section, to introduce fundamental elements of my research to a broader audience.

Moreover, it is also worth mentioning that, a couple of times, while talking with friends, I did not bring up the mathematical background, but told them about the main application of my work related to ship maneuverability, thinking that this would be accessible. One time I received the unexpected answer that ships already navigate and have been doing so for quite a long time. However, the focus of this thesis is not merely navigating, but understanding the details of the model while digging into the depths of the behavior of the system. In particular, the aim of studying models for marine craft maneuvering in this thesis, is to stabilize the straight motion of a ship model via a proportional control mechanism and to recognize its criticality in order to determine whether the dynamics are “safe” (supercritical) or “unsafe” (subcritical) from an engineering standpoint.

From now on, let me continue using the first-person plural, “we”, rather than the singular form thereof, “I”.

1.1 Basic ideas of dynamical systems

As mentioned above, for a better understanding of the importance of bifurcations in dynamical systems, we present first an introduction into the topic for laymen.

1.1.1 Fixed points and stability

To begin with, we introduce the term *dynamical system*, which describes the temporal evolution of a system. In other words, a dynamical system is a model which captures how quantities change over time, where these “quantities” can be almost everything whose status changes with time. We can model many systems in several different fields, for instance biology (population growth), chemistry (autocatalytic reactions), physics (swinging pendulums) and engineering (electrical circuits), to name a few.

We present some examples, to get a better feeling for such systems, starting with the well-known logistic equation:

$$\frac{dN(t)}{dt} = rN(t) \left(1 - \frac{N(t)}{K}\right), \quad (1.1)$$

where $N(t)$ corresponds to the population of a species as a function of time t , the constant r denotes the growth rate, and K is the carrying capacity, which is the maximum population size that the environment can sustain, given the available resources, as water, food and habitat. In [58], this equation was proposed to model the growth of human populations. (We note that, in this example, the quantity for the dynamical system corresponds to a population of organisms.) Furthermore, the notation $\frac{dN(t)}{dt}$ expresses the rate of change at any time of the population N . Since we are differentiating the function N , (1.1) is called a differential equation. In particular, the differentiation is merely on the time variable, and thus it is called an *ordinary differential equation* (ODE). From now on we will use the notation \dot{N} instead of $\frac{dN(t)}{dt}$ to slightly simplify the writing, as well as N instead of $N(t)$, i.e., we will skip the explicit t dependence notation and call N (or the corresponding symbol for each equation) variable of the system. Therefore, such an equation, as in (1.1), will be preferably written as $\dot{N} = rN(1 - N/K)$. Notice that in this simple case there is only one equation, so that (1.1) could be just called a differential equation or an ODE, instead of system. Nevertheless, we will work mainly with systems with two or more equations.

To analyze the dynamics of an equation (or system), we also require an initial state or, in this case, an initial population N_0 , which obviously cannot be negative since we are dealing with organisms. Then, on the one hand, if $N_0 = 0$, clearly the population will always remain (for all time) at zero, $N = 0$, since nobody is there to start reproducing. Substituting $N = 0$ into (1.1) gives $\dot{N} = 0$, and no rate of change occurs, i.e., the population remains constant at zero. Furthermore, if $N_0 = K$, the population also stays constant, but now at $N = K$, since substitution into (1.1) yields $\dot{N} = 0$, and again no change happens.

On the other hand, if $N_0 > K$, which means the initial population already exceeds the carrying capacity K , the function N will shrink in the direction of K . Indeed, from the logistic equation $\dot{N} = rN_0(1 - N_0/K)$, we see that $1 - N_0/K < 0$ and since $r > 0$, the rate of change is negative, $\dot{N} < 0$, meaning that the population decreases over time.

Moreover, if $N_0 < K$, then $1 - N_0/K > 0$ and thus $\dot{N} > 0$, i.e., the population increases towards K .

From this nice example we can define further essential concepts regarding the analysis of

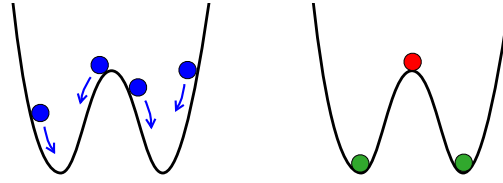


FIGURE 1.1: In the left diagram, the behavior of a ball in a double-well is shown: when placing the ball at diverse points of the double-well, it will move towards one of the lowest positions, except if it is placed exactly at the top of the peak. These three different endings of the ball are exhibited in the right diagram: at the top, the ball is red to remark its instability, while it is green at each well since in these two cases the position is stable.

dynamical systems. As we have seen, $\dot{N} = 0$ for $N_0 = 0$ as well as for $N_0 = K$. In fact, the right-hand side of the differential equation is zero if and only if N takes the values 0 or K . We say then that these two points are *fixed points* or *equilibrium points*, since the variable N of the equation remains constant. More precisely (and here we use a more refined definition), if we consider a general system $\dot{x} = f(x)$ with $x \in \mathbb{R}^n$, then the fixed points are all $x_* \in \mathbb{R}^n$ for which $f(x_*) = 0$.

Next in our example, we observe that for $N_0 \in (0, K)$, the population increases approaching K , while for $N_0 > K$, it decreases to K . This means that the fixed point $N_* = 0$ is *repelling* since the solutions of the equation move away from it, and thus it is called an *unstable fixed point*. A qualitatively different behavior occurs for the point $N_* = K$, which is *attracting* the solutions towards it, and therefore it is denominated a *stable fixed point*. In this way, we talk about the *stability* of the system.

To thoroughly understand the meaning of stability in the current context, we present an example in Figure 1.1. Here, two images with a double-well are shown: the left-hand picture displays the direction of motion of a ball placed at different locations in the double-well. We notice that if the ball is placed precisely on the peak or on one of the basins, then it will remain there. In this sense, these positions are fixed points since the ball will stay there over time. However, if we perturb the ball slightly from one of these locations, we would see that its behavior differs. On the right-hand picture in Figure 1.1, we show these three spots: if the ball on the top (in red) is perturbed, then it will fall either to the right or to the left, depending on the perturbation direction. After some time, the ball will end up at the bottom of one of the wells and cannot ever return to its previous state even by applying some additional small perturbations. By contrast, if we disturb a ball placed at the bottom (in one of the two green positions) it will return to its initial position.

At this stage, it should be clear that the top position of the ball (in red) can be identified as a repelling state, and thus the unstable fixed point; and the bottom positions (in green) with attracting locations, and hence stable equilibrium points.

1.1.2 Bifurcation theory

The previous introduction into dynamical systems paves the way towards the fascinating theory of bifurcations. For that, we first recall the appearance of two parameters in the logistic equation, (1.1): the growth rate r and the carrying capacity K . In this case, modification

of these parameters does not change the qualitative behavior of the system. However, these can play a significant role in dynamical systems since by modifying a particular parameter, the stability of the fixed points can be changed (from stable to unstable or vice versa), or these can be even destroyed or created. In other words, variation of certain parameters may produce a deviation to the qualitative behavior of the system. This qualitative change to the dynamics of the system is called a *bifurcation*, which takes place at a *bifurcation point*, and the characteristic parameter (or parameters) causing this effect is called a *bifurcation parameter*. As one can expect, sometimes the qualitative behavior of a dynamical system is unaffected by perturbations to its parameters, and hence no bifurcation can occur, as we will show later for (1.4). Nevertheless, the identification of bifurcation parameters and their analysis is one of the key goals of bifurcation theory.

Furthermore, there are many kinds of bifurcations which depend on the system and its parameters. As an example, we consider the first order system

$$\dot{u} = \mu u - u^3, \quad (1.2)$$

where $u \in \mathbb{R}$ is the variable and $\mu \in \mathbb{R}$ the parameter, and define the right-hand side of the equation as $f(u) := \mu u - u^3$. As previously explained, the fixed points of the system are the $u_* \in \mathbb{R}$ for which $f(u_*)$ vanishes. Thus, in this case, we have to solve $u_*(\mu - u_*^2) = 0$. Clearly, $u_* = 0$ is a fixed point, and from the second term, we have $u_* = \pm\sqrt{\mu}$. We already see that this second (double) equilibrium depends on the parameter of the system and, more precisely, only exists for $\mu \geq 0$, since for negative μ the square root function does not exist in \mathbb{R} . Therefore, for $\mu < 0$, the system has one single fixed point $u_* = 0$; for $\mu = 0$, the other equilibrium also vanishes since $u_* = \pm\sqrt{\mu} = 0$, and the system again has one fixed point (with multiplicity three); and for $\mu > 0$, the system has three different equilibrium points, namely $u_* \in \{-\sqrt{\mu}, 0, \sqrt{\mu}\}$. The creation/destruction of two equilibria together with the change of stability of the other fixed point while modifying the parameter is called a *pitchfork bifurcation*, and the bifurcation point is, in this case, $u_* = 0$.

Moreover, if instead of (1.2) we have

$$\dot{u} = \mu u + u^3, \quad (1.3)$$

then the fixed points are $u_* \in \{-\sqrt{-\mu}, 0, \sqrt{-\mu}\}$, and thus, now the existence of three equilibria happens for $\mu < 0$, and for $\mu > 0$ only one remains, in contrast to (1.2). We have the same type of bifurcation as before, i.e., the creation or destruction of two fixed points and the change of stability of the other equilibrium point, and hence a pitchfork bifurcation. However, now the *criticality* is different. The pitchfork bifurcation of (1.2) is supercritical while of (1.3), subcritical.

If we remember the double-well from Figure 1.1, we can easily comprehend the meaning of the distinct criticalities as follows: in Figure 1.2 (a), we have on the left-hand side a single-well and next to it, the already shown double-well, exhibiting the creation of two fixed points. The single stable equilibrium is transformed to an unstable fixed point while two stable equilibria pop up. On the other hand, in Figure 1.2 (b), the left-hand side is an inverted

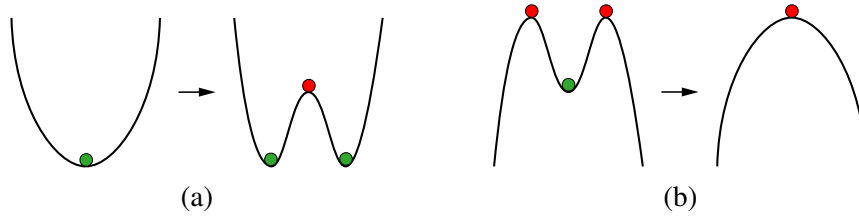


FIGURE 1.2: (a) Supercritical and (b) subcritical pitchfork bifurcation. The green particles correspond to stable equilibria and the red ones to unstable points.

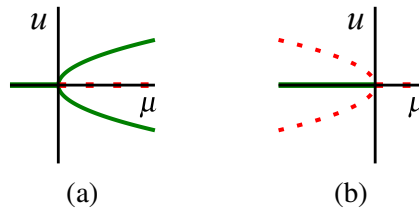


FIGURE 1.3: Bifurcation diagrams showing the (a) supercritical and (b) subcritical pitchfork bifurcation of equations (1.2) and (1.3), respectively, with stable (green) and unstable (red dashed) equilibria.

double-well and right to it, an inverted single-well. Here, the two unstable equilibria disappear and the single stable fixed point becomes an unstable one.

With these pictures in mind, we plot the *bifurcation diagrams* in Figure 1.3, showing the effect of the two different criticalities. The diagrams (a) and (b) correspond to the fixed point u in terms of the parameter μ of systems (1.2) and (1.3), respectively. More precisely, for $\mu < 0$, the equation (1.2) has the single stable fixed point $u_* = 0$ (in green in the diagram), while (1.3) has two more equilibria, $u_* = \pm\sqrt{-\mu}$, which are unstable (and thus in a dashed red curve in the diagram). For $\mu > 0$, the already explained exchange of stability of $u_* = 0$ occurs together with the creation (a) or destruction (b) of the other two equilibria.

In the rest of this section we present some further example systems with different dynamics. These will serve merely as illustrations showing firstly, a qualitatively distinct behavior, and secondly, a variety of bifurcation types. Consequently, we do not pretend to perform a deep analysis of them.

Recalling the logistic equation (1.1), we extended it to a model with more than one species as follows:

$$\begin{cases} \dot{N} = \alpha N - \beta NP, \\ \dot{P} = \gamma NP - \delta P, \end{cases} \quad (1.4)$$

which corresponds to the so-called Lotka–Volterra model, where two species are in competition. For this reason, it is also known as predator–prey system. In this sense, N is the number of prey (let us say rabbits), P the number of predators (foxes for instance), and \dot{N} , as well as \dot{P} , correspond to the instantaneous growth rates of the corresponding species. The parameters $\alpha, \beta, \gamma, \delta \in \mathbb{R}$ are positive and characterize the interaction between both populations. We recall that the variables are in fact functions of time, t , and should be thought as $N(t), P(t)$. As previously mentioned, we will skip the notation for the explicit dependence on time.

System (1.4) is then to be thought as follows: on the one hand, the first equation shows how the presence of foxes P influences the population of rabbits N by the term $-\beta NP$, which

is negative since the more foxes, the less rabbits. On the other hand, for the second equation, the product of preys and predators is a positive value since this makes the population of foxes increase. Notice that from $-\delta P$, if there are no rabbits at all, then the mortality of the foxes surpasses the rate of birth and hence, the predators will become extinct eventually.

Next, we observe that the fixed points are found as before, but working with two variables, and thus, we have to solve $\dot{N} = 0$ together with $\dot{P} = 0$, which gives a couple of equilibria: $(N_*, P_*) = (0, 0)$ and $(N_*, P_*) = (\delta/\gamma, \alpha/\beta)$. However, the stability analysis is now more involved and, as pointed out above, we will not enter into details and just comment on the results.

Then, for the stability analysis of a 2-dimensional system (or higher), we compute first the Jacobian matrix which, in this case, reads

$$J(N, P) = \begin{pmatrix} \alpha - \beta P & -\beta N \\ \gamma P & \gamma N - \delta \end{pmatrix},$$

and evaluate it at the fixed points $(0, 0)$ and $(\delta/\gamma, \alpha/\beta)$, which yields, respectively,

$$J(0, 0) = \begin{pmatrix} \alpha & 0 \\ 0 & -\delta \end{pmatrix}, \quad J(\delta/\gamma, \alpha/\beta) = \begin{pmatrix} 0 & -\beta\delta/\gamma \\ \gamma\alpha/\beta & 0 \end{pmatrix}.$$

The eigenvalues of the first matrix are $\lambda_1 = \alpha$, $\lambda_2 = -\delta$, and since α, δ are positive, λ_1, λ_2 will have always different signs. Therefore, the $(0, 0)$ equilibrium point is a *saddle point*.

For the second matrix, the eigenvalues are given by $\lambda_1 = i\sqrt{\alpha\delta}$, $\lambda_2 = -i\sqrt{\alpha\delta}$, which are purely imaginary and correspond to a complex conjugate pair. This setting for a linear system would mean that the fixed point corresponds to a *center* for closed orbits. However, for a nonlinear system with these eigenvalues, one has to see if it is either a center or a *spiral* (attracting or repelling). In this case, the system is conservative and therefore, closed orbits must exist. Later on we will introduce this concept.

In Figure 1.4, a sample of trajectories of system (1.4), in the phase plane, is displayed, showing that they form closed orbits, also called periodic solutions, around the equilibrium point $(\delta/\gamma, \alpha/\beta)$. Since all trajectories starting at $N_0, P_0 > 0$ rotate about a fixed point forming closed orbits (except the nonzero fixed point, which will remain motionless), this equilibrium is called a center.

From the phase portrait, it is easy to see that, on the one hand, if a starting point is no prey at all, i.e., $N_0 = 0$, and $P_0 > 0$, then the predator will eventually die and reach $P = 0$. On the other hand, if we start with no predator, i.e., $P_0 = 0$, and $N_0 > 0$, then the number of prey will grow (until infinity since there is no restriction on food for this species). If $N_0 = P_0 = 0$, both population will obviously remain at zero forever. Furthermore, if the initial conditions of both populations are strictly positive, $N_0, P_0 > 0$, then the solutions of the system move in cycles as seen in Figure 1.4. For instance, if initially, the number of hunted animals is much larger than the number of predators, this second population will increase while at some point, the prey individuals will decrease, reaching a point in which the predators will start dying due to the drop-off of prey, and once this number is low enough, the prey will expand again, and

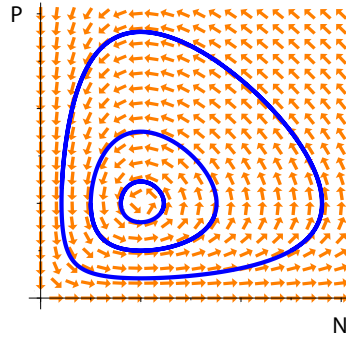


FIGURE 1.4: Phase portrait of (1.4) with $\alpha = \beta = \gamma = \delta = 1$. This portrait exhibits the general behavior of the interaction of both species. The arrows (orange) reveal the flow of the vector field of the system and, in particular, three trajectories are shown (blue), corresponding to three different initial conditions. The axes are $N, P \geq 0$ since negative values make no sense.

this cycle will continue forever. Such qualitative behavior will not be modified by perturbing any parameter of the system and hence, no bifurcation occurs.

It is worth mentioning that this kind of system (Lotka–Volterra) is not used exclusively to model the competition between predator and prey. It can also be used to describe two populations competing for a common food resource, but in this case the dynamics are different! It can exemplify, for instance, the so-called competition exclusion principle, as sheep and rabbits compete for grass. Moreover, we note that such a model is a very simplified version of reality since additional characteristics of the environment are ignored, such as predators, weather, and other food supplies or water. However, such “simple” systems, already provide an approach to better understand reality. In fact, one can introduce more species to the model, and get a dynamical system containing as many variables and equations as correlating species. Then, one can study the interaction between them by analyzing the system as we have briefly shown.

For our next example we have chosen a system which the reader will find familiar, namely, a particle moving in a double-well, as in Figure 1.1. Without entering much into detail, we briefly explain how to get the mentioned system. For that, we consider the well-known Newton’s law $F = ma$, where m is the mass of the particle, a its acceleration and F a nonlinear force. Providing that F only depends on x (the position of the particle), and thus no damping or friction is taken into account, Newton’s law can be expressed as $F(x) = m\ddot{x}$, and we can define the *potential energy* $V(x)$ as $F(x) = -dV/dx$.

Therefore, the equation of motion of a particle with $m = 1$ in a double-well with potential energy $V(x) = -x^2/2 + x^4/4$ reads $\ddot{x} = x - x^3$. This equation can be rewritten as the system

$$\begin{cases} \dot{x} = y, \\ \dot{y} = x - x^3, \end{cases} \quad (1.5)$$

where the new variable y denotes the velocity of the ball. The fixed points are $(0, 0)$ and $(\pm 1, 0)$, and from the Jacobian matrix

$$J(x, y) = \begin{pmatrix} 0 & 1 \\ 1 - 3x^2 & 0 \end{pmatrix},$$

we have that the zero equilibrium corresponds to a saddle point while the nonzero fixed points seem to be centers. We specifically say “seem to be” because this is a nonlinear system and thus, its linearization does not provide the complete information, like in the Lotka–Volterra system mentioned above. However, $(\pm 1, 0)$ are again centers due to the energy conservation, and we plot the phase portrait in Figure 1.5 (a). In this figure we can see how the trajectories are organized, where the more fascinating aspect is that trajectories “coming out” from the origin form a curve “ending” at the same starting point. This particular behavior is called a *homoclinic orbit*. Furthermore, if a trajectory starts inside of one of these homoclinic orbits, then it will enclose the corresponding nonzero fixed point. On the contrary, if it starts outside, the periodic orbit will encircle all three equilibria.

Above we have used the conservation of energy of the system and therefore, we spend now a few lines to explain its meaning. It is said that the energy of a system is conserved when the total energy $E = m\dot{x}^2/2 + V(x)$ is constant in time, and it is then called a conservative system. Indeed, the already mentioned equation $F(x) = -dV/dx$ can be written as $m\ddot{x} + dV/dx = 0$, and multiplying it by \dot{x} , we get

$$\frac{d}{dt} \left(\frac{1}{2} m \dot{x}^2 + V(x) \right) = 0,$$

where the expression in brackets (which is the energy E) must be constant in time.

We recall that the Lotka–Volterra model (1.4) is a conservative system too, which implies that the phase portrait is a nonlinear center, and present here the derivation of the conserved quantity. For that, we divide the two equations of the system (considering $N, P \neq 0$) to eliminate the time dependence as follows:

$$\frac{dP}{dN} = \frac{P(\gamma N - \delta)}{N(\alpha - \beta P)},$$

which can be written as

$$\frac{\alpha - \beta P}{P} dP - \frac{\gamma N - \delta}{N} dN = 0.$$

Straightforward integration yields

$$\alpha \ln(P) - \beta P - \gamma N + \delta \ln(N) = E,$$

where E is constant along any trajectory, i.e., $dE/dt = 0$, and thus, we say that it is conserved on each curve. This quantity is also called a first integral of the system.

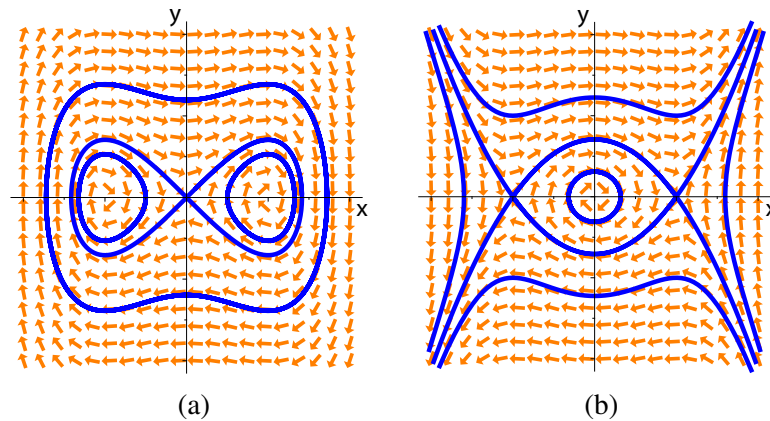


FIGURE 1.5: Phase portraits of system (1.5) in (a), showing homoclinic orbits; and of system (1.6) in (b), exhibiting a heteroclinic cycle. The arrows (orange) show the flow of the vector field of the system while the trajectories are curves (blue), corresponding to different initial conditions. The axes are $x, y \in \mathbb{R}$.

Next, we consider the previous example (1.5) but with opposite sign for the potential energy, which yields

$$\begin{cases} \dot{x} = y, \\ \dot{y} = -x + x^3, \end{cases} \quad (1.6)$$

and the phase portrait is displayed in Figure 1.5 (b). Although the equations of systems (1.5) and (1.6) are very similar, the phase portrait differs considerably. Both systems have three equilibria, but, on the one hand, the first model has two centers (nonzero fixed points) and one saddle point (origin) from which two homoclinic orbits emerge. On the other hand, the second system has one center (origin) and two saddle points (nonzero fixed points) connecting themselves via *heteroclinic orbits*. While a homoclinic orbit is a trajectory linking one single fixed point to itself, a heteroclinic orbit is a solution between two equilibria.

From the systems (1.5) and (1.6), we can already imagine that if the second equation is written as $\dot{y} = g_1x + g_3x^3$ with $g_1, g_3 \in \mathbb{R}$, then these two parameters determine the bifurcation. In Chapter 3, this kind of bifurcation, with homoclinic and heteroclinic orbits, will be accurately analyzed. There, the so-called Bogdanov–Takens bifurcation will be investigated, which will be defined in that chapter.

We recall that here we just want to show some types of other systems and bifurcations, without going into details.

Notice that the more we understand what dynamical systems are, the more we see that the world is filled with them. Nevertheless, these models should not be taken completely literally, but rather as a reference for the essential features of the system. For example, the logistic equation is not a biological truth, but an allusion for populations which have a predisposition to grow towards some carrying capacity. Among the (huge) far-reaching literature about modeling, there are many dynamical systems to be found which excellently describe real-life systems. Despite their precision, they should not to be considered as universal laws. In addition, we seize the moment to mention that, for instance, dynamical systems in books, articles and other publications, are often smooth (continuous and differentiable), but our

surroundings can behave nonsmoothly, as in electronic oscillators and mechanical systems. Therefore, with this thesis, we aim to develop an analysis for a better understanding of some systems with nonsmooth nonlinear terms. Before starting to deal with such systems, we show a few more models to explain other bifurcations.

For our next example we want to show a system in which its linearization does not predict the center or periodic orbits properly. For this purpose, we choose

$$\begin{cases} \dot{u} = -v + \mu u(u^2 + v^2), \\ \dot{v} = u + \mu v(u^2 + v^2), \end{cases} \quad (1.7)$$

where $\mu \in \mathbb{R}$ is a parameter. Firstly, it is easy to see that $(u_*, v_*) = (0, 0)$ is a fixed point. Secondly, the eigenvalues of the linearization of the system at this point are complex conjugates and purely imaginary, which means that the point $(0, 0)$ should be a center. However, this is only true if $\mu = 0$, since in this case, the system becomes linear. To analyze the full nonlinear model, we change the variables (u, v) to *polar coordinates* (r, φ) , where $r \geq 0$ is the radial direction (or radius) from the origin and $\varphi \in [0, 2\pi)$ is the angular coordinate of the ray. This change of coordinates is conducted by $u = r \cos \varphi, v = r \sin \varphi$, and applied to the original system (1.7), yields

$$\begin{cases} \dot{r} = \mu r^3, \\ \dot{\varphi} = 1. \end{cases}$$

From this system we first notice that the radial and angular equations are decoupled and the angular velocity, $\dot{\varphi}$, is constant. This system is therefore easier to analyze. If $\mu = 0$, the origin is indeed a center of closed orbits of the flow since the radius does not change and only the angle moves. Nevertheless, if $\mu < 0$, then $\dot{r} < 0$ and hence, the radius decreases in form of a spiral in towards the fixed point $(u_*, v_*) = (0, 0)$. On the contrary, if $\mu > 0$, then $\dot{r} > 0$ and thus the trajectories spiral out. With this information, we conclude that the equilibrium point is stable for $\mu < 0$, a center for $\mu = 0$, and unstable for $\mu > 0$, where $\mu = 0$ is then the bifurcation point.

Next, we extend, as follows, the previous example (1.7) to be even more interesting:

$$\begin{cases} \dot{u} = \mu u - \omega v - u(u^2 + v^2), \\ \dot{v} = \omega u + \mu v - v(u^2 + v^2), \end{cases}$$

where $\mu, \omega \in \mathbb{R}$ with $\omega \neq 0$ are the parameters of the system. In polar coordinates, it reads

$$\begin{cases} \dot{r} = \mu r - r^3, \\ \dot{\varphi} = \omega. \end{cases} \quad (1.8)$$

Notice that the first equation looks like (1.2), but in this case, since r is the radial direction, it cannot be negative. Hence, the fixed points, which are found solving $\dot{r} = 0$, are $r_* = 0$ and $r_* = \sqrt{\mu}$. The bifurcation diagram for r as a function of μ is similar to Figure 1.3 (a) for $r \geq 0$. Moreover, on the one hand, the parameter $\omega \neq 0$ denotes the velocity of the angle

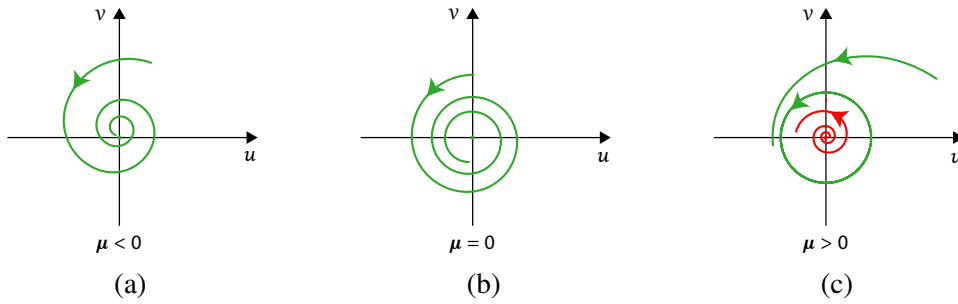


FIGURE 1.6: Phase portrait of (1.8) exemplifying the corresponding supercritical Hopf bifurcation. (a) For $\mu < 0$, the trajectories (green) spiral in towards the origin. (b) For $\mu = 0$, the trajectories (green) spiral in again to the fixed point, but slower than before. (c) For $\mu > 0$, a stable closed orbit is born (green) while the origin is now unstable (the trajectories starting close to it are red colored).

and thus, no qualitative change in the phase portrait can be expected with varying ω . On the other hand, μ plays a significant role in the system and we will show, as for (1.2), that it is the bifurcation parameter.

First of all, if $\mu < 0$, then only one fixed point exists, namely $r_* = 0$, and from the radial equation of (1.8), $\dot{r} < 0$ since the starting point is positive, $r_0 > 0$. Therefore, the origin is a stable, or attracting, equilibrium point. Secondly, if $\mu = 0$, then again $\dot{r} < 0$, but decreases much slower. Finally, if $\mu > 0$, the extra second equilibrium appears, $r_* = \sqrt{\mu}$, meaning that a periodic orbit is born. In this case, for $r_0 \in (0, \sqrt{\mu})$, the radial velocity is positive and thus, the trajectories spiral out towards the closed orbit defined by $r_* = \sqrt{\mu}$. On the contrary, for $r_0 > \sqrt{\mu}$, its velocity is negative and therefore, the solutions spiral in towards the periodic orbits. Hence, the origin is now unstable and a stable closed orbit has been born. This specific switch of qualitative behavior is called a *Andronov–Hopf bifurcation* and will play a very important role within the whole thesis, particularly, in Chapter 2. For simplicity, it is usually referred to as just a Hopf bifurcation. Analytically, this bifurcation is characterized by the existence of a complex conjugate pair of eigenvalues, $\lambda_{\pm} = \mu \pm i\omega$, which cross the imaginary axis, i.e., at some point the real part of the eigenvalues vanishes. In our case, this happens for $\mu = 0$.

Furthermore, as for the pitchfork bifurcation, we also have two different criticalities. For the system (1.8), the criticality is given by the sign of the cubic term in the radial equation, which is negative, and thus, supercritical. This behavior is illustrated in Figure 1.6.

As for (1.3), if the sign of the cubic term is positive, the bifurcation is then subcritical and the phase portrait is inverted as in Figure 1.3. Indeed, for $\mu < 0$, the phase plane would display an unstable periodic orbit with a stable fixed point, and for $\mu \geq 0$, the closed orbit disappears and the origin becomes unstable. In Figure 1.7, we display this behavior. Consequently, we see that the sign of the cubic term in (1.8) decides the criticality of the Hopf bifurcation. Condensing these ideas in a single system in polar coordinates, yields

$$\begin{cases} \dot{r} = \mu r + \sigma_s r^3, \\ \dot{\varphi} = \omega, \end{cases} \quad (1.9)$$

where the Hopf bifurcation occurs in μ and its criticality is given by $\text{sgn}(\sigma_s)$. In particular,

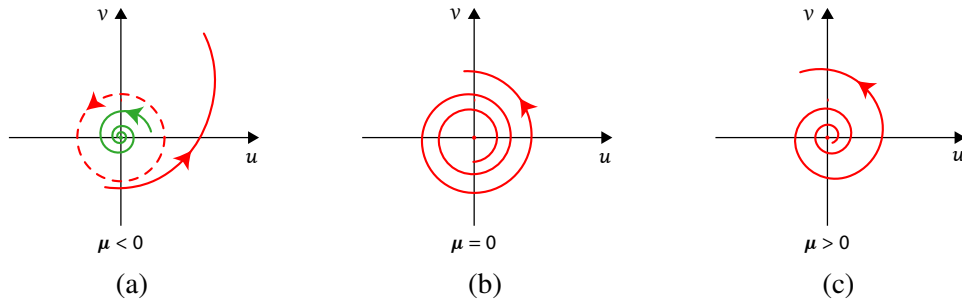


FIGURE 1.7: Phase portrait illustrating the corresponding subcritical Hopf bifurcation. (a) For $\mu < 0$, an unstable closed orbit exists (red dashed) and the fixed point is stable (green). (b) For $\mu = 0$, the periodic orbit disappears and all trajectories spiral out from the unstable origin. (c) For $\mu > 0$, the trajectories move faster away from the origin.

in this system, σ_s is called the *first Lyapunov coefficient*. We already anticipate that this coefficient (and the *second* one) will be of major interest in this thesis; see for instance the title of Chapter 2.

So far, we have observed that, for example, the equations (1.2), (1.3), as well as the planar system (1.9), are pretty straightforward to analyze. This is due to the fact that these models are “prototypes” for pitchfork and Hopf bifurcations. We say that these systems are prototypes since they might be simplified versions of more involved systems, but contain the whole information to study the qualitative behavior of the original model. In particular, such canonical forms are called *normal forms*, and may be obtained applying suitable transformations to the initial system; in other words, they are the same as the original systems, but in different coordinates.

Up to now, we have seen systems which do not explicitly depend on the time variable t . These are then called autonomous systems (or autonomous differential equations), and if the independent variable appears explicitly, the system is then nonautonomous. Further in this manuscript, we will deal with such systems.

After this introduction dedicated to a dynamical systems background for laymen, we proceed with the next section, which addresses to present the type of piecewise smooth nonlinearities considered in this thesis.

1.2 Bifurcations for systems with nonsmooth nonlinearities

Here we introduce the nonsmooth nonlinearities for our setting, which are formed by the product of one variable of the system with the absolute value function of another variable, namely $u_i|u_j|$ with $\mathbf{u} \in \mathbb{R}^n$. The effects of these terms in a system, regarding bifurcation theory, will be compared with a regular smooth system. Furthermore, we point out in which way these nonsmooth terms differ from other nonsmoothnesses and, before finishing this section, related literature considering similar (and not so similar) nonsmooth systems is discussed.

We start by recalling that for the Andronov–Hopf bifurcation from equilibria to periodic orbits, the most relevant characteristic parameter is the first Lyapunov coefficient, $\sigma_s \in \mathbb{R}$; in

particular, its sign. Indeed, if $\sigma_s \neq 0$, it determines the scaling and the direction of bifurcation relative to the real part of the critical eigenvalues of the linearization at the equilibrium point. As previously explained, and going one step further, the truncated normal form of the radial component on the center manifold reads

$$\dot{u} = \mu u + \sigma_s u^3, \quad (1.10)$$

with parameter $\mu \in \mathbb{R}$. For an excellent exposition of Andronov–Hopf bifurcation theory and applications, we refer to [41]; see also [25, 35]. In Figure 1.8 (a,b), we show again the associated pitchfork bifurcation for different signs of σ_s .

Generically, $\sigma_s \neq 0$ and the bifurcating periodic orbits either coexist with the unstable fixed point—the supercritical case, $\sigma_s < 0$; see Figure 1.6 (c)—or with the stable equilibrium—the subcritical case, $\sigma_s > 0$; see Figure 1.7 (a). This distinction is of significant interest for applications since, in the supercritical case, the transition induced by the bifurcation is a “soft” first order phase transition, while in the subcritical case, it is a “hard” one. In other words, the transition is “safe” in a control sense in the supercritical case and “unsafe” in the subcritical one, where the local information near the equilibrium is insufficient to determine the dynamics near the unstable equilibrium. In particular, nowadays this is of extreme importance in engineering applications, since it is the determining factor between safe and unsafe scenarios. For instance, in Chapter 4, we will profoundly explain the application in ship maneuvering models.

Therefore, a formula for the first Lyapunov coefficient is important from a theoretical as well as an applied viewpoint. In generic smooth bifurcation theory, such a formula is well known in terms of quantities derived from the Taylor expansion up to order three in the dependent variables and parameter evaluated at the equilibrium point and bifurcation parameter value, e.g., [35]. However, this cannot be applied, in general, for nonsmooth systems, although many applications show nonsmoothnesses. Nonsmooth terms appear in models for numerous phenomena and their studies have gained momentum in past decades, as illustrated by the enormous amount of literature; see [16, 32, 40, 55] and the references therein to hint at some. Before finishing this introductory section, we will discuss literature that relates to our situation.

In Chapter 2, we provide explicit formulas for the analogues of the first Lyapunov coefficient in systems with regular linear term and Lipschitz continuous but only piecewise smooth

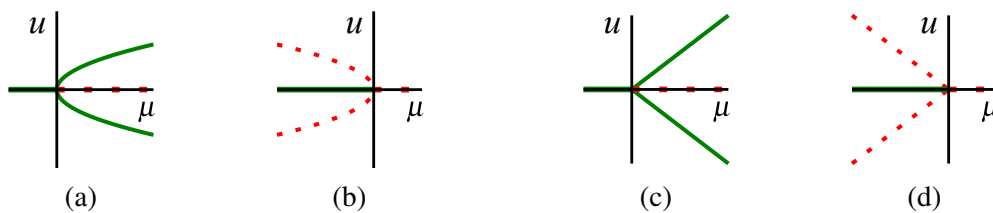


FIGURE 1.8: (a) Supercritical, $\sigma_s = -1$, and (b) subcritical, $\sigma_s = 1$, pitchfork bifurcation of (1.10) with stable (green) and unstable (red dashed) equilibria. In (c), (d) we plot the analogous “degenerate” pitchforks for the nonsmooth case (1.11), with $\sigma_{\#} = -1$ and $\sigma_{\#} = 1$, respectively.

nonlinear terms, with jumps in derivatives across switching surfaces. The system is smooth in the regions delimited by the switching surfaces but nonsmooth when crossing them. In fact, in this thesis, we focus on systems with these type of nonsmooth nonlinearities. Furthermore, we also discuss codimension-one degeneracies and the second Lyapunov coefficient. Such systems can be viewed as mildly nonsmooth but occur in various models, e.g., for systems with stick-slip motion [7, 15, 26], or for ocean circulation models, in particular, in the Stommel's 2-box model, which was firstly introduced in [53]. In a nutshell, this model consists of two containers of water with distinct temperature and salinity, which are connected by a very thin pipe at the bottom. The flow between both repositories is pushed by the difference of pressure. However, at the surface between the boxes there is also a flow to compensate the volume passed through the bottom tube, such that the amount of liquid remains the same in both containers. In this case, the direction of circulation is not relevant since the surface flow compensates the bottom flow in opposite direction, and thus, the absolute value function enters into the rate of flow or advective term. The Stommel's 2-box model has been broadly studied, e.g., [29], and recently in [46]. In these references, the nonsmooth terms are of the form $|x - y|x$, with x and y being the variables of the non-dimensionalized 2D system.

Moreover, nonsmooth nonlinearities are of relevance in ship maneuvering [3, 21, 56], which motivates the present study. Here, the hydrodynamic drag force (or viscous damping force) at high-enough Reynolds number is a nonsmooth function of the velocity u . In the next section, it will be shown that a dimensional and symmetry analysis with ρ being the density of water, C_D the drag coefficient, and A the effective drag area, yield

$$F_D = -\frac{1}{2}\rho C_D A u |u|.$$

Additionally, we remark here that, considering $\mathbf{u} \in \mathbb{R}^n$, where n depends on the specific model, effective hydrodynamic forces among the velocity components u_i, u_j , $1 \leq i, j \leq n$, are often likewise modeled by second order modulus terms: $u_i |u_j|$; cf. [21]. In a few lines, we will illustrate the effects of such terms in bifurcation theory. We consider first the corresponding nonsmooth version of (1.10),

$$\dot{u} = \mu u + \sigma_{\#} u |u|, \tag{1.11}$$

where the nonlinear term has the odd symmetry of the cubic term in (1.10) and is once continuously differentiable, but not twice. Although $|u|$ is not differentiable at zero, the product $u|u|$ is. Indeed, $d(u|u)/du = 2|u|$ exists for all $u \in \mathbb{R}$. However, it is just once differentiable since $d^2(u|u)/du^2 = d(2|u|)/du = 2\operatorname{sgn}(u)$ is not defined at zero. We note that in higher dimensions, the mixed nonlinear terms $u_i |u_j|$ for $i \neq j$ are not differentiable everywhere. Actually, we can briefly show this fact taking just two components, for instance, x, y (to simplify the notation) and the mixed terms $x|y|, y|x|$. The partial derivatives of $x|y|$ read $\left(\frac{\partial(x|y|)}{\partial x}, \frac{\partial(x|y|)}{\partial y}\right) = (|y|, x \operatorname{sgn}(y))$, and similarly for $y|x|$, we have $\left(\frac{\partial(y|x|)}{\partial x}, \frac{\partial(y|x|)}{\partial y}\right) = (y \operatorname{sgn}(x), |x|)$. These derivatives are not defined everywhere and hence, a combination of mixed terms causes the system to be nondifferentiable.

In Figure 1.8 (c,d), we plot the resulting bifurcation diagrams. Although these figures look similar compared to the smooth version, there are two fundamental differences. Choosing the supercritical case for both systems (1.10) and (1.11), i.e., $\sigma_s = \sigma_{\#} = -1$, these variations are the amplitude scaling law of μ , which changes from $\sqrt{\mu}$ to μ ; and the rate of convergence to the bifurcating state, which shifts from -2μ to $-\mu$. For the subcritical case we have an analogous comparison in which the scaling law deviates from $\sqrt{-\mu}$ to $-\mu$ and the rates of convergence are as for the supercritical situation.

Furthermore, we point out that, in this scalar equation, one can circumvent the absolute value by a singular coordinate change which transforms (1.11) into (1.10) up to time rescaling by 2. Indeed, on the one hand, for $u > 0$ we apply the change $u = \tilde{u}^2$ which implies $\tilde{u} \neq 0$. Then, after dividing (1.11) by \tilde{u} , we get

$$2\dot{\tilde{u}} = \mu\tilde{u} + \sigma\tilde{u}^3.$$

The fixed points are $\tilde{u} = 0$ and $\tilde{u}^2 = -\frac{\mu}{\sigma}$. On the other hand, for $u < 0$ we apply $u = -\bar{u}^2$ and similarly, we obtain the same equation as before, from which the fixed points are now $\bar{u} = 0$ and $-\bar{u}^2 = \frac{\mu}{\sigma}$.

Nevertheless, there is no such coordinate change for general systems of equations with nonsmooth terms of this kind. For instance, let us consider the following planar system

$$\begin{cases} \dot{u}_1 = \mu u_2 + u_1 |u_1|, \\ \dot{u}_2 = \omega u_1 + u_2 |u_2|, \end{cases} \quad (1.12)$$

and the change of coordinates $u_1 = \tilde{u}_1^2$. The first equation becomes $2\tilde{u}_1 \dot{\tilde{u}}_1 = \mu u_2 + \tilde{u}_1^4$, where the term $\frac{u_2}{\tilde{u}_1}$ has a singularity for $\tilde{u}_1 = 0$. Therefore, to find the fixed points, one might employ the right-hand side of the equations in (1.12), setting their left-hand side to zero before using $u_1 = \tilde{u}_1^2$ and $u_2 = \tilde{u}_2^2$. This way we would not get any singularity, but possibly artificial solutions.

Next, to show how the mixed nonlinear terms affect the analysis of a 2-dimensional system, we consider the following case with linear part in normal form:

$$\begin{cases} \dot{v} = \mu v - \omega w + f(v, w), \\ \dot{w} = \omega v + \mu w + g(v, w), \end{cases} \quad (1.13)$$

where $f(v, w)$, $g(v, w)$ contain the second order modulus terms as follows:

$$\begin{aligned} f(v, w) &= a_{11}v|v| + a_{12}v|w| + a_{21}w|v| + a_{22}w|w|, \\ g(v, w) &= b_{11}v|v| + b_{12}v|w| + b_{21}w|v| + b_{22}w|w|, \end{aligned} \quad (1.14)$$

and a_{ij}, b_{ij} , $1 \leq i, j \leq 2$, are real parameters.

These kinds of nonsmoothnesses are precisely the ones we focus on in this thesis. We recall that these nonsmooth terms are continuous but nondifferentiable. Nevertheless, it is worth mentioning that many other different nonsmooth systems are found in the literature, as

discontinuous systems. For instance, in mechanics, friction and impacts may produce jumps in the velocity and the force of a rigid-body, making the evolution of the system discontinuous. In particular, in such systems other questions arise regarding well-posedness; in general, it is not guaranteed that the solutions exist uniquely.

Going back to (1.13) with (1.14), our new first Lyapunov coefficient reads

$$\sigma_{\#} = 2a_{11} + a_{12} + b_{21} + 2b_{22}.$$

We remark that $\sigma_{\#}$ cannot be computed in the regular way due to the lack of differentiability. Therefore, a new approach is required, which we explain and prove in detail in Chapter 2.

In comparison, the classical first Lyapunov coefficient for purely cubic nonlinearity, i.e., the absolute value function $|\cdot|$ replaced by $(\cdot)^2$, reads

$$\sigma_s = 3a_{11} + a_{12} + b_{21} + 3b_{22}.$$

Moreover, the leading order expansion of the radius $r_{\#}$ and r_s of bifurcating periodic solutions in these cases read, respectively,

$$r_{\#}(\mu) = -\frac{3\pi}{2\sigma_{\#}}\mu + \mathcal{O}(\mu^2), \quad r_s(\mu) = 2\sqrt{-\frac{2}{\sigma_s}\mu} + \mathcal{O}(\mu).$$

Furthermore, in the case that the first Lyapunov coefficient of the nonsmooth case vanishes, i.e., $\sigma_{\#} = 0$, the amplitude of the periodic orbit takes the form

$$r_0 = \sqrt{-\frac{2\pi\omega}{\sigma_2}\mu} + \mathcal{O}(\mu),$$

analogous to the smooth case, but with second Lyapunov coefficient in this setting given by

$$\begin{aligned} \sigma_2 = & \frac{1}{9} \left[11(2a_{11}a_{22} - a_{12}b_{11} + a_{22}b_{21} - 2b_{11}b_{22}) \right. \\ & \left. + 13a_{11}b_{12} - 13a_{21}b_{22} - 2a_{12}a_{21} + 2b_{12}b_{21} \right] \\ & + \frac{\pi}{4}(2a_{22}b_{22} + a_{11}a_{21} + a_{12}a_{22} - b_{11}b_{21} - b_{12}b_{22} - 2a_{11}b_{11}). \end{aligned}$$

In the presence of smooth quadratic and cubic terms, the latter is modified with the classical terms, as we present in §2.2.1.

Despite the similarity between $\sigma_{\#}$ and σ_s , it turns out that there is no fixed smoothing of the absolute value function that universally predicts the correct criticality of Hopf bifurcations in these systems (§2.2.2). Let us briefly motivate how this issue arises. For that, we consider the absolute value function $f_1(x) = |x|$, and its L^∞ -approximations, with regularization parameter $\varepsilon > 0$, given by the convex approximation $f_2(x) = \frac{2}{\pi} \arctan(\frac{x}{\varepsilon})x$ (cf. [37]), and the nonconvex approximation $f_3(x) = \frac{2}{\pi} \arctan(\frac{x}{\varepsilon}(x-1)(x+1))x$.

Function $f_3(x)$ approximates the absolute value for large (absolute) values of x , as it is exhibited in Figure 1.9 (a). We further consider bifurcation diagrams for $\dot{x} = \mu x - f_i(x)x$,

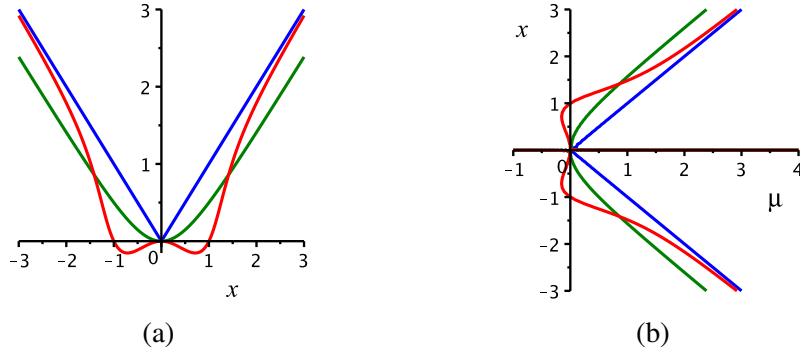


FIGURE 1.9: (a) Functions $f_1(x)$ in blue, $f_2(x)$ in green, and $f_3(x)$ in red, fixing $\varepsilon = 1$. (b) Comparison of bifurcation diagrams for f_1, f_2, f_3 , respect to μ , as explained in the text.

$i \in \{1, 2, 3\}$, in Figure 1.9 (b). In particular, $f_3(x)$ gives a “microscopically” wrong result, which is nevertheless correct “macroscopically”.

Now, we take the opportunity to make a short digression in order to explain the behavior of the bifurcating diagram for the equation with f_3 (fixing $\varepsilon = 1$) close to the origin; see Figure 1.9 (b). For that, let us Taylor expand the function f_3 in $x = 0$ to sixth order, which yields $f_3(x) = -\frac{2}{\pi}x^2 + \frac{8}{3\pi}x^4 + \mathcal{O}(x^6)$. We consider $\dot{x} = \mu x - f_3(x)x$, and truncate it to fifth order,

$$\dot{x} = \mu x + \mu_3 x^3 + \mu_5 x^5, \quad (1.15)$$

defining $\mu_3 = \frac{2}{\pi}$, $\mu_5 = -\frac{8}{3\pi}$ to simplify the exposition. The fixed points are $x_* = 0$ and $x_* = \pm \sqrt{\frac{-\mu_3 \pm \sqrt{\mu_3^2 - 4\mu_5 \mu}}{2\mu_5}}$. Since $\mu_3 > 0$ and $\mu_5 < 0$, for $\mu \in \left(\frac{\mu_3^2}{4\mu_5}, 0\right)$, all five equilibria are real, and the stability of them is exhibited in Figure 1.10 (a). Furthermore, from this image, it is easy to observe that, for small values of x , the plot looks similar to Figure 1.3 (b). However, from the term x^5 , the unstable branches turn around becoming stable branches of larger amplitudes. In particular, the smooth approximation $f_3(x)$ of the absolute value gives a macroscopically supercritical bifurcation (correct approximation) while the microscopic level shows a subcritical behavior (wrong result); see Figure 1.10 (a).

For completeness, we consider $\mu_3 < 0$, which implies that two of the fixed points are imaginary, and thus, the bifurcation diagram has two branches less than in the previous case with $\mu_3 > 0$; see Figure 1.10 (b).

In addition, if μ_5 changes sign, then the whole picture of the diagrams in Figure 1.10 is reversed as for the pitchfork bifurcation in Figure 1.3, meaning that the coefficient μ_5 decides the criticality of the bifurcation in this case.

Finally, and to end our digression, we just note that the kind of behavior depicted in Figure 1.10 (a) is called hysteresis, which denotes a lack of reversibility by means of varying the bifurcation parameter. This is due to the occurrence of different stable and unstable curves, giving a state the chance to jump from one branch to another. Indeed, if a state starts at the stable zero equilibrium in Figure 1.10 (a), and μ is increased, then passing $\mu = 0$, the state will jump to the upper stable branch. Now, if we decrease the parameter, the state will remain in the large amplitude branch and μ will have to be decreased further in order for the state to jump back to the original zero equilibrium curve.

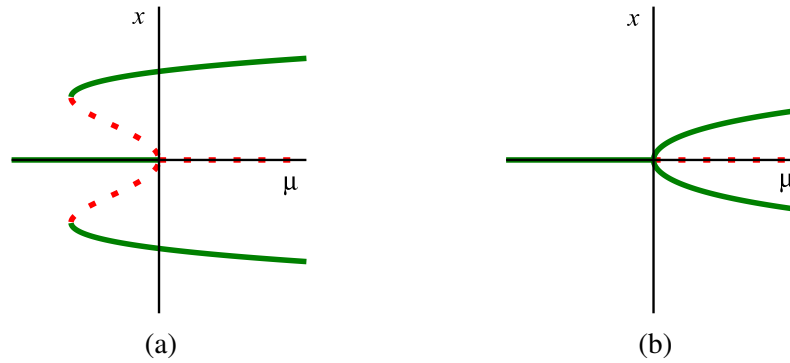


FIGURE 1.10: Bifurcation diagrams for (1.15) with $\mu_5 < 0$. In (a) $\mu_3 > 0$, and in (b) $\mu_3 < 0$. In both cases, stable fixed points are represented with green curves while unstable equilibria are depicted with dashed red curves.

Continuing with the above exposition regarding smoothing of the absolute value, we remark that nonsmooth terms in models typically stem from passing to a macro- or mesoscopic scale such that microscopic and smooth information is lost. Hence, the bifurcations in such models carry a macroscopic character and it is not surprising that an arbitrary smoothing changes this nature microscopically: a macroscopically supercritical bifurcation might show a subcritical behavior on the microscopic level. However, the relevant information for the model is the macroscopic character, and —for the class of models considered here— this is given by our newly derived Lyapunov coefficients.

We briefly discuss here related literature. As mentioned, piecewise smooth vector fields have been widely investigated in many different applications as well as from a theoretical point of view, leading to a broad analysis in terms of bifurcation theory; cf. [17, 32, 40]. Herein theory of continuous as well as discontinuous vector fields, e.g., [20, 31], is used and further developed. A major distinction between our case and the systems studied in the literature is that we assume a separation a priori of a linear part and a nonsmooth nonlinear part. Broadly studied are more general switching differential systems that are discontinuous across a switching surface or piecewise linear. These have been analyzed in various different forms, and we refer to [55] for an exhaustive list of references; a typical case of discontinuity across the switching manifolds arises from the Heaviside step functions in biology neural models, e.g., [1, 14, 27]. In analogy to center manifolds, the existence of invariant manifolds and sets has been investigated in [4] for Carathéodory vector fields and in [33, 60] for vector fields with one switching surface. The bifurcation of periodic orbits in planar vector fields with one axis as the switching line has been studied in [13, 23] via one-forms, and characteristic quantities have been determined, though the aforementioned Lyapunov coefficients are not included. Planar Hopf bifurcations for piecewise linear systems have been studied via return maps for one switching line in [34], for several switching lines meeting at a point in [6, 49, 62], and for a nonintersecting switching manifold using Liénard forms in [39]. Higher dimensional Filippov-type systems with a single switching manifold are considered in [63], which allows us to also abstractly study the occurrence of a Hopf bifurcation for our setting; see also [32]. An approach via averaging with a focus on the number of bifurcating periodic orbits

for discontinuous systems is discussed in [38]. Nevertheless, we are not aware of results in the literature that cover our setting and our results on the explicit derivation of Lyapunov coefficients and the leading order analysis of bifurcating periodic solutions.

1.3 Marine craft modeling and control

As mentioned in the previous section, ship maneuvering models, with piecewise smooth nonlinearities, motivate the current work since an approach for their study, in terms of stability and bifurcation analysis, has not been performed yet.

To start with, we discuss shortly the kinetics of watercraft, which relates the motion of a rigid-body with the forces causing it, and show the vector representation of a marine craft system.

We consider Newton's second law, $ma = f$, with m the mass of the body, a its acceleration and f the force acting on the body; and express it in terms of conservation of linear momentum p and angular momentum h . Then Euler's axioms are obtained: the first law reads $\dot{p} := f$, $p := mv$, where v is the velocity of its center of mass, and the second axiom takes the form $\dot{h} := m_C h$, $h := I\omega$, stating that the rate of change of angular momentum about a fixed point in an inertial reference frame equals the external moment of force m_C acting on the body, with I being the inertia tensor about the center of gravity of the body and ω the angular velocity.

From Euler's axioms the vector form of the rigid-body equations of motion take the form $\mathbf{M}\dot{\nu} = \mathbf{F}(\nu)$, with ν the vector of ship-fixed velocities, $\dot{\nu}$ its time derivative, \mathbf{M} the matrix of added mass coefficients and moments of inertia, and \mathbf{F} containing forces from the hull, rudder, propeller and hydrodynamics, as well as the Coriolis term. In particular, m, m_C, I are combined in \mathbf{M} , and the velocities v, ω are included in ν . For detailed derivations of the equations of motion for a marine craft we refer to [21].

Since now we know how the equations of motion for a marine craft look like, we continue showing which motions a vessel can experience. Models of ship maneuvering entail a selection of independent displacements and rotations, called degrees of freedom (DOF), which determine the orientation and displaced position of the vessel. Three of these motions are principally caused by sea waves: roll (rotation about the longitudinal axis), pitch (rotation about the transverse axis) and heave (vertical —up/down— motion). The other three motions, surge (longitudinal motion), sway (sideways motion) and yaw (rotation about the vertical axis), are caused mainly by internal forces, such as rudders and propellers, and external forces, such as maritime conditions, cf. [21].

By means of these 6 DOF, a marine craft maneuvering model can be represented with 12 ODEs: 6 equations for the position and 6 more for the velocity. We mention that a model including environmental forces (wind, waves, ocean current), for instance, could require additional equations. Nevertheless, reduced order models are frequently considered and a common simplification for relatively weak sea waves is the 3 DOF horizontal plane model for the velocities surge u , sway v , and yaw r ¹ [21, 43]; see Figure 1.11 (a). Even more reduced

¹For the notation of the yaw velocity in marine craft modeling, the use of the letter r is broadly extended. However, it has not to be mistaken with the radial component of the system in polar coordinates.

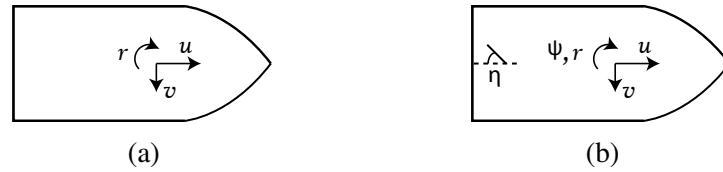


FIGURE 1.11: Ship-fixed coordinates sketches with 3 DOF: surge u , sway v and yaw r velocities. (a) 3-dimensional model. (b) 4-dimensional model including the yaw angle ψ and the steering angle η .

systems are used: 1 DOF models are useful to design forward velocity controllers (surge) or heading autopilot systems (yaw), to mention a few. Notice that although for the purpose of human comfort the motions roll, pitch and heave seem to be of relevance, due to their tendency to cause seasickness, these are not usually considered in reduced order models. One of the reasons is that many vessels actually have no direct control over all of them.

We consider then the mentioned 3 DOF horizontal plane model, with surge, sway and yaw velocities, and following [2, 3, 57], we include explicitly the yaw angle as the fourth variable. The system is further augmented by a P-controller (proportional controller) for yaw damping and yaw restoring. This results in a 4-dimensional system of ODEs; see Figure 1.11 (b) for a sketch of the considered variables in the ship model. This type of control is called “proportional” due to the following reasoning. For a P-control mechanism in the yaw damping, the control is proportional to the difference between the current state $r(t)$ and its target yaw velocity r_0 , resulting in $\varepsilon_r(r - r_0)$ with control strength ε_r . Analogously for the yaw restoring control, we have $\varepsilon_\psi(\psi - \psi_0)$, with target yaw angle ψ_0 and control strength ε_ψ . Notice that such a controller is considered to be a response to the size of the error, since the state of the system is r, ψ but the goal is r_0, ψ_0 , respectively. In this sense, the P-control applies a correction to the course of the vessel, and therefore, we have a linear feedback control.

For the model analyzed in the current manuscript, we follow [3] and therefore combine the rudder and the propeller forces into a single “thruster force”. This acts on the hull with an angle η ; see Figure 1.11 (b). The variable η is an external input which is assumed to obey the following control law design: $\eta = \varepsilon_r(r - r_0) + \varepsilon_\psi(\psi - \psi_0)$ with non-negative control strengths $\varepsilon_r, \varepsilon_\psi$. This realizes a P-control for r, ψ that combines both yaw damping and yaw restoring control, cf. [21]. Moreover, since in this case we have $\dot{\psi} = r$, the control can be viewed as a PD-control (proportional derivative control) for ψ or a PI-control (proportional integral control) for r . For completeness, we mention the existence of a PID-control (proportional integral derivative control), which considers all three terms of control in the same algorithm. However, this kind of controller will not be considered in our study. All these types of controllers are feedback control systems as well.

Before continuing, we spend a few lines to quickly introduce some of the main ship characteristics. First, the hull of a vessel is defined as its watertight body, i.e., the completely water-resistant enclosure of the marine craft. A propeller is a rotating mechanism to push the ship forward. It has blades that spin around in a fan-like structure. Next, a rudder is a vertical, blade-like surface used to steer the vessel, which acts by deflecting the water flow. Both propeller and rudder are generally placed at the back of the ship, also called aft or stern of the watercraft (the front of the marine craft is called fore or stem). As mentioned above,

we consider a combination of the propeller and the rudder forces into a thruster force, and call the resulting system “thruster model”. In particular, the longitudinal location of the ship thruster x_T will be a relevant design parameter in our study, as well as the propeller diameter D_p . The influence of the propeller frequency n_p will also be analyzed. Lastly, we emphasize that the parameters of the ship model are taken from the so-called Hamburg Test Case (HTC).

As we present the most relevant ingredients for our subsequent analysis, we come to the modeling of hydrodynamic forces, whose nature give rise to nonlinear terms, in particular, of nonsmooth character, which is decisive in the analysis of bifurcations, and requires new theory as developed in Chapter 2. We recall that one approach to the nonlinear terms follows the drag equation for high Reynolds number given by

$$F_D = -\frac{1}{2}\rho C_D A u |u|,$$

where u is the velocity of the body, ρ the density of the water, C_D the drag coefficient, and A the effective drag area, [21]. This equation is a consequence of the following reasoning. From experimental observation it is known that the drag force $F_D = F_D(\rho, A, u)$ is a function of ρ, A, u . Next, using dimensional analysis in a power law ansatz $F_D = \rho^\alpha A^\beta u^\gamma C$ with exponents $\alpha, \beta, \gamma \in \mathbb{R}$ and a constant C , we have that $M \cdot L \cdot T^{-2} = M^\alpha \cdot L^{-3\alpha} \cdot L^{2\beta} \cdot L^\gamma \cdot T^{-\gamma}$ must hold, where M denotes the quantity of mass, L of length and T of time, as usual. In the International System of Units these correspond to kilogram kg , meter m and second s , respectively. From the previous equality, we have that $\alpha = \beta = 1, \gamma = 2$, and hence the velocity has to be quadratic. However, since F_D is an opposing force, this must be odd with respect to u , i.e., the sign of the velocity is needed, and therefore, the term $u|u|$ is required.

Specifically, polynomial regression studies on the representation of hydrodynamic forces confirm that $u|u|, v|v|, r|r|$ and the mixed terms $v|r|, r|v|$, are the relevant higher order terms [59, 61]. These *second order modulus terms* can be regarded as square law damping in this context and may also be motivated by a Taylor expansion with correction for the signs [2]. We remark that ship models with third order Taylor approximations have been analyzed, e.g., in [44]. Moreover, a combination of truncated Taylor expansions with odd functions and second order modulus terms have been also considered in the literature, e.g., [43]. Nevertheless, regression studies show that these are in general not appropriate as they may lead to multicollinearity (producing redundant information), cf. [59].

Additionally, we briefly point out that hydrodynamic damping forces have diverse causes, such as skin friction, wave resistance and lifting forces. In particular, these last ones are due to the so-called cross-flow drag [21], which corresponds to the viscous effects in sway and yaw. The cross-flow drag force for the sway and yaw velocities are

$$\begin{aligned} d_v &= -\frac{1}{2}\rho \int_{L_{pp}} T(x) C_D(x) |v + xr|(v + xr) dx, \\ d_r &= -\frac{1}{2}\rho \int_{L_{pp}} T(x) C_D(x) x |v + xr|(v + xr) dx, \end{aligned}$$

respectively, where L_{pp} is the length between the perpendiculars of the hull, x is the longitudinal coordinate, $T(x)$ is the local draught and $C_D(x)$ is the local cross-flow drag coefficient. Notice the extra x term in the equation for the yaw. The idea behind d_v, d_r is to think about the hull of a ship split into strips in the lateral direction, i.e., perpendicular to the longitudinal length, of the same size and then to compute the local viscous drag of each segment, [24]. Finally, approximating the cross-flow drag integrals one gets the mixed second order modulus terms $v|r|, r|v|$, as explained in [43].

We recall that these terms are also obtained from the second order of the Taylor expansion, choosing the absolute values to correct the sign. Moreover, concerning the choice of model, we quote from [2, p. 75] that the “choice of the form of nonlinear terms is a matter of accuracy and convenience [...] also dependent on in which form the hydrodynamic derivatives were obtained in PMM [planar motion mechanism] test”. However, when it comes to bifurcation analysis, there is a significant difference between the second order modulus and cubic terms as discussed in detail in Chapter 2; see also §4.2.3.2.

For our analysis in Chapter 4 we consider a 3 DOF system with second order modulus terms as explained above, where the model parameters are taken from the HTC characteristics; see [57]. We show the instability of the straight motion of the ship without control and present the possibilities of stabilization in terms of the control strengths. More precisely, we analyze the effectiveness of proportional control (P-control) to stabilize the ship’s motion at the linear and nonlinear levels in a standard class of models for ship maneuvering with continuous nonsmooth nonlinearities. Such a theoretical study is not possible by standard center manifold reduction, but is relevant for predicting properties and guiding design choices, also with certification standards in mind [2]. Indeed, linear stability can be misleading if nonlinear effects produce an “unsafe” subcritical bifurcation, where the stabilized state has such a small basin of attraction that its linear stability may be practically irrelevant. In addition, a detailed understanding of the specific possibilities for linear stabilization in parameter space is already a challenge for a given model. In the present thesis, the results developed in Chapter 2 are used in Chapter 4 to analyze a nonsmooth marine craft model and determine the criticality of the Hopf bifurcation for the straight motion equilibrium.

For smooth models of marine vehicles the common reduction techniques (as center manifold reduction) are a standard tool, e.g., [45]. A general review in the context of smooth nonlinear ship models and motion can already be found in [50]. Our main goal in Chapter 4 is to present a method that can also handle the widely used continuous nonsmooth models. Furthermore, in a selected model class, we aim for a rather complete mathematical analysis of controllability and its failure, and of the local and global nonlinear effects associated with such a stabilization. We are specifically concerned with the standard problem of stabilizing the straight motion of a vessel [2, 21], which, however, has so far not been analyzed in this form.

1.4 Outline

This thesis has been written under the supervision of Jens D. M. Rademacher and it is structured as follows.

In Chapter 2, we focus on the analysis of Hopf bifurcations for mildly nonsmooth systems, with continuous linear part and a lack of differentiability in the nonlinear terms. More precisely, the nonlinearities are of the form $u_i|u_j|$ and thus, for $i \neq j$, the system is not differentiable everywhere but Lipschitz continuous. The bifurcation behavior and criticality are characterized, as in the smooth case, by the so-called first Lyapunov coefficient. Therefore, we provide explicit formulas for the corresponding first Lyapunov coefficient in our nonsmooth setting.

Furthermore, averaging theory is applied in order to obtain the first and second Lyapunov coefficients for our nonsmooth setting, and show how the first Lyapunov coefficient differs from the corresponding smooth version of the system. In addition, we show that there is no smoothing possible which brings one system to the other maintaining the sign of the coefficient and therefore the criticality of the bifurcation, meaning that a distinct bifurcation behavior occurs if Lipschitz continuity is considered instead of differentiability. Moreover, we provide a method (which we call the direct method) for demonstrating the existence of a locally unique branch of periodic orbits bifurcating from the bifurcation point. In addition, an explicit expression for the leading order amplitude of the periodic solution is derived, as well as a formula to determine the criticality of the system.

After the analysis of the 2-dimensional system with the absolute value, generalizations are considered, where a different nonsmooth function is presented and the system is extended to higher dimensions. In addition, since the linear part of the systems considered is usually in normal form, we reveal how challenging the previous analysis becomes when considering a general linear part. Finally, the results are applied to a shimming wheel model.

The results of this chapter and Appendix A, except A.2 as well as further explanations and minor corrections, have been published in [51].

In Chapter 3, the unfolding of the Bogdanov–Takens bifurcation is performed on a planar system in normal form with nonlinearities $x|x|, y|x|$. For that, we consider first a smooth system undergoing a symmetric Bogdanov–Takens bifurcation and consider then its nonsmooth version by means of changing x^2 to $|x|$. For this nonsmooth system, results on the criticality of the Hopf bifurcation, as well as the amplitude of the limit cycle, are shown and compared to the smooth case. In particular, the bifurcations for both systems at the distinct fixed points are examined, showing the scaling law of the Hopf bifurcation branches. Moreover, at the nonzero equilibria, it is found that the amplitude of the first Lyapunov coefficient for each system depends on different parameters, while at the zero fixed point the amplitude of the Lyapunov coefficient for the two systems depends on the same parameters. In addition, the presence of homoclinic and heteroclinic orbits is illustrated.

Afterwards, the nonsmooth function is generalized to a “broader” absolute value function, where the left and right slopes are not necessarily the same. We show how these nonsmooth

terms affect the pitchfork as well as the Hopf bifurcation, and compare further these results to the smooth system and to the nonsmooth case with the regular absolute value.

We end this chapter with a short analysis of an example of a system where homoclinic and heteroclinic orbits either occur or are broken depending on an extra parameter.

In Chapter 4 a specific model for ship maneuvering with piecewise nonsmooth nonlinearities is studied in terms of stabilization and bifurcation theory. We start with a 3-dimensional model with surge u , sway v , and yaw r velocities, see Figure 1.11 (a), combine the propeller and rudder forces into a single thruster force and rescale the system to facilitate its implementation and analysis. Next, this model is extended to a 4-dimensional system with yaw angle, ψ , and we add the yaw damping and yaw restoring proportional control $\eta = \varepsilon_r r + \varepsilon_\psi \psi$, see Figure 1.11 (b), with the corresponding rescaled quantities.

Subsequently, a theoretical analysis is presented, starting with the existence of the straight motion as an equilibrium of the system in relation to the propeller diameter D_p and the longitudinal thruster position x_T . Next, the linear stability of the straight motion is investigated, showing first that this equilibrium is unstable for the system without control, and then presenting a detailed analysis regarding stabilization and controllability of the straight motion of the rescaled 4 ODEs thruster model. The impact of the parameters n_p, D_p, x_T in this analysis is investigated as well, where n_p is the propeller frequency. In particular, the existence, location and geometry of the stability boundary is completely determined in terms of the control strengths $\varepsilon_r, \varepsilon_\psi$, considering also the dependence on the previously mentioned parameters.

After the linear analysis, we continue with the nonlinear stability and bifurcation analysis, presenting the case of the pitchfork bifurcation followed by the more involved Hopf bifurcation. We prove results on its existence for the rescaled thruster model as well as a formula for the leading order amplitude of the periodic orbit. It is then shown that for the classical HTC, the Hopf bifurcation is supercritical.

Later, a global bifurcation analysis is performed by numerical continuation, corroborating and illustrating the results of the previous theoretical analysis. Finally, simulations for the motions of the ship in Earth-fixed coordinates are presented.

The results presented in this chapter, together with Appendix B.1, have been submitted for publication [52], and include additional explanations.

A summary of the main results and some possible directions for further research topics are presented in Chapter 5. Regarding the Appendices, A exhibits detailed computations from Chapter 2 which are not shown in the section itself for sake of brevity. B displays the values of the HTC characteristics used for the analysis of the ship maneuvering model in Chapter 4, as well as the expressions of the rudder forces. Finally, C shows some notes concerning the simulations implemented for this thesis.

Chapter 2

Lyapunov Coefficients for Hopf Bifurcations

The focus of this chapter falls on n -dimensional systems of ordinary differential equations (ODEs) of the form $\dot{\mathbf{u}} = A(\mu)\mathbf{u} + G(\mathbf{u})$, with matrix $A(\mu)$ depending on a parameter $\mu \in \mathbb{R}$, and Lipschitz continuous nonlinear function $G(\mathbf{u}) = \mathcal{O}(|\mathbf{u}|^2)$. We shall assume the nonlinearity is smooth away from the smooth hypersurfaces $H_j, j = 1, \dots, n_H$, the *switching surfaces*, which intersect pairwise transversally at the equilibrium point $\mathbf{u}_* = 0$. We assume further that the smoothness of G extends to the boundary within each component of the complement of $\cup_{j=1}^{n_H} H_j \subset \mathbb{R}^n$.

The bifurcation of periodic orbits is —as in the smooth case— induced by the spectral structure of $A(\mu)$, which is (unless stated otherwise) hyperbolic except for a simple complex conjugate pair that crosses the imaginary axis away from the origin as μ crosses zero.

Our main results may be summarized informally as follows.

We infer from the result in [4] that the center manifold of the smooth case is replaced by a Lipschitz continuous invariant manifold (Proposition 2.2) and directly prove that a unique branch of periodic orbits emerges at the bifurcation (Theorem 2.3). Moreover, we prove that the quadratic terms of G are of generalized second order modulus type if G is piecewise C^2 smooth (Theorem 2.6). Here the absolute value in the above terms is replaced by

$$[u]_{p_-}^{p_+} = \begin{cases} p_+ u, & u \geq 0, \\ p_- u, & u < 0, \end{cases} \quad (2.1)$$

where $p_-, p_+ \in \mathbb{R}$ are general different slopes left and right of the origin, respectively.

The first Lyapunov coefficient can already be expressed in an integral form, but its explicit evaluation is somewhat involved, so that we defer it to §2.3.4. Instead, we start with the simpler case when A is in block-diagonal form, in normal form on the center eigenspace, and of pure second order modulus form ($p_+ = -p_- = 1$). For the planar situation, we derive a normal form of the bifurcation equation with rather compact explicit coefficients using averaging theory (Theorem 2.8). Beyond the first Lyapunov coefficient $\sigma_{\#}$, this includes the second Lyapunov coefficient σ_2 , which becomes relevant when $\sigma_{\#} = 0$, and which explains how the smooth quadratic and cubic terms interact with the nonsmooth ones in determining the bifurcation's criticality.

For refinement and generalization, and to provide direct self-contained proofs, we proceed using the Lyapunov–Schmidt reduction for the boundary value problem of periodic solutions and refer to this as the “direct method” (§2.2.3). We also include a discussion of the Bautin-type bifurcation in this setting, when $\sigma_{\#} = 0$. Concluding the planar case, we generalize the results to arbitrary p_+, p_- (§2.3.1).

These results for the planar case readily generalize to higher dimensions, $n > 2$, with additional hyperbolic directions (§2.3.2, §2.3.3). In addition, we apply the direct method to the situation with an additional nonhyperbolic direction in the sense that the linearization at the bifurcation has three eigenvalues on the imaginary axis: one zero eigenvalue and a complex conjugate pair. In this case, we show that either no periodic solutions bifurcate or two curves bifurcate (Corollaries 2.22, 2.26), depending on the sign of a particular combination of coefficients of the system that is assumed to be nonzero. For completeness, in §2.3.4 we discuss the modifications in the situation when the linear part is not in normal form.

Furthermore, we anticipate here that the basic idea of proof is to change coordinates to a nonautonomous system for which the lack of smoothness is in the time variable only, so that averaging and the “direct method” can be applied. We remark that in standard ODE literature on existence and bifurcations, smoothness of the time variable is often assumed, for example, [11], but it is not needed in parts relevant for us. Indeed, mere continuity in time is considered in [12, 28, 30], for instance.

Finally, in order to demonstrate how to apply our method in a concrete case, we discuss in §2.4 the 3-dimensional (3D) model of a shimmying wheel from [5]. This system is of the form presented above with pure second order modulus nonlinearity but linear part not in normal form, though it has a nonzero real eigenvalue, as well as a complex conjugate pair of eigenvalues that crosses the imaginary axis upon parameter change. We fully characterize the resulting bifurcations in Theorem 2.29.

This chapter is organized as follows. In §2.1 we discuss the abstract setting and provide basic results for the subsequent more explicit analysis. This is conducted in §2.2 for the planar case with linear part in normal form and nonlinear part with pure second order modulus terms for the nonsmooth functions, together with quadratic and cubic smooth functions. In §2.3 we generalize the absolute value to arbitrary slopes, and the system to higher space dimensions. Furthermore, we consider the linear part not being in normal form. Finally, in §2.4 we illustrate the application of our method and results to a concrete model.¹

2.1 Abstract viewpoint

In this section we discuss the abstract starting point for our setting and motivate the specific assumptions used in the following sections. We consider an n -dimensional system of autonomous ODEs in an open set $U \subset \mathbb{R}^n$, with the origin in U , of the form

$$\dot{\mathbf{u}} = A(\mu)\mathbf{u} + G(\mathbf{u}), \quad (2.2)$$

¹The main results presented in this chapter have been published in [51].

with matrix $A(\mu)$ depending on a parameter $\mu \in \mathbb{R}$, and Lipschitz continuous nonlinear $G(\mathbf{u})$.

We are interested in a detailed analysis of Hopf-type bifurcations at the equilibrium point $\mathbf{u}_* = 0$. This requires control over the linear part, which is separated a priori in (2.2) from the potentially nondifferentiable nonlinear part —note that G is differentiable at \mathbf{u}_* but not necessarily elsewhere. As usual for Hopf bifurcations, we assume that a pair of simple complex conjugate eigenvalues of $A(\mu)$ crosses the imaginary axis upon moving $\mu \in \mathbb{R}$ through zero. We collect the structural hypotheses on A and G without further loss of generality to our leading order analysis.

Hypothesis 2.1. *The eigenvalues of $A(\mu)$ are given by $\mu \pm i\omega(\mu)$ with smooth nonzero $\omega(\mu) \in \mathbb{R}$ and all other eigenvalues have nonzero real part at $\mu = 0$. The nonlinearity G is Lipschitz continuous and satisfies $G(\mathbf{u}) = \mathcal{O}(|\mathbf{u}|^2)$.*

We denote by E^c the center eigenspace of $A(0)$ corresponding to the eigenvalues $\pm i\omega(0)$ and first note the following result on invariant manifolds due to [4], which corresponds to center manifolds in the smooth case.

Proposition 2.2. *Under Hypothesis 2.1, for $0 \leq |\mu| \ll 1$ there exist 2D Lipschitz continuous invariant manifolds \mathcal{M}_μ in an open neighborhood $U_* \subset U$ of \mathbf{u}_* , which contain \mathbf{u}_* and all solutions that stay in U_* for all time. Furthermore, if at $\mu = 0$ all eigenvalues other than $\pm i\omega(0)$ have strictly negative real part, then each \mathcal{M}_μ is (transversally) exponentially attractive. In addition, each \mathcal{M}_μ is a Lipschitz continuous graph over E^c that depends Lipschitz continuously on μ .*

Proof. The statements follow directly from [4] upon adding a trivial equation for the parameter, as usual in center manifolds. As for center manifolds, the proof relies on cutting off the vector field near \mathbf{u}_* according to [4, Remark 6.2], and infer the existence of \mathcal{M}_μ from [4, Corollary 6.4]. The assumptions are satisfied since G is of quadratic order, which means the Lipschitz constant of G becomes arbitrarily small on small balls centered at \mathbf{u}_* . The stability statement follows from [4, Corollary 6.5]. \square

More refined stability information and estimates can be found in [4].

Next, we present a variant of the standard Andronov–Hopf bifurcation theorem (cf. [11]), which does not use any additional smoothness assumption. Here the uniqueness part relies on Proposition 2.2, but the existence is independent of it. As mentioned, in case of a single switching surface, the abstract bifurcation of periodic solutions without smoothness statement concerning the branch follows from the results in [63]; see also [32].

Theorem 2.3. *Assume Hypothesis 2.1. A locally unique branch of periodic solutions to (2.2) bifurcates from $\mathbf{u}_* = 0$ at $\mu = 0$. Specifically, there is a neighborhood $V \subset U$ of \mathbf{u}_* such that for $0 < |\mu| \ll 1$ periodic solutions to (2.2) in V are given (up to phase shift) by a Lipschitz continuous one-parameter family of $\tilde{\omega}(a)$ -periodic solutions $\mathbf{u}_{\text{per}}(t; a)$, $\mu = \mu(a)$ for $0 \leq a \ll 1$, $\tilde{\omega}(0) = \omega(0)$, $\mu(0) = 0$, whose projections into E^c have the complexified form $ae^{i\tilde{\omega}(a)t} + o(|a|)$. Moreover, we have the estimate $\text{dist}(\mathbf{u}_{\text{per}}(\cdot; a), E^c) = \mathcal{O}(a^2)$.*

This bifurcation is typically “degenerate” compared to the generic smooth Hopf bifurcation as in the example (1.11), where the bifurcating branch is not C^1 through $u = 0$.

Proof. We change coordinates such that $A(\mu)$ is in block-diagonal form with the upper left 2-by-2 block for the eigenspace E^c having diagonal entries μ and antidiagonal $\pm\omega(\mu)$ and the remaining lower right $(n-2)$ -dimensional block invertible at $\mu = 0$; the modified G remains of quadratic order and is Lipschitz continuous. Upon changing to cylindrical coordinates with vertical component $u = (u_3, \dots, u_n)$, where u_j are the scalar components of \mathbf{u} , we obtain

$$\begin{aligned} \dot{r} &= \mu r + \mathcal{R}_1(r, u; \mu), \\ r\dot{\varphi} &= \omega(0)r + \mathcal{R}_2(r, u; \mu), \\ \dot{u} &= \tilde{A}u + \mathcal{R}_3(r, u; \mu). \end{aligned} \tag{2.3}$$

Here \tilde{A} is the invertible right lower block at $\mu = 0$ and we suppress the dependence on φ of \mathcal{R}_j , $j = 1, 2, 3$. Due to Hypothesis 2.1 in these coordinates we have the estimates $\mathcal{R}_1(r, u; \mu) = \mathcal{O}(r^2 + |\mu|(r^2 + |u|) + |u|^2)$, $\mathcal{R}_j(r, u; \mu) = \mathcal{O}(r^2 + |\mu|(r + |u|) + |u|^2)$, $j = 2, 3$. We seek initial conditions r_0, u_0, φ_0 and a parameter μ that permit a periodic solution near the trivial solution $r = u = 0$. By Proposition 2.2 any such periodic orbit is a Lipschitz graph over E^c so that there is a periodic function \tilde{u} with $u = r\tilde{u}$. Let $T > 0$ denote the period and suppose $r(t) = 0$ for some $t \in [0, T]$. Then $u(t) = 0$ and therefore $\mathbf{u}(t) = \mathbf{u}_*$, so that $\mathbf{u} = \mathbf{u}_*$ is the trivial solution. Hence, we may assume that r is nowhere zero and thus \tilde{u} solves

$$\dot{\tilde{u}} = \tilde{A}\tilde{u} + \tilde{\mathcal{R}}_3(r, \tilde{u}; \mu),$$

where $\tilde{\mathcal{R}}_3(r, \tilde{u}; \mu) = \mathcal{O}(r + |\mu| + |\tilde{u}|(|\mu| + r|\tilde{u}|))$. By variation of constants we solve this for given r, φ as

$$\tilde{u}(t) = e^{\tilde{A}t}\tilde{u}_0 + \int_0^t e^{\tilde{A}(t-s)}\tilde{\mathcal{R}}_3(r(s), \tilde{u}(s); \mu)ds, \tag{2.4}$$

with initial condition $\tilde{u}(0) = \tilde{u}_0$. T -periodic solutions solve in particular the boundary value problem

$$\begin{aligned} 0 &= \tilde{u}(T) - \tilde{u}(0) = \int_0^T \dot{\tilde{u}}(s)ds \\ &= \int_0^T \tilde{A}e^{\tilde{A}s}\tilde{u}_0ds + \int_0^T \left(\tilde{A} \int_0^s e^{\tilde{A}(s-\tau)}\tilde{\mathcal{R}}_3(r(\tau), \tilde{u}(\tau); \mu)d\tau + \tilde{\mathcal{R}}_3(r(s), \tilde{u}(s); \mu) \right) ds \\ &= (e^{\tilde{A}T} - \text{Id})\tilde{u}_0 + \tilde{\mathcal{R}}_4(r, \tilde{u}; \mu), \end{aligned} \tag{2.5}$$

where $e^{\tilde{A}T} - \text{Id}$, with Id the identity matrix, is invertible since \tilde{A} is invertible. We have

$$\tilde{\mathcal{R}}_4(r, \tilde{u}; \mu) = \mathcal{O}(r_\infty + |\mu| + \tilde{u}_\infty(|\mu| + r_\infty\tilde{u}_\infty))$$

with

$$r_\infty = \sup\{r(t) \mid t \in [0, T]\}, \quad \tilde{u}_\infty = \sup\{|\tilde{u}(t)| \mid t \in [0, T]\}.$$

By (2.4) there is a $C > 0$ depending on T with

$$\begin{aligned} \tilde{u}_\infty &\leq C(|\tilde{u}_0| + r_\infty + |\mu| + \tilde{u}_\infty(|\mu| + r_\infty \tilde{u}_\infty)) \\ \iff (1 - C(|\mu| + r_\infty \tilde{u}_\infty))\tilde{u}_\infty &\leq C(|\tilde{u}_0| + r_\infty + |\mu|), \end{aligned}$$

so that for $0 \leq |\tilde{u}_0|, r_\infty, |\mu| \ll 1$ it follows $\frac{1}{2} \leq (1 - C(|\mu| + r_\infty \tilde{u}_\infty))$ and therefore $\tilde{u}_\infty \leq 2C(|\tilde{u}_0| + r_\infty + |\mu|)$. Thus,

$$\tilde{\mathcal{R}}_4(r, \tilde{u}; \mu) = \mathcal{O}(r_\infty + |\mu| + |\tilde{u}_0|(|\mu| + r_\infty |\tilde{u}_0|)).$$

Based on this, the uniform Banach contraction principle applies upon rewriting (2.5) as

$$\tilde{u}_0 = \left(e^{\tilde{A}T} - \text{Id} \right)^{-1} \tilde{\mathcal{R}}_4(r, \tilde{u}; \mu),$$

which yields a locally unique Lipschitz continuous solution $\tilde{u}_0(r, \varphi; \mu) = \mathcal{O}(r_\infty + |\mu|)$. Note that together with the aforementioned, this implies the estimate $\tilde{u}_\infty = \mathcal{O}(r_\infty + |\mu|)$.

Substituting $u(t) = r(t)\tilde{u}(t)$ with initial condition $\tilde{u}_0(r, \varphi; \mu)$ for \tilde{u} into the first two equations of (2.3) gives

$$\begin{aligned} \dot{r} &= \mu r + \mathcal{R}_5(r; \mu), \\ \dot{\varphi} &= \omega(0) + \mathcal{R}_6(r; \mu), \end{aligned} \tag{2.6}$$

where we have divided the equation for φ by r , since we look for nonzero solutions, and

$$\begin{aligned} \mathcal{R}_5(r; \mu) &= r\mathcal{O}(r + |\mu|r + |\tilde{u}|(|\mu| + r|\tilde{u}|)) = r\mathcal{O}(r_\infty + |\mu|r_\infty) = r\mathcal{O}(r_\infty), \\ \mathcal{R}_6(r; \mu) &= \mathcal{O}(r_\infty + |\mu|). \end{aligned}$$

Since $\omega(0) \neq 0$, for $0 \leq r, |\mu| \ll 1$ we may normalize the period to $T = 2\pi$ and obtain

$$\frac{dr}{d\varphi} = \frac{\mu r + \mathcal{R}_5(r; \mu)}{\omega(0) + \mathcal{R}_6(r; \mu)} = r \left(\frac{\mu}{\omega(0)} + \mathcal{R}_7(r; \mu) \right), \tag{2.7}$$

where $\mathcal{R}_7(r; \mu) = \mathcal{O}(r_\infty + |\mu|r_\infty) = \mathcal{O}(r_\infty)$ follows from direct computation. Analogous to \tilde{u} above, the boundary value problem $r(2\pi) = r(0)$ can be solved by the uniform contraction principle, which yields a locally unique and Lipschitz continuous solution $\mu(r_0) = \mathcal{O}(r_0)$. Since φ is 2π -periodic, any periodic solution has a period $2\pi m$ for some $m \in \mathbb{N}$, and the previous computation gives a unique solution for any m , from which we took the one with minimal period, i.e., $m = 1$.

Finally, the statement of the form of periodic solutions directly proceeds with $a = r_0$ from changing back to the original time scale and coordinates. Notice that $r_\infty = \mathcal{O}(r_0)$ holds true since we are integrating an ODE over a bounded interval, such that the ratio between r_∞ and r_0 is a bounded quantity, which is uniform because the vector field goes to zero when r goes to zero. Therefore, and together with $\mu(r_0) = \mathcal{O}(r_0)$, the previous estimate $\tilde{u}_\infty = \mathcal{O}(r_\infty + |\mu|)$ becomes $\tilde{u}_\infty = \mathcal{O}(r_0)$. Moreover, applying the supremum norm on both sides of $u = r\tilde{u}$ one gets $u_\infty = r_\infty \tilde{u}_\infty$, which is precisely of order $\mathcal{O}(r_0^2)$, as we wanted to prove. \square

While this theorem proves the existence of periodic orbits, it does not give information about their location in parameter space, scaling properties, and stability; the problem is to control the leading order part of \mathcal{R}_7 in (2.7), which—in contrast to the smooth case—turns out to be tedious. Consequently, we next aim to identify a suitable setting analogous to the center manifold reduction, and normal form transformations for a smooth vector field. In particular, we seek formulas for the analogue of the first Lyapunov coefficient from the smooth framework, whose sign determines whether the bifurcation is sub- or supercritical.

In order to specify a setting that allows for such an analysis, and is also relevant in applications, we will assume additional regularity away from sufficiently regular hypersurfaces $H_j, j = 1, \dots, n_H$, and denote $H := \cup_{j=1}^{n_H} H_j$. We refer to these hypersurfaces as *switching surfaces* and assume these intersect pairwise transversally at the equilibrium point $\mathbf{u}_* = 0$.

Hypothesis 2.4. *The switching surfaces $H_j, j = 1, \dots, n_H$, are C^k smooth, $k \geq 1$, and intersect transversally at $\mathbf{u}_* = 0$. In each connected component of $U \setminus H$ the function G is C^k smooth and has a C^k extension to the component's boundary.*

For simplicity, and with applications in mind, we consider only two switching surfaces, $n_H = 2$. In order to facilitate the analysis, we first map H_1, H_2 locally onto the axes by changing coordinates.

Lemma 2.5. *Assume Hypotheses 2.1 and 2.4 and let $n_H = 2$. There is a neighborhood $V \subset U$ of \mathbf{u}_* and a diffeomorphism Ψ on V such that $\Psi(H_j \cap V) = \{u_j = 0\} \cap \Psi(V), j = 1, 2$; in particular $\Psi(\mathbf{u}_*) = 0$. In subsequent cylindrical coordinates $(r, \varphi, u) \in \mathbb{R}_+ \times [0, 2\pi) \times \mathbb{R}^{n-2}$ with respect to the (u_1, u_2) -coordinate plane, the vector field is C^k with respect to (r, u) .*

Proof. The smoothness of $H_j, j = 1, 2$, and their transverse intersection allow for a smooth change of coordinates that straighten H_1, H_2 locally near \mathbf{u}_* and map these onto the coordinate hypersurfaces $\{u_1 = 0\}, \{u_2 = 0\}$, respectively. The assumed smoothness away from the switching surfaces implies the smoothness in the radial direction. \square

A concrete analysis of the nature of a Hopf bifurcation requires additional information on the leading order terms in G . As shown subsequently, a sufficient condition to identify the structure of the quadratic terms is Hypothesis 2.4 with $k = 2$, where we use the notation $[\cdot]_{p_{\pm}}^{p_{\pm}}$ as defined in (2.1).

Theorem 2.6. *Assume Hypotheses 2.1 and 2.4 for $k \geq 2$ and let $n_H = 2$. In the coordinates of Lemma 2.5, the nonsmooth quadratic order terms in a component $G_j, j = 1, \dots, n$, of G are of the form $u_{\ell} [u_i]_{p_{\pm}}^{p_{\pm}}, 1 \leq \ell \leq n, i = 1, 2$, where $p_+, p_- \in \mathbb{R}$ depend on i, ℓ, j and are the limits of second derivatives of G on the different connected components of $\mathbb{R}^n \setminus H$.*

Proof. Consider a coordinate quadrant and let \tilde{G} be the extension of G to its closure. By assumption, we can Taylor expand $\tilde{G}(\mathbf{u}) = \frac{1}{2} D^2 \tilde{G}(0)[\mathbf{u}, \mathbf{u}] + o(|\mathbf{u}|^2)$ since $G(0) = 0$ as well as $D\tilde{G}(0) = 0$. However, for different coordinate quadrants the second order partial derivatives may differ. By the form of H in Lemma 2.5, one-sided derivatives transverse to the coordinate axes might be distinct only for the u_1, u_2 axes. Hence, at $\mathbf{u} = 0$ second order derivatives involving u_1, u_2 may differ, and we denote by $p_{j\ell i_{\pm}}$ the partial derivatives

$\frac{\partial^2}{\partial u_i \partial u_\ell} G_j(0)$, $1 \leq \ell \leq n$, that are one-sided with respect to $i = 1, 2$ as indicated by the sign. The functions $[u_i]_{p_j \ell i}^{p_j \ell i}$ thus provide a closed formula for the quadratic terms of G_j as claimed. \square

Even with explicit quadratic terms in these coordinates, an analysis based on the coordinates of Lemma 2.5 remains a challenge.

Remark 2.7. *In cylindrical coordinates relative to E^c (cf. (2.3)), the vector field is generally not smooth in the radial direction. In general, smoothness cannot be achieved by changing coordinates as this typically modifies H to be nonradial. In particular, we cannot assume, without loss of generality, that the linear part in the coordinates of Lemma 2.5 is in block-diagonal form or in Jordan normal form as in (2.3).*

We recall from the introduction the planar system with linear part in normal form

$$\begin{cases} \dot{v} = \mu v - \omega w + f(v, w), \\ \dot{w} = \omega v + \mu w + g(v, w), \end{cases} \quad (2.8)$$

where $f(v, w)$, $g(v, w)$ contain the second order modulus terms as follows

$$\begin{aligned} f(v, w) &= a_{11}v|v| + a_{12}v|w| + a_{21}w|v| + a_{22}w|w|, \\ g(v, w) &= b_{11}v|v| + b_{12}v|w| + b_{21}w|v| + b_{22}w|w|, \end{aligned} \quad (2.9)$$

and a_{ij} , b_{ij} , $1 \leq i, j \leq 2$, are real parameters. However, in contrast to (2.8) (and (2.3)), the linear part is generally not in normal form. For exposition, we consider the $n = 2$ situation, where H_1, H_2 are the u_1 - and u_2 -axes, respectively, which reads

$$\begin{pmatrix} \dot{u}_1 \\ \dot{u}_2 \end{pmatrix} = \begin{pmatrix} m_1 & m_2 \\ m_3 & m_4 \end{pmatrix} \begin{pmatrix} u_1 \\ u_2 \end{pmatrix} + \begin{pmatrix} f_1(u_1, u_2) \\ f_2(u_1, u_2) \end{pmatrix}, \quad (2.10)$$

where $G = (f_1, f_2)$ is nonlinear. Based on Hypothesis 2.1 the linear part satisfies $\mu = \frac{1}{2}(m_1 + m_4)$, with $\mu = 0$ at the bifurcation point, and the determinant at $\mu = 0$ is positive so that we get together $m_1^2 + m_2m_3 < 0$ and $m_2m_3 < 0$. Upon changing to polar coordinates we obtain, generally different from (2.6),

$$\begin{cases} \dot{r} = M(\varphi)r + \chi_2(\varphi)r^2 + \mathcal{O}(r^3), \\ \dot{\varphi} = W(\varphi) + \Omega_1(\varphi)r + \mathcal{O}(r^2), \end{cases} \quad (2.11)$$

where M, χ_2, W, Ω_1 are 2π -periodic in φ . Abbreviating $c := \cos \varphi$ and $s := \sin \varphi$, we have explicitly

$$\begin{aligned} M(\varphi) &= m_1c^2 + (m_2 + m_3)sc + m_4s^2, \\ W(\varphi) &= m_3c^2 + (m_4 - m_1)sc - m_2s^2, \end{aligned}$$

where χ_2, Ω_1 are continuous but in general nonsmooth in φ as a combination of generalized absolute value terms (2.1). Due to the conditions at $\mu = 0$ we have $W(\varphi) \neq 0$ for any φ so

that $\dot{\varphi} \neq 0$ for $0 \leq r, |\mu| \ll 1$. This allows us to rescale time in (2.11) analogous to (2.7) and gives

$$r' := \frac{dr}{d\varphi} = \frac{M(\varphi)r + \chi_2(\varphi)r^2}{W(\varphi) + \Omega_1(\varphi)r} + \mathcal{O}(r^3) = \frac{M(\varphi)}{W(\varphi)}r + \left(\frac{\chi_2(\varphi)}{W(\varphi)} - \frac{M(\varphi)\Omega_1(\varphi)}{W(\varphi)^2} \right) r^2 + \mathcal{O}(r^3). \quad (2.12)$$

Using averaging theory, as will be discussed in detail in §2.2.1, periodic orbits of (2.12) are generically in 1-to-1 correspondence with equilibria of the averaged form of (2.12) given by

$$\bar{r}' = \Lambda \bar{r} + \Sigma \bar{r}^2 + \mathcal{O}(\bar{r}^3), \quad (2.13)$$

where $\Lambda, \Sigma \in \mathbb{R}$ are the averages of the linear and quadratic coefficients, respectively:

$$\Lambda = \frac{1}{2\pi} \int_0^{2\pi} \frac{M(\varphi)}{W(\varphi)} d\varphi = \frac{m_1 + m_4}{\sqrt{-4m_2m_3 - (m_1 - m_4)^2}}, \quad (2.14)$$

$$\Sigma = \frac{1}{2\pi} \int_0^{2\pi} \left(\frac{\chi_2(\varphi)}{W(\varphi)} - \frac{M(\varphi)\Omega_1(\varphi)}{W(\varphi)^2} \right) d\varphi. \quad (2.15)$$

The explicit expression in (2.14) follows from a straightforward but tedious calculation; note that $\Lambda \in \mathbb{R}$ for $0 \leq |\mu| \ll 1$ due to the above conditions at bifurcation. Notably, the sign of Λ depends on the choice of the normal form, which in this case corresponds to the first and second row of the linear part being $(\mu, -\omega)$, (ω, μ) , respectively, as in (2.8), with $\omega > 0$. For the situation in which $\omega < 0$, then the expression in (2.14) has to be chosen with opposite sign, i.e., $-\Lambda$.

For $\Sigma \neq 0$, equilibria of (2.13) are $\bar{r} = 0$ and $\bar{r} = -\Lambda/\Sigma$, which gives a branch of non-trivial periodic orbits parameterized by Λ . The direction of branching, and thus the super- and subcriticality, is determined by the sign of Σ , which therefore is a generalized first Lyapunov coefficient. However, this is still unsatisfying as it does not readily provide an explicit algebraic formula for Σ in terms of the coefficients of $A(\mu)$ and G .

In order to further illustrate this issue, let f_1, f_2 be purely quadratic and built from second order modulus terms as in (2.9). In this case we explicitly have

$$\chi_2(\varphi) = c|c|(a_{11}c + b_{11}s) + c|s|(a_{12}c + b_{12}s) + s|c|(a_{21}c + b_{21}s) + s|s|(a_{22}c + b_{22}s), \quad (2.16)$$

$$\Omega_1(\varphi) = - \left[c|c|(a_{11}s - b_{11}c) + c|s|(a_{12}s - b_{12}c) + s|c|(a_{21}s - b_{21}c) + s|s|(a_{22}s - b_{22}c) \right], \quad (2.17)$$

which are continuous but not differentiable due to the terms involving $|c|, |s|$.

Clearly, the building blocks of the integrals in (2.15) are rational trigonometric functions with denominator W of degree 2 and numerators of degrees 3 and 5. However, explicit formulas based on this appear difficult to obtain, so that we instead change to linear normal form as discussed in §2.3.4, with the caveat that the nonlinear terms are, in general, not smooth in the radius.

Indeed, in the normal form case $m_1 = \mu, m_2 = -\omega, m_3 = \omega, m_4 = \mu$, with $\omega > 0$, the

situation becomes manageable: in (2.11) we have constant $M(\varphi) = \mu$ and $W(\varphi) = \omega(\mu)$, and we will show below that then $\Sigma = \frac{2}{3\pi\omega}\sigma_{\#}$, with $\sigma_{\#}$ as defined in §1.2. Therefore, until §2.3.4 we will assume that the linear part is in normal form in the coordinates of Lemma 2.5, which also occurs in applications as mentioned in §1.2.

2.2 Planar normal form case with absolute values

In this section we discuss two approaches to prove existence and bifurcation of periodic orbits in our mildly nonsmooth setting. First, we provide details for the aforementioned approach by averaging, and second we discuss a direct approach that provides a detailed unfolding by Lyapunov–Schmidt reduction and that can also be used in some nongeneric cases.

While we focus here on the planar case, both methods readily generalize to higher dimensional settings. For averaging one needs normal hyperbolicity in general, and for the direct approach we present higher dimensional cases in upcoming sections. Without change in the leading order result, for simplicity we fix the imaginary part $\omega \neq 0$ independent of μ .

To simplify the exposition in this section, we assume the linear part is in normal form and the nonsmooth terms are of second order modulus type, i.e., with the absolute value $|\cdot| = [\cdot]_{-1}^1$. The general case with $[\cdot]_{p_{\pm}}^p$, defined in (2.1), will be discussed in §2.3. With the linear part in normal form and including smooth quadratic and cubic terms we thus consider the form of (2.2) given by (cf. (2.8))

$$\begin{cases} \dot{v} = \mu v - \omega w + f(v, w) + f_q(v, w) + f_c(v, w), \\ \dot{w} = \omega v + \mu w + g(v, w) + g_q(v, w) + g_c(v, w), \end{cases} \quad (2.18)$$

where f, g are as in (2.9), and

$$\begin{aligned} f_q(v, w) &= a_1 v^2 + a_2 v w + a_3 w^2, & f_c(v, w) &= c_{a1} v^3 + c_{a2} v w^2 + c_{a3} v^2 w + c_{a4} w^3, \\ g_q(v, w) &= b_1 v^2 + b_2 v w + b_3 w^2, & g_c(v, w) &= c_{b1} v^3 + c_{b2} v w^2 + c_{b3} v^2 w + c_{b4} w^3, \end{aligned}$$

and $\mu, \omega \in \mathbb{R}$ with $\omega \neq 0$, and $a_{ij}, b_{ij}, a_k, b_k, c_{ah}, c_{bh}, \forall i, j \in \{1, 2\}, \forall k \in \{1, 2, 3\}, \forall h \in \{1, 2, 3, 4\}$ are real constants, all viewed as parameters.

2.2.1 Averaging

We next show how to apply averaging theory to (2.18) in polar coordinates. For that we recall first the coefficients $\sigma_{\#}, \sigma_2$ introduced in §1.2,

$$\sigma_{\#} = 2a_{11} + a_{12} + b_{21} + 2b_{22}, \quad (2.19)$$

$$\begin{aligned} \sigma_2 &= \frac{1}{9} \left[11(2a_{11}a_{22} - a_{12}b_{11} + a_{22}b_{21} - 2b_{11}b_{22}) \right. \\ &\quad \left. + 13a_{11}b_{12} - 13a_{21}b_{22} - 2a_{12}a_{21} + 2b_{12}b_{21} \right] \\ &\quad + \frac{\pi}{4} (2a_{22}b_{22} + a_{11}a_{21} + a_{12}a_{22} - b_{11}b_{21} - b_{12}b_{22} - 2a_{11}b_{11}). \end{aligned} \quad (2.20)$$

In addition to these two terms, the following appear as normal form coefficients:

$$\begin{aligned} S_q &:= a_1 a_2 + a_2 a_3 - b_1 b_2 - b_2 b_3 - 2a_1 b_1 + 2a_3 b_3, \\ S_c &:= 3c_{a1} + c_{a2} + c_{b3} + 3c_{b4}. \end{aligned} \quad (2.21)$$

Notice that $\sigma_{\#}, \sigma_2$ depend only on f, g , i.e., the nonsmooth terms, while S_q depends on the smooth quadratic terms f_q, g_q , and S_c on the cubic ones f_c, g_c .

Theorem 2.8. *For $0 < |\mu| \ll 1$ periodic solutions to (2.18) are locally in 1-to-1 correspondence with equilibria of the averaged normal form in polar coordinates $v = r \cos \varphi$, $w = r \sin \varphi$ of (2.18) given by*

$$\bar{r}' = \frac{\mu}{\omega} \bar{r} + \frac{2}{3\pi\omega} \sigma_{\#} \bar{r}^2 + \left(\frac{1}{8\omega^2} S_q + \frac{1}{8\omega} S_c + \frac{1}{2\pi\omega^2} \sigma_2 \right) \bar{r}^3 + \mathcal{O} \left(\bar{r}^4 + \sigma_{\#} \bar{r}^3 + |\mu| \bar{r}^2 \right). \quad (2.22)$$

We observe that, on the one hand, if $\sigma_{\#} \neq 0$, then the bifurcation structure is determined by the quadratic term and all cubic terms are of higher order. On the other hand, if $\sigma_{\#} = 0$, then the cubic term $\sigma_{\#} \bar{r}^3$ is removed from the remainder terms. In addition, we note that $|\mu| \bar{r}^2$ within the remainder terms is effectively also of higher order.

Furthermore, it is worth to mention that in accordance with the smooth Hopf bifurcation, the quadratic term in \bar{r}' vanishes for vanishing nonsmooth terms $f = g = 0$, so that the leading order nonlinear term in the normal form is cubic. Before giving the proof we note and discuss an important corollary. For this recall the pitchfork bifurcation of (1.11) which is degenerate in that the bifurcating branch is nonsmooth.

Corollary 2.9. *If $\sigma_{\#} \neq 0$, then at $\mu = 0$, the leading order of (2.22) undergoes a degenerate pitchfork bifurcation in μ , where non-trivial equilibria are of the form*

$$r_0(\mu) = -\frac{3\pi}{2\sigma_{\#}} \mu + \mathcal{O}(\mu^2). \quad (2.23)$$

In this case, (2.18) undergoes a degenerate Hopf bifurcation in the sense that for $0 < |\mu| \ll 1$ periodic solutions to (2.18) are locally in 1-to-1 correspondence with $r_0(\mu)$, which is also the expansion of the radial component of the periodic solutions. In particular, this Hopf bifurcation is subcritical if $\text{sgn}(\sigma_{\#}) > 0$ and supercritical if $\text{sgn}(\sigma_{\#}) < 0$. Moreover, the bifurcating periodic orbits of (2.18) are of the same stability as the corresponding equilibria in (2.22).

Proof of Corollary 2.9. The bifurcation statement follows directly from Theorem 2.8 and the statement about stability follows from [48, Thm. 6.3.3]. Since $r_0 \geq 0$ we must have $\frac{\mu}{\sigma_{\#}} \geq 0$. Hence, the sign of $\sigma_{\#}$ determines the criticality of the bifurcation. \square

The radial components $r(\varphi; \mu)$ of the periodic orbits are in general not constant in φ , but this dependence is of order μ^2 . We thus consider (2.23) as the leading order amplitude of the periodic solutions.

Remark 2.10. Since the criticality of the Hopf bifurcation is given by the sign of $\sigma_{\#}$, it is an analogue of the first Lyapunov coefficient in this nonsmooth case. For the smooth case

$f = g = 0$, where $\sigma_{\#} = \sigma_2 = 0$, the classical first Lyapunov coefficient is $\sigma_s := \frac{1}{8\omega}S_q + \frac{1}{8}S_c$. In §2.2.2 we show that there is no canonical way to infer the sign of $\sigma_{\#}$ from smoothing a priori.

Remark 2.11. In the case that $\sigma_{\#} = 0$ but the cubic coefficient in (2.22) is nonzero, the bifurcating branch is a quadratic function of μ to leading order. This readily gives an analogue of the second Lyapunov coefficient in this nonsmooth case. An explicit statement in absence of smooth terms is given in Theorem 2.19 below. Notably, in the smooth case, a vanishing first Lyapunov coefficient together with a nonzero second Lyapunov coefficient yield a quartic bifurcation equation. Hence, the scaling laws for the radius are $\mu^{1/j}$ with $j = 1, 2$ in the nonsmooth case and $j = 2, 4$ in the smooth case, respectively.

Next we give the proof of Theorem 2.8.

Proof of Theorem 2.8. Taking polar coordinates $(v, w) = (r \cos \varphi, r \sin \varphi)$, system (2.18) (cf. (2.11)) becomes

$$\begin{cases} \dot{r} = r\mu + r^2\chi_2(\varphi) + r^3\chi_3(\varphi), \\ \dot{\varphi} = \omega + r\Omega_1(\varphi) + r^2\Omega_2(\varphi), \end{cases} \quad (2.24)$$

where $\chi_2(\varphi)$ and $\Omega_1(\varphi)$ are as in (2.16) and (2.17), respectively, but adding now the contributions of the smooth quadratic terms of f_q, g_q ,

$$\begin{aligned} \chi_2(\varphi) &= c|c|(a_{11}c + b_{11}s) + c|s|(a_{12}c + b_{12}s) + s|c|(a_{21}c + b_{21}s) + s|s|(a_{22}c + b_{22}s) \\ &\quad + (a_1 - b_2 - a_3)c^3 + (b_1 + a_2 - b_3)sc^2 + (b_2 + a_3)c + b_3s, \\ \Omega_1(\varphi) &= -\left[c|c|(a_{11}s - b_{11}c) + c|s|(a_{12}s - b_{12}c) + s|c|(a_{21}s - b_{21}c) + s|s|(a_{22}s - b_{22}c) \right] \\ &\quad + (b_1 + a_2 - b_3)c^3 + (-a_1 + b_2 + a_3)sc^2 + (-a_2 + b_3)c - a_3s, \end{aligned}$$

and $\chi_3(\varphi)$ and $\Omega_2(\varphi)$ are smooth functions of φ and the coefficients of f_c, g_c :

$$\begin{aligned} \chi_3(\varphi) &= (c_{a1} - c_{a2} - c_{b3} + c_{b4})c^4 + (c_{a3} - c_{a4} + c_{b1} - c_{b2})sc^3 \\ &\quad + (c_{a2} + c_{b3} - c_{b4})c^2 + (c_{a4} + c_{b2})sc + c_{b4}s^2, \\ \Omega_2(\varphi) &= (c_{a3} - c_{a4} + c_{b1} - c_{b2})c^4 + (c_{a2} - c_{a1} + c_{b3} - c_{b4})sc^3 - c_{a3}c^2 \\ &\quad + (c_{b4} - c_{a2})sc - c_{a4}s^2 + (c_{b2} + c_{a4})c^2. \end{aligned}$$

To simplify the notation we write, as before, $c := \cos \varphi$, $s := \sin \varphi$.

Analogous to (2.12), we change parametrization such that the return time to $\varphi = 0$ is equal for all orbits starting on this half-axis with initial radius $r_0 > 0$ to get

$$r' := \frac{dr}{d\varphi} = \frac{r\mu + r^2\chi_2(\varphi) + r^3\chi_3(\varphi)}{\omega + r\Omega_1(\varphi) + r^2\Omega_2(\varphi)}.$$

Expanding the right-hand side of r' in small r and μ gives, step by step,

$$\begin{aligned}
r' &= \frac{r\mu + r^2\chi_2(\varphi) + r^3\chi_3(\varphi)}{\omega} \frac{1}{1 + \frac{r\Omega_1(\varphi) + r^2\Omega_2(\varphi)}{\omega}} \\
&= \frac{r\mu + r^2\chi_2(\varphi) + r^3\chi_3(\varphi)}{\omega} \sum_{n=0}^{\infty} \left(-\frac{r\Omega_1(\varphi) + r^2\Omega_2(\varphi)}{\omega} \right)^n \\
&= \frac{r\mu + r^2\chi_2(\varphi) + r^3\chi_3(\varphi)}{\omega} \left[1 - \frac{r\Omega_1(\varphi) + r^2\Omega_2(\varphi)}{\omega} \right. \\
&\quad \left. + \frac{r^2\Omega_1^2(\varphi) + 2r^3\Omega_1(\varphi)\Omega_2(\varphi) + r^4\Omega_2^2(\varphi)}{\omega^2} + \mathcal{O}(r^3) \right] \\
&= \frac{\mu}{\omega} r + \left(\frac{\chi_2}{\omega} - \frac{\mu\Omega_1}{\omega^2} \right) r^2 + \left(\frac{\chi_3}{\omega} - \frac{\mu\Omega_2 + \chi_2\Omega_1}{\omega^2} + \frac{\mu\Omega_1^2}{\omega^3} \right) r^3 + \mathcal{O}(r^4),
\end{aligned}$$

which yields

$$r' = \frac{\mu}{\omega} r + \frac{\chi_2}{\omega} r^2 + \left(\frac{\chi_3}{\omega} - \frac{\chi_2\Omega_1}{\omega^2} \right) r^3 + \mathcal{O}(r^4 + |\mu|r^2). \quad (2.25)$$

To follow the method of averaging (e.g., [25, 48]), we write $r = \epsilon x$ and $\mu = \epsilon m$ for $0 < \epsilon \ll 1$ such that (2.25) in terms of x and m becomes

$$x' = \epsilon \left(\frac{m}{\omega} x + \frac{\chi_2}{\omega} x^2 \right) + \epsilon^2 \left(\frac{\chi_3}{\omega} - \frac{\chi_2\Omega_1}{\omega^2} \right) x^3 + \epsilon^2 \mathcal{O}(\epsilon x^4 + |m|x^2). \quad (2.26)$$

Following [48], there is a near-identity transformation which maps solutions of the truncated averaged equation

$$y' = \epsilon \bar{f}(y) + \epsilon^2 \bar{f}_2(y) + \mathcal{O}(\epsilon^3) \quad (2.27)$$

to solutions of (2.26), where its detailed derivation is given in Appendix A.1, as well as an explanation of the computation of the following functions:

$$\begin{aligned}
\bar{f}(y) &= \frac{m}{\omega} y + \frac{2}{3\pi\omega} \sigma_{\#} y^2, \\
\bar{f}_2(y) &= \left(\frac{1}{8\omega^2} S_q + \frac{1}{8\omega} S_c + \frac{1}{2\pi\omega^2} \sigma_2 \right) y^3 + \mathcal{O}(\sigma_{\#} y^3 + |m|y^2).
\end{aligned} \quad (2.28)$$

We obtain the averaged equation (2.22) from (2.25) by the change of coordinates $y = \frac{\bar{r}}{\epsilon}$ and $m = \frac{\mu}{\epsilon}$ applied to (2.27) with (2.28); this becomes (2.22) since all terms involving ϵ cancel out.

Finally, from [48, Thm. 6.3.2] the existence of a periodic orbit in the averaged system implies the existence of a periodic orbit in the original system. \square

2.2.2 Smoothing and the first Lyapunov coefficient

From Remarks 2.10 and 2.11 on the first and second Lyapunov coefficients, it is natural to ask in what way the nonsmooth first Lyapunov coefficient

$$\sigma_{\#} = 2a_{11} + a_{12} + b_{21} + 2b_{22}$$

from (2.19) differs from the first Lyapunov coefficient of a smoothed version of (2.8).

Specifically, the question is whether one can smooth the vector field in such a way that the sign of the resulting first Lyapunov coefficient is the same as that of the nonsmooth one, $\sigma_{\#}$, in all cases. We shall prove that this is not possible *without using the formula for $\sigma_{\#}$* —with the help of this formula we can find suitable smoothing.

Clearly, nonconvex approximations of the absolute value $|\cdot|$ can change criticality compared to the nonsmooth case (see Figure 1.9). More generally, we have the following result.

Lemma 2.12. *For any f, g with a sign change in the coefficients $a_{11}, a_{12}, b_{21}, b_{22}$, there are smooth approximations $f_{\varepsilon}, g_{\varepsilon}$ with $(f_{\varepsilon}, g_{\varepsilon}) \rightarrow (f, g)$ in L^{∞} such that the criticality of the smoothed Hopf bifurcation is opposite that of the nonsmooth case. Moreover, $f_{\varepsilon}, g_{\varepsilon}$ can be chosen as symmetric smooth convex approximations of the absolute values in f, g .*

Proof. Without loss of generality, we consider system (2.8). For given f, g we can choose a smooth approximation of $|\cdot|$ in the terms with coefficients $a_{11}, a_{12}, b_{21}, b_{22}$ that have quadratic terms with positive coefficients of the form $\varepsilon^{-1}\tilde{a}_{11}, \varepsilon^{-1}\tilde{a}_{12}, \varepsilon^{-1}\tilde{b}_{21}, \varepsilon^{-1}\tilde{b}_{22}$, respectively. Then the (smooth) first Lyapunov coefficient reads

$$\sigma_{s,\varepsilon} := \varepsilon^{-1} \left(3\tilde{a}_{11}a_{11} + \tilde{a}_{12}a_{12} + \tilde{b}_{21}b_{21} + 3\tilde{b}_{22}b_{22} \right),$$

which is the same as S_c in §2.2.1 when replacing accordingly coefficients of f, g and f_c, g_c , respectively.

Suppose now $\sigma_{\#} < 0$; then the sign change within $(a_{11}, a_{12}, b_{21}, b_{22})$ allows us to choose $(\tilde{a}_{11}, \tilde{a}_{12}, \tilde{b}_{21}, \tilde{b}_{22}) > 0$ such that $\sigma_{s,\varepsilon} > 0$. Likewise for $\sigma_{\#} > 0$ we can arrange $\sigma_{s,\varepsilon} < 0$. \square

Remark 2.13. *If all of $a_{11}, a_{12}, b_{21}, b_{22}$ have the same sign, then any convex smoothing of the absolute value with nonzero quadratic terms will yield a first Lyapunov coefficient of the same sign as $\sigma_{\#} \neq 0$. Moreover, having derived the formula for $\sigma_{\#}$, we can—a posteriori—identify a smoothing that preserves the criticality for all f, g . With the notation of Lemma 2.12 this is $\tilde{a}_{11} = \tilde{b}_{22} = 2/3, \tilde{a}_{12} = \tilde{b}_{21} = 1$.*

Lemma 2.14. *There is no smooth approximation of the absolute value function with nonzero quadratic term that preserves the criticality of the nonsmooth case for all f, g .*

Proof. In contrast to Lemma 2.12, here all absolute value terms in f, g are approximated in the same way so that in the notation of the proof of Lemma 2.12 we have $\tilde{a}_{11} = \tilde{a}_{12} = \tilde{b}_{21} = \tilde{b}_{22} > 0$. Without loss of generality we can assume these coefficients are all equal to 1 due to the prefactor ε^{-1} , so that the first Lyapunov coefficient is

$$\sigma_{s,\varepsilon} = \varepsilon^{-1} (3a_{11} + a_{12} + b_{21} + 3b_{22}),$$

and we readily find examples of $(a_{11}, a_{12}, b_{21}, b_{22})$ such that the signs of $\sigma_{\#}$ and $\sigma_{s,\varepsilon}$ differ. \square

The discrepancies shown here for the absolute value function readily carry over to the generalized absolute value function (2.1).

2.2.3 Direct method

In Theorem 2.8, the conclusion for (2.18) does not cover the bifurcation point $\mu = 0$ so that we cannot infer uniqueness of the branch of bifurcating periodic orbits directly. In order to directly include $\mu = 0$ in the bifurcation analysis and to facilitate the upcoming generalizations, we present a “direct” method for a general (possibly) nonsmooth planar system. This does not rely on the existence of an invariant manifold as in Proposition 2.2 or results from averaging theory.

The basic result is the following bifurcation of periodic solutions for a radial equation with quadratic nonlinear terms, which cannot stem from a smooth planar vector field, but occurs in our setting as in (2.11).

Proposition 2.15. *Consider a planar system in polar coordinates $(r, \varphi) \in \mathbb{R}_+ \times [0, 2\pi)$ periodic in φ of the form*

$$\begin{cases} \dot{r} = r\mu + r^2\chi_2(\varphi), \\ \dot{\varphi} = \omega + r\Omega_1(\varphi), \end{cases} \quad (2.29)$$

where $\mu \in \mathbb{R}$, $\omega \neq 0$ and continuous $\chi_2(\varphi), \Omega_1(\varphi)$ with minimal period 2π .

If $\int_0^{2\pi} \chi_2(\varphi)d\varphi \neq 0$, then a locally unique branch of periodic orbits bifurcates at $\mu = 0$. These orbits have period $2\pi + \mathcal{O}(\mu)$ and leading order constant radius satisfying

$$r_0 = \frac{-2\pi}{\int_0^{2\pi} \chi_2(\varphi)d\varphi} \mu + \mathcal{O}(\mu^2). \quad (2.30)$$

In particular, since $r_0 \geq 0$, the criticality of the bifurcation is determined by the sign of $\int_0^{2\pi} \chi_2(\varphi)d\varphi$.

For later reference we present a rather detailed proof.

Proof. As in the proof of Theorem 2.8, for small r the radius satisfies

$$r' := \frac{r\mu + r^2\chi_2(\varphi)}{\omega + r\Omega_1(\varphi)} =: \Psi(r, \varphi). \quad (2.31)$$

We fix the initial time at $\varphi_0 = 0$ and for any initial $r(0) = r_0$, a unique local solution is guaranteed from the Picard–Lindelöf theorem with continuous time dependence, e.g., [28]. This also guarantees existence on any given time interval for sufficiently small $|\mu|, r_0$. Moreover, the solution $r(\varphi; r_0)$ can be Taylor expanded with respect to r_0 due to the smoothness of $\Psi(r, \varphi)$ in r and continuity in the time component using the uniform contraction principle for the derivatives; cf. [28].

On the one hand, we may thus expand $r(\varphi) = r(\varphi; r_0)$ as

$$r(\varphi) = \alpha_1(\varphi)r_0 + \alpha_2(\varphi)r_0^2 + \mathcal{O}(r_0^3), \quad (2.32)$$

and differentiate with respect to φ ,

$$r'(\varphi) = \alpha_1'(\varphi)r_0 + \alpha_2'(\varphi)r_0^2 + \mathcal{O}(r_0^3), \quad (2.33)$$

where $\alpha_1(0) = 1$ and $\alpha_2(0) = 0$ since $r(0) = r_0$.

On the other hand, we Taylor expand $\Psi(r, \varphi)$ in $r = 0$ from (2.31), using $\Psi(0, \varphi) = 0$, as

$$\begin{aligned} r' = \Psi(r, \varphi) &= \Psi(0, \varphi) + \partial_r \Psi(0, \varphi)r + \frac{1}{2} \partial_r^2 \Psi(0, \varphi)r^2 + \mathcal{O}(r^3) \\ &= k_1 r + k_2 r^2 + \mathcal{O}(r^3), \end{aligned} \quad (2.34)$$

where we denote $\partial_r^i \Psi(0, \varphi) = \frac{\partial^i \Psi(r, \varphi)}{\partial r^i} \Big|_{r=0}$, $i \in \mathbb{N}$, and set

$$k_1 := \partial_r \Psi(0, \varphi) = \frac{\mu}{\omega}, \quad k_2(\varphi) := \frac{1}{2} \partial_r^2 \Psi(0, \varphi) = \frac{\omega \chi_2(\varphi) - \mu \Omega_1(\varphi)}{\omega^2}. \quad (2.35)$$

Next, we substitute (2.32) into (2.34) and match the resulting coefficients of r_0 and r_0^2 with the corresponding coefficients in (2.33). This gives the ODEs $\alpha_1' = k_1 \alpha_1$ and $\alpha_2' = k_1 \alpha_2 + k_2 \alpha_1^2$. The solutions with $\alpha_1(0) = 1$ and $\alpha_2(0) = 0$ read

$$\alpha_1(\varphi) = e^{k_1 \varphi}, \quad \alpha_2(\varphi) = e^{k_1 \varphi} \int_0^\varphi e^{-k_1 s} k_2(s) ds.$$

Indeed, one can solve the equation for $\alpha_2(\varphi)$ as follows:

$$\alpha_2(\varphi) = e^{k_1 \varphi} \left[e^{-k_1 \varphi_0} \alpha_2(\varphi_0) + \int_0^\varphi e^{-k_1 s} k_2(s) (e^{k_1 s})^2 ds \right],$$

which gives the expression mentioned above for $\varphi_0 = 0$.

Periodic orbits necessarily have period $2\pi m$ for some $m \in \mathbb{N}$, which yields the condition

$$\begin{aligned} 0 &= r(2\pi m) - r(0) \\ &= \int_0^{2\pi m} r' d\varphi = r_0 \int_0^{2\pi m} \alpha_1'(\varphi) d\varphi + r_0^2 \int_0^{2\pi m} \alpha_2'(\varphi) d\varphi + \mathcal{O}(r_0^3). \end{aligned} \quad (2.36)$$

Using the series expansion of $e^{2\pi m k_1}$ in $\mu = 0$ we have

$$\int_0^{2\pi m} \alpha_1'(\varphi) d\varphi = \alpha_1(2\pi m) - \alpha_1(0) = e^{2\pi m k_1} - 1 = 2\pi m k_1 + \mathcal{O}(\mu^2),$$

and similarly,

$$\begin{aligned}
\int_0^{2\pi m} \alpha_2'(\varphi) d\varphi &= \alpha_2(2\pi m) - \alpha_2(0) = e^{2\pi m k_1} \int_0^{2\pi m} e^{k_1 \varphi} k_2(\varphi) d\varphi - 0 \\
&= \left(1 + 2\pi m k_1 + \mathcal{O}(\mu^2)\right) \int_0^{2\pi m} \left(1 + k_1 \varphi + \mathcal{O}(\mu^2)\right) k_2(\varphi) d\varphi \\
&= \int_0^{2\pi m} k_2(\varphi) d\varphi + k_1 \int_0^{2\pi m} \varphi k_2(\varphi) d\varphi + 2\pi m k_1 \int_0^{2\pi m} k_2(\varphi) d\varphi \\
&\quad + 2\pi m k_1^2 \int_0^{2\pi m} \varphi k_2(\varphi) d\varphi + \mathcal{O}(\mu^2) \\
&= (1 + 2\pi m k_1) \int_0^{2\pi m} k_2(\varphi) d\varphi + k_1 \int_0^{2\pi m} \varphi k_2(\varphi) d\varphi + \mathcal{O}(\mu^2).
\end{aligned}$$

For $r_0 \neq 0$, we divide (2.36) by r_0 , which provides the bifurcation equation

$$0 = 2\pi m k_1 + r_0 \left((1 + 2\pi m k_1) \int_0^{2\pi m} k_2(\varphi) d\varphi + k_1 \int_0^{2\pi m} \varphi k_2(\varphi) d\varphi \right) + \mathcal{O}(\mu^2),$$

where the factor of r_0 is nonzero at $\mu = 0$ by assumption. Hence, the implicit function theorem applies and gives a unique solution. Since the solution for $m = 1$ is a solution for any m , this is the unique periodic solution. Solving the bifurcation equation for $m = 1$ yields

$$r_0 = \frac{-2\pi\mu}{(\omega + 2\pi\mu) \int_0^{2\pi} k_2(\varphi) d\varphi + \mu \int_0^{2\pi} \varphi k_2(\varphi) d\varphi} + \mathcal{O}(\mu^2),$$

whose expansion in $\mu = 0$ gives the claimed (2.30) and in particular the direction of branching.

Finally, the exchange of stability between the trivial equilibrium and the periodic orbit follows from the monotonicity of the 1D Poincaré map on an interval that contains $r = 0$ and $r = r_0(\mu)$ by uniqueness of the periodic orbit. \square

In A.2 we present in detail how to compute the Poincaré map in our nonsmooth setting.

We next note that higher order perturbations do not change the result to leading order.

Corollary 2.16. *The statement of Proposition 2.15 holds for a planar system in polar coordinates $(r, \varphi) \in \mathbb{R}_+ \times [0, 2\pi)$ periodic in φ , of the form*

$$\begin{cases} \dot{r} = r\mu + r^2\chi_2(\varphi) + r^3\chi_3(r, \varphi), \\ \dot{\varphi} = \omega + r\Omega_1(\varphi) + r^2\Omega_2(r, \varphi), \end{cases} \quad (2.37)$$

where $\mu \in \mathbb{R}$, $\omega \neq 0$, and χ_{j+1} , Ω_j , $j = 1, 2$, are continuous in their variables.

Note that (2.37) is a generalization of (2.24) in which χ_3 and Ω_2 depend now on r .

Proof. Following the proof of Proposition 2.15 we write system (2.37) analogous to (2.31) with

$$\Psi(r, \varphi) = \frac{r\mu + r^2\chi_2(\varphi) + r^3\chi_3(r, \varphi)}{\omega + r\Omega_1(\varphi) + r^2\Omega_2(r, \varphi)}.$$

Upon subtracting the leading order part of (2.34), a direct computation produces a remainder term of order $\mathcal{O}(r^3)$, which leads to the claimed result. \square

Next we show how these results can be directly used to determine the Hopf bifurcation and its super- or subcriticality. Starting with the simplest model, we return to system (2.18) with $f_q, g_q, f_c, g_c \equiv 0$, i.e., (2.8). Recall $\sigma_{\#} = 2a_{11} + a_{12} + b_{21} + 2b_{22}$ from (2.19) was identified as determining the criticality in Corollary 2.9. With the direct method we obtain the following result.

Theorem 2.17. *If $\sigma_{\#} \neq 0$, then there exists an interval I around $\mu = 0$ such that at $\mu = 0$ system (2.8) with f, g from (2.9) undergoes a degenerate Hopf bifurcation in μ where the amplitudes of the locally unique periodic orbits are given by (2.23), in polar coordinates. In particular, the unique bifurcating branch of periodic solutions emerges subcritically if $\text{sgn}(\sigma_{\#}) > 0$ and supercritically if $\text{sgn}(\sigma_{\#}) < 0$. Moreover, the bifurcating periodic orbits have exchanged stability with the equilibrium at $r = 0$, i.e., are stable if they exist for $\mu > 0$ and unstable if this is for $\mu < 0$.*

Proof. Taking polar coordinates $(v, w) = (r \cos \varphi, r \sin \varphi)$ for system (2.8) gives (2.29), where $\chi_2(\varphi)$ and $\Omega_1(\varphi)$ are as in (2.16) and (2.17), respectively. Applying Proposition 2.15 and computing the integral of χ_2 in each quadrant as in the proof of Theorem 2.8, we obtain (2.23), and the criticality follows as in Corollary 2.9.

Finally, the exchange of stability is due to the monotonicity of the 1D Poincaré map. \square

We next note that, proceeding as for Corollary 2.16, the coefficients from the quadratic and cubic terms do not affect the bifurcation to leading order.

Corollary 2.18. *If $\sigma_{\#} \neq 0$, then the statement of Theorem 2.17 holds for the more general system (2.18). In particular, f_q, g_q, f_c, g_c affect neither $\sigma_{\#}$ nor the leading order bifurcation.*

Having investigated $\sigma_{\#} \neq 0$, we next consider the degenerate case $\sigma_{\#} = 0$. For that, recall Remark 2.11 and σ_2 from (2.20).

Theorem 2.19. *If $\sigma_{\#} = 0$ and $\sigma_2 \neq 0$, then there exists an interval I around $\mu = 0$ such that at $\mu = 0$ system (2.8) with f, g from (2.9) undergoes a degenerate Hopf bifurcation in μ where the leading order amplitude of the locally unique periodic orbit is given by*

$$r_0 = \sqrt{-\frac{2\pi\omega}{\sigma_2}\mu + \mathcal{O}(\mu)}. \quad (2.38)$$

In particular, the unique bifurcating branch of periodic solutions emerges subcritically if $\text{sgn}(\omega\sigma_2) > 0$ and supercritically if $\text{sgn}(\omega\sigma_2) < 0$. Moreover, the bifurcating periodic orbits have exchanged stability with the equilibrium at $r = 0$, i.e., are stable if they exist for $\mu > 0$ and unstable if this is for $\mu < 0$.

Proof. Proceeding as before, we write (2.8) in polar coordinates $(v, w) = (r \cos \varphi, r \sin \varphi)$ and change the time parametrization to obtain the form (2.31) for the radial equation.

On the one hand, we expand the solution $r(\varphi) = r(\varphi; r_0)$ with $r(0) = r_0$ as

$$r(\varphi) = \alpha_1(\varphi)r_0 + \alpha_2(\varphi)r_0^2 + \alpha_3(\varphi)r_0^3 + \mathcal{O}(r_0^4), \quad (2.39)$$

and differentiate with respect to φ ,

$$r'(\varphi) = \alpha'_1(\varphi)r_0 + \alpha'_2(\varphi)r_0^2 + \alpha'_3(\varphi)r_0^3 + \mathcal{O}(r_0^4), \quad (2.40)$$

where $\alpha_1(0) = 1$ and $\alpha_2(0) = \alpha_3(0) = 0$.

On the other hand, we compute the Taylor expansion of r' from (2.31) up to third order in $r = 0$ as

$$r' = \Psi(r, \varphi) = k_1 r + k_2 r^2 + k_3 r^3 + \mathcal{O}(r^4), \quad (2.41)$$

where we use $\Psi(0, \varphi) = 0$ and the notation (2.35) as well as

$$k_3(\varphi) := \frac{1}{3!} \partial_r^3 \Psi(0, \varphi) = \frac{-\omega \chi_2(\varphi) \Omega_1(\varphi) + \mu \Omega_1(\varphi)^2}{\omega^3}.$$

Analogous to the proof of Proposition 2.15, substituting (2.39) into (2.41) and comparing coefficients with (2.40), we obtain the ODEs

$$\alpha'_1 = k_1 \alpha_1, \quad \alpha'_2 = k_1 \alpha_2 + k_2 \alpha_1^2, \quad \alpha'_3 = k_1 \alpha_3 + 2k_2 \alpha_1 \alpha_2 + k_3 \alpha_1^3.$$

We solve these by variation of constants using $\alpha_1(0) = 1$ and $\alpha_2(0) = \alpha_3(0) = 0$ as

$$\begin{aligned} \alpha_1(\varphi) &= e^{k_1 \varphi}, \\ \alpha_2(\varphi) &= e^{k_1 \varphi} \int_0^\varphi e^{-k_1 s} k_2(s) ds, \\ \alpha_3(\varphi) &= e^{k_1 \varphi} \left[2 \int_0^\varphi k_2(s) \alpha_2(s) ds + \int_0^\varphi e^{2k_1 s} k_3(s) ds \right]. \end{aligned}$$

Periodic orbits are the solutions with $r_0 \neq 0$ of

$$\begin{aligned} 0 &= r(2\pi) - r(0) \\ &= r_0 \int_0^{2\pi} \alpha'_1(\varphi) d\varphi + r_0^2 \int_0^{2\pi} \alpha'_2(\varphi) d\varphi + r_0^3 \int_0^{2\pi} \alpha'_3(\varphi) d\varphi + \mathcal{O}(r_0^4). \end{aligned} \quad (2.42)$$

Similarly as for the proof of Proposition 2.15, straightforward computations give

$$\int_0^{2\pi} \alpha'_1(\varphi) d\varphi = \alpha_1(2\pi) - \alpha_1(0) = e^{2\pi k_1} - 1 = \frac{2\pi}{\omega} \mu + \mathcal{O}(\mu^2).$$

In order to calculate the integrals of α'_2 and α'_3 , we accommodate the nonsmooth terms by splitting the integration over quadrants. For the integral of α'_2 we have first

$$\begin{aligned} \int_0^{2\pi} \alpha'_2(\varphi) d\varphi &= \alpha_2(2\pi) - \alpha_2(0) \\ &= \left(1 + k_1 2\pi + \mathcal{O}(\mu^2)\right) \int_0^{2\pi} \left(1 + k_1 \varphi + \mathcal{O}(\mu^2)\right) \frac{\omega \chi_2(\varphi) - \mu \Omega_1(\varphi)}{\omega^2} d\varphi, \end{aligned}$$

which yields

$$\int_0^{2\pi} \alpha'_2(\varphi) d\varphi = \frac{1}{\omega} \int_0^{2\pi} \chi_2(\varphi) d\varphi + \mathcal{O}(\mu) = \frac{4}{3\omega} \sigma_{\#} + \mathcal{O}(\mu).$$

To better understand the outcome of the integral of α'_3 , we show some intermediate steps of its computation:

$$\begin{aligned} \int_0^{2\pi} \alpha'_3(\varphi) d\varphi &= \alpha_3(2\pi) - \alpha_3(0) \\ &= \left(1 + k_1 2\pi + \mathcal{O}(\mu^2)\right) \left[2 \int_0^{2\pi} \frac{\omega \chi_2(\varphi) - \mu \Omega_1(\varphi)}{\omega^2} \right. \\ &\quad \cdot \left(1 + k_1 \varphi + \mathcal{O}(\mu^2)\right) \int_0^\varphi \left(1 + k_1 s + \mathcal{O}(\mu^2)\right) \frac{\omega \chi_2(s) - \mu \Omega_1(s)}{\omega^2} ds d\varphi \\ &\quad \left. + \int_0^{2\pi} \left(1 + 2k_1 \varphi + \mathcal{O}(\mu^2)\right) \frac{-\omega \chi_2(\varphi) \Omega_1(\varphi) + \mu \Omega_1(\varphi)^2}{\omega^3} d\varphi \right], \end{aligned}$$

which results in

$$\begin{aligned} \int_0^{2\pi} \alpha'_3(\varphi) d\varphi &= 2 \int_0^{2\pi} \frac{\chi_2(\varphi)}{\omega} \int_0^\varphi \frac{\chi_2(s)}{\omega} ds d\varphi - \int_0^{2\pi} \frac{\chi_2(\varphi) \Omega_1(\varphi)}{\omega^2} d\varphi + \mathcal{O}(\mu), \\ &= \frac{1}{\omega^2} \sigma_2 + \mathcal{O}(\mu). \end{aligned}$$

Substitution into (2.42) for periodic orbits and dividing out $r_0 \neq 0$, yields the bifurcation equation

$$0 = \frac{2\pi}{\omega} \mu + \frac{4}{3\omega} \sigma_{\#} r_0 + \frac{1}{\omega^2} \sigma_2 r_0^2 + \mathcal{O}(\mu^2 + \mu r_0 + r_0^3). \quad (2.43)$$

Since $\sigma_{\#} = 0$, the previous equation reads

$$0 = \frac{2\pi}{\omega} \mu + \frac{1}{\omega^2} \sigma_2 r_0^2 + \mathcal{O}(\mu^2 + \mu r_0 + r_0^3). \quad (2.44)$$

Here the implicit function theorem applies a priori to provide a unique branch $\mu(r_0)$ with

$$\mu = -\frac{\sigma_2}{2\pi\omega} r_0^2 + \mathcal{O}(r_0^3). \quad (2.45)$$

Solving this for r_0 provides (2.38), where the square root to be real requires $\mu\omega\sigma_2 > 0$, which gives the claimed sub/supercriticality. \square

Notice that to express r_0 in terms of μ , one may write $r_0 = p_1 \sqrt{\mu} + p_2 \mu^n + \mathcal{O}(\mu^m)$ and substitute this expression into (2.45) to find the values of $p_1, p_2, n, m \in \mathbb{R}$. This yields $\mu = \frac{\sigma_2}{2\pi\omega} p_1^2 \mu + 2 \frac{\sigma_2}{2\pi\omega} p_1 p_2 \mu^{n+1/2} + \mathcal{O}(p_1^3 \mu^{3/2})$, and matching coefficients and exponents, result into $p_1^2 = \frac{2\pi\omega}{\sigma_2}$ and $n + 1/2 = 3/2$ to become of higher order. Hence, choosing the positive expression for p_1 (since $r \geq 0$), yields (2.38).

We remark that in the nonsmooth case, as expected, for $\sigma_{\#} = 0$ one gets indeed the same second Lyapunov coefficient from both the averaging and the direct method. This means that the same expression for σ_2 is obtained and, in particular, the same criticality for the system, cf. (2.22) with $S_q = S_c = 0$ and (2.44).

This last theorem readily extends to the analogue of the so-called Bautin bifurcation for smooth vector fields, also called the generalized Hopf bifurcation, which unfolds from zero first Lyapunov coefficient and identifies a curve of fold points for periodic orbits. From (2.43) we directly derive the loci fold points in the $(\mu, \sigma_{\#})$ -parameter plane as

$$\mu = \frac{2\omega}{9\pi\sigma_2}\sigma_{\#}^2$$

to leading order with respect to $\sigma_{\#}$.

Notably, the loci of fold points for the smooth Bautin bifurcation also lies on a quadratic curve in terms of the first Lyapunov coefficient. This last similarity is due to the fact that the ODE of the smooth case has no even terms in the radial component. For instance, we consider

$$\dot{r} = \mu r + \sigma_s r^3 + \sigma_l r^5,$$

which is the simplest example for such an equation. To find the loci fold points in the (μ, σ_s) -parameter plane, we write $\mu = \mu(r; \sigma_s) = -(\sigma_s + \sigma_l r^2)r^2$, from which its derivative in $r \neq 0$ vanishes if and only if $r = \sqrt{-\frac{\sigma_s}{2\sigma_l}}$, and hence,

$$\mu(\sigma_s) = \frac{\sigma_s^2}{4\sigma_l}, \quad \text{for } \frac{\sigma_s}{\sigma_l} < 0.$$

For a direct comparison of this last expression, we assume the radial equation of the nonsmooth system to be

$$\dot{r} = \mu r + \sigma_{\#} r^2 + \sigma_2 r^3,$$

and compute the analogous curve in the $(\mu, \sigma_{\#})$ -parameter plane. Similarly as before, $\mu = \mu(r; \sigma_{\#}) = -(\sigma_{\#} + \sigma_2 r)r$, from which its derivative in $r \neq 0$ vanishes if and only if $r = -\frac{\sigma_{\#}}{2\sigma_2}$, yielding

$$\mu(\sigma_{\#}) = \frac{\sigma_{\#}^2}{4\sigma_2}, \quad \text{for } \frac{\sigma_{\#}}{\sigma_2} < 0.$$

Although it looks as both curves $\mu(\sigma_s), \mu(\sigma_{\#})$ have the same scaling, that is not directly true since the vertical axis of both cases are different from each other.

Specifically, in the parameter plane, the origin corresponds to the Bautin point and the vertical axis, $\mu = 0$, to the sub- and supercritical Hopf bifurcations for positive and negative values of $\sigma_{\#}$ (as well as of σ_s), respectively. In Figure 2.1 we illustrate the bifurcation diagram for the nonsmooth Bautin situation. On the one hand, in Figure 2.1 (a), which corresponds to $\sigma_2 = 1$, the fixed point of the system is stable in region 1 and the limit cycle is unstable. In region 2, the fixed point changes stability and a stable periodic limit cycle is born. The two periodic orbits collide and disappear while moving to region 3 through the fold point curve, obtaining an unstable fixed point. On the other hand, in Figure 2.1 (b), for $\sigma_2 = -1$, the creation of an unstable limit cycle and further exchange of stability of the fixed point occurs while moving from region 1 to region 2, where two limit cycle coexist. In the curve of fold points the two cycles collide. Finally, in region 3 no periodic orbits happen and the fixed point remains stable.

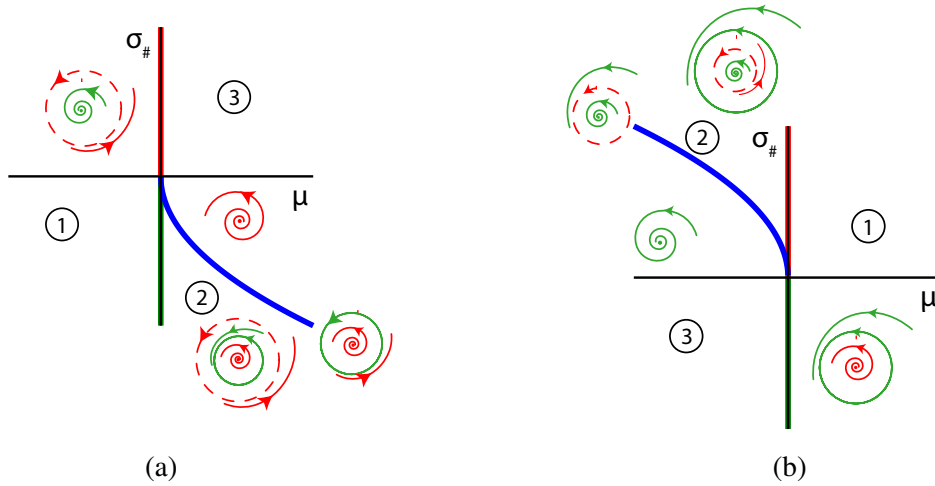


FIGURE 2.1: Bifurcation diagram for the nonsmooth Bautin situation. In both cases, the vertical axis ($\mu = 0$) corresponds to the Hopf bifurcation, where the upper branch, in red ($\sigma_{\#} > 0$), denotes the subcritical case, while the lower branch, in green ($\sigma_{\#} < 0$), indicates the supercritical bifurcation. The Bautin point occurs at the origin. The loci fold points $\mu(\sigma_{\#}) = \sigma_{\#}^2 / (4\sigma_2)$ is illustrated by the blue curve in both diagrams. In (a) $\sigma_2 = 1$, and in (b) $\sigma_2 = -1$. The stable periodic orbits are pictured in green while the unstable ones in dashed red. The trajectories approaching the stable fixed point are green and the ones leaving the unstable fixed point are red.

2.3 Generalizations

In this section we discuss analogous bifurcation results for the generalization from the absolute value, (2.1), and then turn to higher dimensional systems as well as general linear form of the linear part.

2.3.1 Generalization from the absolute value

Recall our notation for different left and right slopes (2.1), and consider the generalized canonical equation

$$\dot{u} = \mu u + \sigma_{\#} u^j [u]_{p_{-}}^{p_{+}}, \quad (2.46)$$

with left slope p_{-} , right slope p_{+} , and $j \in \mathbb{N}$ measuring the degree of smoothness such that the right-hand side is C^j but not C^{j+1} smooth. Sample bifurcation diagrams for $j = 1$ and $j = 2$ are plotted in Figure 2.2 for $\sigma_{\#} = -1$.

The case $j = 2$ highlights that also lack of smoothness in the cubic terms impacts the bifurcation in general. We do not pursue this further here, but analogous to the following discussion, it is possible to derive a modified normal form coefficient S_c .

For the Hopf bifurcation analysis, we analogously replace the absolute value in (2.9) by (2.1), and thus replace f, g in (2.8) by

$$f(v, w; \alpha) = a_{11}v[v]_{\alpha_{1-}}^{\alpha_{1+}} + a_{12}v[w]_{\alpha_{2-}}^{\alpha_{2+}} + a_{21}w[v]_{\alpha_{3-}}^{\alpha_{3+}} + a_{22}w[w]_{\alpha_{4-}}^{\alpha_{4+}}, \quad (2.47)$$

$$g(v, w; \beta) = b_{11}v[v]_{\beta_{1-}}^{\beta_{1+}} + b_{12}v[w]_{\beta_{2-}}^{\beta_{2+}} + b_{21}w[v]_{\beta_{3-}}^{\beta_{3+}} + b_{22}w[w]_{\beta_{4-}}^{\beta_{4+}}, \quad (2.48)$$

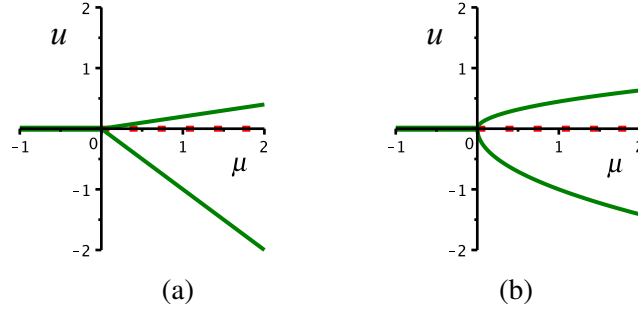


FIGURE 2.2: Degenerate supercritical pitchfork bifurcation of (2.46) for $p_- = -1$, $p_+ = 5$ of degree $j = 1$ in (a), and $j = 2$ in (b).

where $\alpha = (\alpha_{1\pm}, \alpha_{2\pm}, \alpha_{3\pm}, \alpha_{4\pm})$, $\beta = (\beta_{1\pm}, \beta_{2\pm}, \beta_{3\pm}, \beta_{4\pm}) \in \mathbb{R}^8$. This generalization leads to the generalized nonsmooth first Lyapunov coefficient given by

$$\tilde{\sigma}_{\#} := a_{11}(\alpha_{1+} - \alpha_{1-}) + \frac{1}{2}a_{12}(\alpha_{2+} - \alpha_{2-}) + \frac{1}{2}b_{21}(\beta_{3+} - \beta_{3-}) + b_{22}(\beta_{4+} - \beta_{4-}). \quad (2.49)$$

Notably, in the smooth case, where the left and right slopes coincide, we have $\tilde{\sigma}_{\#} = 0$, and if left and right slopes are -1 and 1 , respectively, we recover $\sigma_{\#}$.

Theorem 2.20. *If $\tilde{\sigma}_{\#} \neq 0$, then the statement of Theorem 2.17 holds true for (2.8) with f, g from (2.47), (2.48), respectively, with $\sigma_{\#}$ replaced by $\tilde{\sigma}_{\#}$.*

Proof. Taking polar coordinates we obtain (2.29), where

$$\begin{aligned} \chi_2(\varphi) = & c^2 \left(a_{11}[c]_{\alpha_{1-}^{\alpha_{1+}}} + a_{12}[s]_{\alpha_{2-}^{\alpha_{2+}}} \right) + s^2 \left(b_{21}[c]_{\beta_{3-}^{\beta_{3+}}} + b_{22}[s]_{\beta_{4-}^{\beta_{4+}}} \right) \\ & + sc \left(a_{21}[c]_{\alpha_{3-}^{\alpha_{3+}}} + a_{22}[s]_{\alpha_{4-}^{\alpha_{4+}}} + b_{11}[c]_{\beta_{1-}^{\beta_{1+}}} + b_{12}[s]_{\beta_{2-}^{\beta_{2+}}} \right), \end{aligned}$$

again with $s := \sin(\varphi)$, $c := \cos(\varphi)$. Applying Proposition 2.15 we compute $\int_0^{2\pi} \chi_2(\varphi) d\varphi$, which gives $\frac{4}{3}\tilde{\sigma}_{\#}$. Indeed, from (2.1) we obtain

$$\begin{aligned} \int_0^{2\pi} c^2 a_{11}[c]_{\alpha_{1-}^{\alpha_{1+}}} d\varphi &= \int_0^{\frac{\pi}{2}} c^3 a_{11} \alpha_{1+} d\varphi + \int_{\frac{\pi}{2}}^{\frac{3\pi}{2}} c^3 a_{11} \alpha_{1-} d\varphi + \int_{\frac{3\pi}{2}}^{2\pi} c^3 a_{11} \alpha_{1+} d\varphi \\ &= \frac{4}{3} a_{11} (\alpha_{1+} - \alpha_{1-}), \\ \int_0^{2\pi} c^2 a_{12}[s]_{\alpha_{2-}^{\alpha_{2+}}} d\varphi &= \int_0^{\pi} c^2 s a_{12} \alpha_{2+} d\varphi + \int_{\pi}^{2\pi} c^2 s a_{12} \alpha_{2-} d\varphi \\ &= \frac{2}{3} a_{12} (\alpha_{2+} - \alpha_{2-}), \end{aligned}$$

and similarly for the other terms. Note that

$$\int_0^{2\pi} sc \left(a_{21}[c]_{\alpha_{3-}^{\alpha_{3+}}} + a_{22}[s]_{\alpha_{4-}^{\alpha_{4+}}} + b_{11}[c]_{\beta_{1-}^{\beta_{1+}}} + b_{12}[s]_{\beta_{2-}^{\beta_{2+}}} \right) d\varphi = 0,$$

i.e., the integral of the third term on the right-hand side of χ_2 , vanishes due to the symmetry of sc . Thus, as we wanted to show, we get (2.23) with $\sigma_{\#}$ replaced by $\tilde{\sigma}_{\#} = 0$, i.e.,

$$r_0(\mu) = -\frac{3\pi}{2\tilde{\sigma}_{\#}}\mu + \mathcal{O}(\mu^2).$$

□

Notice that in the (v, w) -plane, the function $[\cdot]_{p_{\pm}}^{p_{\pm}}$ is linear in each quadrant, with $p_{+} \in \{\alpha_{i_{+}}, \beta_{i_{+}}\}$, $p_{-} \in \{\alpha_{i_{-}}, \beta_{i_{-}}\}$ for $i \in \{1, 2, 3, 4\}$. In polar coordinates, we can remove the nonsmoothnesses as follows. Using the definition (2.1), we have $[c]_{p_{-}}^{p_{+}} = p_{+}c$ for $\varphi \in \left[\frac{3\pi}{2}, \frac{\pi}{2}\right]$ and $[c]_{p_{-}}^{p_{+}} = p_{-}c$ for $\varphi \in \left(\frac{\pi}{2}, \frac{3\pi}{2}\right)$; while $[s]_{p_{-}}^{p_{+}} = p_{+}c$ for $\varphi \in [0, \pi]$ and $[s]_{p_{-}}^{p_{+}} = p_{-}c$ for $\varphi \in (\pi, 2\pi)$. Therefore, splitting the integrals as in the proof, one can easily integrate each term considering the corresponding slope.

For completeness, although it is not used for our analysis, we additionally exhibit the expression of $\Omega_1(\varphi)$ in (2.29) for the current setting:

$$\begin{aligned} \Omega_1(\varphi) = & c^2 \left(b_{11}[c]_{\beta_{1-}}^{\beta_{1+}} + b_{12}[s]_{\beta_{2-}}^{\beta_{2+}} \right) - s^2 \left(a_{21}[c]_{\alpha_{3-}}^{\alpha_{3+}} + a_{22}[s]_{\alpha_{4-}}^{\alpha_{4+}} \right) \\ & + sc \left(b_{21}[c]_{\beta_{3-}}^{\beta_{3+}} + b_{22}[s]_{\beta_{4-}}^{\beta_{4+}} - a_{11}[c]_{\alpha_{1-}}^{\alpha_{1+}} - a_{12}[s]_{\alpha_{2-}}^{\alpha_{2+}} \right). \end{aligned}$$

2.3.2 3D system

In this section we extend the previous results to higher dimensional systems. Recall that Proposition 2.2 and Theorem 2.3 rely on hyperbolicity of the spectrum of $A(0)$ from (2.2) except for a simple pair of complex conjugate eigenvalues. Analogously, averaging theory can be used in this setting to obtain a normal form as in Theorem 2.8. Here we follow the “direct method” and obtain bifurcation results also without normal hyperbolicity.

To simplify the exposition, we start with the absolute value $|\cdot|$ and consider an extension of the planar quadratic case (2.8), (2.9), motivated by the example in [3], which is a simplification of a model used for ship maneuvering. As discussed in §2.1, we first assume the linear part is in normal form—a general linear part will be considered in §2.3.4—which gives

$$\begin{pmatrix} \dot{u} \\ \dot{v} \\ \dot{w} \end{pmatrix} = \begin{pmatrix} c_1u + c_2u^2 + c_3uv + c_4uw + c_5vw + h(v, w) \\ \mu v - \omega w + c_6uv + c_7uw + f(v, w) \\ \omega v + \mu w + c_8uv + c_9uw + g(v, w) \end{pmatrix}, \quad (2.50)$$

where f, g are as in (2.9), $h(v, w) = h_{11}v|v| + h_{12}v|w| + h_{21}w|v| + h_{22}w|w|$ and h_{ij}, c_k , $\forall i, j \in \{1, 2\}, \forall k \in \{1, \dots, 9\}$, are real constants, all viewed as parameters. Again we assume $\omega \neq 0$ and take μ as the bifurcation parameter.

With linear part in normal form in the coordinates of Lemma 2.5, the vector field is actually smooth in the additional variable u . It turns out that in the generic case $c_1 \neq 0$, this additional smoothness will not be relevant for the leading order analysis, while we make use of it in the degenerate case $c_1 = 0$.

We define the following quantities that appear in the upcoming results:

$$\begin{aligned}
\bar{\gamma}_{10} &= e^{\frac{2\pi c_1}{\omega}} - 1, & \bar{\gamma}_{20} &= \frac{e^{\frac{2\pi c_1}{\omega}} \left(e^{\frac{2\pi c_1}{\omega}} - 1 \right)}{c_1} \left(c_2 - \frac{c_1 \rho_2}{\omega(c_1^2 + 4\omega^2)} \right), \\
\bar{\gamma}_{02} &= \frac{1}{\omega} e^{\frac{2\pi c_1}{\omega}} \int_0^{2\pi} e^{s \frac{2\mu - c_1}{\omega}} \Upsilon(s) ds, & \bar{\gamma}_{11} &= \frac{2}{3\omega^2} e^{\frac{2\pi c_1}{\omega}} \left[c_1 \left(2\tau_2 + \frac{P}{3\omega} \mu \right) - 3\pi c_4 \mu \right] + \mathcal{O}(\mu^2), \\
\bar{\delta}_{01} &= \frac{2\pi\mu}{\omega} + \mathcal{O}(\mu^2), & \bar{\delta}_{02} &= \frac{2}{3\omega} \left[\sigma_{\#} \left(2 + \frac{6\pi}{\omega} \mu \right) + \frac{Q}{3\omega} \mu \right] + \mathcal{O}(\mu^2), \\
& & \bar{\delta}_{11} &= \frac{e^{\frac{2\pi c_1}{\omega}} - 1}{c_1} \frac{1}{\omega(c_1^2 + 4\omega^2)} [\omega \rho_1 + R\mu] + \mathcal{O}(\mu^2),
\end{aligned} \tag{2.51}$$

where we shortened the notation by lumping the weighted sums of coefficients from f, g and from the smooth quadratic terms, respectively, given by

$$\begin{aligned}
\tau_1 &= 4a_{22} + 5a_{21} - 5b_{12} - 4b_{11}, & P &= 3\pi(2\tau_2 - a_{11} + b_{21}) + 4\tau_3, \\
\tau_2 &= 2a_{22} + a_{21} - b_{12} - 2b_{11}, & Q &= -3\pi(b_{11} + a_{21}) + 2\tau_1, \\
\tau_3 &= a_{11} - a_{12} - b_{21} + b_{22}, & R &= 2\pi\rho_1 - \rho_2, \\
\rho_1 &= c_6 c_1^2 - c_7 c_1 \omega + 2c_6 \omega^2 - c_8 c_1 \omega + 2c_9 \omega^2, \\
\rho_2 &= c_8 c_1^2 - c_9 c_1 \omega + 2c_8 \omega^2 + c_6 c_1 \omega - 2c_7 \omega^2,
\end{aligned}$$

as well as the h -dependent

$$\Upsilon(\varphi) = c_5 c s + h_{11} c |c| + h_{12} c |s| + h_{21} s |c| + h_{22} s |s|.$$

The explicit form of $\bar{\gamma}_{02}$ can be found in Appendix A.3.1.

Theorem 2.21. *In cylindrical coordinates $(u, v, w) = (u, r \cos \varphi, r \sin \varphi)$, up to time shifts, periodic solutions to (2.50) with $r(0) = r_0, u(0) = u_0$ for $0 \leq |\mu| \ll 1$ near $r = u = 0$ are in 1-to-1 correspondence with solutions to the algebraic equation system*

$$0 = \bar{\gamma}_{10} u_0 + \bar{\gamma}_{20} u_0^2 + \bar{\gamma}_{02} r_0^2 + \bar{\gamma}_{11} u_0 r_0 + \mathcal{O}(3), \tag{2.52}$$

$$0 = \bar{\delta}_{01} r_0 + \bar{\delta}_{02} r_0^2 + \bar{\delta}_{11} u_0 r_0 + \mathcal{O}(3), \tag{2.53}$$

where $\mathcal{O}(3)$ are terms of at least cubic order in u_0, r_0 .

Proof. In cylindrical coordinates $(u, v, w) = (u, r \cos \varphi, r \sin \varphi)$ system (2.50) becomes

$$\begin{cases} \dot{u} = c_1 u + c_2 u^2 + (c_3 c u + c_4 s u) r + \Upsilon(\varphi) r^2, \\ \dot{r} = (\mu + \chi_1(\varphi) u) r + \chi_2(\varphi) r^2, \\ \dot{\varphi} = \omega + \Omega_0(\varphi) u + \Omega_1(\varphi) r, \end{cases} \tag{2.54}$$

where $\chi_1(\varphi) = c_6c^2 + (c_7 + c_8)cs + c_9s^2$, $\Omega_0(\varphi) = c_8c^2 + (c_9 - c_6)cs - c_7s^2$, and the nonsmooth functions $\chi_2(\varphi)$ and $\Omega_1(\varphi)$ are as in (2.16) and (2.17), respectively.

Upon rescaling time the equations for u and r of the previous system become

$$\begin{cases} u' = \frac{du/dt}{d\varphi/dt} = \frac{c_1u + c_2u^2 + (c_3cu + c_4su)r + \Upsilon(\varphi)r^2}{\omega + \Omega_0(\varphi)u + \Omega_1(\varphi)r} =: \Psi_u(u, r, \varphi), \\ r' = \frac{dr/dt}{d\varphi/dt} = \frac{(\mu + \chi_1(\varphi)u)r + \chi_2(\varphi)r^2}{\omega + \Omega_0(\varphi)u + \Omega_1(\varphi)r} =: \Psi_r(u, r, \varphi). \end{cases} \quad (2.55)$$

Taylor expansion of u' and r' in $(u, r) = (0, 0)$ up to third order gives

$$\begin{aligned} u' &= \Psi_u(0, 0, \varphi) + \partial_u \Psi_u(0, 0, \varphi)u + \partial_r \Psi_u(0, 0, \varphi)r \\ &\quad + \frac{1}{2} \partial_u^2 \Psi_u(0, 0, \varphi)u^2 + \frac{1}{2} \partial_r^2 \Psi_u(0, 0, \varphi)r^2 + \partial_{ur}^2 \Psi_u(0, 0, \varphi)ur + \mathcal{O}(3), \end{aligned} \quad (2.56a)$$

$$\begin{aligned} r' &= \Psi_r(0, 0, \varphi) + \partial_u \Psi_r(0, 0, \varphi)u + \partial_r \Psi_r(0, 0, \varphi)r \\ &\quad + \frac{1}{2} \partial_u^2 \Psi_r(0, 0, \varphi)u^2 + \frac{1}{2} \partial_r^2 \Psi_r(0, 0, \varphi)r^2 + \partial_{ur}^2 \Psi_r(0, 0, \varphi)ur + \mathcal{O}(3). \end{aligned} \quad (2.56b)$$

On the other hand, and similarly to the procedure of the 2D case, we write $u(\varphi)$ and $r(\varphi)$ as the following expansions with coefficients γ_{ij}, δ_{ij} :

$$\begin{aligned} u(\varphi) &= \gamma_{10}(\varphi)u_0 + \gamma_{20}(\varphi)u_0^2 + \gamma_{01}(\varphi)r_0 + \gamma_{02}(\varphi)r_0^2 + \gamma_{11}(\varphi)u_0r_0 + \mathcal{O}(3), \\ r(\varphi) &= \delta_{10}(\varphi)u_0 + \delta_{20}(\varphi)u_0^2 + \delta_{01}(\varphi)r_0 + \delta_{02}(\varphi)r_0^2 + \delta_{11}(\varphi)u_0r_0 + \mathcal{O}(3), \end{aligned} \quad (2.57)$$

with the initial conditions $u(0) = u_0$ and $r(0) = r_0$, which imply $\gamma_{10}(0) = \delta_{01}(0) = 1$ and the rest zero.

Substituting (2.57) into (2.56a) and (2.56b) and matching the coefficients of the powers of u_0 and r_0 we get to solve a set of ODEs in order to obtain the expressions for γ_{ij} and δ_{ij} (see Appendix A.3.1 for the details). Using these, the system of boundary value problems $0 = u(2\pi) - u(0)$, $0 = r(2\pi) - r(0)$ for periodic solutions precisely yields (2.52), (2.53), where $\bar{\gamma}_{ij} = \gamma_{ij}(2\pi) - \gamma_{ij}(0)$ and $\bar{\delta}_{ij} = \delta_{ij}(2\pi) - \delta_{ij}(0)$. \square

The solution structure of (2.52), (2.53) strongly depends on whether $c_1 = 0$ or not. If not, then the transverse direction is hyperbolic and Theorem 2.17 implies a locally unique branch of periodic solutions. In the nonhyperbolic case the situation is different and we note that if $c_1 = 0$, then with $\gamma_{\#} := 2h_{21} + c_5 + \pi h_{22}$, we have

$$\bar{\gamma}_{10} = 0, \quad \bar{\gamma}_{11} = -\frac{2\pi c_4}{\omega^2} \mu + \mathcal{O}(\mu^2), \quad \bar{\gamma}_{20} = \frac{2\pi c_2}{\omega}, \quad \bar{\gamma}_{02} = -\frac{\pi \gamma_{\#}}{\omega^2} \mu + \mathcal{O}(\mu^2). \quad (2.58)$$

Corollary 2.22. *Consider (2.50) in cylindrical coordinates $(u, v, w) = (u, r \cos \varphi, r \sin \varphi)$. If $c_1 \neq 0$, then $u = u(\varphi; \mu) = \mathcal{O}(\mu^2)$ and the statement of Theorem 2.17 holds true. If $c_1 = 0$ and $\omega c_2 \gamma_{\#} \mu > 0$, then precisely two curves of periodic solutions bifurcate at $\mu = 0$ for $\mu \sigma_{\#} \leq 0$, each in the sense of Theorem 2.3, and their initial conditions $r(0) = r_0$,*

$u(0) = u_0^\pm$ satisfy

$$u_0^\pm = u_0^\pm(\mu) = \mp \frac{3\pi}{2\sigma_\#} \sqrt{\frac{\gamma_\#}{2\omega c_2}} \mu^3 + \mathcal{O}(\mu^2) = \mathcal{O}(|\mu|^{3/2}), \quad (2.59)$$

$$r_0 = r_0(\mu) = -\frac{3\pi}{2\sigma_\#} \mu + \mathcal{O}(|\mu|^{3/2}). \quad (2.60)$$

In the case that $c_1 = 0$ and $\omega c_2 \gamma_\# \mu < 0$, there is no bifurcation through μ .

Proof. In the (transversely) hyperbolic case $c_1 \neq 0$ we have $\bar{\gamma}_{10} \neq 0$, and thus one may solve (2.52) for u_0 by the implicit function theorem as $u_0 = u_0(r_0) = \mathcal{O}(r_0^2)$. Substitution into (2.53) changes the higher order term only, so that, to leading order, we obtain the same problem as in Theorem 2.17 with solution given by (2.23). The stability statement of Theorem 2.17 holds true from the existence of a 2D Lipschitz continuous invariant manifold given by Proposition 2.2.

We now consider $c_1 = 0$. Using (2.58) we can cast (2.52), (2.53) as

$$0 = \frac{2\pi c_2}{\omega} u_0^2 - \frac{\pi \gamma_\#}{\omega^2} \mu r_0^2 - \frac{2\pi c_4}{\omega^2} \mu u_0 r_0 + \mathcal{O}(\mu^2 r_0^2) + \mathcal{O}(3), \quad (2.61)$$

$$0 = \bar{\delta}_{01} r_0 + \frac{4\sigma_\#}{3\omega} r_0^2 + \mathcal{O}(|u_0 r_0| + |\mu r_0|(|u_0| + |r_0|)) + \mathcal{O}(3), \quad (2.62)$$

so that we may solve (2.61) as

$$\begin{aligned} u_0 = u_0^\pm(r_0; \mu) &= \frac{c_4}{\omega c_2} \mu r_0 \pm r_0 \sqrt{\frac{c_4^2}{4c_2^2} \mu^2 + \frac{\gamma_\#}{2\omega c_2} \mu} + \mathcal{O}(|\mu|) \\ &= \pm r_0 \sqrt{\frac{\gamma_\#}{2\omega c_2} \mu} + \mathcal{O}(|\mu|). \end{aligned} \quad (2.63)$$

Substitution into (2.53) gives a factor r_0 corresponding to the trivial solution $u_0 = r_0 = 0$. For non-trivial solutions we divide the equation by $r_0 \neq 0$ and solve it as

$$r_0 = -\frac{\bar{\delta}_{01}}{\frac{4\sigma_\#}{3\omega} + \mathcal{O}(\sqrt{|\mu|})} = -\frac{3\pi}{2\sigma_\#} \mu + \mathcal{O}(|\mu|^{3/2}).$$

Next, we substitute this into (2.63) and note that perturbation by the higher order terms yields (2.59), (2.60). These give positive r_0 in the case that $\mu \sigma_\# < 0$ and therefore, real valued u_0 in the case that $\omega c_2 \gamma_\# \mu > 0$. However, if $\omega c_2 \gamma_\# \mu < 0$, then for any $0 < |\mu| \ll 1$ either $r_0 < 0$ or u_0 is imaginary. \square

We subsequently consider the degenerate case $\sigma_\# = 0$ but assume $c_1 \neq 0$, which generalizes Theorem 2.19 to the present 3D setting. We will show that the generalization of σ_2 is given by $\omega^2 \tilde{\Gamma}_3$, where

$$\tilde{\Gamma}_3 := \tilde{\delta}_{03} - \tilde{\delta}_{11} \frac{\tilde{\gamma}_{02}}{\tilde{\gamma}_{10}}, \quad (2.64)$$

with $\bar{\gamma}_{10}$ from (2.51), and

$$\begin{aligned}\tilde{\delta}_{11} &:= \bar{\delta}_{11}|_{\mu=0} = \frac{e^{\frac{2\pi c_1}{\omega}} - 1}{c_1} \frac{\rho_1}{c_1^2 + 4\omega^2}, & \tilde{\gamma}_{02} &:= \bar{\gamma}_{02}|_{\mu=0} = \frac{1}{\omega} e^{\frac{2\pi c_1}{\omega}} \int_0^{2\pi} e^{-s\frac{c_1}{\omega}} \Upsilon(s) ds, \\ \tilde{\delta}_{03} &:= \Gamma_3 + \frac{1}{\omega^2} \int_0^{2\pi} \chi_1(s) \int_0^s e^{c_1 \frac{s-\tau}{\omega}} \Upsilon(\tau) d\tau ds,\end{aligned}$$

where

$$\Gamma_3 = \frac{2}{\omega^2} \int_0^{2\pi} \chi_2(s) \int_0^s \chi_2(\tau) d\tau ds - \frac{1}{\omega^2} \int_0^{2\pi} \chi_2(s) \Omega_1 ds.$$

Comparing $\tilde{\Gamma}_3$ with Γ_3 , we thus expect $\tilde{\Gamma}_3 \neq \Gamma_3$, as a result of the coupling with the additional variable u . We omit here the fully explicit approach for $\tilde{\Gamma}_3$, since the expressions become too lengthy for practical use. However, for illustration, we consider the simpler case $h = 0$ in (2.50), which yields

$$\tilde{\delta}_{03} = \Gamma_3 + \frac{c_5 \pi (c_6 + c_9)}{c_1^2 + 4\omega^2} \left(e^{\frac{2\pi}{\omega} c_1} - 1 \right), \quad \tilde{\delta}_{11} \frac{\tilde{\gamma}_{02}}{\bar{\gamma}_{10}} = \frac{c_5 \rho_1 \omega}{c_1 (c_1^2 + 4\omega^2)^2} \left(e^{\frac{2\pi}{\omega} c_1} - 1 \right),$$

and hence,

$$\tilde{\Gamma}_3 = \Gamma_3 + \frac{c_5 \left(e^{\frac{2\pi}{\omega} c_1} - 1 \right)}{c_1^2 + 4\omega^2} \left[\pi (c_6 + c_9) - \frac{\rho_1 \omega}{c_1 (c_1^2 + 4\omega^2)} \right].$$

Corollary 2.23. Consider (2.50) in cylindrical coordinates $(u, v, w) = (u, r \cos \varphi, r \sin \varphi)$ and $\sigma_{\#} = 0$. If $c_1 \neq 0$, then $u = u(\varphi; \mu) = \mathcal{O}(\mu^2)$ and the statement of Theorem 2.19 holds true with σ_2 replaced by $\omega^2 \tilde{\Gamma}_3$.

Proof. Upon rescaling time the equations for u, r in cylindrical coordinates of (2.50) become (2.55). Similarly to the proof of Theorem 2.21, we compute the Taylor expansion of u' and r' in $(u, r) = (0, 0)$ up to fourth order (see Appendix A.3.2 for the details) and we write $u(\varphi)$ and $r(\varphi)$ as the following expansions:

$$\begin{aligned}u(\varphi) &= \gamma_{10}(\varphi) u_0 + \gamma_{20}(\varphi) u_0^2 + \gamma_{30}(\varphi) u_0^3 + \gamma_{01}(\varphi) r_0 + \gamma_{02}(\varphi) r_0^2 + \gamma_{03}(\varphi) r_0^3 \\ &\quad + \gamma_{11}(\varphi) u_0 r_0 + \gamma_{21}(\varphi) u_0^2 r_0 + \gamma_{12}(\varphi) u_0 r_0^2 + \mathcal{O}(4), \\ r(\varphi) &= \delta_{10}(\varphi) u_0 + \delta_{20}(\varphi) u_0^2 + \delta_{30}(\varphi) u_0^3 + \delta_{01}(\varphi) r_0 + \delta_{02}(\varphi) r_0^2 + \delta_{03}(\varphi) r_0^3 \\ &\quad + \delta_{11}(\varphi) u_0 r_0 + \delta_{21}(\varphi) u_0^2 r_0 + \delta_{12}(\varphi) u_0 r_0^2 + \mathcal{O}(4),\end{aligned}\tag{2.65}$$

with the initial conditions $u(0) = u_0$ and $r(0) = r_0$, which imply $\gamma_{10}(0) = \delta_{01}(0) = 1$ and the rest zero. With these expressions we compute, as before, the functions γ_{ij} and $\delta_{ij} \forall i, j \in \mathbb{N}_0$, such that $i + j = 3$. Note that the others are the same as for Theorem 2.21. The periodic solutions with $r(0) = r_0, u(0) = u_0$ for $0 \leq |\mu| \ll 1$ near $r = u = 0$ are in 1-to-1 correspondence with solutions to the algebraic equation system

$$0 = \bar{\gamma}_{10} u_0 + \bar{\gamma}_{20} u_0^2 + \bar{\gamma}_{30} u_0^3 + \bar{\gamma}_{02} r_0^2 + \bar{\gamma}_{03} r_0^3 + \bar{\gamma}_{11} u_0 r_0 + \bar{\gamma}_{21} u_0^2 r_0 + \bar{\gamma}_{12} u_0 r_0^2 + \mathcal{O}(4),\tag{2.66}$$

$$0 = \bar{\delta}_{01} r_0 + \bar{\delta}_{02} r_0^2 + \bar{\delta}_{03} r_0^3 + \bar{\delta}_{11} u_0 r_0 + \bar{\delta}_{21} u_0^2 r_0 + \bar{\delta}_{12} u_0 r_0^2 + \mathcal{O}(4),\tag{2.67}$$

where $\mathcal{O}(4)$ are terms of at least fourth order in u_0, r_0 , and $\bar{\gamma}_{ij} = \gamma_{ij}(2\pi) - \gamma_{ij}(0)$, $\bar{\delta}_{ij} = \delta_{ij}(2\pi) - \delta_{ij}(0)$. Moreover, since $c_1 \neq 0$ we have $\bar{\gamma}_{10} \neq 0$. Therefore, we may solve (2.66) for u_0 by the implicit function theorem as $u_0 = -\frac{\bar{\gamma}_{02}}{\bar{\gamma}_{10}}r_0^2 + \mathcal{O}(r_0^3) = \mathcal{O}(r_0^2)$.

Substitution into (2.67) and dividing out $r_0 \neq 0$ yield

$$0 = \bar{\delta}_{01} + \bar{\delta}_{02}r_0 + \left(\bar{\delta}_{03} - \bar{\delta}_{11} \frac{\bar{\gamma}_{02}}{\bar{\gamma}_{10}} \right) r_0^2 + \mathcal{O}(3),$$

which we rewrite, similarly to (2.43) in Theorem 2.19, as

$$0 = \frac{2\pi}{\omega} \mu + \tilde{\Gamma}_2 r_0 + \tilde{\Gamma}_3 r_0^2 + \mathcal{O}(\mu^2 + \mu r_0 + r_0^3), \quad (2.68)$$

where $\tilde{\Gamma}_2 = \bar{\delta}_{02}|_{\mu=0}$, which vanishes for $\sigma_{\#} = 0$ analogous as for equation (2.44), and $\tilde{\Gamma}_3$ is as defined in (2.64); the expression for $\bar{\delta}_{03}$ stems from (A.9). Hence, assuming $\tilde{\Gamma}_3$ to be nonzero, the solution for (2.68) is given by (2.38) replacing σ_2 by $\omega^2 \tilde{\Gamma}_3$:

$$r_0 = \sqrt{-\frac{2\pi}{\omega \tilde{\Gamma}_3} \mu} + \mathcal{O}(\mu),$$

as we wanted to show. The stability statement of Theorem 2.17 holds true from the existence of a 2D Lipschitz continuous invariant manifold given by Proposition 2.2. \square

Lastly, we use these results to extend system (2.50) to a higher order model with the generalized absolute value (2.1) as follows:

$$\begin{pmatrix} \dot{u} \\ \dot{v} \\ \dot{w} \end{pmatrix} = \begin{pmatrix} c_1 u + c_2 u^2 + c_3 uv + c_4 uw + c_5 vw + h(v, w; \gamma) \\ \mu v - \omega w + c_6 uv + c_7 uw + f(v, w; \alpha) + f_q(v, w) + f_c(v, w) \\ \omega v + \mu w + c_8 uv + c_9 uw + g(v, w; \beta) + g_q(v, w) + g_c(v, w) \end{pmatrix}, \quad (2.69)$$

where $f(v, w; \alpha)$ and $g(v, w; \beta)$ are (2.47) and (2.48), respectively, and the functions f_q, g_q, f_c, g_c are as in system (2.18). The expression of h is analogous to f, g . We recall also $\tilde{\sigma}_{\#}$ from (2.49).

Corollary 2.24. *If $\tilde{\sigma}_{\#} \neq 0$, the statement of Corollary 2.22 for system (2.69) holds true with $\sigma_{\#}$ replaced by $\tilde{\sigma}_{\#}$.*

Proof. The proof follows from Theorems 2.20 and 2.21 and Corollary 2.18. \square

This concludes our analysis for the 3D case, which paves the way for the n -dimensional case discussed thereafter.

2.3.3 n -dimensional system

We consider the n -dimensional generalization of (2.50) with additional component $u = (u_1, \dots, u_{n-2}) \in \mathbb{R}^{n-2}$ given by

$$\begin{pmatrix} \dot{u} \\ \dot{v} \\ \dot{w} \end{pmatrix} = \begin{pmatrix} \tilde{A}u + U(u, v, w) \\ \mu v - \omega w + \sum_{i=1}^{n-2} (c_{6i} u_i v + c_{7i} u_i w) + \tilde{f}(v, w) \\ \omega v + \mu w + \sum_{i=1}^{n-2} (c_{8i} u_i v + c_{9i} u_i w) + \tilde{g}(v, w) \end{pmatrix}, \quad (2.70)$$

where $\tilde{A} = (c_{1ij})_{1 \leq i, j \leq n-2}$ is an $(n-2) \times (n-2)$ matrix and $U : \mathbb{R}^{n-2} \times \mathbb{R} \times \mathbb{R} \rightarrow \mathbb{R}^{n-2}$ is a nonlinear function, smooth in u and possibly nonsmooth in v, w with absolute values as in (2.50). Hence, $U(u, v, w) = \mathcal{O}(2)$, where $\mathcal{O}(2)$ are terms of at least second order in u_i, v, w . The constants $c_{1ij}, c_{6i}, c_{7i}, c_{8i}, c_{9i}$ are all real $\forall i, j \in \{1, \dots, n-2\}$, and the functions \tilde{f}, \tilde{g} are of the same form as the nonlinear part of system (2.18).

We present now analogous results as before for this n -dimensional case. However, we refrain from explicitly determining the coefficients involved.

Theorem 2.25. *Consider (2.70) in cylindrical coordinates $(u, v, w) = (u, r \cos \varphi, r \sin \varphi)$ analogous to Theorem 2.21 with $u \in \mathbb{R}^{n-2}$. Up to time shifts, periodic solutions to (2.70) with $r(0) = r_0, u(0) = u_0 \in \mathbb{R}^{n-2}$ for $0 \leq |\mu|, r_0, |u_0| \ll 1$ are in 1-to-1 correspondence with solutions to the algebraic $(n-1)$ -dimensional system given by equations analogous to (2.52) and (2.53), where $\bar{\delta}_{01}, \bar{\delta}_{02}$ are scalars and $\bar{\gamma}_{10}, \bar{\gamma}_{11}, \bar{\gamma}_{02}, \bar{\gamma}_{20}, \bar{\delta}_{11}$ are linear maps and quadratic forms in $n-2$ dimensions.*

Proof. The proof is analogous to that of Theorem 2.21, now by setting up a boundary value problem with $n-2$ equations for $0 = u(2\pi) - u(0)$ and one for $0 = r(2\pi) - (0)$. This results in a system of $n-1$ equations formed by direct analogues to (2.52) and (2.53), where $\mathcal{O}(3)$ contains all terms of at least cubic order in u_{0i}, r_0 , and $\bar{\gamma}_{20}u_0^2$ is a quadratic form in $n-2$ dimensions. \square

Similar to the 3D case, the solution structure of the $(n-1)$ -dimensional system (2.52), (2.53) depends on whether the matrix \tilde{A} is hyperbolic (i.e., the full linear part A satisfies Hypothesis 2.1) or not, as shown in the next result.

Corollary 2.26. *Consider (2.70) in cylindrical coordinates $(u, v, w) = (u, r \cos \varphi, r \sin \varphi)$. If \tilde{A} is hyperbolic, then the solution vector $u = u(\varphi; \mu)$ is of order $\mathcal{O}(\mu^2)$ and the statement of Theorem 2.17 holds true. If \tilde{A} is not hyperbolic with 1D generalized kernel, then there are constants $c_2, \gamma_{\#}$ such that the statements of Corollary 2.22 for $c_1 = 0$ hold true.*

Proof. From Theorem 2.25 we have the corresponding equations (2.52), (2.53) for the n -dimensional system (2.70), where $\bar{\gamma}_{20}u_0^2$ is a quadratic form in $n-2$ dimensions. If \tilde{A} is hyperbolic, then the $(n-2) \times (n-2)$ matrix $\bar{\gamma}_{10} = e^{2\pi\tilde{A}/\omega} - \text{Id}$ is invertible. Solving the $(n-1)$ -dimensional system gives the same as in the proof of Corollary 2.22 to leading order.

If \tilde{A} is not hyperbolic, then by assumption it has a 1D generalized kernel. In this case, we change coordinates in the analogue of (2.52) such that the matrix $\bar{\gamma}_{10}$ is block-diagonal with the kernel in the top left, and an invertible $(n-3) \times (n-3)$ block $\bar{\gamma}'_{10}$ on the lower right of the matrix. Thus, we split (2.52) into a scalar equation and an $(n-3)$ -dimensional system. By the implicit function theorem we solve the equations corresponding to $\bar{\gamma}'_{10}$ and substitute the result into the other two equations: the one with the 1D kernel and the corresponding (2.53) with $\bar{\delta}_{01} = \frac{2\pi\mu}{\omega} + \mathcal{O}(\mu^2), \bar{\delta}_{02} = \frac{4\sigma_{\#}}{3\omega} + \mathcal{O}(\mu)$. We obtain then two scalar equations of the same type as in Corollary 2.22 for the case $c_1 = 0$. \square

We omit explicit formulas for $c_2, \gamma_{\#}$, but note that these can be provided in terms of data from \tilde{A} . Before concluding this section, we remark that these results directly extend to the

more general nonsmooth terms (2.1) and to additional higher order functions as in (2.18). For that, we present the following corollary, recalling $\tilde{\sigma}_\#$ from (2.49):

$$\tilde{\sigma}_\# = a_{11}(\alpha_{1+} - \alpha_{1-}) + \frac{1}{2}a_{12}(\alpha_{2+} - \alpha_{2-}) + \frac{1}{2}b_{21}(\beta_{3+} - \beta_{3-}) + b_{22}(\beta_{4+} - \beta_{4-}).$$

Corollary 2.27. *Consider system (2.70) with \tilde{f}, \tilde{g} as the nonlinear part of (2.18), but with f, g as in (2.47), (2.48), respectively. If \tilde{A} is hyperbolic and $\tilde{\sigma}_\# \neq 0$, then the statement of Corollary 2.26 holds true with $\sigma_\#$ replaced by $\tilde{\sigma}_\#$.*

Recall from §2.1 that we have presented results for systems where the linear part is in block-diagonal form and normal form for the oscillatory part, while the nonlinear part is smooth in the radial direction. For completeness, we next discuss the case of general linear part, i.e., not necessarily in normal form.

2.3.4 General linear part

Here we show that our analysis also applies to systems with general linear part. First, we consider the planar case (2.10) with

$$\begin{aligned} f_1(u_1, u_2) &= a_{11}u_1|u_1| + a_{12}u_1|u_2| + a_{21}u_2|u_1| + a_{22}u_2|u_2| + \mathcal{O}(3), \\ f_2(u_1, u_2) &= b_{11}u_1|u_1| + b_{12}u_1|u_2| + b_{21}u_2|u_1| + b_{22}u_2|u_2| + \mathcal{O}(3). \end{aligned}$$

Under Hypothesis 2.1, changing the linear part of (2.10) to normal form by the associated matrix \mathbf{T} , i.e., $\mathbf{T} \cdot (v_1, v_2)^\top = (u_1, u_2)^\top$, the system becomes

$$\begin{pmatrix} \dot{v}_1 \\ \dot{v}_2 \end{pmatrix} = \begin{pmatrix} \mu & -\omega \\ \omega & \mu \end{pmatrix} \begin{pmatrix} v_1 \\ v_2 \end{pmatrix} + \mathbf{T}^{-1} \begin{pmatrix} g_1(v_1, v_2) \\ g_2(v_1, v_2) \end{pmatrix}, \quad (2.71)$$

where $g_i(v_1, v_2) = f_i(\mathbf{T} \cdot (v_1, v_2)^\top)$ for $i \in \{1, 2\}$ and with $\mathbf{T} = (z_{ij})_{1 \leq i, j \leq 2}$, as well as the shorthand $[[\cdot]] := |\cdot|$, we have

$$\begin{aligned} g_1(v_1, v_2) &= a_{11}[[z_{11}v_1 + z_{12}v_2]] + a_{12}(z_{11}v_1 + z_{12}v_2)|z_{21}v_1 + z_{22}v_2| \\ &\quad + a_{21}(z_{21}v_1 + z_{22}v_2)|z_{11}v_1 + z_{12}v_2| + a_{22}[[z_{21}v_1 + z_{22}v_2]] + \mathcal{O}(3), \\ g_2(v_1, v_2) &= b_{11}[[z_{11}v_1 + z_{12}v_2]] + b_{12}(z_{11}v_1 + z_{12}v_2)|z_{21}v_1 + z_{22}v_2| \\ &\quad + b_{21}(z_{21}v_1 + z_{22}v_2)|z_{11}v_1 + z_{12}v_2| + b_{22}[[z_{21}v_1 + z_{22}v_2]] + \mathcal{O}(3). \end{aligned}$$

We use polar coordinates for $(v_1, v_2) = (r \cos(\varphi), r \sin(\varphi))$ as before, and

$$(z_{11}, z_{12}) = (C \cos(\phi), C \sin(\phi)), \quad (z_{21}, z_{22}) = (D \cos(\vartheta), D \sin(\vartheta)),$$

where $C, D \in \mathbb{R}$, $\phi, \vartheta \in [0, 2\pi)$ are fixed constants. System (2.71) can be written as

$$\begin{cases} \dot{r} = \mu r + \chi_2(\varphi)r^2 + \mathcal{O}(r^3), \\ \dot{\varphi} = \omega + \Omega_1(\varphi)r + \mathcal{O}(r^2), \end{cases} \quad (2.72)$$

where, using trigonometric identities, we have

$$\begin{aligned}\chi_2(\varphi) = & \frac{1}{\det(\mathbf{T})} \left([[\cos(\varphi - \phi)]] C|C|(a_{11}R + b_{11}S) \right. \\ & + \cos(\varphi - \phi) |\cos(\varphi - \vartheta)| C|D|(a_{12}R + b_{12}S) \\ & + \cos(\varphi - \vartheta) |\cos(\varphi - \phi)| C|D|(a_{21}R + b_{21}S) \\ & \left. + [[\cos(\varphi - \vartheta)]] D|D|(a_{22}R + b_{22}S) \right),\end{aligned}$$

with $R := D \sin(\vartheta - \varphi)$, $S := C \sin(\varphi - \phi)$. By assumption, $\omega \neq 0$ so that rescaling time in (2.72) analogous to (2.7) gives (2.12) with $M(\varphi) = \mu$ and $W(\varphi) = \omega$. Following the approach described in §2.1, for the analogue of (2.13) we obtain

$$\Lambda = \frac{1}{2\pi} \int_0^{2\pi} \frac{\mu}{\omega} d\varphi = \frac{\mu}{\omega}, \quad (2.73)$$

$$\Sigma = \frac{1}{2\pi} \int_0^{2\pi} \frac{\chi_2(\varphi)}{\omega} d\varphi, \quad (2.74)$$

where we set $\mu = 0$ in (2.74) (unlike in (2.15)) and the expression for Σ can be determined explicitly. For instance, the first term of $\chi_2(\varphi)$ can be integrated as

$$\frac{C|C|D}{\det(\mathbf{T})} a_{11} \int_0^{2\pi} [[\cos(\varphi - \phi)]] \sin(\vartheta - \varphi) d\varphi = \frac{8C|C|D}{3\det(\mathbf{T})} a_{11} \sin(\vartheta - \phi) = \frac{8}{3} |C| a_{11},$$

with last equality due to $\det(\mathbf{T}) = CD \sin(\vartheta - \phi)$. Computing the integral of $\chi_2(\varphi)$, (2.74) turns into

$$\begin{aligned}\Sigma = & \frac{2}{3\pi\omega} \left[2|C|a_{11} + |D|a_{12} + |C|b_{21} + 2|D|b_{22} \right. \\ & \left. + \cos(\vartheta - \phi) (\operatorname{sgn}(C)Da_{21} + \operatorname{sgn}(D)Cb_{12}) \right].\end{aligned} \quad (2.75)$$

In the case that $\phi = 0$ and $\vartheta = \frac{\pi}{2}$, we have $\cos(\vartheta - \phi) = 0$ so that the last few terms in (2.75) vanish and for $C = D = 1$ the same expression as in (2.28) is obtained, i.e., $\Sigma = \frac{2}{3\pi\omega} \sigma_{\#}$. Notice that this set of parameters gives $z_{11} = z_{22} = 1$, $z_{12} = z_{21} = 0$, i.e., \mathbf{T} is the identity.

General linear part with generalized absolute value

We can derive the analogue of (2.75) for the generalized nonsmooth function (2.1) and compute the integrals involved in the generalized $\chi_2(\varphi)$ as in the proof of Theorem 2.20. For instance, some of them read, omitting the factor $\det(\mathbf{T})^{-1}$,

$$\begin{aligned}& C|C| \int_0^{2\pi} \cos(\varphi - \phi) \\ & \cdot \left([\cos(\varphi - \phi)]_{\alpha_{1-}}^{\alpha_{1+}} D \sin(\vartheta - \varphi) a_{11} + [\cos(\varphi - \phi)]_{\beta_{1-}}^{\beta_{1+}} C \sin(\varphi - \phi) b_{11} \right) d\varphi \\ & = \frac{4}{3} C|C|D \sin(\vartheta - \phi) a_{11} (\alpha_{1+} - \alpha_{1-}),\end{aligned}$$

$$\begin{aligned}
& C|D| \int_0^{2\pi} \cos(\varphi - \phi) \\
& \cdot \left([\cos(\varphi - \vartheta)]_{\alpha_{2-}}^{\alpha_{2+}} D \sin(\vartheta - \varphi) a_{12} + [\cos(\varphi - \vartheta)]_{\beta_{2-}}^{\beta_{2+}} C \sin(\varphi - \phi) b_{12} \right) d\varphi \\
& = \frac{1}{3} C|D| \left[2D \sin(\vartheta - \phi) a_{12} (\alpha_{2+} - \alpha_{2-}) + C \sin(2(\vartheta - \phi)) b_{12} (\beta_{2+} - \beta_{2-}) \right].
\end{aligned}$$

The full expression can be simplified to

$$\begin{aligned}
\tilde{\Sigma} := & \frac{2}{3\pi\omega} \left[|C| a_{11} (\alpha_{1+} - \alpha_{1-}) + \frac{|D|}{2} a_{12} (\alpha_{2+} - \alpha_{2-}) \right. \\
& + \frac{|C|}{2} b_{21} (\beta_{3+} - \beta_{3-}) + |D| b_{22} (\beta_{4+} - \beta_{4-}) \\
& \left. + \frac{\cos(\vartheta - \phi)}{2} \left(\operatorname{sgn}(C) D a_{21} (\alpha_{3+} - \alpha_{3-}) + \operatorname{sgn}(D) C b_{12} (\beta_{2+} - \beta_{2-}) \right) \right].
\end{aligned}$$

As above, for $\phi = 0$ and $\vartheta = \frac{\pi}{2}$ the last few terms vanish, and for $C = D = 1$ we have $\tilde{\Sigma} = \frac{2}{3\pi\omega} \tilde{\sigma}_{\#}$ with $\tilde{\sigma}_{\#}$ from (2.49).

Furthermore, we can extend these results for the case $n > 2$ in the form of a coupled system similar to (2.3) using the approach presented in the proof of Theorem 2.3. This gives an integral expression for the generalized first Lyapunov coefficient which provides an explicit algebraic formula for an adjusted $\tilde{\sigma}_{\#}$. We summarize this in the following result.

Theorem 2.28. *Consider system (2.2) with general linear part $A(\mu)$ and satisfying the hypotheses of Theorem 2.6. The statement of Corollary 2.27 holds true with $\tilde{\sigma}_{\#}$ replaced by $\frac{3\pi\omega}{2} \tilde{\Sigma}$.*

In particular, this theorem covers system (2.10) with general matrix $A = (m_{ij})_{1 \leq i, j \leq 2}$. We also remark that the system considered here is neither of the form of (2.50) nor of (2.70) in terms of smoothness of the u variable.

Proof. We proceed as before to get the analogue of system (2.71), i.e., transforming the linear part into a block-diagonal matrix and normal form in E^c . From Theorem 2.6 the nonlinear terms are second order modulus terms, which in this case are of the form

$$(L_i(v, w) + K_i(u)) [L_j(v, w) + K_j(u)]_{p_{\pm}}^{p_{\pm}}, \quad i, j \in \{1, 2\},$$

with variables $u \in \mathbb{R}^{n-2}$, $v, w \in \mathbb{R}$. The functions $L_i(v, w)$ are linear combinations of v, w ; $K_i(u)$ are linear combinations of the components of the vector u , i.e., $u_l \forall l \in \{1, \dots, n-2\}$; and $p_+, p_- \in \mathbb{R}$ are as in (2.1). Note that L_1, K_1 are not necessarily equal to L_2, K_2 , respectively.

The previous product can be expanded as

$$(L_i(v, w) + K_i(u)) [L_j(v, w) + K_j(u)]_{p_{\pm}}^{p_{\pm}} = L_i [L_j]_{p_{\pm}}^{p_{\pm}} + \mathcal{O}(L_i K_j + L_j K_i + K_i K_j), \quad (2.76)$$

since the error term $p_+ L_i L_j - L_i [L_j]_{p_{\pm}}^{p_{\pm}}$ (resp., $p_- L_i L_j - L_i [L_j]_{p_{\pm}}^{p_{\pm}}$) is of order $|u|^2$, i.e., contained in the higher order terms of (2.76). More precisely, consider the case $L_j + K_j \geq 0$.

Then, the error term is $p_+L_iL_j - L_i[L_j]_{p_-}^{p_+}$, which is zero for $L_j \geq 0$, and otherwise $(p_+ - p_-)L_iL_j$. However, in order to have both $L_j + K_j \geq 0$ and $L_j < 0$, the signs of L_j and K_j have to differ, which happens only if these magnitudes are comparable. Hence, $\mathcal{O}(L_j) = \mathcal{O}(K_j)$, and thus this error term enters as higher order. For the case $L_j + K_j < 0$ one proceeds analogously.

In particular, $\mathcal{O}(L_iK_j + L_jK_i + K_iK_j) = \mathcal{O}(K(\check{K} + L))$, where K, \check{K} are linear combinations of the components of u , and L of v, w .

Following the proof of Theorem 2.3, we write $u = r\tilde{u}$ and, together with the change of polar coordinates from above, $L_i = r \cos(\varphi - \zeta_i)$ (where ζ_i is either ϕ or ϑ), so that

$$(L_i(v, w) + rK_i(\tilde{u}))[L_j(v, w) + rK_j(\tilde{u})]_{p_-}^{p_+} = r^2 \cos(\varphi - \zeta_i)[\cos(\varphi - \zeta_j)]_{p_-}^{p_+} + r^2\mathcal{O}(\tilde{u}).$$

From Theorem 2.3 we have $\tilde{u} = \mathcal{O}(r_0)$ and thus $r^2\mathcal{O}(\tilde{u})$ is of higher order. We can then integrate explicitly the leading order as done for (2.74). \square

We implement now these results to an applied 3D model in the field of land vehicles.

2.4 A 3D example: Shimmying wheel

For illustration of the theory and its practice, we consider as an example the model of a shimmying wheel with contact force analyzed in [5], where a towed caster with an elastic tire is studied. The equations of motion of the towed wheel can be written as follows:

$$\begin{pmatrix} \dot{\Omega} \\ \dot{\psi} \\ \dot{q} \end{pmatrix} = \mathbf{J} \begin{pmatrix} \Omega \\ \psi \\ q \end{pmatrix} + \tilde{c}_4 \begin{pmatrix} q|q| \\ 0 \\ 0 \end{pmatrix}, \quad \mathbf{J} := \begin{pmatrix} \tilde{c}_1 & \tilde{c}_2 & \tilde{c}_3 \\ 1 & 0 & 0 \\ \tilde{c}_5 & \tilde{c}_6 & \tilde{c}_7 \end{pmatrix}, \quad (2.77)$$

where ψ is the yaw angle, q is the deformation angle of the tire due to the contact with the ground and $\Omega = \dot{\psi}$, and the parameters $\tilde{c}_i \in \mathbb{R}$ are constants determined by the system. We can readily see that there is only one switching surface in this case, namely $\{q = 0\}$. Furthermore, \mathbf{J} is the Jacobian matrix at the equilibrium point $(\Omega, \psi, q) = (0, 0, 0)$.

The system is of the form (2.2) and suitable parameter choices yield a complex conjugate pair of eigenvalues crossing the imaginary axis, as well as one nonzero real eigenvalue. The resulting bifurcations were studied in [5] and termed “dynamic loss of stability”. Here we expound how our approach applies to this system.

Clearly, Theorem 2.3 applies for any Hopf bifurcation eigenvalue configuration, which proves that a unique branch of periodic solutions bifurcates. In order to identify the direction of bifurcation, we first aim to apply the results of §2.3.2 and thus attempt to bring the nonlinear part into a second order modulus form, while also bringing the linear part into Jordan normal form.

We therefore suppose the parameters are such that the Jacobian matrix has a complex conjugate pair of eigenvalues $\lambda_{\pm} = \mu \pm i\omega$, where $\mu, \omega, \lambda_3 \in \mathbb{R}$, $\omega, \lambda_3 \neq 0$, with the corresponding eigenvectors $\mathbf{s}_1 = \mathbf{u} + i\mathbf{v}$, $\mathbf{s}_2 = \mathbf{u} - i\mathbf{v}$, and \mathbf{s}_3 , where $\mathbf{u}, \mathbf{v}, \mathbf{s}_3 \in \mathbb{R}^3$. In particular, we write $\mathbf{u} = (u_1, u_2, u_3)$, $\mathbf{v} = (v_1, v_2, v_3)$, $\mathbf{s}_3 = (s_1, s_2, s_3)$. Such parameter

choices are possible as it can be seen from inspecting the characteristic equation with the Routh–Hurwitz criterion; we omit the details and refer to [5]. Defining $\mathbf{T} = (\mathbf{u}|\mathbf{v}|\mathbf{s}_3)$ with columns $\mathbf{u}, \mathbf{v}, \mathbf{s}_3$, and considering the new state variables (ξ_1, ξ_2, ξ_3) , we have that the transformation $(\xi_1, \xi_2, \xi_3)^\top = \mathbf{T}^{-1}(\Omega, \psi, q)^\top$ turns (2.77) into

$$\begin{pmatrix} \dot{\xi}_1 \\ \dot{\xi}_2 \\ \dot{\xi}_3 \end{pmatrix} = \mathbf{A} \begin{pmatrix} \xi_1 \\ \xi_2 \\ \xi_3 \end{pmatrix} + \mathbf{h}_2(\xi_1, \xi_2, \xi_3), \quad \mathbf{A} = \begin{pmatrix} \mu & \omega & 0 \\ -\omega & \mu & 0 \\ 0 & 0 & \lambda_3 \end{pmatrix}. \quad (2.78)$$

Here \mathbf{h}_2 contains the quadratic terms and reads, using the shorthand $[[\cdot]] := \cdot|\cdot|$,

$$\mathbf{h}_2(\xi_1, \xi_2, \xi_3) = (\tilde{T}_1, \tilde{T}_2, \tilde{T}_3)^\top [[u_3\xi_1 + v_3\xi_2 + s_3\xi_3]], \quad (2.79)$$

where $u_j, v_j, s_j, j \in \{1, 2, 3\}$, are the components of the vectors $\mathbf{u}, \mathbf{v}, \mathbf{s}_3$, respectively, and

$$\tilde{T}_1 := \tilde{c}_4 \frac{v_2 s_3 - v_3 s_2}{\det(\mathbf{T})}, \quad \tilde{T}_2 := \tilde{c}_4 \frac{s_2 u_3 - s_3 u_2}{\det(\mathbf{T})}, \quad \tilde{T}_3 := \tilde{c}_4 \frac{u_2 v_3 - u_3 v_2}{\det(\mathbf{T})}.$$

If $u_3 = v_3 = 0$, then the nonlinear term \mathbf{h}_2 in (2.79) is of second order modulus form:

$$\mathbf{h}_2(\xi_1, \xi_2, \xi_3) = s_3 |s_3| (\tilde{T}_1, \tilde{T}_2, 0)^\top \xi_3 |\xi_3|, \quad (2.80)$$

where $\det(\mathbf{T}) \neq 0$ implies $s_3 \neq 0$. In this case, we need no further theory as we can directly solve (2.78): the equation for ξ_3 becomes decoupled and reads $\dot{\xi}_3 = \lambda_3 \xi_3$, with solution $\xi_3(t) = \xi_3(0)e^{\lambda_3 t}$, where periodic orbits require $\xi_3(t) \equiv 0$, and thus, $\xi_3(0) = 0$. The remaining system for ξ_1, ξ_2 is then the purely linear part

$$\begin{pmatrix} \dot{\xi}_1 \\ \dot{\xi}_2 \end{pmatrix} = \begin{pmatrix} \mu & \omega \\ -\omega & \mu \end{pmatrix} \begin{pmatrix} \xi_1 \\ \xi_2 \end{pmatrix},$$

yielding the solutions

$$\begin{aligned} \xi_1(t) &= e^{\mu t} (\sin(\omega t)\xi_2(0) + \cos(\omega t)\xi_1(0)), \\ \xi_2(t) &= e^{\mu t} (\cos(\omega t)\xi_2(0) - \sin(\omega t)\xi_1(0)), \end{aligned}$$

which consist of periodic orbits (except the origin) for $\mu = 0$. The unique branch of bifurcating periodic solutions is thus vertical, i.e., has $\mu = 0$ constant.

Next, we consider the case when one of u_3, v_3 is nonzero. In order to simplify the nonlinear term, we apply a rotation \mathbf{R}_θ about the ξ_3 -axis with angle θ ,

$$\mathbf{R}_\theta = \begin{pmatrix} \cos \theta & -\sin \theta & 0 \\ \sin \theta & \cos \theta & 0 \\ 0 & 0 & 1 \end{pmatrix},$$

which keeps the Jordan normal form matrix invariant, and in the new variables $(v, w, u)^\top = \mathbf{R}_\theta^{-1}(\xi_1, \xi_2, \xi_3)^\top$, in particular $\xi_3 = u$, the nonlinear term from (2.79) reads

$$|u_3(v \cos \theta - w \sin \theta) + v_3(v \sin \theta + w \cos \theta) + s_3 u| = |\tilde{d}v + w(v_3 \cos \theta - u_3 \sin \theta) + s_3 u|, \quad (2.81)$$

where $\tilde{d} = u_3 \cos \theta + v_3 \sin \theta$. We select θ to simplify (2.81) as follows: if $u_3 \neq 0$, we choose $\theta = \tilde{\theta} = \arctan(\frac{v_3}{u_3})$ such that the coefficient of w in (2.81) vanishes, i.e., $v_3 \cos \tilde{\theta} - u_3 \sin \tilde{\theta} = 0$. Note that $\tilde{d} \neq 0$ since otherwise $v_3 \tan \tilde{\theta} = -u_3$, but $\tan \tilde{\theta} = \frac{v_3}{u_3}$, so that combining both expressions we would have $v_3^2 = -u_3^2$ and thus $u_3 = v_3 = 0$ (which has been discussed above). If $u_3 = 0$ and $v_3 \neq 0$, we choose $\theta = \tilde{\theta} = \arctan(-\frac{u_3}{v_3})$ such that the coefficient of v vanishes, i.e., $u_3 \cos \tilde{\theta} + v_3 \sin \tilde{\theta} = 0$, and the following computation is analogous.

Hence, in the case that $u_3 \neq 0$, system (2.78) becomes

$$\begin{pmatrix} \dot{v} \\ \dot{w} \\ \dot{u} \end{pmatrix} = \mathbf{A} \begin{pmatrix} v \\ w \\ u \end{pmatrix} + \mathbf{h}_3(v, w, u), \quad \mathbf{h}_3(v, w, u) = \begin{pmatrix} \tilde{T}_1 \cos \tilde{\theta} + \tilde{T}_2 \sin \tilde{\theta} \\ -\tilde{T}_1 \sin \tilde{\theta} + \tilde{T}_2 \cos \tilde{\theta} \\ \tilde{T}_3 \end{pmatrix} [|\tilde{d}v + s_3 u|]. \quad (2.82)$$

Notably, since $\tilde{d} \neq 0$, the nonlinear term is of second order modulus form for $s_3 = 0$, and we consider this degenerate situation first; as mentioned, the case $u_3 = 0, v_3 \neq 0$ is analogous.

If $s_3 = 0$ (which means that the third component of the third eigenvector of the matrix \mathbf{T} is zero) the nonlinear term in (2.82) is of second order modulus form. We can write system (2.82) in the notation of system (2.50):

$$\begin{pmatrix} \dot{u} \\ \dot{v} \\ \dot{w} \end{pmatrix} = \begin{pmatrix} c_1 u + h_{11} v |v| \\ \mu v - \omega w + a_{11} v |v| \\ \omega v + \mu w + b_{11} v |v| \end{pmatrix}, \quad (2.83)$$

where we changed ω to $-\omega$ and set

$$\begin{aligned} c_1 &:= \lambda_3, & a_{11} &:= (\tilde{T}_1 \cos \tilde{\theta} + \tilde{T}_2 \sin \tilde{\theta}) \tilde{d} |\tilde{d}|, \\ h_{11} &:= \tilde{T}_3 \tilde{d} |\tilde{d}|, & b_{11} &:= (-\tilde{T}_1 \sin \tilde{\theta} + \tilde{T}_2 \cos \tilde{\theta}) \tilde{d} |\tilde{d}|. \end{aligned}$$

Since $s_3 = 0$, we have $a_{11} = 0$ by choice of $\tilde{\theta}$, which implies $\sigma_\# = 0$. Furthermore, $\sigma_2 = 0$ holds so that Theorem 2.19 does not apply. However, at $\mu = 0$ we have

$$\begin{cases} \dot{v} = -\omega w, \\ \dot{w} = \omega v + b_{11} v |v|, \end{cases}$$

which can be written as

$$\ddot{v} = -\omega^2 v - \omega b_{11} v |v| = -\frac{d}{dv} P$$

with potential energy

$$P(v) = \frac{\omega^2}{2}v^2 + \frac{\omega b_{11}}{3}v^2|v|,$$

which is globally convex if $\omega b_{11} \geq 0$. Otherwise, it is convex in an interval around zero and concave outside of it. In both cases there is a vertical branch of periodic solutions, which is either unbounded or bounded by heteroclinic orbits.

Let us now come back to (2.82) for $s_3 \neq 0$, where the nonlinearity is of the form $\mathbf{h}_3 = (h_{31}, h_{32}, h_{33})^T [[\tilde{d}v + s_3u]]$. We first note that in the cylindrical coordinates from (2.3) with the rescaled $u = r\tilde{u}$ for $r \neq 0$, we have

$$\begin{aligned}\dot{r} &= \mu r + r^2 [[\tilde{d} \cos(\varphi) + s_3 \tilde{u}]] (h_{31} \cos(\varphi) + h_{32} \sin(\varphi)), \\ \dot{\varphi} &= \omega + r [[\tilde{d} \cos(\varphi) + s_3 \tilde{u}]] (h_{32} \cos(\varphi) - h_{31} \sin(\varphi)), \\ \dot{\tilde{u}} &= \lambda_3 \tilde{u} + \tilde{T}_3 r [[\tilde{d} \cos(\varphi) + s_3 \tilde{u}]].\end{aligned}$$

Following the notation of the proof of Theorem 2.3, we have the estimate $|\tilde{u}_\infty| = \mathcal{O}(r_\infty)$ and together with the expansion of the $[[\cdot]]$ terms from the proof of Theorem 2.28, we can write

$$\dot{r} = \mu r + r^2 [[\tilde{d} \cos(\varphi)]] (h_{31} \cos(\varphi) + h_{32} \sin(\varphi)) + \mathcal{O}(r^2 r_\infty).$$

In the notation of Proposition 2.15, in this case

$$\chi_2(\varphi) = [[\tilde{d} \cos(\varphi)]] (h_{31} \cos(\varphi) + h_{32} \sin(\varphi)),$$

and according to Corollary 2.16 the bifurcating branch is given by (2.30) with

$$\int_0^{2\pi} \chi_2(\varphi) d\varphi = \tilde{d} |\tilde{d}| h_{31} \int_0^{2\pi} \cos^2(\varphi) |\cos(\varphi)| d\varphi = \frac{8}{3} \tilde{d} |\tilde{d}| h_{31} = \frac{8}{3} |\tilde{d}| \frac{\tilde{d} s_3 \tilde{c}_4}{\det(\mathbf{T})}.$$

Since $\tilde{d} \neq 0$ the direction of bifurcation is determined by the sign of $\tilde{d} s_3 \tilde{c}_4 \det(\mathbf{T})$. Note that \tilde{d} , s_3 , $\det(\mathbf{T})$ are independent of \tilde{c}_4 , and $\tilde{d} s_3 \tilde{c}_4 \det(\mathbf{T}) = 0$ requires $s_3 = 0$ as discussed above, or $\tilde{c}_4 = 0$, which implies vanishing nonlinearity. Thus, in all degenerate cases the branch is vertical and we have proven the following result.

Theorem 2.29. *Any Hopf bifurcation in (2.77) either yields a vertical branch of periodic solutions or is super-/subcritical as in Proposition 2.15. Using the above notation, the branch is vertical if and only if $\tilde{d} s_3 \tilde{c}_4 = 0$, where $\tilde{d} = 0$ means $u_3 = v_3 = 0$. The bifurcation is supercritical if $\tilde{d} s_3 \tilde{c}_4 \det(\mathbf{T}) < 0$ and subcritical for positive sign. In particular, reversing the sign of \tilde{c}_4 switches the criticality of the bifurcation.*

This conclusion is consistent with the results in [5].

Chapter 3

Bogdanov–Takens Bifurcation

As mentioned in the introduction, this chapter is dedicated to the Bogdanov–Takens (BT) bifurcation, a bifurcation occurring from the variation of two parameters (codimension-two), characterized by the existence of a double zero eigenvalue. More precisely, if we consider a planar system $\dot{x} = f(x; \mu)$ with variable $x \in \mathbb{R}^2$ and parameter $\mu \in \mathbb{R}^2$, and f a smooth function in x , then the Jacobian matrix $J(x_*) \neq 0$, at the fixed point x_* , has a double zero eigenvalue $\lambda_1 = \lambda_2 = 0$. In addition, some nondegeneracy conditions must hold; see [35, Theorem 8.4].

In the previous chapter, we have analyzed the Andronov–Hopf bifurcation and its criticality for nonsmooth systems and derived explicit formulas for the generalization of the first and second Lyapunov coefficients. For this kind of model with piecewise smooth nonlinearity, an analysis of normal forms for coefficients for other bifurcations can be done. Specifically, in Chapter 2, we have shown that for systems of the form (2.8) with (2.9), the criticality of the Hopf bifurcation cannot be, in general, inferred from the smooth case.

Motivated by this idea, we will now investigate nonsmooth systems undergoing a symmetric Bogdanov–Takens bifurcation, showing that, in contrast to before, one can, in fact, infer the criticality of the nonsmooth system—with regular absolute value functions—from the smooth case. We will further show that, when considering the generalized absolute value (2.1), one has to pay attention to the different slopes which enter into the bifurcation analysis and hence, into the criticality of the Hopf bifurcation.

This chapter is structured as follows. In §3.1, the nonsmooth normal form of a system undergoing a BT bifurcation is presented. Hopf bifurcation results for this system are developed and compared to the smooth situation. A generalization from the absolute value is considered in §3.2 and the study of the resulting system is shown. Finally, an example for the unfolding of homoclinic and heteroclinic orbits is briefly explained in §3.3.

3.1 Planar normal form case with absolute value

A generic smooth system undergoing a symmetric Bogdanov–Takens bifurcation takes the following normal form

$$\begin{cases} \dot{x} = y, \\ \dot{y} = g_1x + g_3x^3 + y(g_2 + g_4x^2), \end{cases} \quad (3.1)$$

where $g_1, g_2, g_3, g_4 \in \mathbb{R}$ and $g_3 \neq 0$, see [10]. The fixed points are given by $(x_0, y_0) = (0, 0)$ and $(x_0, y_0) = (\pm\sqrt{-g_1/g_3}, 0)$ for $\text{sgn}(g_1) = -\text{sgn}(g_3)$.

If we replace x^2 in (3.1) by $|x|$, the system becomes

$$\begin{cases} \dot{x} = y, \\ \dot{y} = g_1x + g_3x|x| + y(g_2 + g_4|x|), \end{cases} \quad (3.2)$$

where the nonlinear terms have the same odd symmetry as the cubic terms in the previous smooth system. Thus, we consider (3.2) to be the corresponding nonsmooth version of (3.1) for our analysis. The three steady states are now $(x_0, y_0) = (0, 0)$ and $(|x_0|, y_0) = (-g_1/g_3, 0)$. As for the smooth system, the nonzero equilibria exist only for $\text{sgn}(g_1) = -\text{sgn}(g_3)$.

In the next sections it is shown that for $g_1 = g_2 = 0$, the linearization of both systems, at the zero and nonzero fixed points, have a double zero eigenvalue. In this case, Bogdanov–Takens bifurcations occur.

We recall that the normal form transformation requires differentiability, while in the nonsmooth case it is even not assured that the Taylor expansion exists in general. Therefore, we choose the nonsmooth system consisting basically of replacing the normal form terms from (3.1) by the absolute value function, as done for (3.2). We observe that the quadratic term x^2 with coefficient g_4 needs also to be changed to $|x|$. Otherwise, the cubic term g_4yx^2 would not enter into the Hopf bifurcation analysis.

Furthermore, regarding the singular change of variables used in §1.2 to transform the nonsmooth system into a smooth one, we observe that in this case, there is again no such a coordinate change, see (1.12), which would exist for the scalar case, similar to (1.11), and thus, a “nonsmooth” approach is required, as done in Chapter 2.

In the succeeding subsections we present results about the Hopf bifurcation curve bifurcating from the BT point $(g_1, g_2) = (0, 0)$.

3.1.1 Bifurcation analysis at the zero equilibrium

In this subsection we consider the nonsmooth system (3.2) at the zero fixed point and, applying the bifurcation analysis developed in Chapter 2 for a planar system with general linear part (2.10), as well as the averaging theory from §2.2.1, we obtain the following first result.

Theorem 3.1. *If $g_4 \neq 0$, then at $g_1 < 0$, $g_2 = 0$, (3.2) undergoes a degenerate Hopf bifurcation in g_1, g_2 , for the zero equilibrium. To leading order, the limit cycle is given by*

$$\bar{r} = -\frac{g_2}{C(g_1)g_4\sqrt{-4g_1 - g_2^2}}, \quad \text{where} \quad C(g_1) := \frac{1}{2\pi} \int_0^{2\pi} \frac{s^2|c|}{(g_1c^2 - s^2)^2} d\varphi > 0, \quad (3.3)$$

with \bar{r} the averaged radial component of the system in polar coordinates. In particular, the bifurcation is supercritical if $\text{sgn}(g_4) < 0$ and subcritical if $\text{sgn}(g_4) > 0$.

Proof. From the linearization of (3.2) at $(0, 0)$ and computing its Jordan form, we obtain the eigenvalues $\lambda_{\pm} = \frac{g_2}{2} \pm \frac{\sqrt{g_2^2 + 4g_1}}{2}$. These are purely imaginary if and only if $g_2 = 0$ and $g_1 < 0$, yielding $\lambda_{\pm} = \pm\sqrt{g_1}$, and thus, Hopf bifurcations occur for this set of parameters.

Upon changing to polar coordinates $(x, y) = (r \cos \varphi, r \sin \varphi)$, system (3.2) reads

$$\begin{cases} \dot{r} = M(\varphi)r + \chi_2(\varphi)r^2, \\ \dot{\varphi} = W(\varphi) + \Omega_1(\varphi)r, \end{cases} \quad (3.4)$$

where

$$\begin{aligned} M(\varphi) &= (1 + g_1)sc + g_2s^2, & W(\varphi) &= (1 + g_1)c^2 + g_2sc - 1, \\ \chi_2(\varphi) &= g_3sc|c| + g_4s^2|c|, & \Omega_1(\varphi) &= g_3c^2|c| + g_4sc|c|, \end{aligned} \quad (3.5)$$

defining $s := \sin \varphi$, $c := \cos \varphi$ for abbreviation.

Following the same approach as for (2.11) in Chapter 2, we rescale time and expand in $r = 0$, which yields

$$r' := \frac{dr}{d\varphi} = \frac{M(\varphi)r + \chi_2(\varphi)r^2}{W(\varphi) + \Omega_1(\varphi)r} = \frac{M(\varphi)}{W(\varphi)}r + \frac{W(\varphi)\chi_2(\varphi) - M(\varphi)\Omega_1(\varphi)}{W(\varphi)^2}r^2 + \mathcal{O}(r^3).$$

Notice that the Taylor expansion exists since only differentiation in the smooth variable r is required. By means of averaging theory, see §2.2.1 (in particular, Theorem 2.8), the previous equation is transformed into $\bar{r}' = \Lambda\bar{r} + \Sigma\bar{r}^2 + \mathcal{O}(\bar{r}^3)$, with coefficients

$$\Lambda = \frac{1}{2\pi} \int_0^{2\pi} \frac{M(\varphi)}{W(\varphi)} d\varphi = -\frac{g_2}{\sqrt{-4g_1 - g_2^2}}, \quad (3.6)$$

$$\Sigma = \frac{1}{2\pi} \int_0^{2\pi} \frac{W(\varphi)\chi_2(\varphi) - M(\varphi)\Omega_1(\varphi)}{W(\varphi)^2} d\varphi, \quad (3.7)$$

where $g_1 < 0$ and we have employed (2.14) for the explicit formula of Λ , which vanishes at $g_2 = 0$. In addition, $\Lambda > 0$ for $g_2 \in (-\sqrt{-4g_1}, 0)$, and $\Lambda < 0$ for $g_2 \in (0, \sqrt{-4g_1})$, providing in the (g_1, g_2) -plane, the left-sided parabola $g_2 = \pm\sqrt{-4g_1}$, which serves as a boundary for the parameter values, i.e., neither the formula for Λ nor Σ are considered if $g_2 \notin (-\sqrt{-4g_1}, \sqrt{-4g_1})$, which is a non-trivial interval by assumption on g_1 .

Furthermore, we bring to attention that, regardless of whether the explicit form of Λ is known, one can easily check that for $g_2 = 0$, the integral expression over 2π equals zero since $M = (1 + g_1)sc$ is an odd function and $W = (1 + g_1)c^2 - 1$ is even. We observe that the integral kernel of (3.6) exists for all $g_1 < 0$ since the zeros of W are given by $\arctan(\pm\sqrt{g_1})$.

Next, the integration of (3.7) results in

$$\Sigma = \frac{1}{2\pi} \int_0^{2\pi} \frac{-s|c|(g_3c + g_4s)}{(g_1c^2 - s^2)^2} d\varphi = -C(g_1)g_4, \quad (3.8)$$

where $C(g_1) \in \mathbb{R}_+$ depends on $g_1 < 0$. Notice that Σ is independent of g_3 since this is the coefficient of an odd term and W is an even function. Therefore, only the coefficient g_4 remains. Moreover, $W^2 > 0$ and thus $C > 0$. We see that for $g_4 \neq 0$, the steady state of the leading order averaged equation for $\bar{r} \neq 0$ corresponds to $\bar{r} = -\Lambda/\Sigma$, yielding (3.3). In particular, the criticality of the Hopf bifurcation is given by the sign of Σ , but since for fixed $g_1 < 0$, we have $C > 0$, the criticality is provided by the sign of g_4 as $\text{sgn}(\Sigma) = -\text{sgn}(g_4)$. Hence, for $g_4 < 0$ the system undergoes a supercritical Hopf bifurcation, while for $g_4 > 0$ the bifurcation is subcritical, as we wanted to prove. \square

We observe that g_4 can be thought as the degenerate first Lyapunov coefficient for this nonsmooth case since its sign gives the criticality of the bifurcation. However, this coefficient is actually the “regular” first Lyapunov coefficient as we will prove next, where we relate the previous result for the nonsmooth system to the corresponding smooth case, showing these are qualitatively similar.

Corollary 3.2. *Consider the nonsmooth system (3.2) at the zero fixed point. The conditions for this system to undergo a Hopf bifurcation and its criticality can be inferred from the corresponding analysis of the smooth system (3.1) at the zero fixed point.*

Proof. The eigenvalues of the linear part of (3.1) at $(0, 0)$ are purely imaginary if and only if $g_2 = 0$ and $g_1 < 0$. In this case, $\lambda_{\pm} = \pm\sqrt{g_1}$ and therefore Hopf bifurcations occur.

Proceeding as for the proof of Theorem 3.1, we write (3.1) in polar coordinates,

$$\begin{cases} \dot{r} = M(\varphi)r + \chi_3(\varphi)r^3, \\ \dot{\varphi} = W(\varphi) + \Omega_2(\varphi)r^2, \end{cases} \quad (3.9)$$

where the functions $M(\varphi), W(\varphi)$ are as in (3.5), and

$$\chi_3(\varphi) = g_3sc^3 + g_4s^2c^2, \quad \Omega_2(\varphi) = g_3c^4 + g_4sc^3. \quad (3.10)$$

Rescaling time and applying averaging theory, the averaged equation of (3.9) reads $\bar{r}' = \Lambda_s\bar{r} + \Sigma_s\bar{r}^3 + \mathcal{O}(\bar{r}^4)$, with coefficients

$$\Lambda_s = 0, \quad \Sigma_s = \frac{1}{2\pi} \int_0^{2\pi} \frac{W(\varphi)\chi_3(\varphi) - M(\varphi)\Omega_2(\varphi)}{W(\varphi)^2} d\varphi,$$

at the Hopf bifurcation curve. Furthermore, using symmetry arguments of the trigonometric functions again, the integral for Σ_s can be simplified as

$$\Sigma_s = \frac{1}{2\pi} \int_0^{2\pi} \frac{-sc^2(g_3c + g_4s)}{(g_1c^2 - s^2)^2} d\varphi = \frac{-(1 - \sqrt{-g_1})^2 g_4}{2\sqrt{-g_1}(1 + g_1)^2} = -C_s(g_1)g_4, \quad (3.11)$$

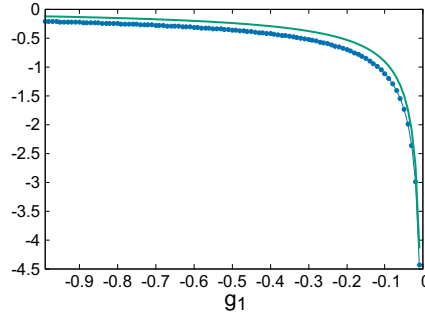


FIGURE 3.1: The blue dots correspond to the values of Σ from (3.8) for a set of points, and the green curve corresponds to the algebraic expression Σ_s from (3.11), which has been checked numerically by individual computations of g_1 . The parameters are $g_1 \in (-1, 0)$, $g_2 = 0$ and $g_4 = 1$ (i.e., subcritical Hopf bifurcation). Both Σ and Σ_s are independent of g_3 .

where $C_s(g_1) \in \mathbb{R}_+$ depends on $g_1 < 0$, and thus the criticality is given by $\text{sgn}(g_4)$ in the same way as in Theorem 3.1. \square

We remark that, in this particular situation for Σ_s , the algebraic expression is given explicitly (by the software MAPLE). However, this is not the relevant aspect we want to point out here. Moreover, although the explicit formula holds for $g_1 < 0$, $g_1 \neq -1$, its limit for $g_1 \rightarrow -1$ exists, and can be computed basically using the quotient rule as well as L'Hôpital's rule as follows:

$$\begin{aligned} \lim_{g_1 \rightarrow -1} \frac{-(1 - \sqrt{-g_1})^2 g_4}{2\sqrt{-g_1}(1 + g_1)^2} &= \frac{g_4}{2} \lim_{g_1 \rightarrow -1} \frac{2\sqrt{-g_1} + g_1 - 1}{\sqrt{-g_1}(1 + g_1)^2} = \frac{g_4}{2} \lim_{g_1 \rightarrow -1} \frac{2\sqrt{-g_1} + g_1 - 1}{(1 + g_1)^2} \\ &= \frac{g_4}{2} \lim_{g_1 \rightarrow -1} \frac{\sqrt{-g_1} - 1}{2\sqrt{-g_1}(1 + g_1)} = \frac{g_4}{4} \lim_{g_1 \rightarrow -1} \frac{\frac{\sqrt{-g_1} - 1}{1 + g_1}}{\sqrt{-g_1}} \\ &= \frac{g_4}{4} \lim_{g_1 \rightarrow -1} \frac{-1}{2\sqrt{-g_1}} = -\frac{g_4}{8}. \end{aligned}$$

Nevertheless, since g_1 is a perturbation, we consider $g_1 \in (-1, 0)$. Additionally, it is easy to see that $\lim_{g_1 \rightarrow 0^-} \Sigma_s = -\infty$. In particular, from the leading order averaged equation, the periodic orbits are given by $\bar{r} = \sqrt{-\Lambda_s/\Sigma_s}$ and therefore, for $g_1 \rightarrow 0^-$ the limit cycles converge to the origin.

In Figure 3.1, we compare the function Σ , from the nonsmooth system (3.2), with Σ_s , from the smooth system (3.1), for the same set of parameter values, where $g_4 = 1$ and hence, the bifurcation is subcritical. Notably, their behavior is closely related. Indeed, $\Sigma < \Sigma_s$, which actually holds for all $g_4 > 0$. To prove that, we compare the amplitudes of $\Sigma = -Cg_4$ and $\Sigma_s = -C_s g_4$ as follows. Firstly, we note that g_3 does not enter into either (3.8) or (3.11), as previously explained, and we thus consider the functions inside the integral which contain g_4 only. These do not change sign for any $\varphi \in [0, 2\pi]$, for fixed parameter values. Hence, it suffices to compare Σ and Σ_s by means of

$$\frac{-g_4 s^2 |c|}{(g_1 c^2 - s^2)^2}, \quad \frac{-g_4 s^2 c^2}{(g_1 c^2 - s^2)^2},$$

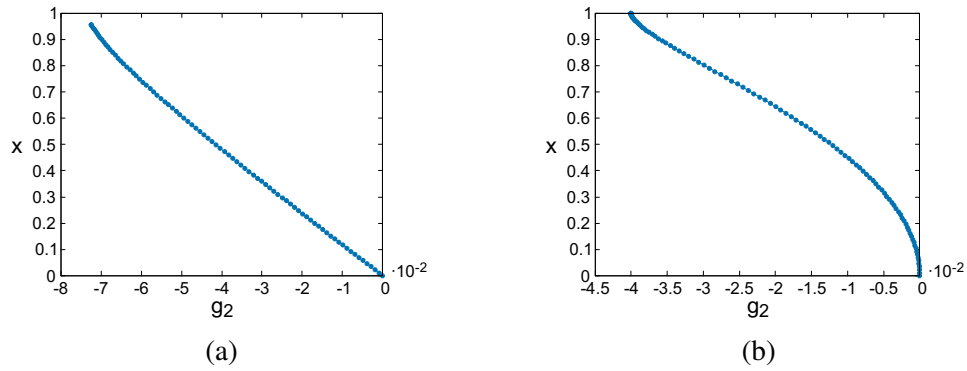


FIGURE 3.2: Subcritical Hopf bifurcations of (3.2) in (a), and (3.1) in (b), from the zero equilibrium point, with $g_1 = -0.5$, $g_3 = 0.5$, $g_4 = 0.2$, where the maximum of x is plotted.

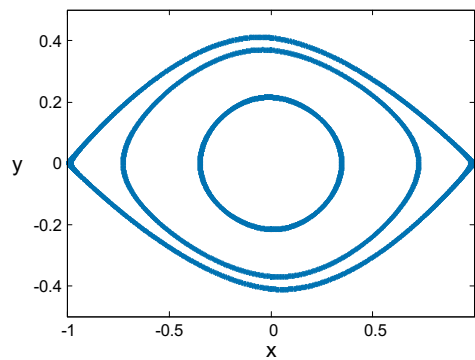


FIGURE 3.3: Periodic orbits of the nonsmooth system (3.2), with $g_1 = -0.5$, $g_3 = 0.5$, $g_4 = 0.2$ fixed and for different values of g_2 , approaching a heteroclinic cycle. The inner orbit corresponds to $g_2 \approx -2.91 \cdot 10^{-2}$, and the outer trajectory to $g_2 \approx -7.32 \cdot 10^{-2}$. Notice that there is no even symmetry.

respectively. Furthermore, the denominator is the same in both cases and positive, and clearly $s^2 c^2 < s^2 |c|$ holds. This yields $C > C_s$ and therefore, for $g_4 > 0$, we have $\Sigma < \Sigma_s < 0$, as observed in Figure 3.1. For $g_4 < 0$, the relation becomes then $\Sigma > \Sigma_s > 0$. We remark that, since g_4 is fixed in Figure 3.1, the functions Σ, Σ_2 plotted correspond in fact to $-C, -C_s$, respectively.

Finally, in Figure 3.2 we plot the Hopf bifurcation diagram for (3.2) and (3.1) at the zero equilibrium, where it is shown that, near the bifurcation point, the scaling law of the nonsmooth case behaves linearly, while in the smooth system it is of order $\sqrt{g_2}$, similarly to the pitchfork bifurcation; cf. Figure 1.8. Additionally, whereas the shape of these scaling laws is independent of the precise value of g_4 , the direction of the branch is determined by its sign. Indeed, if $\text{sgn}(g_4) > 0$, the bifurcating branch has negative g_2 -values (subcritical), while for $\text{sgn}(g_4) < 0$, the curve is found for positive g_2 -values (supercritical). Moreover, computing numerically the profile of the periodic solutions, we observe, as expected, heteroclinic loops for the upper-left end of either curve in Figure 3.2, connecting the symmetric nonzero equilibria and encircling the zero fixed point. We show in Figure 3.3 an example of how the periodic orbits from Figure 3.2 (a) increase in period while decreasing g_2 (or increasing its length), which clearly approach the predicted heteroclinic behavior. In the smooth situation a similar organization of periodic orbits and heteroclinic loops occurs.

In particular, the bifurcation diagram in the (g_1, g_2) -plane includes the curve of Hopf bifurcations (horizontal axis $g_1 < 0$) as well as the curve of heteroclinic orbits, with the Bogdanov–Takens point at the origin.

Next, the more involved analysis of the nonzero fixed points of systems (3.1) and (3.2) is presented.

3.1.2 Bifurcation analysis at the nonzero equilibria

As before, we start developing the analysis for the nonsmooth case, and subsequently compare this with the equivalent analysis for the smooth model, both at the corresponding nonzero equilibria.

We note first that the Jacobian matrix of the nonsmooth system (3.2) at $(|x_0|, y_0) = (-g_1/g_3, 0)$ reads

$$L = \begin{pmatrix} 0 & 1 \\ -g_1 & g_2 - \frac{g_1 g_4}{g_3} \end{pmatrix},$$

with trace $\text{tr}(L) = g_2 - \frac{g_1 g_4}{g_3}$ and determinant $\det(L) = g_1$. On the one hand, for $g_1 < 0$ we are in the same situation as above and these fixed points correspond to saddles. On the other hand, for $g_1 > 0$ and $g_2 = \frac{g_1 g_4}{g_3}$, we get Hopf bifurcations at the nonzero equilibria and the zero fixed point becomes then the saddle point.

Theorem 3.3. *If $g_3, g_4 \neq 0$, then at $g_1 > 0$, $g_2 = \frac{g_1 g_4}{g_3}$, (3.2) undergoes a Hopf bifurcation in g_1, g_2 , for the non-trivial equilibria. The leading order amplitude of the limit cycle is given by*

$$\bar{r} = \sqrt{-\frac{g_2}{K(g_1)g_3g_4\sqrt{-4g_1 - g_2^2}}}, \quad \text{where} \quad K(g_1) := \frac{1}{2\pi} \int_0^{2\pi} \frac{2s^2 c^4}{(g_1 c^2 + s^2)^3} d\varphi > 0, \quad (3.12)$$

with \bar{r} the averaged radial component of the system in polar coordinated. In particular, the bifurcation is supercritical if $\text{sgn}(g_4) > 0$ and subcritical if $\text{sgn}(g_4) < 0$.

Proof. The eigenvalues of the Jacobian matrix of (3.2) at the nonzero equilibria for $g_1 > 0$ and $g_2 = \frac{g_1 g_4}{g_3}$ are given by $\lambda_{\pm} = \pm\sqrt{-g_1}$, which correspond to purely complex conjugates. We recall $\text{sgn}(g_1) = -\text{sgn}(g_3)$, and thus we require $g_3 < 0$ in this case.

For the analysis of the system at $(|x_0|, y_0) = (-g_1/g_3, 0)$, we compute its linearization and keep the quadratic terms as follows. We begin shifting the nonzero equilibrium (x_0, y_0) to the origin $(0, 0)$ by $x = x_0 + z$, where z is a perturbation of the location of the equilibrium state, and rewrite the system for (z, y) . The second equation of (3.2) becomes

$$\begin{aligned} \dot{y} &= g_1(x_0 + z) + g_3(x_0 + z)|x_0 + z| + g_2 y + g_4|x_0 + z|y \\ &= g_1 x_0 + g_1 z + g_3 \text{sgn}(x_0 + z)(x_0^2 + 2x_0 z + z^2) \\ &\quad + g_2 y + g_4 \text{sgn}(x_0 + z)x_0 y + g_4 \text{sgn}(x_0 + z)zy. \end{aligned}$$

Using now $x_0 = \text{sgn}(x_0)|x_0|$ and $|x_0| = -g_1/g_3$, the previous equation turns into

$$\begin{aligned} \dot{y} = & -\frac{g_1^2}{g_3} \text{sgn}(x_0) + g_1 z + \frac{g_1^2}{g_3} \text{sgn}(x_0 + z) - 2g_1 \text{sgn}(x_0 + z) \text{sgn}(x_0) z + g_3 \text{sgn}(x_0 + z) z^2 \\ & + \left(g_2 - \frac{g_1 g_4}{g_3} \text{sgn}(x_0 + z) \text{sgn}(x_0) \right) y + g_4 \text{sgn}(x_0 + z) z y. \end{aligned}$$

Furthermore, for the purpose of the bifurcation analysis, we consider the sign of $x_0 + z$ to be equivalent to the sign of x_0 , since $x_0 \neq 0$, yielding the following quadratic smooth vector field:

$$\begin{cases} \dot{z} = y, \\ \dot{y} = -g_1 z + \left(g_2 - \frac{g_1 g_4}{g_3} \right) y + g_3 \text{sgn}(x_0) z^2 + g_4 \text{sgn}(x_0) z y. \end{cases} \quad (3.13)$$

Writing (3.13) in polar coordinates we get (3.4) with coefficients

$$\begin{aligned} M(\varphi) &= (1 - g_1) s c + \left(g_2 - \frac{g_1 g_4}{g_3} \right) s^2, & W(\varphi) &= (1 - g_1) c^2 + \left(g_2 - \frac{g_1 g_4}{g_3} \right) s c - 1, \\ \chi_2(\varphi) &= (g_3 s c^2 + g_4 s^2 c) \text{sgn}(x_0), & \Omega_1(\varphi) &= (g_3 c^3 + g_4 s c^2) \text{sgn}(x_0), \end{aligned} \quad (3.14)$$

and the Taylor expansion in $r = 0$ of the rescaled system yields

$$r' := \frac{dr}{d\varphi} = \frac{Mr + \chi_2 r^2}{W + \Omega_1 r} = \frac{M}{W} r + \frac{W\chi_2 - M\Omega_1}{W^2} r^2 + \frac{(M\Omega_1 - W\chi_2)\Omega_1}{W^3} r^3 + \mathcal{O}(r^4),$$

with leading order averaged equation $\bar{r}' = \Lambda \bar{r} + \Sigma \bar{r}^2 + \Sigma_1 \bar{r}^3$, where the coefficients Λ, Σ are computed as for (3.6), (3.7), respectively. Since Λ, Σ vanish at the Hopf bifurcation points given by $g_1 > 0, g_2 = g_1 g_4 / g_3$, the leading order bifurcation equation can be written as $\bar{r}' = \Lambda \bar{r} + \Sigma_2 \bar{r}^3$, where Σ_1 equals Σ_2 evaluated at the bifurcation points, and Λ is considered to be the parameter. Notice that even though we start from the nonsmooth setting (3.2), at the nonzero equilibria the system behaves as a smooth system, (3.13). The coefficients of the leading order bifurcation equation read

$$\Lambda = 0, \quad \Sigma_2 = \frac{1}{2\pi} \int_0^{2\pi} \frac{(M\Omega_1 - W\chi_2)\Omega_1}{W^3} d\varphi, \quad (3.15)$$

at the Hopf bifurcation curve. Σ_2 can be computed as follows:

$$\Sigma_2 = \frac{1}{2\pi} \int_0^{2\pi} \frac{s c^3 (g_3 c + g_4 s)^2 \text{sgn}(x_0)^2}{((1 - g_1) c^2 - 1)^3} d\varphi = \frac{1}{2\pi} \int_0^{2\pi} \frac{2g_3 g_4 s^2 c^4}{-(s^2 + g_1 c^2)^3} d\varphi = -K(g_1) g_3 g_4, \quad (3.16)$$

where $K(g_1) \in \mathbb{R}_+$ depends on $g_1 > 0$. Notice that from the product $M\Omega_1$, we only get g_1 in $(g_3 c + g_4 s) s c^3 \text{sgn}(x_0) g_1$, which is the same as in $W\chi_2$, and thus the coefficient g_1 in the numerator disappears. Moreover, from the initial step, we see that the sign of x_0 does not affect the result, which is consistent with the fact that the bifurcating branch of one nonzero fixed point behaves as the other. Next, both terms with g_3^2 and g_4^2 in the first fraction cancel

out integrating over the four quadrants since they are the coefficients of odd functions and the denominator is even. Therefore, only g_3g_4 remains, which is the coefficient of an even function. Furthermore, s^2c^4 is positive and the denominator is negative, yielding $K > 0$.

Finally, since $g_3 < 0$, we have $\text{sgn}(\Sigma_2) = \text{sgn}(g_4)$, and hence, the sign of g_4 determines the criticality of the bifurcation. \square

As for Theorem 3.1, we may call g_4 the first Lyapunov coefficient for the Hopf bifurcations in this case. Notice that the nonsmooth system at the nonzero equilibria behaves smoothly, (3.13), and therefore, we have again a regular first Lyapunov coefficient rather than degenerate.

As in the previous subsection, we compare now this result with the smooth case by means of the following corollary, noting first that although (3.13) is a smooth system, it is not obvious that the organization of the criticality behaves as in the smooth situation.

Corollary 3.4. *Consider the nonsmooth system (3.2) at the nonzero steady states. The conditions for this system to undergo a Hopf bifurcation and its criticality can be inferred from the corresponding analysis of the smooth system (3.1) at the nonzero equilibria.*

Proof. The linear part of (3.1) at $(x_0, y_0) = (\pm\sqrt{-g_1/g_3}, 0)$ reads

$$L_s = \begin{pmatrix} 0 & 1 \\ -2g_1 & g_2 - \frac{g_1g_4}{g_3} \end{pmatrix},$$

with trace $\text{tr}(L_s) = \text{tr}(L)$ and determinant $\det(L_s) = 2g_1$. For $g_1 > 0$ and $g_2 = \frac{g_1g_4}{g_3}$, Hopf bifurcations occur. In this case, we consider $g_3 < 0$ for the fixed points to exist.

Pursuing a similar proof as for Theorem 3.3, we shift the nonzero equilibria (x_0, y_0) to the origin by $x = x_0 + z$, where z is small, and rewriting the system for (z, y) , we get

$$\begin{cases} \dot{z} = y, \\ \dot{y} = -2g_1z + \left(g_2 - \frac{g_1g_4}{g_3}\right)y + 3g_3x_0z^2 + 2g_4x_0zy + g_5z^3 + g_6z^2y, \end{cases} \quad (3.17)$$

where we have redefined the coefficients of the cubic terms from g_3, g_4 to g_5, g_6 , respectively, in order to examine the effect of these into the criticality of the bifurcation. Writing the system in polar coordinates and expanding the rescaled system as above, yield

$$\begin{aligned} r' &:= \frac{dr}{d\varphi} = \frac{Mr + \chi_2r^2 + \chi_3r^3}{W + \Omega_1r + \Omega_2r^2} \\ &= \frac{M}{W}r + \frac{W\chi_2 - M\Omega_1}{W^2}r^2 + \left(\frac{W\chi_3 - M\Omega_2}{W^2} + \frac{(M\Omega_1 - W\chi_2)\Omega_1}{W^3}\right)r^3 + \mathcal{O}(r^4), \end{aligned}$$

where

$$\begin{aligned} M(\varphi) &= (1 - 2g_1)sc + \left(g_2 - \frac{g_1g_4}{g_3}\right)s^2, & W(\varphi) &= (1 - 2g_1)c^2 + \left(g_2 - \frac{g_1g_4}{g_3}\right)sc - 1, \\ \chi_2(\varphi) &= (3g_3sc^2 + 2g_4s^2c)x_0, & \Omega_1(\varphi) &= (3g_3c^3 + 2g_4sc^2)x_0, \\ \chi_3(\varphi) &= g_5sc^3 + g_6s^2c^2, & \Omega_2(\varphi) &= g_5c^4 + g_6sc^3. \end{aligned} \quad (3.18)$$

Notice that M, W, χ_2, Ω_1 are similar to the corresponding functions in (3.14), while χ_3, Ω_2 are the same as in (3.10). Next, the leading order averaged equation reads $\bar{r}' = \Lambda_s \bar{r} + \Sigma_s \bar{r}^2 + \Sigma_{s_1} \bar{r}^3$, where $\Lambda_s = \Sigma_s = 0$ at the Hopf bifurcation points given by $g_1 > 0$ and $g_2 = \frac{g_1 g_4}{g_3}$, and hence, the leading order bifurcation equation can be written as $\bar{r}' = \Lambda_s \bar{r} + \Sigma_{s_2} \bar{r}^3$, where Σ_{s_2} results from evaluating Σ_{s_1} at the bifurcation points, and Λ_s is thought to be the parameter. The criticality of the system is then given by

$$\Sigma_{s_2} = \frac{1}{2\pi} \int_0^{2\pi} \frac{W\chi_3 - M\Omega_2}{W^2} + \frac{(M\Omega_1 - W\chi_2)\Omega_1}{W^3} d\varphi.$$

More precisely, the integral of the first fraction becomes

$$\begin{aligned} \int_0^{2\pi} \frac{W\chi_3 - M\Omega_2}{W^2} d\varphi &= \int_0^{2\pi} \frac{-sc^2(g_5c + g_6s)}{((1 - 2g_1)c^2 - 1)^2} d\varphi = \int_0^{2\pi} \frac{-g_6s^2c^2}{(s^2 + 2g_1c^2)^2} d\varphi \\ &= -2\pi K_1(g_1)g_6, \end{aligned} \quad (3.19)$$

where $K_1(g_1) \in \mathbb{R}_+$ depends on $g_1 > 0$. In the second equality, the term with g_5 does not enter after integrating since it is an odd function and the denominator is even. Additionally, since s^2c^2 is positive, $K_1 > 0$. For the second fraction of Σ_{s_2} we have

$$\begin{aligned} \int_0^{2\pi} \frac{(M\Omega_1 - W\chi_2)\Omega_1}{W^3} d\varphi &= \int_0^{2\pi} \frac{-g_1sc^3(9g_3c^2 + 12g_4sc + 4g_4^2s^2/g_3) \operatorname{sgn}(x_0)^2}{((1 - 2g_1)c^2 - 1)^3} d\varphi, \\ &= \int_0^{2\pi} \frac{-12g_1g_4s^2c^4}{-(s^2 + 2g_1c^2)^3} d\varphi = \int_0^{2\pi} \frac{12g_1g_4s^2c^4}{(s^2 + 2g_1c^2)^3} d\varphi \\ &= 2\pi K_2(g_1)g_4, \end{aligned} \quad (3.20)$$

where $K_2(g_1) \in \mathbb{R}_+$ depends on $g_1 > 0$ and $K_2 > K_1$. We note that in order to compute that integral, we have written the value x_0 , which corresponds to the fixed point $\pm\sqrt{-g_1/g_3}$, as $x_0 = \operatorname{sgn}(x_0)\sqrt{-g_1/g_3}$, and therefore, the explicit expression $\operatorname{sgn}(x_0)$ appears in the previous integration. In particular, in the numerator of the integrand we have $x_0^2 \operatorname{sgn}(x_0)^2 = -g_1/g_3$. Moreover, and in contrast to the nonsmooth case, here g_1 in the numerator does not vanish since χ_2, Ω_1 in (3.18) have x_0 instead of only $\operatorname{sgn}(x_0)$, which happens in (3.14). Furthermore, the only term remaining is the even term $-12g_1g_4s^2c^4$, and since g_4 is the coefficient of a positive function, $K_2 > 0$ holds. We recall $g_1 > 0$ since we are analyzing the Hopf bifurcation.

The criticality of the bifurcation is then given by $\Sigma_{s_2} = -K_1g_6 + K_2g_4$, where $g_6 = g_4$, and therefore $\Sigma_{s_2} = K_s g_4$, with $K_s \in \mathbb{R}_+$. Hence, as in the nonsmooth case, we have $\operatorname{sgn}(\Sigma_{s_2}) = \operatorname{sgn}(g_4)$. We do get the same criticality also for the nonzero equilibria for both the smooth and the nonsmooth system, as we wanted to prove. \square

We first recall that the coefficients of the cubic terms of (3.17) have been defined as g_5, g_6 , instead of g_3, g_4 , respectively, to easily track the effects of these terms into the bifurcation analysis. This is relevant since the nonsmooth system shifted to the nonzero equilibria (3.13) is quadratic while the smooth case (3.17) is cubic. For instance, the cubic terms in the smooth

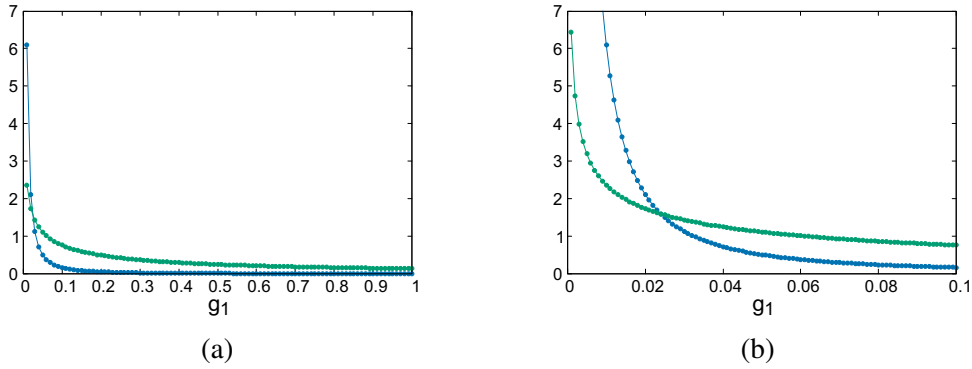


FIGURE 3.4: For a set of g_1 , the values of Σ_2 from (3.16) are displayed in blue, and in green, the values of Σ_{s_2} from (3.19) + (3.20), corresponding to the systems (3.13) and (3.17), respectively. The parameters for both figures are $g_3 = -0.025$ and $g_4 = 1$ (i.e., supercritical Hopf bifurcation). A set of 100 points is displayed in each figure, where (a) has a larger horizontal axis with $g_1 \in (0, 1)$, and in (b) we have chosen $g_1 \in (0, 0.1)$ in order to distinguish better the crossing point. Upon changing $g_3 < 0$, the blue curve can be made arbitrarily small/large, while the green curve would remain unaltered.

situation have a contribution in Σ_{s_2} , as we have seen in the previous proof. In addition, below we present a remark considering $g_5 = g_6 = 0$.

Now, comparing the functions Σ_2 and Σ_{s_2} from above, we observe that their scaling differs since g_3 enters into Σ_2 , while Σ_{s_2} is completely independent of it, meaning that in the nonsmooth system, the value of g_3 modifies the amplitude of the bifurcating solutions. In Figure 3.4, we compare both Σ_2 , Σ_{s_2} for fixed $g_4 = 1$, where we have chosen $g_3 = -0.025$ to get a better comparison between both curves since, in this case, Σ_2 scales similar to Σ_{s_2} . Additionally, the size of the coefficients cannot be related in the same way as before, i.e., neither $\Sigma_2 \geq \Sigma_{s_2}$ nor $\Sigma_2 \leq \Sigma_{s_2}$ occur for all $g_1 > 0$. To show that this is the case, in general, we compare Σ_2 and Σ_{s_2} as follows. For Σ_2 , we consider again the function inside the integral of (3.16), since it does not change sign,

$$\frac{2g_3g_4s^2c^4}{-(s^2 + g_1c^2)^3} = -g_4s^2c^2 \frac{2g_3c^2}{(s^2 + 2g_1c^2)^3},$$

where the numerator depends on g_3 . For Σ_{s_2} , we take also the integral kernel of (3.19) (with $g_6 = g_4$) and (3.20),

$$\frac{-g_4s^2c^2}{(s^2 + 2g_1c^2)^2} + \frac{12g_1g_4s^2c^4}{(s^2 + 2g_1c^2)^3} = -g_4s^2c^2 \frac{s^2 - 10g_1c^2}{(s^2 + 2g_1c^2)^3},$$

where the numerator depends on g_1 . Clearly, the expressions to be compared are $2g_3c^2$ and $s^2 - 10g_1c^2$, and thus, the existence of the crossing point is contingent upon g_3 . If this crossing exists, then its location depends on g_1 , as observed in Figure 3.4.

In addition, in Figure 3.5 we plot the Hopf bifurcation diagram for the nonsmooth and smooth cases for the equilibria $-g_1/g_3$ and $\sqrt{-g_1/g_3}$, respectively. Notably, since at the nonzero equilibria the nonsmooth system is smooth, (3.13), both bifurcating curves behave similarly near the bifurcation, while they slightly deviate further away. Furthermore, looking at the profile of the periodic solutions, which we compute numerically employing the software

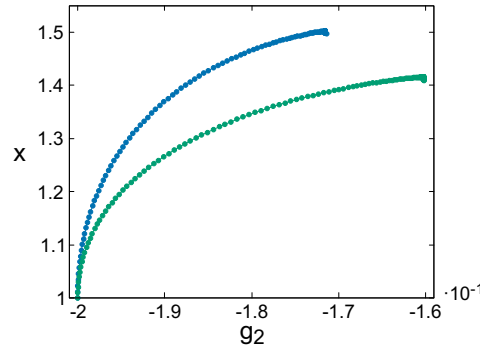


FIGURE 3.5: Supercritical Hopf bifurcations of (3.2) in blue, and (3.1) in green, from the nonzero equilibria, with $g_1 = 0.5$, $g_3 = -0.5$, $g_4 = 0.2$, where the maximum of x is plotted.

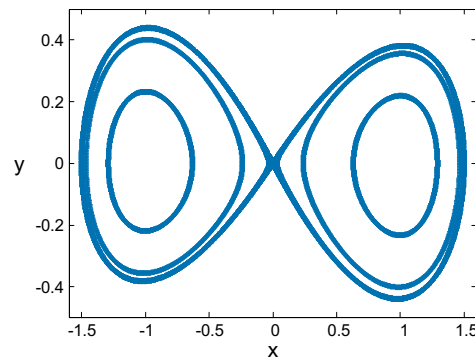


FIGURE 3.6: Periodic orbits of the nonsmooth system (3.2), for different values of g_2 , approaching homoclinic trajectories with $g_1 = 0.5$, $g_3 = -0.5$, $g_4 = 0.2$. The inner orbits correspond to $g_2 \approx -0.194$, and the outer trajectories to $g_2 \approx -0.172$. Notice that there is no even symmetry.

AUTO (as done for the analysis above), homoclinic orbits occur for the upper-right end of either curve, as one would expect. In Figure 3.6 we plot such orbits for the nonsmooth system (3.2) at both nonzero equilibria. We observe that, while increasing g_2 (or decreasing it in absolute value), the period of the limit cycles grow, as displayed in Figure 3.5, approaching homoclinic loops. A similar behavior happens for the smooth case.

Motivated by the fact that the nonsmooth system at the nonzero equilibria behaves as a smooth system, we present the following result, which shows that there is a direct correspondence between the leading order vector field of (3.17) and (3.13). For that, we call \tilde{g}_j the parameters of (3.13), and keep the notation g_j for the parameters of (3.17). We consider the first component x_0 of the fixed point in both systems to have the same sign, i.e., $\text{sgn}(\pm\sqrt{-g_1g_4/g_3}) = \text{sgn}(\mp g_1/g_3)$.

Remark 3.5. *There exists a homeomorphism between the normal form of the quadratic part of (3.17), i.e., setting $g_5 = g_6 = 0$, and (3.13) in terms of the parameter space. This direct correspondence is orientation preserving and thus, a priori, the criticality of the Bogdanov–Takens bifurcation is the same. In the case $g_5, g_6 \neq 0$, this can only be concluded a posteriori after the computations above.*

Proof. Firstly, for the linear part of z from both systems considered, we straightforwardly require $g_1 = \tilde{g}_1/2$. Next, for the coefficient of z^2 and zy , we need, respectively,

$$3g_3\sqrt{\frac{-g_1}{g_3}} = \tilde{g}_3, \quad 2g_4\sqrt{\frac{-g_1}{g_3}} = \tilde{g}_4.$$

We recall that $g_1 > 0$, which implies $g_3 < 0$ to have the existence of the nonzero equilibria. Therefore, we solve the equation for g_3 and g_4 , respectively, as

$$g_3 = -\frac{2\tilde{g}_3^2}{9\tilde{g}_1}, \quad g_4 = \frac{|\tilde{g}_3|\tilde{g}_4}{3\tilde{g}_1}.$$

The last coefficient which has to match is the one of y , i.e., $g_2 - \frac{g_1g_4}{g_3} = \tilde{g}_2 - \frac{\tilde{g}_1\tilde{g}_4}{\tilde{g}_3}$. Substitution of the previous mappings gives

$$g_2 = \tilde{g}_2 + \frac{\tilde{g}_1\tilde{g}_4}{4\tilde{g}_3}.$$

Hence, we have a bijection between both vector fields in terms of the parameter space. Furthermore, this is orientation preserving because it does not change the sign of any parameter since it is just a scaling mapping, meaning that the parameters change in the same direction with the same monotonicity, but with different speeds. Moreover, for $g_1, \tilde{g}_1 > 0$ and $g_3, \tilde{g}_3 < 0$ the bijection is continuous with continuous inverse and, therefore, we have a homeomorphism between the normal forms in terms of the parameter space.

Finally, since this correspondence is local, the criticality can be inferred from one system to the other. More precisely, for $g_5 = g_6 = 0$, (3.19) vanishes and the homeomorphism between (3.20) and (3.16) holds, as we wanted to show. \square

To extend the analysis of the Bogdanov–Takens bifurcation, we introduce subsequently the generalization from the absolute value defined in (2.1), with different left and right slopes, as done in §2.3.1.

3.2 Generalized absolute value

The corresponding nonsmooth system (3.2) replacing the regular absolute value by the generalized function (2.1) reads

$$\begin{cases} \dot{x} = y, \\ \dot{y} = g_1x + g_3x[x]_{p1_-}^{p1_+} + y \left(g_2 + g_4[x]_{p2_-}^{p2_+} \right), \end{cases} \quad (3.21)$$

where $p_{1\pm}, p_{2\pm} \in \mathbb{R}$. The fixed points are $(x_0, y_0) = (0, 0)$ and $([x_0]_{p1_-}^{p1_+}, y_0) = (-\frac{g_1}{g_3}, 0)$. Note that the nonzero equilibria correspond to $(x_0, y_0) = (-\frac{g_1}{g_3p_{1_-}}, 0)$ for $x_0 < 0$, and $(x_0, y_0) = (-\frac{g_1}{g_3p_{1_+}}, 0)$ for $x_0 \geq 0$.

From the previous results, we get the following corollaries.

Corollary 3.6. *If $g_4 \neq 0$ and $p_{2_+} \neq p_{2_-}$, then at $g_1 < 0, g_2 = 0$ the system (3.21) undergoes a degenerate Hopf bifurcation for the zero equilibrium. The leading order amplitude of the limit*

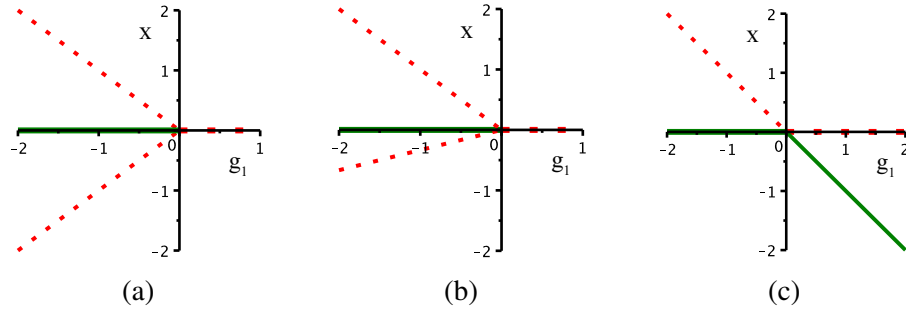


FIGURE 3.7: Bifurcation diagrams of (3.21) for g_1 , fixing $g_3 = 1$: (a) subcritical pitchfork for $p_{1+} = 1, p_{1-} = -1$; (b) subcritical pitchfork for $p_{1+} = 1, p_{1-} = -3$; and (c) transcritical bifurcation for $p_{1+} = p_{1-} = 1$.

cycle is given by (3.3) multiplying it by the factor $2/(p_{2+} - p_{2-})$. In particular, the bifurcation is supercritical if $\text{sgn}(g_4(p_{2+} - p_{2-})) < 0$ and subcritical if $\text{sgn}(g_4(p_{2+} - p_{2-})) > 0$.

Proof. Following the proof of Theorem 3.1, (3.21) in polar coordinates becomes as in (3.4) and the corresponding averaged equation reads $\bar{r}' = \tilde{\Lambda}\bar{r} + \tilde{\Sigma}\bar{r}^2 + \mathcal{O}(\bar{r}^3)$, where the absolute value is now the generalized one, and the expressions of $\tilde{\Lambda}$ and $\tilde{\Sigma}$ are as in (3.6) and (3.7), respectively. At the Hopf bifurcation points, given by $g_1 < 0, g_2 = 0$, we have $\tilde{\Lambda} = 0$. Furthermore, out of the different slopes, repercussions are present on the second coefficient:

$$\tilde{\Sigma} = \frac{1}{2\pi} \int_0^{2\pi} \frac{\chi_2(\varphi)}{W(\varphi)} - \frac{M(\varphi)\Omega_1(\varphi)}{W(\varphi)^2} d\varphi = -\frac{C(g_1)}{2} g_4(p_{2+} - p_{2-}), \quad (3.22)$$

where $C(g_1) \in \mathbb{R}_+$ is the same as in (3.3), and to leading order, the limit cycle is then given by

$$\bar{r} = -\frac{2g_2}{C(g_1)(p_{2+} - p_{2-})g_4\sqrt{-4g_1 - g_2^2}},$$

as claimed. We observe that $[c]_{p_{j-}}^{p_{j+}} = p_{j+}c$ for $\varphi \in (3\pi/2, \pi/2)$ and $[c]_{p_{j-}}^{p_{j+}} = p_{j-}c$ for $\varphi \in (\pi/2, 3\pi/2)$, where $j \in \{1, 2\}$. As above, g_3 vanishes, and thus we only have the impact of $p_{2\pm}$. \square

We remark that for $p_{1+} = 1, p_{1-} = -1$, the pitchfork bifurcation is obtained, as in Figure 3.7 (a). For slopes $p_{1+} \neq p_{1-}$ different from the regular absolute value, we get a degenerate pitchfork bifurcation for the parameter g_1 , where an example is displayed in Figure 3.7 (b). Recall that this case has been analyzed in §2.3.1 for the more general (2.46). In addition, for the case $p_{1+} = p_{1-}$, the system undergoes a transcritical bifurcation; see Figure 3.7 (c).

Next in line, we analyze the effect of $p_{2\pm}$ into the Hopf bifurcation. For that, and without loss of generality, we fix $p_{1+} = 1, p_{1-} = -1$, as the absolute value function, together with $p_{2+} = 1$ and the parameter $g_4 > 0$. We then examine how different values of p_{2-} affect the behavior of the system. We point out that for $p_{2-} = -1$, we recover the same result as for the regular absolute value function; see Figure 3.2 (a). Note that fixing g_4 , the Hopf bifurcation of system (3.21) changes criticality when $p_{2+} - p_{2-}$ switches sign; see $\tilde{\Sigma}$ in (3.22). If $p_{2+} > 0$,

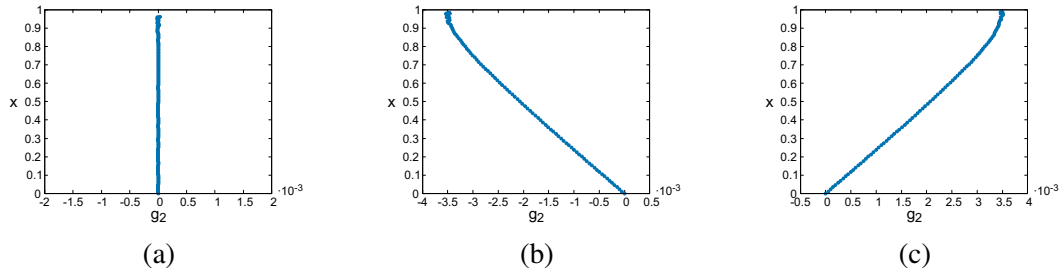


FIGURE 3.8: Bifurcation diagrams of (3.21) where the maximum of x is plotted: (a) degenerate case for $p_{2-} = 1$, (b) subcritical Hopf for $p_{2-} = 0.9$, and (c) supercritical Hopf for $p_{2-} = 1.1$. The parameter values are $g_1 = -0.5, g_3 = 0.5, g_4 = 0.2$ and $p_{2+} = 1$.

this switch happens for $p_{2-} > p_{2+}$, while if $p_{2+} < 0$, $\tilde{\Sigma}$ changes sign for $p_{2-} < p_{2+}$. We consider here the first case and explore the bifurcation diagrams when p_- is close to p_+ .

Firstly, if both slopes are the same, we have $[x]_{p_{2-}}^{p_{2+}} = p_2 x$, which is smooth, and $\tilde{\Sigma} = 0$. The bifurcation diagram is then a vertical branch, where an example of this curve is exhibited in Figure 3.8 (a). We remark that for these figures we have used the numerical continuation software AUTO and thus some numerical errors are expected. In particular, this program implicitly assumes differentiability so that it is not guaranteed a priori that the computations work. The Hopf bifurcation branches shown in this manuscript have been computed with this software and hence, the same considerations have to be taken into account for the other diagrams, e.g., Figure 3.8 (b,c).

Secondly, for $p_{2-} < 1$, $\tilde{\Sigma} < 0$ and therefore, the Hopf bifurcation is subcritical while, if $p_{2-} > 1$, then $\tilde{\Sigma} > 0$ and the bifurcation is supercritical; see Figure 3.8 (b,c). Note that this different behavior of the bifurcation curves coming from modifying p_{2-} , is a bifurcation induced by changing the nonlinearity rather than varying only the coefficient. Hence, this has no direct analogue in the smooth situation, and the results regarding Hopf bifurcations and their criticality, in this case, cannot be inferred from the analysis of the smooth system (3.1). Furthermore, the curve close to the bifurcation point behaves linearly, as for the regular absolute value case. We recall that in the smooth case this is a square root behavior. In addition, at the end of the bifurcating branches in Figure 3.8, heteroclinic orbits occur.

Observe that for the diagrams in Figure 3.8, $p_{1\pm} = \pm 1$ is considered. However, if $p_{1+} = p_{1-}$ as well as $p_{2+} = p_{2-}$, the bifurcating branch behaves similarly as illustrated in Figure 3.2 (b), i.e., as in the smooth system (3.1), where the system is then of second order in x rather than cubic.

Corollary 3.7. Consider (3.21) at the nonzero equilibria $([x_0]_{p_{1-}}^{p_{1+}}, y_0) = (-\frac{g_1}{g_3}, 0)$. If $g_3, g_4 \neq 0$ as well as $p_1, p_2 \neq 0$, where p_1 and p_2 represent the corresponding slope p_{1-} or p_{1+} and p_{2-} or p_{2+} , respectively, depending on the sign of the fixed point $x_0 \neq 0$, then the system undergoes a Hopf bifurcation at $g_1 > 0, g_2 = \frac{g_1 g_4 p_2}{g_3 p_1}$. The leading order amplitude of the limit cycle is given by (3.12) multiplying it by the factor $1/\sqrt{p_1 p_2}$. In addition, the criticality of the bifurcation is given by the sign of $g_4 p_1 p_2$.

Proof. Following the proof of Theorem 3.3, we shift the non-trivial steady states of (3.22) to the origin, with $z = x - x_0$ denoting a small disturbance from the equilibrium, yielding

$$\begin{cases} \dot{z} = y, \\ \dot{y} = -g_1 z + \left(g_2 - \frac{g_1 g_4 p_2}{g_3 p_1}\right) y + g_3 p_1 z^2 + g_4 p_2 z y, \end{cases} \quad (3.23)$$

where p_1 and p_2 represent the corresponding slope p_{1-} or p_{1+} and p_{2-} or p_{2+} , respectively, depending on the sign of the fixed point $x_0 \neq 0$. Here, the Hopf bifurcations happen for $g_1 > 0$ and $g_2 = \frac{g_1 g_4 p_2}{g_3 p_1}$.

The leading order averaged equation of the system in polar coordinates reads $\bar{r}' = \tilde{\Lambda}\bar{r} + \tilde{\Sigma}\bar{r}^2 + \tilde{\Sigma}_1\bar{r}^3$, where $\tilde{\Lambda}, \tilde{\Sigma}$ vanish at the Hopf bifurcation points given by $g_1 > 0$ and $g_2 = \frac{g_1 g_4 p_2}{g_3 p_1}$. Furthermore, we write the leading order bifurcation equation as $\bar{r}' = \tilde{\Lambda}\bar{r} + \tilde{\Sigma}_2\bar{r}^3$, where $\tilde{\Sigma}_1$ equals $\tilde{\Sigma}_2$ at the bifurcation points and, in this case, $\tilde{\Lambda}$ is considered to be the parameter of the system. The coefficient of the cubic term has the same expression as in (3.16), but with $g_3 \operatorname{sgn}(x_0)$ and $g_4 \operatorname{sgn}(x_0)$ replaced by $g_3 p_1$ and $g_4 p_2$, respectively, and its integral reads

$$\tilde{\Sigma}_2 = \frac{1}{2\pi} \int_0^{2\pi} \frac{sc^3(g_3 p_1 c + g_4 p_2 s)^2}{-(s^2 + g_1 c^2)^3} d\varphi = \frac{1}{2\pi} \int_0^{2\pi} \frac{2g_3 g_4 p_1 p_2 s^2 c^4}{-(s^2 + g_1 c^2)^3} d\varphi = -K(g_1) g_3 g_4 p_1 p_2, \quad (3.24)$$

where, analogous to (3.16), only the term with the product $g_3 g_4$ remains from the integration. In addition, $K(g_1) \in \mathbb{R}_+$ is exactly as in (3.12) and $g_3 < 0$. Finally, to leading order, the limit cycle is then given by

$$\bar{r} = \sqrt{-\frac{g_2}{K(g_1) g_3 g_4 p_1 p_2 \sqrt{-4g_1 - g_2^2}}},$$

as claimed. \square

Notice that for $\operatorname{sgn}(p_1) = \operatorname{sgn}(p_2)$ we have $\operatorname{sgn}(\tilde{\Sigma}_2) = \operatorname{sgn}(\Sigma_2)$, with Σ_2 from (3.16), and the criticality is the same as for the case with the regular absolute value. Here, homoclinic loops also occur. However, a difference from the other situations is that the amplitude of the bifurcating branch depends on the choice of the slopes $p_{1\pm}, p_{2\pm}$.

Before moving on to the next section, we point out the following observations.

Remark 3.8. *At the nonzero equilibria, the location of the Hopf bifurcations in the (g_1, g_2) -plane differs between the smooth system (3.1) and the nonsmooth case (3.21) with $p_1 \neq p_2$, i.e., $p_{1-} \neq p_{2-}$ or $p_{1+} \neq p_{2+}$. Nevertheless, for the system (3.2) with the regular absolute value, the location of the Hopf bifurcations is the same as in the smooth case.*

Remark 3.9. *The generalized absolute value (2.1) can always be decomposed between a linear and an absolute value shape function as follows:*

$$[x]_{p_-}^{p_+} = \frac{p_+ + p_-}{2} x + \frac{p_+ - p_-}{2} |x|.$$

For instance, if $p_{2+} = 1$ and $p_{2-} = 0.9$, as chosen for Figure 3.8 (b), the decomposition reads $[x]_{p_{2-}^+}^{p_{2+}^+} = 0.95x + 0.05|x|$, showing an expression which behaves similar to the regular x function. In order for this splitting to diverge further from the smooth x function shape, and approach the absolute value contour, we require $|p_+ - p_-| > |p_+ + p_-|$. Hence, dealing with nonsmooth functions it is, practically speaking, more significant to consider the generalized function $[x]_{p_-^+}^{p_+^+}$ with $\text{sgn}(p_+) \neq \text{sgn}(p_-)$, so that $-p_+p_- > p_+p_-$ and thus $|p_+ - p_-| > |p_+ + p_-|$ holds.

From this decomposition, it is easy to see the weights of x and $|x|$ which contribute to $[x]_{p_-^+}^{p_+^+}$. However, considering the whole system (3.21), this splitting would introduce the factors x^2 and xy , deviating further from the normal form situation. For that reason, we employ the expression $[x]_{p_-^+}^{p_+^+}$.

With this last remark we complete the study of the impact of the generalized absolute value into the system undergoing a Bogdanov–Takens bifurcation discussed before and give way to our last section, where we briefly consider homoclinic and heteroclinic loops.

3.3 Example for homoclinic and heteroclinic bifurcations

It is well known that for the BT bifurcation, homoclinic and heteroclinic orbits occur—as we have seen in the previous sections—which in the present context, we expect to differ from the smooth case. However, we refrain from doing the detailed analysis of the nonsmooth BT case for these bifurcations here, and instead we point out, by way of an example, the similarities, as well as the differences, between a nonsmooth setting and its corresponding smooth version. Therefore, we present an artificial model, motivated by Hamiltonian systems, which deviates from the usual normal form. In addition, we introduce an extra parameter $\mu \in \mathbb{R}$ to illustrate how to break the homoclinic or heteroclinic loops and, at the same time, get periodic orbits varying μ .

As for the previous sections, we present a smooth system and its nonsmooth version to study how the effects of the absolute value function move the dynamics of the nonsmooth system away from the smooth situation.

The models to analyze are chosen adapting (3.1) and (3.2) to Example 6.16 in [47] as follows. For the smooth systems we have

$$\begin{cases} \dot{x} = y, \\ \dot{y} = g_1x + g_3x^3 + yG_s(x, y), \end{cases} \quad (3.25)$$

where $G_s(x, y) = 2g_1x^2 + g_3x^4 - 2y^2 + 4\mu_s$, and for the nonsmooth system,

$$\begin{cases} \dot{x} = y, \\ \dot{y} = g_1x + g_3x|x| + yG(x, y), \end{cases} \quad (3.26)$$

where $G(x, y) = 3g_1x^2 + 2g_3x^2|x| - 3y^2 + 6\mu$.

To begin with, we point out that, for $G_s, G \equiv 0$, both systems are Hamiltonian and they exhibit a similar behavior as for the systems shown in the previous sections. Indeed, on the one hand, if $g_1 < 0$, $g_3 > 0$, heteroclinic connections exist between the two fixed points $(|x_0|, y_0) = (-g_1/g_3, 0)$ for the nonsmooth case, or $(x_0, y_0) = (\pm\sqrt{-g_1/g_3}, 0)$ for the smooth case, and the origin is a center. On the other hand, if $g_1 > 0$, $g_3 < 0$, the nonzero equilibria are centers and the origin connects the two homoclinic orbits. Notice that the condition $G_s, G \equiv 0$ is equivalent to $g_2 = g_4 = 0$ in (3.1) and (3.2).

We briefly observe that, in particular for $G_s \equiv 0$, the smooth system corresponds to the so-called Duffing oscillator, [25]. For $g_1 < 0$, this system can be considered as the oscillatory behavior of a nonlinear spring with a mass, describing the hardening and softening spring effects. In this case, $g_1x + g_3x^3$ would correspond to the restoring force. If $g_3 < 0$, then it is called a “hard spring” since the restoring force is greater for larger values of $|x|$. On the other hand, for $g_3 > 0$ the system is called a “soft spring” since the restoring force is weaker for big $|x|$. For $g_1 > 0$ and $g_3 < 0$, we have a double-well potential, cf. Figure 1.1, and the system may be used to model a slender steel beam which is bent towards two permanent magnets; see [42]. If $g_3 > 0$, then the unique fixed point of the system (the origin) is a saddle point.

Coming back to the full system (3.26) (resp. (3.25)), we have that for $G \neq 0$ (resp. $G_s \neq 0$) the symmetry is broken and the existence of the aforementioned heteroclinic and homoclinic orbits depends on the parameter μ (resp. μ_s).

Without loss of generality, we consider from now on $g_1 > 0$ and $g_3 < 0$, and thus we expect the occurrence of homoclinic orbits. The analysis regarding $g_1 < 0$ and $g_3 > 0$ is analogous to that, but we would then expect heteroclinic orbits instead.

We start analyzing the nonsmooth system and afterwards we compare it with the smooth version of it.

For $G \equiv 0$, the energy function of (3.26) reads

$$H(x, y) = \frac{y^2}{2} - g_1 \frac{x^2}{2} - g_3 \frac{x^2|x|}{3},$$

and its time derivative becomes $\dot{H} = 6y^2(\mu - H)$, where the equations of the full system (3.26) are used. \dot{H} vanishes if and only if $H = \mu$, and the level curves are then given by

$$y(x; \mu) = \pm \sqrt{\frac{6\mu + 3g_1x^2 + 2g_3x^2|x|}{3}}. \quad (3.27)$$

To facilitate the further exposition of results, we write (3.27) as $y(x; \mu) = \pm\sqrt{\gamma(x; \mu)}$, where $\gamma(x; \mu)$ behaves as a quartic polynomial function in x centered horizontally at zero and crossing the x -axis up to four times. Fixing g_1, g_3 , the number of zeros of $\gamma(x; \mu)$ depends on the value of μ . We recall that $g_1 > 0, g_3 < 0$ are considered to be fixed. Moreover, at the nonzero equilibria $(|x_0|, y_0) = (-g_1/g_3, 0)$, the function $\gamma(x_0; \mu)$ vanishes if and only if $\mu = \bar{\mu} := -g_1^3/6g_3^2 < 0$. In addition, and regarding the zero steady state, we observe that the linearization of (3.26) at this point has negative determinant since $g_1 > 0$, so that this is always a saddle point.

With that, we now present the analysis of the behavior of the trajectories of (3.26) by means of (3.27) and in terms of μ :

- For $\mu = 0$, $\gamma(x)$ vanishes at $x = 0$ and at the two symmetric points $|x| = -3g_1/2g_3$. Thus, in (3.26) two stable homoclinic orbits exist, where each of them encloses one of the nonzero unstable fixed points. By contrast, for $\mu \neq 0$, the homoclinic orbits are broken.
- If $\mu > 0$, the zeros of $\gamma(x)$ are $\pm\delta = \pm\delta(g_1, g_3)$ with $\delta > 0$, and hence, $\gamma(x)$ is strictly positive for $x \in (-\delta, \delta)$. For the ODE system, this means that a larger periodic orbit exists, which is stable and the two nonzero fixed points remain unstable.
- For $\mu \in (\bar{\mu}, 0)$, the function $\gamma(x)$ vanishes at $\pm\delta = \pm\delta(g_1, g_3)$, $\pm\rho = \pm\rho(g_1, g_3)$ with $\delta > \rho > 0$. Therefore, $\gamma(x)$ is strictly positive for $x \in (-\delta, -\rho) \cup (\rho, \delta)$. In this case, the two homoclinic orbits are disconnected from zero so that they become stable periodic orbits, with unstable nonzero equilibria.
- If $\mu = \bar{\mu}$, $\gamma(x) \leq 0$ with two symmetric zeros. The previous periodic orbits collide into the nonzero equilibria, where the trajectories spiral into these two points.
- For $\mu < \bar{\mu}$, $\gamma(x) < 0$ and thus $y(x) \notin \mathbb{R}$. The nonzero equilibria of (3.26) are then stable point.

For the smooth system (3.25), we now perform an analogous analysis to the aforementioned explanation. For that, the energy function reads

$$H_s(x, y) = \frac{y^2}{2} - g_1 \frac{x^2}{2} - g_3 \frac{x^4}{4},$$

with the time derivative $\dot{H}_s = 4y^2(\mu_s - H)$. The trajectories are then curves defined by the contours of constant energy $H_s = \mu_s$, which can be written as

$$y(x; \mu_s) = \pm \sqrt{\frac{4\mu_s + 2g_1x^2 + g_3x^4}{2}}. \quad (3.28)$$

Notice that these functions scale differently from the level curves from (3.27). The expression inside the square root of (3.28), which we call $\gamma_s(x; \mu_s)$, is a quartic polynomial in x with a similar behavior as $\gamma(x; \mu)$ from (3.27). For instance, at $(x_0, y_0) = (\pm\sqrt{-g_1/g_3}, 0)$, the function $\gamma_s(x_0; \mu_s)$ vanishes if and only if $\mu_s = \bar{\mu}_s := g_1^2/4g_3 < 0$, and the study of the behavior of the trajectories of system (3.25), with help of (3.28), can be carried on equivalently here as done before.

To conclude this chapter, we briefly comment on the main results as follows. In the first part, we have seen that, at first glance, the bifurcation analysis for both nonsmooth (3.2) and smooth systems (3.1) at the zero equilibrium appear to be quite similar, e.g., Figure 3.1, although the scaling laws of the Hopf bifurcation branch at the zero steady state are different between both systems, cf. Figure 3.2 (a,b). While the criticality of the Hopf bifurcation of the nonsmooth system at the trivial fixed point can be inferred from the corresponding results of the smooth situation, this is not the case for the nonzero equilibria, e.g., Figure 3.4, in which a proper study for the nonsmooth case is required to get a complete analysis, even though the criticality is as for the smooth case.

Further on, we have shown that the generalized absolute value may produce a change in the criticality of the Hopf bifurcation depending on the slopes of the nonsmooth function; see Figure 3.8.

Finally, a short comparison between (3.26) and (3.25), regarding homoclinic and heteroclinic loops has been performed, revealing that one has to pay attention to the scaling differences between both systems.

Chapter 4

Stabilizing Nonsmooth Ship Models with P-Control

In this chapter, a 3 DOF marine craft model, with surge u , sway v , and yaw r velocities, is considered. This is extended to 4 ODEs including the yaw angle ψ , and adding the yaw damping and yaw restoring P-control $\eta = \varepsilon_r r + \varepsilon_\psi \psi$, with control strengths $\varepsilon_r, \varepsilon_\psi$. Furthermore, in order to facilitate the analysis of the model, we rescale the 4-dimensional system with control in terms of the length L_{pp} between perpendiculars of the ship. Specifically, we focus on stabilizing the straight motion, which appears to be an unstable fixed point in the 4D system.

For this system, we determine the existence, location and geometry of the region in the positive quadrant of the $(\varepsilon_r, \varepsilon_\psi)$ -plane for which the straight motion is linearly stable. In fact, we provide this in terms of an explicit formula. We show that the stability region may be bounded or even empty (within the positive quadrant). For this, we investigate exhaustively the influence on the stability region of the propeller diameter D_p and the longitudinal thruster location x_T in percent of length from midship. In Figure 4.1 we illustrate the resulting different forms of the stability region depending on the value of x_T with respect to certain thresholds $x_{T_0}, x_{T_-}, x_{T_1}, x_{T_s}$. Note that the natural domain of x_T is $[-0.5, 0.5]$. For instance, if the thruster (the combination of the rudder and the propeller of the ship) was placed at the very end of the vessel, at the aft, then $x_T = -0.5$.

As might be expected, the further away from the aft, the more constrained the stability region is, and beyond the threshold x_{T_s} the straight motion cannot be stabilized at all, at least not by the fixed P-control design. In a nutshell, either stabilization is possible by ε_r alone (for $\varepsilon_\psi = 0$) or by no means, and—except in the case 4 in Figure 4.1—the stable region is unbounded and can be reached by increasing ε_r for any $\varepsilon_\psi \geq 0$. In fact, we prove that this scenario occurs not only for the Hamburg Test Case (HTC) but much more broadly in the space of model parameters.

Concerning nonlinear effects of the stabilizing control, we study the character of the bifurcations of the system. This is complicated by the fact that the nonlinear terms in the model equations are nonsmooth, featuring second order modulus terms such as $v|r|$ due to the hydrodynamic forces, cf. §4.1. Such terms prevent the use of standard bifurcation theory, in particular for the Andronov–Hopf bifurcations to periodic solutions. For vanishing yaw restoring control, $\varepsilon_\psi = 0$, steady state bifurcations occur and we prove that this is a nonsmooth

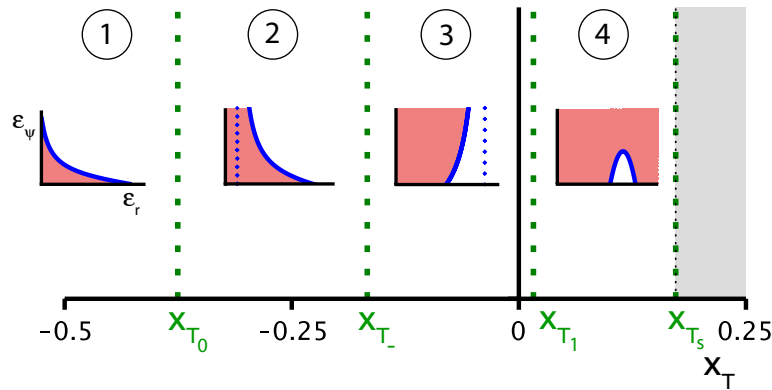


FIGURE 4.1: The insets show the possible forms of the stability region in the $(\varepsilon_r, \varepsilon_\psi)$ -plane in terms of the thresholds on the x_T -axis (green dashed), where the red shaded areas mean unstable straight motion. Cases 2 and 3 feature a vertical asymptote of the corresponding stability boundary curve (blue dashed); the stability region is bounded in case 4 only. For $x_T \geq x_{T_s}$ the straight motion cannot be stabilized (is uncontrollable). For the HTC, $x_{T_0} \approx -0.38$, $x_{T_-} \approx -0.17$, $x_{T_1} \approx 0.016$, $x_{T_s} \approx 0.17$. The specific values for the insets are (1) $x_T \approx -0.49$, (2) $x_T = -0.3$, (3) $x_T = -0.16$, (4) $x_T = 0.16$.

pitchfork bifurcation. For $\varepsilon_\psi > 0$, the mentioned Hopf bifurcations occur, which we handle by the method developed in Chapter 2. Our approach transforms the problem to a system of the form

$$\begin{cases} \dot{r} = \mu r + \chi(\varphi)r^2 + \mathcal{O}(r^3), \\ \dot{\varphi} = \omega + \Omega(\varphi)r + \mathcal{O}(r^2), \end{cases}$$

for certain polar coordinates (r, φ) , bifurcation parameter μ and 2π -periodic functions χ, Ω . As detailed in Chapter 2, it follows that a Hopf-type bifurcation occurs, where the amplitudes of the emerging periodic solutions are given by

$$r = -\frac{2\pi}{\Sigma}\mu + \mathcal{O}(\mu^2), \quad \text{where} \quad \Sigma := \int_0^{2\pi} \chi(\varphi)d\varphi.$$

This bifurcation comes in two generic types, analogous to the usual smooth case: supercritical (unstable fixed point coexists with stable periodic orbits, $\Sigma < 0$) or subcritical (stable fixed point coexists with unstable periodic orbits, $\Sigma > 0$). In the subcritical case, upon moving the control parameter through the stability threshold, the corresponding solution will typically not track the stabilized equilibrium but will be repelled from the unstable periodic orbit. In contrast, in the supercritical (“safe”) case, the trajectories will track the stabilized state. Hence, from a mathematical as well as an engineering point of view, it is relevant to a priori determine this criticality from the equations, i.e., to obtain a formula for Σ . In the smooth setting this corresponds to the first Lyapunov coefficient, which is found from a center manifold reduction and normal form computation based on Taylor expansion. This expansion cannot be used for the nonsmooth models and we instead employ the aforementioned approach to determine Σ . We emphasize that in the smooth case, the amplitudes of the bifurcating periodic orbits, and thus the basin of attraction, scale as $|\mu|^{1/2}$, rather than linearly as happens in the present nonsmooth case. As mentioned, this analysis reveals that for the ship model the bifurcations at the stability boundary are supercritical in the HTC and for different thruster

positions. While this means all bifurcations are safe for the parameter values we considered, it is not clear at all for which other modification of the HTC parameters this remains the case.

However, the local analysis near a bifurcation does not reveal the overall organization of nonlinear states. In order to gain additional insight into this, we have performed a numerical continuation analysis, still focusing on the setup for the straight motion stabilization. This corroborates our analytical predictions and reveals how the stable and unstable equilibria, as well as periodic orbits, are organized globally in the positive quadrant of control strengths $\varepsilon_r, \varepsilon_\psi$. As expected, we find that periodic orbits continue to the stability boundary curve and to the steady states at $\varepsilon_\psi = 0$. In addition, we also find that periodic orbits continue to certain heteroclinic bifurcations, as discussed in §4.3. Such a global analysis requires the vector field to be 2π -periodic with respect to the yaw angle ψ and, for definiteness, we modify the control law to $\eta = \varepsilon_r r + \varepsilon_\psi \sin(\psi)$, which is nonlinear and has no impact on the local bifurcations. This global cylinder geometry also induces a winding number for periodic orbits, which is a topological invariant and enters into the global bifurcation scenario. We remark that this change for the model to be periodic in ψ is exclusively applied for the global bifurcation analysis in §4.3.

For further illustration, we present several simulations of solutions from ship motions also on Earth-fixed position coordinates.

This chapter is structured as follows. We present the rescaled 4-dimensional thruster model for ship maneuvering with control in §4.1. In the main section §4.2, we theoretically analyze the straight motion in terms of linear stability and bifurcations and continue with a nonlinear analysis. The numerical bifurcation investigation is presented in §4.3 and concludes this chapter.¹

4.1 Governing equations and thruster model

The specific model equations that we will investigate are a variation of the 3 DOF model from [2, 57], for which some basic analysis was conducted in [3]. The model parameters stem from the Hamburg Test Case (HTC) characteristics that we collect in B.1 as needed. We adopt these values throughout, except when analyzing the impact of selected parameter changes. The general 3 DOF model takes the form

$$\begin{pmatrix} m + m_{uu} & 0 & 0 \\ 0 & m + m_{vv} & m_{vr} \\ 0 & m_{rv} & I_z + m_{rr} \end{pmatrix} \begin{pmatrix} \dot{u} \\ \dot{v} \\ \dot{r} \end{pmatrix} = \begin{pmatrix} mvr + X \\ -mur + Y \\ N \end{pmatrix}, \quad (4.1)$$

where u , v and r are the surge, sway and yaw velocities, respectively, m is the mass of the rigid-body, m_{ij} the added mass coefficients for $i, j \in \{u, v, r\}$, and I_z the moment of inertia in yawing. The external forces X, Y, N for the “rudder model” of [57] are of the form

$$X = X_H + X_R + X_P, \quad Y = Y_H + Y_R, \quad N = N_H + N_R,$$

¹Most of the results in this chapter have been submitted for publication and can be found in the preprint [52].

with the contributions from the hull (H), the rudder (R) and the propeller (P) of the vessel.

In order to facilitate the presentation of the mathematical method and analysis, we combine the rudder and propeller forces as in [3] into a simpler thruster force, which gives

$$\begin{aligned} X &= X_H + X_P \cos \eta, \\ Y &= Y_H + X_P \sin \eta, \\ N &= N_H + x_T X_P \sin \eta. \end{aligned} \quad (4.2)$$

Here the thruster acts on the hull at a longitudinal position x_T relative to the length L_{pp} between perpendiculars of the hull, and exerts a force in the direction η of amplitude given by the propeller force X_P . We recall that η is an external input assumed to obey a control law design. As the default position we take that of the rudder in the HTC, namely $x_T = -(0.5 + \frac{x_B}{100})L_{pp} = -0.49429L_{pp}$, with $x_B = -0.571$ being the longitudinal center of gravity with respect to midship in percent of length. Note that x_T is measured from the midship towards the front, and thus the domain in this case is $[-0.5L_{pp}, 0.5L_{pp}]$.

The hull forces have the following general expressions, cf. [2, 57]:

$$\begin{aligned} X_H &= \frac{1}{2} \rho L_{pp} T \left(X_{u|u} |u| |u| + X_{\beta\gamma} L_{pp} v r \right), \\ Y_H &= \frac{1}{2} \rho L_{pp} T \left(Y_{\beta} |u| |v| + Y_{\gamma} L_{pp} u r + Y_{\beta|\beta} |v| |v| + Y_{\gamma|\gamma} L_{pp}^2 r |r| + Y_{\beta|\gamma} L_{pp} v |r| \right. \\ &\quad \left. + Y_{|\beta|\gamma} L_{pp} |v| |r| + Y_{ab} |u^{a_y} v^{b_y}| \operatorname{sgn}(v) V^{2-a_y-b_y} \right), \\ N_H &= \frac{1}{2} \rho L_{pp}^2 T \left(N_{\beta} u v + N_{\gamma} L_{pp} r |u| + N_{\gamma|\gamma} L_{pp}^2 r |r| + N_{\beta|\beta} |v| |v| \right. \\ &\quad \left. + N_{\beta\beta\gamma} r v^2 L_{pp} V^{-1} + N_{\beta\gamma\gamma} v r^2 L_{pp}^2 V^{-1} \operatorname{sgn}(u) + N_{u'\gamma c} L_{pp}^{c_n} |u r^{c_n}| V^{-c_n+1} \operatorname{sgn}(r) \right. \\ &\quad \left. + N_{ab} |u^{a_n} v^{b_n}| V^{-a_n-b_n+2} \operatorname{sgn}(u v) \right), \end{aligned}$$

where $V = \sqrt{u^2 + v^2}$ and all coefficients are by default those of the HTC as listed in B.1, from which we note a_n, b_n, c_n as well as a_y, b_y are all positive integers. We observe that these forces implement the aforementioned second order modulus form of the drag.

The propeller force taken from [57] reads

$$X_P = (1 - t) T_p(u),$$

with thrust deduction fraction t and propeller thrust $T_p(u) = \rho n_p^2 D_p^4 K_T$, where ρ is the water density, n_p the propeller frequency, and D_p the propeller diameter. Further, $K_T = \sum_{i=0}^5 K_{Ti} J_p^i$ with $J_p = \frac{u(1-w)}{n_p D_p}$, where w is the wake fraction. Later, it turns out to be relevant that the propeller thrust is monotone decreasing with respect to the surge u , i.e.,

$$\partial_u X_P < 0, \quad (4.3)$$

which can readily be verified numerically for the HTC. Specifically, since $(1-t)\rho n_p^2 D_p^4 > 0$, see B.1, the condition $\partial_u X_P < 0$ is equivalent to $\partial_u K_T < 0$. In addition, $J_p > 0$ holds considering forward motion $u > 0$.

For completeness, we present the rudder forces X_R, Y_R, N_R in B.2, although these are not relevant for our analysis.

The model is completed by the control law for the steering angle $\eta = \eta_1 + \eta_2$, which is a combination of the yaw damping P-control η_1 and yaw restoring P-control η_2 ; we refer to [21] for a general background. The first one consists of adding a proportional compensation to the yaw velocity r by setting $\eta_1 = \eta_0 + \varepsilon_r(r - r_0)$, with target yaw velocity r_0 , initial thruster angle η_0 , and control parameter $\varepsilon_r \geq 0$. Analogously, for the yaw angle ψ we have $\eta_2 = \eta_0 + \varepsilon_\psi(\psi - \psi_0)$, with target yaw angle ψ_0 and second control parameter $\varepsilon_\psi \geq 0$. Notably, for $\varepsilon_\psi > 0$ this requires to add $\dot{\psi} = r$ as a fourth equation to (4.1). Since we are focusing on controlling a straight line trajectory, we set $r_0 = \psi_0 = 0$, and consider, without loss of generality, $\eta_0 = 0$, which gives

$$\eta = \varepsilon_r r + \varepsilon_\psi \psi. \quad (4.4)$$

Regarding the propeller frequency n_p , we reflect the following reasoning: all forces scale quadratically with respect to the velocities so that $u = n_p \tilde{u}$ gives, e.g., $X_P = n_p^2 \tilde{X}_P(\tilde{u})$, where \tilde{X}_P is independent of n_p . This implies the natural relation that all velocities are proportional to the propeller speed: rescaling all velocities proportional to n_p gives a factor n_p^2 on the right-hand side of (4.1) and a factor n_p on the left-hand side. Time rescaling with n_p gives a second factor on the left so that n_p is removed upon division. Hence, any motion for one value of $n_p > 0$ can directly be rescaled to the motion corresponding to another positive value of n_p . Therefore, without loss of information, we can fix $n_p > 0$ arbitrarily; as in [3], we choose $n_p = 2$. Concerning the propeller diameter D_p , we also observe that scaling $u = D_p \tilde{u}$ gives $X_P = D_p^4 \tilde{X}_P(\tilde{u})$, where \tilde{X}_P is independent of D_p . However, not all forces scale in the same way and, as we will explain below, the value of D_p enters into the analysis of the model.

In order to simplify the implementation and analysis, we rescale (4.1) in terms of the length L_{pp} between perpendiculars of the vessel, but do not pursue a full non-dimensionalization. As the starting point, we note that the surge and sway velocities have dimensions $[u] = [v] = \text{m/s}$, while the dimension of the angular yaw velocity is $[r] = 1/\text{s}$. It is worth to mention that, although the angular velocity is radians per second, i.e., rad/s , since the radian is a dimensionless quantity, it may be written as $1/\text{s}$ in the International System of Units. Next, we equate these by introducing $\bar{r} = L_{pp} r$ and then rescale (4.1), together with (4.2), accordingly. Denoting the rescaled quantities with overbar, except using τ for the rescaled thruster force amplitude, we obtain

$$\begin{pmatrix} \bar{m} + \bar{m}_{uu} & 0 & 0 \\ 0 & \bar{m} + \bar{m}_{vv} & \bar{m}_{vr} \\ 0 & \bar{m}_{rv} & \bar{I}_z + \bar{m}_{rr} \end{pmatrix} \begin{pmatrix} \dot{u} \\ \dot{v} \\ \dot{\bar{r}} \end{pmatrix} = \begin{pmatrix} L_{pp}^{-1} \bar{m} v \bar{r} + \bar{X}_H + \tau \cos \eta \\ -L_{pp}^{-1} \bar{m} u \bar{r} + \bar{Y}_H + \tau \sin \eta \\ \bar{N}_H + \bar{x}_T \tau \sin \eta \end{pmatrix}, \quad (4.5)$$

where we have scaled

$$\begin{aligned}\bar{m} &= B_2^{-1}m, & \bar{m}_{uu} &= B_2^{-1}m_{uu}, & \bar{m}_{vv} &= B_2^{-1}m_{vv}, & \bar{I}_z &= B_4^{-1}I_z, \\ \bar{m}_{vr} &= B_3^{-1}m_{vr}, & \bar{m}_{rv} &= B_3^{-1}m_{rv}, & \bar{m}_{rr} &= B_4^{-1}m_{rr}, & \tau &= B_2^{-1}X_P, \\ \bar{X}_H &= B_2^{-1}X_H, & \bar{Y}_H &= B_2^{-1}Y_H, & \bar{N}_H &= B_3^{-1}N_H, & \bar{x}_T &= L_{pp}^{-1}x_T,\end{aligned}$$

with $B_i = \frac{1}{2}\rho L_{pp}^i T$. More specifically, this gives

$$\begin{aligned}\bar{X}_H &= L_{pp}^{-1} \left(X_{u|u} u^2 + X_{\beta\gamma} v \bar{r} \right), \\ \bar{Y}_H &= L_{pp}^{-1} \left(Y_{\beta} u v + Y_{\gamma} u \bar{r} + Y_{\beta|\beta} |v| |v| + Y_{\gamma|\gamma} |\bar{r}| |\bar{r}| + Y_{\beta|\gamma} |v| |\bar{r}| + Y_{|\beta|\gamma} |v| |\bar{r}| \right. \\ &\quad \left. + Y_{ab} u^{a_y} |v|^{b_y} \operatorname{sgn}(v) V^{2-a_y-b_y} \right), \\ \bar{N}_H &= L_{pp}^{-1} \left(N_{\beta} u v + N_{\gamma} u \bar{r} + N_{u'\gamma c} u |\bar{r}|^{c_n} |V|^{-c_n+1} \operatorname{sgn}(\bar{r}) + N_{\gamma|\gamma} |\bar{r}| |\bar{r}| + N_{\beta|\beta} |v| |v| \right. \\ &\quad \left. + N_{\beta\beta\gamma} \bar{r} v^2 V^{-1} + N_{\beta\gamma\gamma} v \bar{r}^2 V^{-1} + N_{ab} u^{a_n} |v|^{b_n} |V|^{-a_n-b_n+2} \operatorname{sgn}(v) \right),\end{aligned}$$

where the general assumption $u \geq 0$ is considered since the ship is pushed forward due to the thruster force (combination of the propeller and rudder forces). To ease the exposition, in the following we refer to the rescaled hydrodynamic bare hull coefficients $\bar{X}_j = L_{pp}^{-1} X_j$, $\bar{Y}_j = L_{pp}^{-1} Y_j$, $\bar{N}_j = L_{pp}^{-1} N_j$, where $j \neq H$ denotes the corresponding subindex; and likewise introduce $m_L = L_{pp}^{-1} \bar{m}$.

Concerning the control law (4.4), it is natural to scale $\bar{\psi} = L_{pp} \psi$ so that the added equation $\dot{\psi} = r$ becomes $\dot{\bar{\psi}} = \bar{r}$; note that $\bar{\psi}$ is then $2\pi/L_{pp}$ -periodic. Therefore, in (4.4) we scale further $\bar{\varepsilon}_r = L_{pp}^{-1} \varepsilon_r$ and $\bar{\varepsilon}_\psi = L_{pp}^{-1} \varepsilon_\psi$, which yields

$$\eta = \bar{\varepsilon}_r \bar{r} + \bar{\varepsilon}_\psi \bar{\psi}. \quad (4.6)$$

From now on, we omit all overbars and study the rescaled 4D ‘‘thruster model’’

$$\begin{pmatrix} m + m_{uu} & 0 & 0 & 0 \\ 0 & m + m_{vv} & m_{vr} & 0 \\ 0 & m_{rv} & I_z + m_{rr} & 0 \\ 0 & 0 & 0 & 1 \end{pmatrix} \begin{pmatrix} \dot{u} \\ \dot{v} \\ \dot{r} \\ \dot{\psi} \end{pmatrix} = \begin{pmatrix} m_L v r + X_H + \tau(u) \cos \eta \\ -m_L u r + Y_H + \tau(u) \sin \eta \\ N_H + x_T \tau(u) \sin \eta \\ r \end{pmatrix}, \quad (4.7)$$

written more compactly as $M\dot{\nu} = F(\nu)$, with M the invertible matrix on the left-hand side and $F(\nu)$ the right-hand side. The equivalent explicit compact form of (4.7) thus reads

$$\dot{\nu} = M^{-1} F(\nu). \quad (4.8)$$

4.2 Theoretical analysis

In this section, we investigate the impact of the yaw damping and yaw restoring control (4.6) on the stability and bifurcation analysis of the straight motion with constant speed. We include variations of the selected design parameters D_p , the propeller diameter, and x_T , the thruster position, in order to illustrate the methodology. We start discussing the existence of the straight motion as an equilibrium in the ship-fixed coordinates, then turn to the linear stability and finally analyze the resulting bifurcations.

4.2.1 Equilibrium straight motion

The straight motion of the vessel with constant speed corresponds to an equilibrium point $(u_0, v_0, r_0, \psi_0) = (u_0, 0, 0, 0)$, with $u_0 > 0$ and the reference direction $\psi_0 = 0$ of system (4.7). Equilibria are those $\nu = (u, v, r, \psi)^\top$ for which $F(\nu)$ in (4.8) vanishes. Setting $v = r = \psi = 0$, the last three components of $F(\nu)$ vanish, which in fact holds for any ψ_0 if $\varepsilon_\psi = 0$, so that in this case we obtain a line of equilibrium motion in any direction. For $\varepsilon_\psi \neq 0$, this is constrained to the reference direction $\psi_0 = 0$. The remaining first component of $F(\nu)$ now reads $X_H + \tau(u) \cos(0)$, which gives the condition for the equilibrium straight velocity u_0 as

$$X_{u|u} u_0^2 + \tau(u_0) = 0, \quad (4.9)$$

independent of the control parameters $\varepsilon_r, \varepsilon_\psi$. This equation possesses a unique positive solution if (4.3) holds, i.e., $\partial_u \tau(u) < 0$, since $\tau(0) > 0$ and $X_{u|u} < 0$, and therefore the left-hand side is strictly decreasing for $u > 0$. These conditions hold for the HTC values (see B.1), and then $u_0 = u_0^{\text{HTC}} \approx 8.71$.

Regarding the parameters D_p, x_T , the equilibrium location is independent of x_T since this does not appear in (4.9). For the propeller diameter D_p , we scale $u = D_p \tilde{u}$ and $\tilde{\tau}(\tilde{u}) := \frac{\tau(u)}{D_p^4}$ so that (4.9) becomes $X_{u|u} \tilde{u}_0^2 + D_p^2 \tilde{\tau}(\tilde{u}_0) = 0$, where the first addend is independent of D_p . Hence, the equilibrium depends on D_p , but for large values its location is approximately proportional to D_p , cf. Figure 4.2 (a,b): indeed, the rescaled (4.9), upon multiplication by $(D_p^2 X_{u|u})^{-1}$, takes the form

$$D_p^{-2} \tilde{u}_0^2 + C_0 + P(\tilde{u}_0) = 0, \quad (4.10)$$

with $P(\tilde{u}_0) := C_1 \tilde{u}_0 + \dots + C_5 \tilde{u}_0^5$, where the C_i are real constants. In the limit $D_p \rightarrow \infty$, the term $D_p^{-2} \tilde{u}_0^2$ vanishes, and \tilde{u}_0 converges to the unique positive solution \tilde{u}_0^* of $C_0 + P(\tilde{u}_0) = 0$, which is independent of D_p so that the resulting u_0 is proportional to D_p . The condition (4.3), with the rescaled τ function, is readily verified numerically for any D_p , cf. Figure 4.2 (c); for large D_p we can also see this rigorously by inspecting the expression for $\partial_u \tau(u_0)$ as a function of D_p , which reads

$$\partial_u \tau(u_0, D_p) = \tilde{C}_5 D_p^3 \left(-\tilde{C}_4 \left(\frac{u_0}{D_p} \right)^4 + \tilde{C}_3 \left(\frac{u_0}{D_p} \right)^3 - \tilde{C}_2 \left(\frac{u_0}{D_p} \right)^2 + \tilde{C}_1 \frac{u_0}{D_p} - \tilde{C}_0 \right),$$

where all \tilde{C}_i are positive constants. Therefore, for u_0 exactly proportional to D_p we have $\partial_u \tau(u_0, D_p) = \tilde{C} D_p^3$, with $\tilde{C} < 0$ and the approximate proportionality implies $\partial_u \tau(u_0) < 0$ for $D_p \gg 1$.

4.2.2 Linear stability of the straight motion

From [3], we first point out that the straight motion without control is unstable. Linearizing the right-hand side of (4.5) without control at $u = u_0, v = r = 0$ and multiplying by the

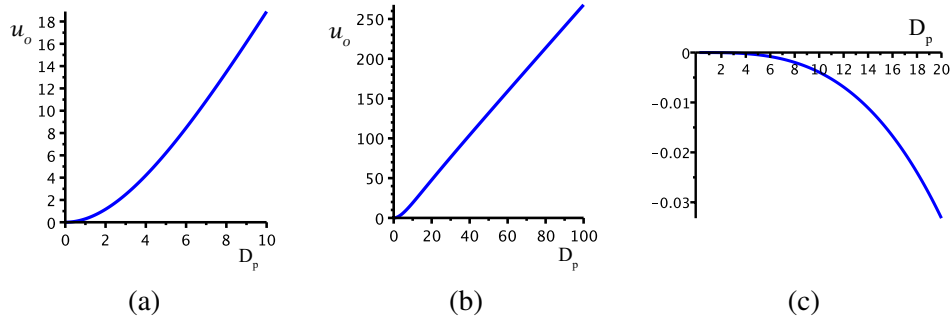


FIGURE 4.2: Solution function $u_0(D_p)$ from (4.9) for (a) $D_p \in [0, 10]$, and (b) $D_p \in [0, 100]$. In (c) $\partial_u \tau(u_0)$ is plotted as a function of $D_p > 0$, where it is shown that $\partial_u \tau(u_0) < 0$ holds.

inverse of the mass matrix yield

$$\tilde{S} := \frac{1}{D} \begin{pmatrix} \frac{D}{m+m_{uu}} & 0 & 0 \\ 0 & I_z + m_{rr} & -m_{vr} \\ 0 & -m_{rv} & m + m_{vv} \end{pmatrix} \begin{pmatrix} 2X_{u|u}u_0 + \partial_u \tau(u_0) & 0 & 0 \\ 0 & Y_\beta u_0 & (Y_\gamma - m_L)u_0 \\ 0 & N_\beta u_0 & N_\gamma u_0 \end{pmatrix}$$

with $D := (m + m_{vv})(I_z + m_{rr}) - m_{rv}m_{vr}$. We recall that the system we are working with is rescaled but we omit the overbars to simplify the notation. Next, due to the block structure, the upper left entry is an eigenvalue $\lambda_1 = (2X_{u|u}u_0 + \partial_u \tau(u_0))/(m + m_{uu})$ of \tilde{S} , which is always negative since $X_{u|u}u_0 < 0$ and $\partial_u \tau(u_0) < 0$ as just discussed. More specifically, for the HTC, see B.1, $X_{u|u} \approx -0.00009$, $m = 0.2328$, $m_{uu} = 0.0247$ and $u_0 = u_0^{\text{HTC}} \approx 8.71$, $\partial_u \tau(u_0) \approx -0.0008$, yielding $\lambda_1 \approx -0.0094$. Since $\lambda_1 < 0$, the stability of the straight motion equilibrium point $(u_0, 0, 0)$ is determined by the lower right 2×2 submatrix of \tilde{S} , which we denote by S . Its trace and determinant are, respectively,

$$\begin{aligned} \text{tr}(S) &= D^{-1}((I_z + m_{rr})Y_\beta + (m + m_{vv})N_\gamma - m_{vr}N_\beta - m_{rv}(Y_\gamma - m_L))u_0, \\ \det(S) &= D^{-1}(Y_\beta N_\gamma - N_\beta(Y_\gamma - m_L))u_0^2. \end{aligned}$$

For the HTC, see again B.1, both trace and determinant are negative, which implies that the eigenvalues λ_2, λ_3 are nonzero with opposite signs. Specifically, $\text{tr}(S) \approx -0.0657$, $\det(S) \approx -0.0059$, $\lambda_2 \approx 0.0506$ and $\lambda_3 \approx -0.1163$.

Hence, for the system without control, the straight motion equilibrium is unstable and we subsequently discuss the impact of the P-control (4.6) on the eigenvalues. Before that, we note that the free parameters D_p, x_T do not change the instability. Indeed, the longitudinal thruster position x_T clearly does not influence the stability analysis since the matrix and fixed point do not depend on it. The propeller diameter D_p enters only in $\partial_u \tau(u_0)$, which modifies the first eigenvalue λ_1 of \tilde{S} , but—as noted above—it is negative for any value of D_p .

In the remainder of this subsection we analyze the eigenvalues for the rescaled thruster model (4.7) with the P-control (4.6). For that, we denote by J the linearization of the

right-hand matrix of (4.7) at the equilibrium point $(u, v, r, \psi) = (u_0, 0, 0, 0)$, which reads

$$J = \begin{pmatrix} 2X_{u|u|}u_0 + \partial_u \tau(u_0) & 0 & 0 & 0 \\ 0 & Y_\beta u_0 & (Y_\gamma - m_L)u_0 + \tau(u_0)\varepsilon_r & \tau(u_0)\varepsilon_\psi \\ 0 & N_\beta u_0 & N_\gamma u_0 + x_T \tau(u_0)\varepsilon_r & x_T \tau(u_0)\varepsilon_\psi \\ 0 & 0 & 1 & 0 \end{pmatrix}.$$

Then, $F(\nu) = J\nu + h(\nu)$, where the function $h(\nu) = \mathcal{O}(|\nu|^2)$ contains the quadratic and higher order terms; we recall that due to the second order modulus terms, $h(\nu)$ is Lipschitz continuous but not differentiable. The resulting linear part of (4.8) is $M^{-1}J$ (with upper left 3×3 block \tilde{S} from above) and has the form

$$A := M^{-1}J = \begin{pmatrix} p_{11} & 0 & 0 & 0 \\ 0 & p_{22} & p_{23} & p_{24} \\ 0 & p_{32} & p_{33} & p_{34} \\ 0 & 0 & 1 & 0 \end{pmatrix}, \quad (4.11)$$

where

$$p_{11} = (m + m_{uu})^{-1} (2X_{u|u|}u_0 + \partial_u \tau(u_0)),$$

and we define the other matrix entries as follows, noting the dependencies on $u_0, \varepsilon_\psi, \varepsilon_r$:

$$\begin{aligned} p_{22} &= p_{22u}u_0, & p_{23} &= p_{23u}u_0 + q_{23}\tau(u_0)\varepsilon_r, & p_{24} &= q_{23}\tau(u_0)\varepsilon_\psi, \\ p_{32} &= p_{32u}u_0, & p_{33} &= p_{33u}u_0 + q_{33}\tau(u_0)\varepsilon_r, & p_{34} &= q_{33}\tau(u_0)\varepsilon_\psi, \end{aligned}$$

with

$$\begin{aligned} p_{22u} &= D^{-1}((I_z + m_{rr})Y_\beta - m_{vr}N_\beta), \\ p_{23u} &= D^{-1}((I_z + m_{rr})(Y_\gamma - m_L) - m_{vr}N_\gamma), \\ q_{23} &= D^{-1}(I_z + m_{rr} - m_{vr}x_T), \\ p_{32u} &= D^{-1}(-m_{rv}Y_\beta + (m + m_{vv})N_\beta), \\ p_{33u} &= D^{-1}(-m_{rv}(Y_\gamma - m_L) + (m + m_{vv})N_\gamma), \\ q_{33} &= D^{-1}(-m_{rv} + (m + m_{vv})x_T). \end{aligned}$$

We remark that the coefficient q_{23} is the same in the expressions for p_{23} and p_{24} , as well as q_{33} for p_{33} and p_{34} . Further, we define the following terms, which enter in the stability result:

$$\begin{aligned} K_{11} &= q_{33}^2 \tau(u_0)^2, \\ K_{02} &= q_{33}(p_{32u}q_{23} - p_{22u}q_{33})u_0 \tau(u_0)^2, \\ K_{01} &= [(p_{22u} + p_{33u})(p_{32u}q_{23} - p_{22u}q_{33}) + q_{33}(p_{23u}p_{32u} - p_{22u}p_{33u})] u_0^2 \tau(u_0), \\ K_{10} &= [(p_{22u} + p_{33u})q_{33} + p_{32u}q_{23} - p_{22u}q_{33}] u_0 \tau(u_0), \\ K_{00} &= (p_{22u} + p_{33u})(p_{23u}p_{32u} - p_{22u}p_{33u})u_0^3. \end{aligned} \quad (4.12)$$

With these preparations we can formulate our main result concerning the change of stability of the unstable straight motion equilibrium for the HTC values. This is a refinement of the result in [54], and implies “global controllability” of the straight motion in the sense that the stabilization by the P-control is possible along any direction in the control parameter space, i.e., the positive quadrant of the $(\varepsilon_r, \varepsilon_\psi)$ -plane.

Theorem 4.1. *Consider the rescaled thruster model (4.7) with the HTC values and define*

$$\varepsilon_\psi(\varepsilon_r) := -\frac{K_{02}\varepsilon_r^2 + K_{01}\varepsilon_r + K_{00}}{K_{11}\varepsilon_r + K_{10}}, \quad (4.13)$$

with K_{ij} from (4.12) and $\varepsilon_r, \varepsilon_\psi$ the P-control parameters from (4.6). Fix any $\underline{\varepsilon}_r, \underline{\varepsilon}_\psi \geq 0$ and for $s \geq 0$ consider control parameters on the ray $s \cdot (\underline{\varepsilon}_r, \underline{\varepsilon}_\psi)$. Then, as s increases, the equilibrium $(u_0, 0, 0, 0)$ of (4.7) is stabilized when $s \cdot (\underline{\varepsilon}_r, \underline{\varepsilon}_\psi)$ crosses the curve defined by (4.13). This crossing point lies at a unique $s^* > 0$ for each fixed $\underline{\varepsilon}_r, \underline{\varepsilon}_\psi$. For the eigenvalues of J the following holds: for $\underline{\varepsilon}_\psi > 0$, a complex conjugate pair of eigenvalues traverses the imaginary axis as s crosses s^* , while for $\underline{\varepsilon}_\psi = 0$ one eigenvalue is fixed at zero and a simple real eigenvalue traverses zero at $s = s^*$. In both cases, the real part of the traversing eigenvalues has nonzero derivative with respect to s at $s = s^*$.

We emphasize that in the special case $\varepsilon_\psi = 0$, the system is degenerate in the sense that the right-hand side of (4.8) is independent of ψ . This immediately implies that J always possesses one zero eigenvalue. Hence, the change in stability mentioned in the theorem results from another real eigenvalue. In fact, for $\varepsilon_\psi \neq 0$ the continuation of these two eigenvalues forms the complex conjugate pair of the Hopf bifurcation. While this eigenvalue configuration near $\varepsilon_\psi = 0$, $\varepsilon_r = s^*\underline{\varepsilon}_r$ is similar to a Bogdanov–Takens (BT) point, unlike a generic BT unfolding, the straight motion equilibrium exists for all parameters $\varepsilon_r, \varepsilon_\psi \geq 0$, and for $\varepsilon_\psi = 0$ the system is completely independent of ψ , having an eigenvalue fixed at zero. We discuss aspects of the resulting bifurcation in §4.2.3.1.

Proof. We analyze the eigenvalues of the linear part of (4.7) given by A in (4.11). As noted above, $p_{11} < 0$ for the HTC values, so that it suffices to consider the lower right 3×3 matrix, which we denote by P , and reads

$$P = \begin{pmatrix} p_{22} & p_{23} & p_{24} \\ p_{32} & p_{33} & p_{34} \\ 0 & 1 & 0 \end{pmatrix}.$$

Its characteristic polynomial is given by

$$Q_P(\lambda) = \det(\lambda \text{Id} - P) = \lambda^3 + c_2\lambda^2 + c_1\lambda + c_0,$$

with Id the 3×3 identity matrix and

$$\begin{aligned} c_0 &= p_{34}p_{22} - p_{24}p_{32} = (p_{22u}q_{33} - p_{32u}q_{23})u_0\tau(u_0)\varepsilon_\psi, \\ c_1 &= p_{22}p_{33} - p_{23}p_{32} - p_{34} \\ &= (p_{22u}p_{33u} - p_{23u}p_{32u})u_0^2 + (p_{22u}q_{33} - p_{32u}q_{23})u_0\tau(u_0)\varepsilon_r - q_{33}\tau(u_0)\varepsilon_\psi, \\ c_2 &= -p_{22} - p_{33} = -(p_{22u} + p_{33u})u_0 - q_{33}\tau(u_0)\varepsilon_r. \end{aligned}$$

The Routh–Hurwitz criterion, see [22], states that all eigenvalues of P have negative real part if and only if $c_2, c_0 > 0$ and $c_2c_1 - c_0 > 0$ hold. The first condition is always satisfied for the HTC values and for $\varepsilon_\psi > 0$ since for these we have $p_{22}, p_{33} < 0$, which implies $c_2 > 0$; and $p_{24} > 0, p_{32}, p_{34}, p_{22} < 0$ yield $c_0 > 0$. Concerning the second condition, using K_{ij} from (4.12) gives

$$\begin{aligned} c_2c_1 - c_0 &= q_{33}^2\tau(u_0)^2\varepsilon_\psi\varepsilon_r + q_{33}(p_{32u}q_{23} - p_{22u}q_{33})u_0\tau(u_0)^2\varepsilon_r^2 \\ &\quad + [(p_{22u} + p_{33u})(p_{32u}q_{23} - p_{22u}q_{33}) + q_{33}(p_{23u}p_{32u} - p_{22u}p_{33u})]u_0^2\tau(u_0)\varepsilon_r \\ &\quad + [(p_{22u} + p_{33u})q_{33} + p_{32u}q_{23} - p_{22u}q_{33}]u_0\tau(u_0)\varepsilon_\psi \\ &\quad + (p_{22u} + p_{33u})(p_{23u}p_{32u} - p_{22u}p_{33u})u_0^3 \\ &= K_{11}\varepsilon_\psi\varepsilon_r + K_{02}\varepsilon_r^2 + K_{01}\varepsilon_r + K_{10}\varepsilon_\psi + K_{00}. \end{aligned}$$

Hence, as claimed, precisely those $(\varepsilon_r, \varepsilon_\psi)$ “above” the convex curve defined by $c_2c_1 - c_0 = 0$ or equivalently (4.13), provide eigenvalues with negative real part.

In addition, for the control values satisfying (4.13) and $\varepsilon_\psi(\varepsilon_r) \neq 0$, it follows that there exist a complex conjugate pair with vanishing real part. Indeed, for the curve $c_2c_1 - c_0 = 0$ the characteristic polynomial can be factorized as $Q_P(\lambda) = (c_2\lambda^2 + c_0)\left(\frac{1}{c_2}\lambda + 1\right)$, and since $c_2, c_0 > 0$, the eigenvalues of the first factor correspond to a purely complex conjugate pair, $\lambda_\pm = \pm\sqrt{-\frac{c_0}{c_2}}$.

Finally, if $\varepsilon_\psi = 0$, then the last column of the matrix A in (4.11) vanishes, and $c_0 = 0$ holds, so that the matrix has a fixed zero eigenvalue. The conditions for the other eigenvalues to have negative real parts are $c_2, c_1 > 0$. Here $c_2 > 0$ holds as above since $p_{22}, p_{33} < 0$ for the HTC values and $\varepsilon_r \geq 0$. On the one hand, c_1 is linear in ε_r with positive slope, and $c_1 < 0$ at $\varepsilon_r = 0$ for the HTC. Therefore, c_1 changes sign from negative to positive at a unique $\varepsilon_{r_1} > 0$. Moreover, at ε_{r_1} the characteristic polynomial reads $Q_P(\lambda) = \lambda^2(\lambda + c_2)$, with a double root. On the other hand, since $c_0 = 0$ and $c_2 > 0$ in the present case, the sign of c_1 is that of $c_2c_1 - c_0$ so that $\varepsilon_\psi(\varepsilon_r) = 0$ is the stability threshold as claimed. \square

We plot the curve defined by (4.13) with the HTC parameter values in Figure 4.3. Although the (complete) theoretical analysis has been performed with the rescaled P-control (4.6), the figures in this chapter regarding the stability boundary curve, use $\varepsilon_r, \varepsilon_\psi$ from the unscaled P-control (4.4), and hence, with a scaling difference of L_{pp} . We chose to plot the unscaled control strengths to show the “real” control parameter values which would be used in the model.

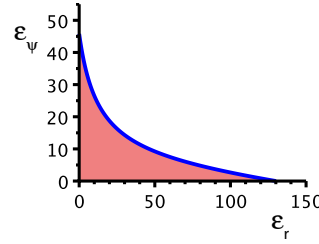


FIGURE 4.3: Stability boundary of the straight motion for the HTC values in the positive quadrant of the $(\varepsilon_r, \varepsilon_\psi)$ -plane, in terms of the *unscaled control parameters*, i.e., corresponding to (4.4) rather than (4.6). The straight motion is unstable in the colored area below the curve, and it is stable in the white region. The transition to stability for $\varepsilon_\psi > 0$ goes via a complex conjugate pair of eigenvalues, and the transition for $\varepsilon_\psi = 0$ via a real eigenvalue.

Furthermore, in agreement with the theorem statement, we numerically find that the linearization of the system at the equilibrium straight motion, i.e., the matrix A , on this curve possesses two real negative eigenvalues and a complex conjugate pair with zero real part. In Figure 4.3, in the shaded region below the curve, two eigenvalues have positive real part while in the white region beyond this curve, the real part of all eigenvalues is negative. Thus, one expects that a Hopf bifurcation occurs at $(\varepsilon_r, \varepsilon_\psi)$ satisfying (4.13). However, as mentioned before, for this nonsmooth system, the analysis is more delicate than usual.

Next we discuss the impact of varying the parameters n_p , D_p and x_T on the stabilization and therefore, the linear controllability of the straight motion.

4.2.2.1 Impact of changing the parameters n_p and D_p

To begin with, we briefly discuss the influence of the propeller frequency n_p . From §4.1 we recall that n_p can be removed from the uncontrolled system by rescaling. Here we consider the dependence on n_p of $\varepsilon_\psi(\varepsilon_r)$, i.e., of K_{ij} in (4.12). As in §4.1, we scale $u = n_p \check{u}$ and $\tau(u) = n_p^2 \check{\tau}(\check{u})$. Note that q_{23}, q_{33} in K_{ij} are multiplied by τ and thus $K_{11} = \mathcal{O}(\tau^2)$, $K_{02} = \mathcal{O}(u\tau^2)$, $K_{01} = \mathcal{O}(u^2\tau)$, $K_{10} = \mathcal{O}(u\tau)$, $K_{00} = \mathcal{O}(u^3)$. This yields

$$\varepsilon_\psi(\varepsilon_r, \check{u}; n_p) = -\frac{\check{K}_{02}n_p^2\check{u}\check{\tau}^2\varepsilon_r^2 + \check{K}_{01}n_p\check{u}^2\check{\tau}\varepsilon_r + \check{K}_{00}\check{u}^3}{\check{K}_{11}n_p\check{\tau}^2\varepsilon_r + \check{K}_{10}\check{u}\check{\tau}},$$

where \check{K}_{ij} are real constants. Hence, ε_r should be scaled as $\varepsilon_r = \check{\varepsilon}_r/n_p$, with $\check{\varepsilon}_r$ independent of n_p , so that ε_r is inversely proportional to n_p . In this case, $\varepsilon_\psi(\check{\varepsilon}_r, \check{u}; n_p)$ is independent of n_p . We note that ε_r and ε_ψ differ in units of second s, so that $\check{\varepsilon}_r$ and $\varepsilon_\psi(\check{\varepsilon}_r, \check{u}; n_p)$ have the same units.

Furthermore, the qualitative shape of the curve (4.13) for distinct values of n_p is similar as to the one shown in Figure 4.3, where the crossing point with the ε_r -axis depends on n_p . For instance, if we consider the values for Figure 4.3 as a reference, i.e., for the HTC characteristics and $n_p = 2$, and divide now by two the value of n_p in (4.13), then the crossing point $(\varepsilon_r, 0)$ has ε_r doubled, as we see from the relation $\varepsilon_r = \check{\varepsilon}_r/n_p$. Clearly, $(0, \varepsilon_\psi)$ remains the same.

Concerning D_p , we scale as in §4.2.1, $u = D_p \tilde{u}$ and $\tau(u) = D_p^4 \tilde{\tau}(\tilde{u})$, so that $\tilde{\tau}$ is independent of D_p and (4.13) becomes

$$\varepsilon_\psi(\varepsilon_r, \tilde{u}; D_p) = -\frac{\widetilde{K}_{02} D_p^6 \tilde{u} \tilde{\tau}^2 \varepsilon_r^2 + \widetilde{K}_{01} D_p^3 \tilde{u}^2 \tilde{\tau} \varepsilon_r + \widetilde{K}_{00} \tilde{u}^3}{\widetilde{K}_{11} D_p^5 \tilde{\tau}^2 \varepsilon_r + \widetilde{K}_{10} D_p^2 \tilde{u} \tilde{\tau}}, \quad (4.14)$$

where \widetilde{K}_{ij} are real constants. From (4.10) we have $\tilde{u}_0 = \tilde{u}_0(D_p) \rightarrow \tilde{u}_0^* \neq 0$, as $D_p \rightarrow \infty$, where \tilde{u}_0^* is independent of D_p . Setting in (4.14) $E := \tilde{\tau} D_p^3 \varepsilon_r$, $\Upsilon := \tilde{\tau} D_p^2$ gives

$$\varepsilon_\psi(E, \Upsilon) = -\frac{\widetilde{K}_{02} \tilde{u} E^2 + \widetilde{K}_{01} \tilde{u}^2 E + \widetilde{K}_{00} \tilde{u}^3}{(\widetilde{K}_{11} E + \widetilde{K}_{10} \tilde{u}) \Upsilon},$$

which has the same functional form with same signs of coefficients as (4.13). Therefore, the stability boundary is qualitatively the same for different D_p . Specifically, on the one hand, for $\varepsilon_r = 0$ we get from (4.14) that

$$\varepsilon_\psi(0, \tilde{u}; D_p) = -\frac{\widetilde{K}_{00} \tilde{u}^2}{\widetilde{K}_{10} D_p^2 \tilde{\tau}} = \mathcal{O}(D_p^{-2}).$$

On the other hand, for $\varepsilon_\psi = 0$ in (4.14) we obtain the function

$$\varepsilon_r(\tilde{u}; D_p) = \frac{\tilde{u}}{D_p^3 \tilde{\tau}} \frac{-\widetilde{K}_{01} \pm \sqrt{\widetilde{K}_{01}^2 - 4\widetilde{K}_{02} \widetilde{K}_{00}}}{2\widetilde{K}_{02}},$$

and $\tilde{u}_0(D_p) \rightarrow \tilde{u}_0^* \neq 0$ implies $\varepsilon_r(\tilde{u}_0; D_p) = \mathcal{O}(D_p^{-3})$. This means that for larger propeller diameter D_p it is “easier” to stabilize the straight motion by ε_r , in the sense that a smaller value of the control strength ε_r is required for the stabilization. In fact, numerically this holds for all D_p .

4.2.2.2 Impact of changing the thruster position parameter x_T

As shown next, understanding the impact of the thruster position is more involved. It turns out that for the HTC, when increasing x_T from the default value near -0.49 , i.e., placing the thruster more forwards, beyond $x_T \approx -0.38$ we lose the ability to stabilize the straight motion by ε_ψ alone, meaning that there exists an $\varepsilon_r^* > 0$ such that for $\varepsilon_r \in [0, \varepsilon_r^*]$ there is no ε_ψ that stabilizes the straight motion. Moreover, beyond $x_T \approx 0.17$ the P-control cannot stabilize the fixed point at all, thus creating an “uncontrollable” situation.

Before preparing the precise statement and proof, we first note that while (4.9) does not depend on x_T , the function (4.13) does. In fact, all q_{ij} in (4.12), i.e., q_{23}, q_{33} , depend on x_T , which results in K_{02}, K_{11} being quadratic in x_T , and K_{01}, K_{10} linear; only K_{00} does not depend on x_T . However, it is not clear that the graph of $\varepsilon_\psi(\varepsilon_r; x_T)$ remains a stability boundary since this only accounts for one of the criteria for stable eigenvalues. Indeed, the first condition for the Routh-Hurwitz criterion in the proof of Theorem 4.1 requires $c_0 \geq 0$ and $c_2 > 0$, but for instance at $x_T = 0.3$ we have $\varepsilon_\psi(\varepsilon_r; x_T) < 0$ for $\varepsilon_r < \varepsilon_{r_2} \approx 144.47$, and $c_2 < 0$ for $\varepsilon_r > \varepsilon_{r_2}$, where ε_{r_2} is the unique root of c_2 ; see Figure 4.4 (a). Therefore, in

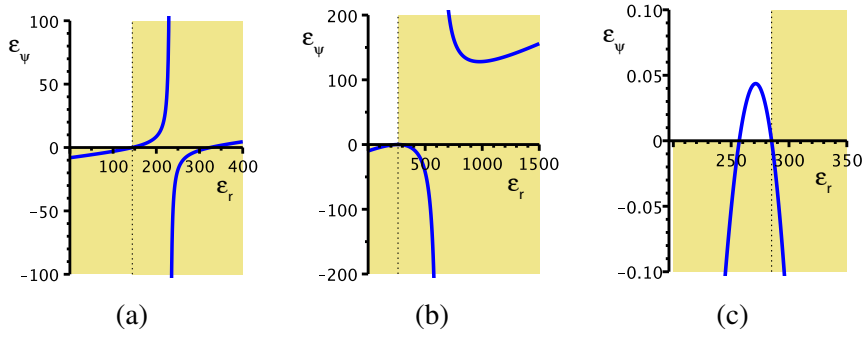


FIGURE 4.4: We display different forms of the curve $\varepsilon_\psi(\varepsilon_r)$ (blue) together with violations of the stability criteria $c_0 < 0$, $c_2 < 0$ (colored regions), where $c_0 < 0$ for $\varepsilon_\psi < 0$, and $c_2 < 0$ for large ε_r . (a) $x_T = 0.3$, (b) $x_T = x_{T_s} \approx 0.17$, and (c) $x_T = 0.16$, where we omit the second blue branch which is similar to that in (b). This last plot corresponds to the case 4 in the proof of Theorem 4.2.

this case the curve $\varepsilon_\psi(\varepsilon_r; x_T)$ is not a stability boundary, and the straight motion cannot be stabilized by the P-control (4.6).

In the following we provide a detailed, and somewhat tedious, analysis that explains all possibilities to stabilize the straight motion depending on x_T . We recall that u_0 does not depend on x_T , but for the coefficients c_0, c_1, c_2 of the eigenvalue problem we have

$$\begin{aligned} c_0 &= p_{34}p_{22} - p_{24}p_{32} = (\tilde{\alpha} + \tilde{\beta}x_T)\varepsilon_\psi, \\ c_1 &= p_{22}p_{33} - p_{23}p_{32} - p_{34} = \delta + (\tilde{\alpha} + \tilde{\beta}x_T)\varepsilon_r + (\alpha + \beta x_T)\varepsilon_\psi, \\ c_2 &= -p_{22} - p_{33} = \gamma + (\alpha + \beta x_T)\varepsilon_r, \end{aligned}$$

where

$$\begin{aligned} \alpha &:= D^{-1}m_{rv}\tau(u_0) > 0, \\ \beta &:= -D^{-1}(m + m_{vv})\tau(u_0) < 0, \\ \tilde{\alpha} &:= -D^{-1}[m_{rv}p_{22u} + (I_z + m_{rr})p_{32u}]u_0\tau(u_0) > 0, \\ \tilde{\beta} &:= D^{-1}[(m + m_{vv})p_{22u} + m_{vr}p_{32u}]u_0\tau(u_0) < 0, \\ \gamma &:= D^{-1}[m_{vr}N_\beta - (I_z + m_{rr})Y_\beta - (m + m_{vv})N_\gamma + m_{rv}(Y_\gamma - m_L)]u_0 > 0, \\ \delta &:= D^{-1}[(m + m_{vv})N_\gamma - m_{rv}(Y_\gamma - m_L)]p_{22u} \\ &\quad + (m_{vr}N_\gamma - (I_z + m_{rr})(Y_\gamma - m_L))p_{32u}]u_0^2 < 0. \end{aligned}$$

The signs of all these coefficients are given by the values of the HTC and remain the same for any $D_p > 0$ due to (4.3). Furthermore, the stability boundary (4.13) can be written in terms of x_T as

$$\varepsilon_\psi(\varepsilon_r; x_T) = \frac{\gamma\delta + [\gamma\tilde{\alpha} + \delta\alpha + (\gamma\tilde{\beta} + \delta\beta)x_T + (\alpha\tilde{\alpha} + (\alpha\tilde{\beta} + \tilde{\alpha}\beta)x_T + \beta\tilde{\beta}x_T^2)]\varepsilon_r}{\tilde{\alpha} - \gamma\alpha + (\tilde{\beta} - \gamma\beta)x_T - (\alpha + \beta x_T)^2\varepsilon_r},$$

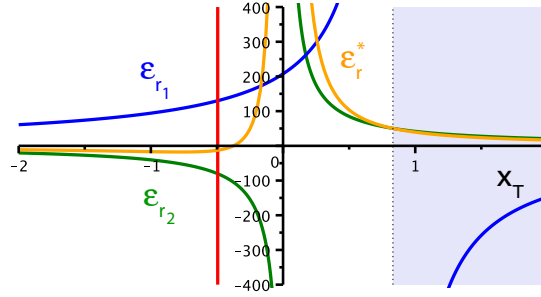


FIGURE 4.5: We plot relevant quantities as functions of x_T , and mark the HTC value $x_T = -0.49429$ (red vertical line) as well as the region $x_T > -\tilde{\alpha}/\tilde{\beta}$ (shaded area). Orange curves: $\varepsilon_r^*(x_T)$ from (4.15) for the singularity of $\varepsilon_\psi(\varepsilon_r; x_T)$; blue curves: $\varepsilon_{r_1}(x_T)$, the root of c_1 at $\varepsilon_\psi = 0$; green curves: $\varepsilon_{r_2}(x_T)$, the root of c_2 . Although the domain of x_T is $[-0.5, 0.5]$, we extend it to illustrate better the shape of the curves as well as the location of the shaded region.

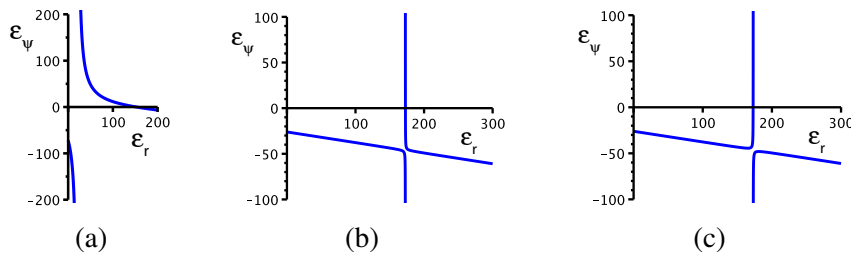


FIGURE 4.6: The function $\varepsilon_\psi(\varepsilon_r)$ is plotted for (a) $x_T = -0.3$, where $\varepsilon_r^* \approx 20.94$; (b) $x_T = -0.1669$; and (c) $x_T = -0.1668$. A change of convexity/concavity occurs between (b) and (c).

from which the singularity reads

$$\varepsilon_r^* = \frac{\tilde{\alpha} - \gamma\alpha + (\tilde{\beta} - \gamma\beta)x_T}{(\alpha + \beta x_T)^2}, \quad (4.15)$$

i.e., the denominator of $\varepsilon_\psi(\varepsilon_r; x_T)$ vanishes for $\varepsilon_r = \varepsilon_r^*$; see Figure 4.5. For the HTC values, large negative values of x_T give negative $\varepsilon_r^* < 0$, a sign change occurs at $x_T \approx -0.38$, and a singularity near $x_T = 0.016$ takes place. In particular, $\varepsilon_r^* < 0$ for the HTC default value $x_T \approx -0.49$. As long as $\varepsilon_r^* < 0$, the singularity lies outside the positive range of the control parameters and is thus disregarded. However, for values of x_T where $\varepsilon_r^* > 0$, stabilization by ε_ψ alone is not possible and fixing $\varepsilon_r < \varepsilon_r^*$ creates an “uncontrollable” situation. We plot an example in Figure 4.6 (a), showing also negative values of ε_ψ for completeness. Furthermore, for $\varepsilon_r^* > 0$, there may be two positive values of ε_r for which $\varepsilon_\psi(\varepsilon_r; x_T) = 0$, i.e., potentially a stabilization and subsequent destabilization when increasing ε_r from zero, for instance, as plotted in Figure 4.4 (c). In addition, we emphasize that, comparing Figures 4.6 (a) and 4.4 (a), a switching from convexity to concavity of $\varepsilon_\psi(\varepsilon_r; x_T)$ has occurred, which in particular takes place at $x_T \approx -0.17$, cf. Figure 4.6 (b,c). This switch corresponds to the transition between regions 2 and 3 in Figure 4.1. These different regions (or cases) are explained in detail in the proof of Theorem 4.2.

With these preparations we formulate the following main result concerning controllability of the straight motion in terms of x_T . This involves the threshold for x_T given by

$$x_{T_s} = \frac{\delta\alpha - \gamma\tilde{\alpha}}{\gamma\tilde{\beta} - \delta\beta} > 0,$$

which is independent of u_0 and therefore of D_p . Specifically, it is the unique value of x_T for which the roots $\varepsilon_r = \varepsilon_{r_j}$ of c_j , $j = 1, 2$, at fixed $\varepsilon_\psi = 0$ coincide, i.e., $\varepsilon_{r_1}(x_{T_s}) = \varepsilon_{r_2}(x_{T_s})$. For the HTC values we have $x_{T_s} \approx 0.17$. As before, the stability region and its boundary refer to the positive quadrant in the $(\varepsilon_r, \varepsilon_\psi)$ -plane.

Theorem 4.2. *Consider x_T as a free parameter and assume for all other parameters the same signs of coefficients within c_0, c_1, c_2 as above for the HTC values. Then two scenarios occur. In the case that $-\alpha/\beta < -\tilde{\alpha}/\tilde{\beta}$, for any $x_T \leq -\alpha/\beta$ the statement of Theorem 4.1 holds true for all $\varepsilon_r > 0$, and the stability boundary is a strictly monotone curve intersecting the ε_r -axis, but possibly not the ε_ψ -axis, with a vertical asymptote at ε_r^* . Moreover, if $x_T \geq x_{T_s}$, the straight motion cannot be stabilized by any $\varepsilon_r, \varepsilon_\psi > 0$, while for $-\alpha/\beta < x_T < x_{T_s}$, the stability region is bounded with boundary of parabolic shape, intersecting twice the ε_r -axis. In the case that $-\tilde{\alpha}/\tilde{\beta} < -\alpha/\beta$, the stability boundary is strictly monotone if $x_T < -\tilde{\alpha}/\tilde{\beta}$ and otherwise stabilization is impossible.*

Before presenting the proof we proceed with some remarks. The theorem in particular implies the following alternative: either the straight motion can be stabilized by increasing ε_r for all $\varepsilon_\psi \geq 0$ or none, except in the case of a bounded stability region, cf. Figure 4.1. In all situations, the possibility to stabilize is determined by the case $\varepsilon_\psi = 0$ alone. Specifically, for the HTC values, occurring in the case $-\alpha/\beta < x_{T_s} < -\tilde{\alpha}/\tilde{\beta}$, if the longitudinal location of the thruster of the vessel, x_T , is too far from the aft, i.e., near the fore, then the straight motion cannot be stabilized by the P-control (4.6).

Proof of Theorem 4.2. We recall that the Routh-Hurwitz criterion from the proof of Theorem 4.1 consists of $c_0, c_2 > 0$ and $c_2c_1 > c_0$, which must be attainable for stabilization in case $\varepsilon_\psi > 0$; for $\varepsilon_\psi = 0$ we have $c_0 = 0$ and the criterion becomes $c_1, c_2 > 0$. The common condition $c_2 > 0$ is independent of the control parameter ε_ψ and equivalent to either $x_T \leq -\alpha/\beta$ (and any $\varepsilon_r \geq 0$), or $\varepsilon_r < \varepsilon_{r_2} = -\gamma/(\alpha + \beta x_T)$. Note that $-\alpha/\beta > 0$ by the sign conditions $\alpha > 0, \beta < 0$ on the coefficients (for the HTC $-\alpha/\beta \approx 0.016$).

Concerning $\varepsilon_\psi = 0$, the sign conditions $\tilde{\alpha} > 0$ and $\delta, \tilde{\beta} < 0$ yield $c_1 > 0$ if and only if $x_T < -\tilde{\alpha}/\tilde{\beta}$ and $\varepsilon_r > \varepsilon_{r_1} = -\delta/(\tilde{\alpha} + \tilde{\beta}x_T)$. In particular, only $\varepsilon_{r_1} > 0$ is relevant. In the case that $x_T > -\alpha/\beta$, the two bounds on ε_r are compatible if and only if $\varepsilon_{r_1} < \varepsilon_{r_2}$, which is equivalent to $x_T < x_{T_s}$. Hence, we find that controllability for $\varepsilon_\psi = 0$ requires

$$x_T < \min \left\{ -\tilde{\alpha}/\tilde{\beta}, \max \{ -\alpha/\beta, x_{T_s} \} \right\},$$

which covers the claimed statements in this case. (In particular, for the HTC values we have $x_{T_s} = (\delta\alpha - \gamma\tilde{\alpha})/(\gamma\tilde{\beta} - \delta\beta) \approx 0.17$, and $-\tilde{\alpha}/\tilde{\beta} \approx 0.83$, so the threshold would be $x_T = x_{T_s}$.)

We now turn to controllability for $\varepsilon_\psi > 0$. First we note that the condition $c_0 > 0$ is then equivalent to $\tilde{\alpha} + \tilde{\beta}x_T > 0$, i.e., $x_T < -\tilde{\alpha}/\tilde{\beta}$ so that again $\varepsilon_{r_1} > 0$. It remains to incorporate the last condition, $c_1c_2 > c_0$, whose boundary is given by $\varepsilon_\psi(\varepsilon_r)$, which solves $c_1c_2 = c_0$ (we omit the dependence on x_T for brevity). In the case that $\alpha + \beta x_T = 0$, we have $\varepsilon_\psi(\varepsilon_r) = \gamma\delta/(\tilde{\alpha} + \tilde{\beta}x_T) + \gamma\varepsilon_r$ with positive slope and root at ε_{r_1} . This is the stability boundary since in this case $c_2 > 0$ and $c_0 > 0$ for $\varepsilon_\psi > 0$. For $\alpha + \beta x_T \neq 0$, the value $\varepsilon_{r_2} = -\gamma/(\alpha + \beta x_T)$ is finite and we can write

$$\varepsilon_\psi(\varepsilon_r) = a \frac{(\varepsilon_r - \varepsilon_{r_2})(\varepsilon_r - \varepsilon_{r_1})}{\varepsilon_r - \varepsilon_r^*}, \quad a = -\frac{\tilde{\alpha} + \tilde{\beta}x_T}{\alpha + \beta x_T},$$

with $\varepsilon_r^* = \varepsilon_{r_2} + (\tilde{\alpha} + \tilde{\beta}x_T)/(\alpha + \beta x_T)^2$, so that $\varepsilon_r^* > \varepsilon_{r_2}$. The sign of a is that of $\alpha + \beta x_T$ since we only consider $x_T < -\tilde{\alpha}/\tilde{\beta}$. Notably, the graph consists of one convex and one concave branch, and at least one intersects $\varepsilon_\psi = 0$ at $\varepsilon_r = \varepsilon_{r_1} > 0$. On the one hand, we directly compute

$$\partial_{\varepsilon_r}\varepsilon_\psi(\varepsilon_{r_1}) = a \frac{(\varepsilon_{r_1} - \varepsilon_{r_2})(\varepsilon_{r_1} - \varepsilon_r^*)}{(\varepsilon_{r_1} - \varepsilon_r^*)^2},$$

which has the sign of $-(\alpha + \beta x_T)(\varepsilon_{r_1} - \varepsilon_{r_2})(\varepsilon_{r_1} - \varepsilon_r^*)$. On the other hand, via $F := c_1c_2 - c_0 = 0$, which defines $\varepsilon_\psi(\varepsilon_r)$, we have $\partial_{\varepsilon_r}\varepsilon_\psi(\varepsilon_r) = -\frac{\partial_{\varepsilon_r}F}{\partial_{\varepsilon_\psi}F}$, and $\varepsilon_r = \varepsilon_{r_2}$ gives $\partial_{\varepsilon_r}F = (\partial_{\varepsilon_r}c_2)c_1$, with $\partial_{\varepsilon_r}c_2 = \alpha + \beta x_T$, and $\partial_{\varepsilon_\psi}F = -\partial_{\varepsilon_\psi}c_0 = -(\tilde{\alpha} + \tilde{\beta}x_T)$. Since $\tilde{\alpha} + \tilde{\beta}x_T > 0$, we have

$$\text{sgn}(\partial_{\varepsilon_r}\varepsilon_\psi(\varepsilon_{r_2})) = \text{sgn}((\alpha + \beta x_T)c_1).$$

Due to the conditions $\varepsilon_{r_1} > 0$ and $\varepsilon_{r_2} < \varepsilon_r^*$ from above, we have six possible orderings of $\varepsilon_{r_1}, \varepsilon_{r_2}, \varepsilon_r^*$ and $\varepsilon_r = 0$ which we present below. In addition, we discuss the relation of these cases to the value of x_T . For that, we define $x_{T_0} = (\gamma\alpha - \tilde{\alpha})/(\tilde{\beta} - \gamma\beta)$, which solves $\varepsilon_r^*(x_{T_0}) = 0$, and x_{T_-}, x_{T_+} as the roots of $\varepsilon_r^* - \varepsilon_{r_1}$, where $x_{T_-} < x_{T_+}$. From the sign conditions, we note that $\delta\alpha - \gamma\tilde{\alpha} < 0$ and $\gamma\tilde{\beta} - \delta\beta < 0$. Furthermore, it turns out that relevant is the sign of $\alpha/\beta - \tilde{\alpha}/\tilde{\beta}$. We first consider $-\alpha/\beta < -\tilde{\alpha}/\tilde{\beta}$, in which $\varepsilon_{r_1}(x_{T_s}) = \varepsilon_{r_2}(x_{T_s}) > 0$; see Figure 4.5 for the HTC values. Here $x_{T_0} < x_{T_-} < x_{T_s} < x_{T_+}$ applies. Indeed, since ε_r^* vanishes for a unique x_{T_0} , left and right of this point the function is negative and positive, respectively, and $\varepsilon_{r_1} > 0$ is monotone increasing, so that $x_{T_0} < x_{T_-}$ holds. Note that $\forall x_T < -\tilde{\alpha}/\tilde{\beta}$, we have $\varepsilon_r^* > \varepsilon_{r_2}$, and therefore $x_{T_s} < x_{T_+}$. Finally, again since $\varepsilon_{r_1} > 0$ is monotone increasing, $x_{T_-} < x_{T_s}$ holds.

Case (1). $\varepsilon_{r_2} < \varepsilon_r^* < 0 < \varepsilon_{r_1}$ (which occurs in the HTC). Here $\partial_{\varepsilon_r}\varepsilon_\psi(\varepsilon_{r_1}) < 0$ and the graph of $\varepsilon_\psi(\varepsilon_r) \geq 0$ connects the ε_r and ε_ψ -axes, is strictly decreasing and forms the stability boundary as in Figure 4.3. This case is equivalent to $x_T < x_{T_0}$ if $\tilde{\beta} > \gamma\beta$, or $x_T > x_{T_0}$ if $\tilde{\beta} < \gamma\beta$, since then $\varepsilon_r^* < 0$. However, as for the HTC values, we assume $\tilde{\beta} > \gamma\beta$ and thus this case corresponds to $x_T < x_{T_0}$.

Case (2). $\varepsilon_{r_2} < 0 \leq \varepsilon_r^* < \varepsilon_{r_1}$. Here $\partial_{\varepsilon_r}\varepsilon_\psi(\varepsilon_{r_1}) < 0$ and again the graph of $\varepsilon_\psi(\varepsilon_r) \geq 0$ is strictly decreasing and forms the stability boundary, but it no longer connects to the ε_ψ -axis. More precisely, ε_r^* is the lower bound for the stability threshold ε_r at any given $\varepsilon_\psi > 0$. The

situation is as in Figure 4.6 (a). Regarding x_T we consider, as before, $\tilde{\beta} > \gamma\beta$, and we then require $x_T \leq (\gamma\alpha - \tilde{\alpha})/(\tilde{\beta} - \gamma\beta)$ for $\varepsilon_r^* \geq 0$. Furthermore, $\varepsilon_r^* < \varepsilon_{r_1}$ means $x_T \notin (x_{T_-}, x_{T_+})$ and hence, in this case, $x_T \in (x_{T_0}, x_{T_-})$.

Case (3). $\varepsilon_{r_2} < 0 < \varepsilon_{r_1} < \varepsilon_r^*$. Here $\partial_{\varepsilon_r} \varepsilon_\psi(\varepsilon_{r_1}) > 0$ and the graph of $\varepsilon_\psi(\varepsilon_r) \geq 0$ is now strictly increasing; it still forms the stability boundary without connecting to the ε_ψ -axis as in Figure 4.6 (c). Here ε_r^* is an upper bound for the stability threshold ε_r at any given $\varepsilon_\psi > 0$. As for the previous cases, we have $x_T < -\alpha/\beta$ such that $\varepsilon_{r_2} < 0$. Moreover, $x_T \in (x_{T_-}, x_{T_+})$ for $\varepsilon_{r_1} < \varepsilon_r^*$. Thus, $x_T \in (x_{T_-}, -\alpha/\beta)$. Notice that at $\varepsilon_r = \varepsilon_{r_1} = \varepsilon_r^*$, i.e., at $x_T = x_{T_-}$, the graph of the function $\varepsilon_\psi(\varepsilon_r)$ degenerates to the union of a vertical and a non-vertical line; cf. Figure 4.6 (b,c).

Case (4). $0 < \varepsilon_{r_1} < \varepsilon_{r_2} < \varepsilon_r^*$. Here $\partial_{\varepsilon_r} \varepsilon_\psi(\varepsilon_{r_1}) > 0 > \partial_{\varepsilon_r} \varepsilon_\psi(\varepsilon_{r_2})$, the graph of $\varepsilon_\psi(\varepsilon_r) \geq 0$ is strictly increasing near ε_{r_1} with a local maximum below ε_{r_2} , and this part forms the stability boundary to a bounded stable region since $c_2 > 0$ between both roots; see Figure 4.4 (c). In terms of x_T , this case is translated into $x_T \in (-\alpha/\beta, x_{T_s})$. The transition between case 3 and 4 occurs at $x_T = -\alpha/\beta$, where we have confirmed controllability in this situation above.

The remaining two cases have $x_T \geq x_{T_s}$ and correspond to fully uncontrollable situations.

Case (5). $0 < \varepsilon_{r_2} < \varepsilon_{r_1} < \varepsilon_r^*$. Here $\partial_{\varepsilon_r} \varepsilon_\psi(\varepsilon_{r_1}) < 0 < \partial_{\varepsilon_r} \varepsilon_\psi(\varepsilon_{r_2})$, the graph of $\varepsilon_\psi(\varepsilon_r) \geq 0$ is strictly increasing near ε_{r_2} with a local maximum below ε_{r_1} , but it does not form a stability boundary since $c_2 < 0$ for $\varepsilon_r > \varepsilon_{r_2}$. This situation happens for $x_T \in (x_{T_s}, x_{T_+})$. The transition between case 4 and 5 takes place at $x_T = x_{T_s}$, which yields $\varepsilon_{r_1} = \varepsilon_{r_2}$ and thus $\partial_{\varepsilon_r} \varepsilon_\psi(\varepsilon_{r_1}) = 0$. The graph is negative or concave and therefore no control is possible; see Figure 4.4 (b).

Case (6). $0 < \varepsilon_{r_2} < \varepsilon_r^* < \varepsilon_{r_1}$. Here $\partial_{\varepsilon_r} \varepsilon_\psi(\varepsilon_{r_1}) > 0$ and the graph of $\varepsilon_\psi(\varepsilon_r) \geq 0$ is strictly increasing, but no longer forms a stability boundary since $c_2 < 0$ in the region where $\varepsilon_\psi(\varepsilon_r) > 0$; see Figure 4.4 (a). It is easy to see that this case is equivalent to $x_T \in (x_{T_+}, -\tilde{\alpha}/\tilde{\beta})$. For $\varepsilon_r = \varepsilon_{r_1} = \varepsilon_r^*$, i.e., at $x_T = x_{T_+}$, again the graph of the function $\varepsilon_\psi(\varepsilon_r)$ degenerates to the union of a vertical line in the region where $c_2 < 0$, and a line with positive slope and root at $c_2 = 0$.

Now we consider the second situation, $-\tilde{\alpha}/\tilde{\beta} < -\alpha/\beta$, where $\varepsilon_{r_1}(x_{T_s}) = \varepsilon_{r_2}(x_{T_s}) < 0$. The scenario is analogous to the previous cases 1 to 3 when accounting for the reversed ordering $x_{T_-} < x_{T_0} < x_{T_+} < x_{T_s}$. Indeed, case 1 happens for $x_T \in (x_{T_0}, -\tilde{\alpha}/\tilde{\beta})$, case 2 for $x_T \in (x_{T_-}, x_{T_0})$, and case 3 for $x_T < x_{T_-}$. Notice that controllability requires $\varepsilon_{r_1} > 0$, which happens only for $x_T < -\tilde{\alpha}/\tilde{\beta}$, and then $\varepsilon_{r_2} < 0$. Therefore, the straight motion is fully uncontrollable for $x_T > -\tilde{\alpha}/\tilde{\beta}$ and cases 4 to 6 do not occur. \square

From this result, we observe that, on the one hand, in the case $-\alpha/\beta < x_{T_s} < -\tilde{\alpha}/\tilde{\beta}$, which happens in the HTC, for small values of x_T (close to the aft of the ship), the first intersection point of the stability boundary curve with the positive ε_r -axis is also “small”. On the contrary, for larger x_T , we have $\varepsilon_\psi(\varepsilon_r) = 0$ for larger (first intersection point) $\varepsilon_r > 0$, until reaching a threshold x_{T_s} in which stabilization is not possible anymore by the P-control (4.6). Therefore, the smaller the value of x_T , the easier the stabilization is, in the sense that one needs

less control strength ε_r to achieve that. On the other hand, in the case $-\tilde{\alpha}/\tilde{\beta} < x_{T_s} < -\alpha/\beta$, we also have a threshold for which increasing x_T , the stabilization of the straight motion is impossible, namely, for $x_T > -\tilde{\alpha}/\tilde{\beta}$. However, stabilizing this equilibrium, by the P-control considered here, is not easier the closer the thruster is to the aft, as occurs for the HTC, though we do not know whether this case can be realized in an actual ship.

With this last theorem, the study of linear stability is completed and now we move to the nonlinear analysis.

4.2.3 Nonlinear stability and bifurcation analysis

Here we analyze the nonlinear effects of the stabilizing control based on the linear stability analysis of the previous section. In order to facilitate the bifurcation analysis, we first shift the straight motion equilibrium state $(u_0, 0, 0, 0)$ of (4.8) to the origin by writing the surge variable as $u = u_0 + \tilde{u}$, where \tilde{u} is a perturbation of the location of the fixed point. In terms of (\tilde{u}, v, r, ψ) we thus obtain

$$\begin{pmatrix} \dot{\tilde{u}} \\ \dot{v} \\ \dot{r} \\ \dot{\psi} \end{pmatrix} = M^{-1} \begin{pmatrix} m_L v r + X_H(\tilde{u}) + \tilde{\tau}(\tilde{u}) \cos \eta \\ -m_L(u_0 + \tilde{u})r + Y_H(\tilde{u}) + \tilde{\tau}(\tilde{u}) \sin \eta \\ N_H(\tilde{u}) + x_T \tilde{\tau}(\tilde{u}) \sin \eta \\ r \end{pmatrix}, \quad (4.16)$$

where $\tilde{\tau}(\tilde{u}) := \tau(u_0 + \tilde{u})$. In the following we omit the tilde from \tilde{u} to simplify the notation. We rewrite and expand the previous system in u , showing the cubic and higher order terms for completeness, which give

$$\begin{pmatrix} \dot{u} \\ \dot{v} \\ \dot{r} \\ \dot{\psi} \end{pmatrix} = \begin{pmatrix} \tau_{11}(\cos \eta - 1) + k_1 u + k_2 u^2 + k_3 v r + [\tau_{12} u + \tau_{13} u^2] \cos \eta \\ p_{22} v + k_5 r + k_6 u v + k_7 u r + f_1(v, r) + [\tau_{21} + \tau_{22} u + \tau_{23} u^2] \sin \eta \\ p_{32} v + k_9 r + k_{10} u v + k_{11} u r + f_2(v, r) + [\tau_{31} + \tau_{32} u + \tau_{33} u^2] \sin \eta \\ r \end{pmatrix} \quad (4.17)$$

$$+ \begin{pmatrix} 0 \\ f_c(v, r) + k_{a1} u v |v| + k_{a2} u r |r| + k_{a3} u^2 v |v| + k_{a4} u^3 v |v| + k_{a5} v^2 |v| + k_{a6} u v^2 |v| \\ g_c(v, r) + k_{b1} u v |v| + k_{b2} u r |r| + k_{b3} u^2 v |v| + k_{b4} u^3 v |v| + k_{b5} v^2 |v| + k_{b6} u v^2 |v| \\ 0 \end{pmatrix},$$

where τ_{ij} are the coefficients resulting from the expansion and

$$\begin{aligned} f_1(v, r) &= a_{11} v |v| + a_{12} v |r| + a_{21} r |v| + a_{22} r |r|, \\ f_2(v, r) &= b_{11} v |v| + b_{12} v |r| + b_{21} r |v| + b_{22} r |r|, \\ f_c(v, r) &= c_{a2} v r^2 + c_{a3} v^2 r, \quad g_c(v, r) = c_{b2} v r^2 + c_{b3} v^2 r. \end{aligned}$$

We omit the explicit expressions of the coefficients except for a_{ij}, b_{ij} in f_1, f_2 , which are going to be relevant:

$$\begin{aligned}
a_{11} &= D^{-1} \left((I_z + m_{rr})Y_{\beta|\beta|} - m_{vr}N_{\beta|\beta|} \right), & a_{12} &= D^{-1}(I_z + m_{rr})Y_{\beta|\gamma|}, \\
a_{21} &= D^{-1}(I_z + m_{rr})Y_{\beta|\gamma|}, & a_{22} &= D^{-1} \left((I_z + m_{rr})Y_{\gamma|\gamma|} - m_{vr}N_{\gamma|\gamma|} \right), \\
b_{11} &= D^{-1} \left((m + m_{vv})N_{\beta|\beta|} - m_{rv}Y_{\beta|\beta|} \right), & b_{12} &= -D^{-1}m_{rv}Y_{\beta|\gamma|}, \\
b_{21} &= -D^{-1}m_{rv}Y_{\beta|\gamma|}, & b_{22} &= D^{-1} \left((m + m_{vv})N_{\gamma|\gamma|} - m_{rv}Y_{\gamma|\gamma|} \right).
\end{aligned}$$

Using again that our analysis focuses on the vicinity of the origin, we expand the functions $\cos \eta = 1 + \mathcal{O}(\eta^2)$, $\sin \eta = \eta + \mathcal{O}(\eta^3)$ and, based on the results in Chapter 2, we omit all cubic and higher order terms. Employing also the control form $\eta = \varepsilon_r r + \varepsilon_\psi \psi$ from (4.6), this reduces (4.17) to

$$\begin{pmatrix} \dot{u} \\ \dot{v} \\ \dot{r} \\ \dot{\psi} \end{pmatrix} = \begin{pmatrix} p_{11}u + U(u, v, r) \\ p_{22}v + p_{23}r + p_{24}\psi + k_6uv + (k_7 + \tau_{22}\varepsilon_r)ur + \tau_{22}\varepsilon_\psi u\psi + f_1(v, r) \\ p_{32}v + p_{33}r + p_{34}\psi + k_{10}uv + (k_{11} + \tau_{32}\varepsilon_r)ur + \tau_{32}\varepsilon_\psi u\psi + f_2(v, r) \\ r \end{pmatrix}, \quad (4.18)$$

where $U(u, v, r)$ is a second order nonlinear function. In agreement with §4.2.2, the coefficients $p_{11} = k_1 + \tau_{12}$, $p_{23} = k_5 + \tau_{21}\varepsilon_r$, $p_{24} = \tau_{21}\varepsilon_\psi$, $p_{33} = k_9 + \tau_{31}\varepsilon_r$, $p_{34} = \tau_{31}\varepsilon_\psi$ are the entries of the matrix A from (4.11). These p_{ij} are exactly the same as before since we have moved the fixed point to the origin and expanded the function τ .

As a first step towards the nonlinear analysis, we discuss the simpler case of the pitchfork bifurcation, and then turn to the more involved Hopf bifurcation analysis.

4.2.3.1 Pitchfork bifurcation for $\varepsilon_\psi = 0$

We keep $\varepsilon_\psi = 0$ fixed so that the last equation in (4.18) can be dropped since the coefficients p_{24}, p_{34} as well as the terms with $u\psi$ vanish. The linearization in the steady forward motion gives then the matrix A from (4.11) reduced to the upper left 3×3 matrix, with block diagonal structure and hence, an eigenvalue $p_{11} \neq 0$ for the HTC values. The remaining 2×2 block, which we call B , i.e.,

$$B := \begin{pmatrix} p_{22} & p_{23} \\ p_{32} & p_{33} \end{pmatrix} = \begin{pmatrix} p_{22u}u_0 & p_{23u}u_0 + q_{23}\tau(u_0)\varepsilon_r \\ p_{32u}u_0 & p_{33u}u_0 + q_{33}\tau(u_0)\varepsilon_r \end{pmatrix},$$

has determinant that is linear in ε_r and vanishes at the unique positive value ε_{r_1} from (4.13), as in the proof of Theorem 4.1, where ε_{r_1} is the root of c_1 . Notice that here, for $\varepsilon_\psi = 0$, we have $\det(B) = c_1$. We readily find numerically that for the HTC values, $B_0 := B|_{\varepsilon_r = \varepsilon_{r_1}}$ has eigenvectors e_0 for the eigenvalue zero, and e_1 for the nonzero eigenvalue λ . This means that the bifurcation upon changing ε_r will be purely of equilibria states and we thus seek solutions of the reduced (4.18) with zero left-hand side. Since f_1, f_2 are quadratic of second order modulus type, we expect a nonsmooth pitchfork bifurcation as in the truncated normal form $\tilde{\varepsilon}_r x + \sigma x|x| = 0$. Here the sign of $\sigma \neq 0$ determines the super- or subcritical character of the bifurcation (cf. (1.11)) with parameter $\tilde{\varepsilon}_r = g(\varepsilon_r)$, where g is a local bijection.

The first steady state equation of the reduced (4.18),

$$\begin{pmatrix} \dot{u} \\ \dot{v} \\ \dot{r} \end{pmatrix} = \begin{pmatrix} p_{11}u + U(u, v, r) \\ p_{22}v + p_{23}r + k_6uv + (k_7 + \tau_{22}\varepsilon_r)ur + f_1(v, r) \\ p_{32}v + p_{33}r + k_{10}uv + (k_{11} + \tau_{32}\varepsilon_r)ur + f_2(v, r) \end{pmatrix}, \quad (4.19)$$

can be solved for u by the implicit function theorem since $p_{11} \neq 0$ and U is nonlinear; the resulting solution satisfies $u = \mathcal{O}(v^2 + r^2)$ so that substitution into the second and third equations contributes a term of cubic order.

We write $\varepsilon_r = \varepsilon_{r_1} + \tilde{\varepsilon}_r$ and $B = B_0 + \tilde{\varepsilon}_r B_1$,

$$B = \begin{pmatrix} p_{22u}u_0 & p_{23u}u_0 + q_{23}\tau(u_0)\varepsilon_{r_1} \\ p_{32u}u_0 & p_{33u}u_0 + q_{33}\tau(u_0)\varepsilon_{r_1} \end{pmatrix} + \tilde{\varepsilon}_r \begin{pmatrix} 0 & q_{23}\tau(u_0) \\ 0 & q_{33}\tau(u_0) \end{pmatrix},$$

and choose the eigenvectors e_j^* of the adjoint B_0^\top so that $\langle e_j, e_{1-j}^* \rangle = 0$ and $\langle e_j, e_j^* \rangle = 1$, $j = 0, 1$. Changing coordinates $(v, r)^\top = xe_0 + ye_1$ and defining $f(v, r) = (f_1(v, r), f_2(v, r))^\top$, we project the second and third equations of (4.19) onto $\text{span}(e_1)$, which results in

$$\begin{aligned} 0 &= \langle B(v, r)^\top, e_1^* \rangle + \langle (f_1(v, r), f_2(v, r))^\top, e_1^* \rangle \\ &= \langle (B_0 + \tilde{\varepsilon}_r B_1)(xe_0 + ye_1), e_1^* \rangle + \langle f(v, r), e_1^* \rangle \\ &= y \langle B_0 e_1, e_1^* \rangle + \langle \tilde{\varepsilon}_r B_1(xe_0 + ye_1), e_1^* \rangle + \langle f(v, r), e_1^* \rangle \\ &= \lambda y + \tilde{\varepsilon}_r (x \langle B_1 e_0, e_1^* \rangle + y \langle B_1 e_1, e_1^* \rangle) + \langle f(v, r), e_1^* \rangle. \end{aligned}$$

Once more, we may solve this equation by the implicit function theorem since $\lambda \neq 0$, yielding $y = y(x, \tilde{\varepsilon}_r) = \mathcal{O}(|\tilde{\varepsilon}_r x| + x^2)$. It remains to solve the projection onto $\text{span}(e_0)$, which is given by

$$\begin{aligned} 0 &= \langle (B_0 + \tilde{\varepsilon}_r B_1)(xe_0 + ye_1), e_0^* \rangle + \langle f(v, r), e_0^* \rangle \\ &= \tilde{\varepsilon}_r (x \langle B_1 e_0, e_0^* \rangle + y \langle \tilde{\varepsilon}_r, x \rangle \langle B_1 e_1, e_0^* \rangle) + \langle f(v, r), e_0^* \rangle \\ &= \tilde{\varepsilon}_r x \langle B_1 e_0, e_0^* \rangle + x|x| \langle f(e_0), e_0^* \rangle + \mathcal{O}(3), \end{aligned}$$

where $\mathcal{O}(3)$ is of cubic order in $x, \tilde{\varepsilon}_r$, and we used that the function f is of second order modulus form. Thus, the truncated bifurcation equation reads

$$\tilde{\varepsilon}_r x \langle B_1 e_0, e_0^* \rangle + x|x| \langle f(e_0), e_0^* \rangle = 0,$$

which is indeed of the expected form. Numerical evaluation for the HTC values gives negative coefficients

$$\begin{aligned} \langle B_1 e_0, e_0^* \rangle &\approx -4.04 \cdot 10^{-2}, \\ \langle f(e_0), e_0^* \rangle &\approx -1.32 \cdot 10^{-3}. \end{aligned}$$

Therefore, a nonsmooth pitchfork bifurcation occurs and it is supercritical since the steady state is stable for $\tilde{\varepsilon}_r > 0$. This means that a branch of equilibrium motions emerges when

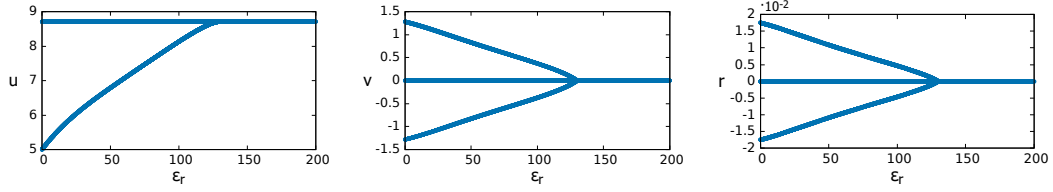


FIGURE 4.7: Different views of the nonsmooth supercritical pitchfork bifurcation diagram of equilibrium points in the 3D reduced system for $\varepsilon_\psi = 0$ computed by numerical continuation. The dimensions correspond to $[u] = [v] = \text{m/s}$, $[r] = \text{rad/s}$, $[\varepsilon_r] = \text{s}$, i.e., the unscaled model.

decreasing ε_r from ε_{r_1} . Indeed, we numerically find this as plotted in Figure 4.7.

For the full 4D system (4.18) we remark that the pitchfork bifurcation manifests itself in a non-standard way. Firstly, for any $\varepsilon_r, \varepsilon_\psi$, the straight motion always appears as the equilibrium point with $v = r = \psi = 0$, and $u = u_0$ solving (4.9). Secondly, for $\varepsilon_\psi = 0$ the system is independent of ψ , which induces a line of equilibria in the phase space given by $v = r = 0$, $u = u_0$ and arbitrary ψ . Indeed, the pitchfork bifurcation discussed above appears in the 4D system as follows: let r_0 be the r -component of one of the bifurcated equilibria, then the ψ -component of the resulting solution ψ_0 in the 4D system is $\psi_0(t) = r_0 t + \psi_0(0)$, which is in particular unbounded in the angular variable ψ . In addition, at $\varepsilon_\psi = 0$ the 4×4 linearization A from (4.11) possesses a zero eigenvalue for any ε_r , which is double at ε_{r_1} with a 2×2 Jordan block, as well as two nonzero real eigenvalues. This is similar to a Bogdanov–Takens bifurcation with symmetry, e.g., [8]; see also Chapter 3. Hence, we expect the unfolding beyond the pitchfork to contain additional elements of a symmetric BT bifurcation, including various heteroclinic orbits. However, a rigorous analysis is beyond the scope of this thesis since the situation is degenerate owing to the occurrence of a line of equilibria and the nonsmooth nonlinearity, which already makes the Hopf bifurcation analysis more involved as discussed subsequently.

4.2.3.2 Hopf bifurcation

We have shown in §4.2.2 that, for any pair of control parameters $(\varepsilon_r, \varepsilon_\psi)$ with $\varepsilon_r \geq 0$, $\varepsilon_\psi > 0$ on the stability boundary, satisfying (4.13), the eigenvalues of the linearization at the equilibrium point $(u, v, r, \psi) = (u_0, 0, 0, 0)$ possess one complex conjugate pair with nonzero imaginary part, and the two other eigenvalues are real and negative. Therefore, for any such $(\varepsilon_r, \varepsilon_\psi)$, the linear part of (4.18) can be transformed into

$$\begin{pmatrix} \lambda_1 & 0 & 0 & 0 \\ 0 & \mu & -\omega & 0 \\ 0 & \omega & \mu & 0 \\ 0 & 0 & 0 & \lambda_4 \end{pmatrix},$$

where $\mu \in \mathbb{R}$, $\omega > 0$ and the eigenvalues are $\lambda_1, \lambda_4 < 0$ and $\lambda_\pm = \mu \pm i\omega$. Note that from (4.18) we have $\lambda_1 = p_{11}$.

In the following, we perform the coordinate changes and identification of terms that allow to apply the theory from Chapter 2. This will then justify to neglect the terms we drop in the coming steps. In particular, since $\lambda_1 \neq 0$ the results from §2.3 imply that we can neglect the first equation of (4.18) for our bifurcation analysis. Hence, we next analyze the lower right 3×3 matrix (v, r, ψ) , which contains the linearly oscillating part and the coupled equation $\dot{\psi} = r$. Moreover, we define the matrix $\mathbf{T} = (\mathbf{a}|\mathbf{b}|\mathbf{s})$ with columns $\mathbf{a}, \mathbf{b}, \mathbf{s} \in \mathbb{R}^3$ coming from the eigenvectors $\zeta_+ = \mathbf{a} + i\mathbf{b}$, $\zeta_- = \mathbf{a} - i\mathbf{b}$, \mathbf{s} , of the eigenvalues $\mu + i\omega$, $\mu - i\omega$, λ_4 , respectively. Notably, $\mu = 0$ along the curve $\varepsilon_\psi(\varepsilon_r)$.

Setting $\xi := (\xi_1, \xi_2, \xi_3)^\top = \mathbf{T}^{-1}(v, r, \psi)^\top$, the (v, r, ψ) -subsystem of (4.18) takes the form

$$\begin{pmatrix} \dot{\xi}_1 \\ \dot{\xi}_2 \\ \dot{\xi}_3 \end{pmatrix} = \begin{pmatrix} \mu & -\omega & 0 \\ \omega & \mu & 0 \\ 0 & 0 & \lambda_4 \end{pmatrix} \begin{pmatrix} \xi_1 \\ \xi_2 \\ \xi_3 \end{pmatrix} + h_2(\xi) + \mathcal{R}, \quad (4.20)$$

where $h_2(\xi)$ contains all relevant quadratic order terms. These have the form

$$h_2(\xi) = \mathbf{T}^{-1} \begin{pmatrix} f_1(\mathbf{T} \cdot \xi) \\ f_2(\mathbf{T} \cdot \xi) \\ 0 \end{pmatrix} = \begin{pmatrix} Z_{11} & Z_{12} & Z_{13} \\ Z_{21} & Z_{22} & Z_{23} \\ Z_{31} & Z_{32} & Z_{33} \end{pmatrix} \begin{pmatrix} g_1(\xi) \\ g_2(\xi) \\ 0 \end{pmatrix} = \begin{pmatrix} Z_{11}g_1(\xi) + Z_{12}g_2(\xi) \\ Z_{21}g_1(\xi) + Z_{22}g_2(\xi) \\ Z_{31}g_1(\xi) + Z_{32}g_2(\xi) \end{pmatrix},$$

with quadratic order functions g_1, g_2 discussed below, and the coefficients

$$\begin{aligned} Z_{11} &= \frac{b_2 s_3 - b_3 s_2}{\det(\mathbf{T})}, & Z_{12} &= \frac{-b_1 s_3 + b_3 s_1}{\det(\mathbf{T})}, \\ Z_{21} &= \frac{-a_2 s_3 + a_3 s_2}{\det(\mathbf{T})}, & Z_{22} &= \frac{a_1 s_3 - a_3 s_1}{\det(\mathbf{T})}, \end{aligned}$$

where $a_j, b_j, s_j, j \in \{1, 2, 3\}$ are the components of the vectors $\mathbf{a}, \mathbf{b}, \mathbf{s}$, respectively.

All remainder terms are collected in \mathcal{R} , including the nonlinear terms involving u , i.e., $uv, ur, u\psi$, from (4.18), which turn out to be irrelevant to leading order due to §2.1, §2.3. Furthermore, Theorem 2.3 implies that the third component of the transformed system (4.20), ξ_3 , will belong to higher order terms (perturbation) as well. With these preparations, and using the shorthand $[[\cdot]] := \cdot |\cdot|$ for the second order modulus terms, the relevant functions g_1, g_2 are

$$\begin{aligned} g_1(\xi_1, \xi_2) &= a_{11}[[a_1 \xi_1 + b_1 \xi_2]] + a_{12}(a_1 \xi_1 + b_1 \xi_2)|a_2 \xi_1 + b_2 \xi_2| \\ &\quad + a_{21}(a_2 \xi_1 + b_2 \xi_2)|a_1 \xi_1 + b_1 \xi_2| + a_{22}[[a_2 \xi_1 + b_2 \xi_2]], \\ g_2(\xi_1, \xi_2) &= b_{11}[[a_1 \xi_1 + b_1 \xi_2]] + b_{12}(a_1 \xi_1 + b_1 \xi_2)|a_2 \xi_1 + b_2 \xi_2| \\ &\quad + b_{21}(a_2 \xi_1 + b_2 \xi_2)|a_1 \xi_1 + b_1 \xi_2| + b_{22}[[a_2 \xi_1 + b_2 \xi_2]]. \end{aligned}$$

The leading order part of (4.20) has the equation for $\dot{\xi}_3$ decoupled from the others, such that only the first two equations in (4.20) remain of interest. Using polar coordinates

$(\xi_1, \xi_2) = (r \cos \varphi, r \sin \varphi)$, these become

$$\begin{cases} \dot{r} = \mu r + \chi(\varphi)r^2 + \mathcal{O}(r^3), \\ \dot{\varphi} = \omega + \Omega(\varphi)r + \mathcal{O}(r^2), \end{cases} \quad (4.21)$$

where

$$\begin{aligned} \chi(\varphi) = & (a_{11}\Lambda + b_{11}\Gamma)[a_1c + b_1s] + (a_{12}\Lambda + b_{12}\Gamma)(a_1c + b_1s)|a_2c + b_2s| \\ & + (a_{21}\Lambda + b_{21}\Gamma)(a_2c + b_2s)|a_1c + b_1s| + (a_{22}\Lambda + b_{22}\Gamma)[a_2c + b_2s], \end{aligned} \quad (4.22)$$

with $c := \cos \varphi$, $s := \sin \varphi$ and $\Lambda := cZ_{11} + sZ_{21}$, $\Gamma := cZ_{12} + sZ_{22}$ to simplify the notation. More specifically, we use cylindrical coordinates and then apply Theorem 2.3 in order to obtain (4.21).

As an aside before continuing with this analysis, we point out that for the variables of a ship model, the yaw velocity is represented by the symbol r , as we have used during this chapter. However, this letter has not to be mistaken with the radial component of the system in polar coordinates, which we are using now.

Prior to formulating the bifurcation theorem, we recall the two generic forms of a Hopf bifurcation: in the supercritical (or safe) case the stable fixed point changes stability when the stable limit cycle is created, while in the subcritical (or unsafe) scenario the unstable fixed point becomes stable when an unstable limit cycle is born.

Theorem 4.3. *For the rescaled thruster model (4.7) in the HTC, and considering $\varepsilon_\psi > 0$, the system undergoes a Hopf bifurcation for the control values (4.13), which is supercritical if $\int_0^{2\pi} \chi(\varphi)d\varphi < 0$ and subcritical for positive sign. Furthermore, the amplitude of the periodic orbit is given by*

$$r = \frac{-2\pi}{\int_0^{2\pi} \chi(\varphi)d\varphi} \mu + \mathcal{O}(\mu^2).$$

Proof. We recall from Theorem 4.1 that a complex conjugate pair of eigenvalues crosses the imaginary axis for $(\varepsilon_r, \varepsilon_\psi)$ crossing the values of (4.13). Therefore, the equivalent system (4.18) is amenable to Corollary 2.26. In particular, the non-oscillatory linear part is invertible since $\lambda_1, \lambda_4 < 0$ on the stability boundary by Theorem 4.1. Due to Corollary 2.26, the criticality of the Hopf bifurcation is that of (4.21), and determined by the sign of $\int_0^{2\pi} \chi(\varphi)d\varphi$. Finally, the claimed leading order amplitude of the bifurcating periodic orbits follows directly from Proposition 2.15. \square

This result reduces the problem of determining the criticality of the Hopf bifurcation, i.e., the safety of the stabilizing control, to computing the sign of

$$\Sigma := \int_0^{2\pi} \chi(\varphi)d\varphi.$$

We remark that Σ from (2.74) is the same up to the natural positive factor $2\pi\omega$. However, even with the formula (4.22), and despite the fact that all terms in χ can be explicitly integrated,

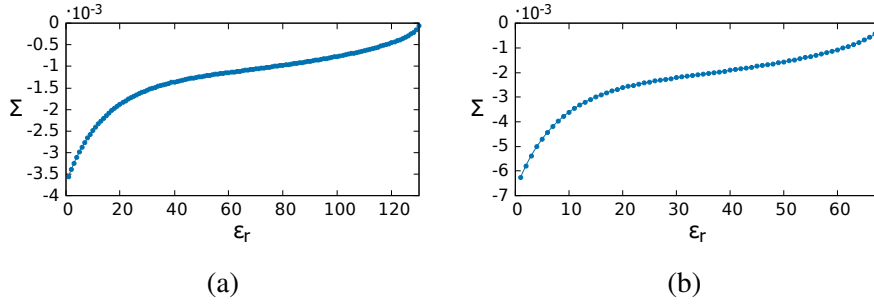


FIGURE 4.8: Values of Σ for (a) $\varepsilon_r \in \{1, 2, \dots, 130\}$ for the HTC values, and (b) $\varepsilon_r \in \{1, 2, \dots, 68\}$ with $D_p = 9.1575$. These two situations correspond to case 1 in Figure 4.1.

it appears difficult to determine the sign of Σ analytically since the eigenvectors enter non-trivially. For illustration, two of the terms that arise in Σ for $(\varepsilon_r, \varepsilon_\psi) = (0, \varepsilon_\psi(0))$ from (4.13) are given by

$$\int_0^{2\pi} a_{11}\Lambda[[a_1c + b_1s]]d\varphi = \frac{8\sqrt{a_1^2 + b_1^2}}{3}a_{11}(Z_{11}a_1 + Z_{12}b_1),$$

$$\int_0^{2\pi} a_{12}\Lambda(a_1c + b_1s)|a_2c + b_2s|d\varphi = \frac{4}{3\sqrt{a_2^2 + b_2^2}}a_{12}\left(Z_{11}(a_1(2a_2^2 + b_2^2) + a_2b_1b_2) + Z_{12}(b_1(2b_2^2 + a_2^2) + a_1a_2b_2)\right).$$

Computing the sign of Σ requires summing up terms of this form so that we generally need details on each of these, which requires knowing all entries of the matrix \mathbf{T} , i.e., the eigenvectors.

Nevertheless, numerical evaluation of all these quantities and thus of Σ is highly accurate and almost instantaneous on modern computers. This makes it possible to readily predict the criticality, as well as the leading order expansion of the bifurcating periodic solutions. We next show various evaluations of Σ along the stability boundary (4.13) determined in §4.2.2. These are all negative for the values of the classical HTC, see Figure 4.8 (a). Therefore, the Hopf bifurcation appears to be supercritical for any stabilizing P-control, which means a safe control scenario.

Furthermore, and regarding the propeller diameter D_p , Σ is as well always negative for the different values that we have taken of this parameter. For instance, in Figure 4.8 (b) we plot Σ for $D_p = 1.5D_p^{\text{HTC}}$, which has the same qualitative behavior as in Figure 4.8 (a). Notice that we use the notation D_p^{HTC} to remark that this corresponds to the HTC value for the propeller diameter. In addition, we point out that here Σ is much smaller for small ε_r , where ε_ψ is relatively big, than for larger ε_r . In view of Theorem 4.3, this means that the amplitudes of the bifurcating periodic orbits grow much quicker for large ε_r . Hence, the transition from stable straight motion to the motion induced by the stable periodic orbits is much more abrupt for larger ε_r values.

Concerning the thruster position x_T , we recall from §4.2.2 that there are four cases, as shown in Figure 4.1, to stabilize the straight motion. At $x_T = -0.3$, which is case 2, control is possible for approximately $\varepsilon_r \in (21, 152.5)$; see Figure 4.6 (a). We plot the resulting

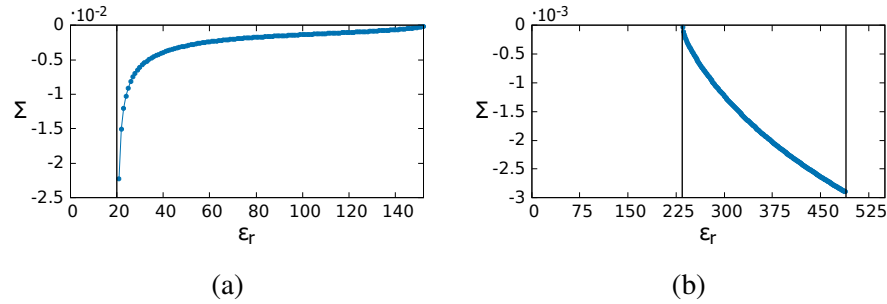


FIGURE 4.9: Values of Σ for (a) $\varepsilon_r \in \{21, 22, \dots, 152\}$ with $x_T = -0.3$, see Figure 4.1 case 2; and (b) $\varepsilon_r \in \{226, 227, \dots, 488\}$ with $x_T = 0.1$, corresponding to case 4 in Figure 4.1. The vertical lines mark in (a) the vertical asymptote and in (b) the intersections of the stability boundary with the ε_r -axis.

values of Σ in Figure 4.9 (a). For $x_T = -0.16$, which corresponds to case 3 in Figure 4.1, we numerically find a qualitatively reflected Σ graph. Further, we compute Σ for $x_T = 0.1$, which corresponds to case 4, and display the results in Figure 4.9 (b). In this last example, the interval of ε_r -values for which the straight motion is stable is bounded by the zeros of the concave branch, which are approximately $\varepsilon_r \in (225.9, 488.6)$; compare with Figure 4.4 (c), where $x_T = 0.16$. In both of these last cases, the abruptness mentioned above, regarding the transition from stable straight motion to the motion caused by the stable limit cycles, occurs for smaller ε_r , i.e., closer to the (first) intersection of the stability boundary curve with the ε_r -axis.

4.3 Numerical bifurcation analysis

In this section we present numerical results that corroborate and illustrate the analysis of the previous sections based on implementing the model in the continuation software AUTO [18]. In Figure 4.10 we plot the stability boundary for the HTC that results from such a numerical continuation, which tracks the Hopf bifurcation locus. Up to numerical error, this agrees with (4.13) plotted in Figure 4.3, based on the analytical prediction of Theorem 4.1.

In order to accordingly relate the results of the simulations with the physical implications for the ship motion, we plot the values of the unscaled model, meaning that the units of the variables are $[r] = \text{rad/s}$, $[\psi] = [\eta] = \text{rad}$. Although the radian is a dimensionless quantity, we explicitly write here that the angle variables are in radians and not in degrees. Furthermore, the control strengths correspond to the unscaled control law (4.4) as well, and thus $[\varepsilon_\psi] = -$, $[\varepsilon_r] = \text{s}$. Notice that we have not rescaled u, v , so that their dimensions are $[u] = [v] = \text{m/s}$ always.

We have employed numerical bifurcation and continuation to compute the periodic orbits that bifurcate from this stability boundary along curves in the $(\varepsilon_r, \varepsilon_\psi)$ -plane for $\varepsilon_\psi > 0$; in Figure 4.10 two such curves are plotted in violet and green. Notably, these curves lie “under” the stability boundary, which corroborates the analytically predicted supercritical nature of the Hopf bifurcations. For instance, simulations for the violet vertical line in Figure 4.10 are exhibited in Figure 4.12. Moreover, we have checked numerically that for values on

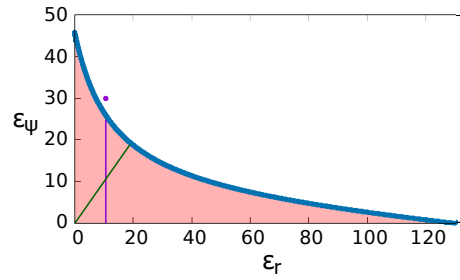


FIGURE 4.10: Stability boundary curve $\varepsilon_\psi(\varepsilon_r)$ for the HTC values in blue, separating the unstable region, which is shaded, from the stable region, in white. The existence of periodic solutions at $\varepsilon_r \approx 10.6$ is indicated by the violet vertical line, and on the near diagonal by the green line; both extend until $\varepsilon_\psi \approx 0.408$ just above heteroclinic bifurcations. The dot marks the point $(10.6, 30)$ for which time simulations are plotted in Figure 4.18.

the green line under the stability boundary, periodic orbits occur. As shown in §4.2.3.1, along the ε_r -axis, i.e., for $\varepsilon_\psi = 0$, the Hopf bifurcation turns into a pitchfork bifurcation. Specifically, for $\varepsilon_\psi = 0$, (4.18) reduces to a 3D system for u, v, r since the vector field is then independent of ψ . The numerical results plotted in Figure 4.7 illustrate the analytically predicted supercritical pitchfork bifurcation. We observe that the resulting curve of (ε_r, u) is smooth while those for (ε_r, v) , (ε_r, r) are nonsmooth, having limiting nonzero slopes at the bifurcation point.

We recall that in the 4D system (4.18), the ψ -component generated by such a fixed point is $\psi_0(t) = r_0 t + \psi_0(0)$, with r_0 the equilibrium value and $\psi_0(0)$ arbitrary. Any straight motion with $u = u_0$ has either $v_0 = r_0 = 0$ and $\psi_0 = 0$ if $\varepsilon_\psi \neq 0$, or otherwise the ψ -axis as a line of equilibria. The trajectories of the solutions that bifurcate from the pitchfork for $\varepsilon_\psi = 0$ take the form $\nu_\pm(t) = (u_0, v_\pm, r_\pm, \psi_\pm(t)) \in \mathbb{R}^4$. Here $v_\pm, r_\pm \neq 0$ are the bifurcating (constant) v, r -values, respectively, and $\psi_\pm(t) = r_\pm t + \psi_\pm(0)$.

While these solutions have unbounded ψ -component, $\varepsilon_\psi = 0$ so that the system (4.18) is independent of ψ . However, perturbing to $\varepsilon_\psi > 0$, the vector field is linear in ψ through the P-control (4.4), but the perturbed trajectories would perform full rotations in ψ . Hence, in this case the linear dependence on ψ becomes incompatible with the periodic nature of the yaw angle ψ in the ship model. Therefore, for such solutions the control law needs to be modified to be periodic in ψ . Another reason for such a modification is that we find solutions which perform full rotations can occur along branches of periodic solutions that bifurcate from Hopf points.

Thus far, this did not play a role since ψ only entered as a perturbation, and the P-control is precisely intended to be applied in this regime. Indeed, any P-control involving ψ is consistent merely for sufficiently small values of ψ . This is not relevant in practice (usually) and not for the existence and linear stability analysis of the straight motion, and not even for the local bifurcation analysis, where amplitudes are small. For definiteness, we choose to replace the linear ψ -term by a sinus function,

$$\eta = \varepsilon_r r + \varepsilon_\psi \sin(\psi),$$

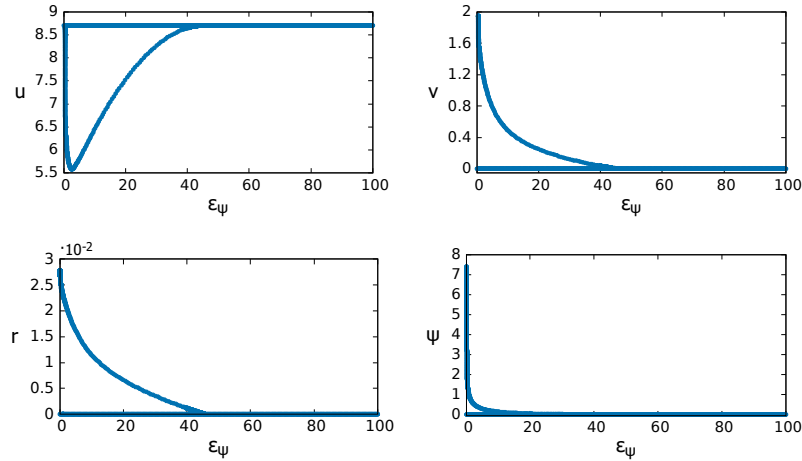


FIGURE 4.11: Different views of the nonsmooth Hopf bifurcation diagram computed by numerical continuation in the 4D system for the HTC and $\varepsilon_r = 0$. The dimensions correspond to the unscaled model: $[u] = [v] = \text{m/s}$, $[r] = \text{rad/s}$, $[\psi] = \text{rad}$, $[\varepsilon_\psi] = -$.

so that ψ replaced by ψ modulo 2π makes no difference. Being smooth and satisfying $\sin'(0) = 1$, this modification has no influence on the results so far. In particular, the stability boundary, the supercritical nature of the bifurcations and, in fact, the pitchfork branches of the 3D reduced system are identical to before. However, this choice has an impact on the solutions along curves in the $(\varepsilon_r, \varepsilon_\psi)$ -plane for $\varepsilon_\psi > 0$ further away from the stability boundary. Nevertheless, we numerically checked numerous curves and found that there is even no qualitative impact for $\varepsilon_\psi \geq 1$. Here we have chosen 1 as a relative small reference value and will discuss smaller values later. Note that instead of the sinus we could choose a function that is the identity for $|\psi|$ below some threshold, but globally smooth and periodic, which would provide results that fully coincide with the P-control as long as $|\psi|$ is below the threshold.

For the sinusoidal control law, we thus find numerically the presence of a smooth surface of periodic solutions, parameterized by the control parameter values “under” the stability boundary curve within the range $\varepsilon_r \geq 0, \varepsilon_\psi \geq 1$. We have confirmed this along a number of different axis-aligned curves, in particular including the ε_ψ -axis, for $1 \leq \varepsilon_\psi < 45.8$, which in fact shows that the surface of periodic solutions extends into negative ε_r . In Figure 4.11 we plot distinct views of the bifurcation diagram along the ε_ψ -axis; the analytical predictions are again matched by a smooth diagram for (ε_ψ, u) and nonsmooth along the center eigenspace within the (v, r, ψ) -subspace. This is completely analogous for other continuations along different curves, in particular, along the colored curves in Figure 4.10. Furthermore, in Figure 4.12 we plot some views of the profiles of the periodic solutions along the violet line in Figure 4.10, and note the growth of the ψ -range as ε_ψ decreases.

On the one hand, for decreasing values of ε_ψ , the branch appears to terminate for $\varepsilon_\psi \approx 0.408$ in a heteroclinic bifurcation, where the periodic orbit limits on a heteroclinic cycle between a pair of nearly straight motion equilibrium points and $\psi \approx \pm\pi$ rad. Note that this means the ship direction completes a circle. We show one view near this cycle in Figure 4.12 (c). On the other hand, increasing ε_ψ from zero, we observe that ν_\pm perturb to

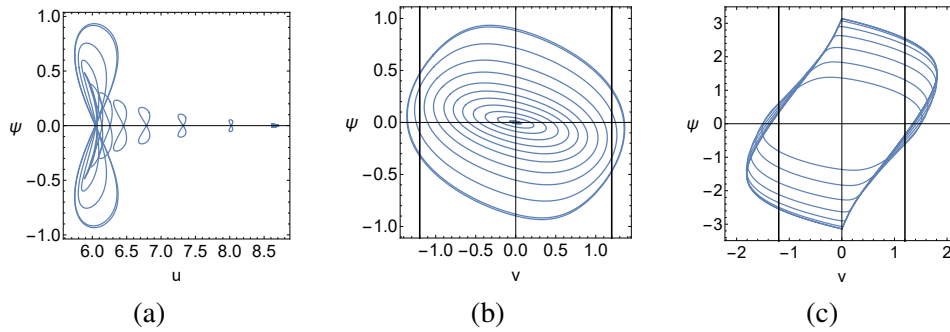


FIGURE 4.12: (a,b) Sample profiles of periodic orbits for $\varepsilon_r \approx 10.6$ fixed, and ε_ψ between 25.9 at the Hopf bifurcation and $\varepsilon_\psi = 1$ computed by numerical continuation. In (c) we plot periodic solutions approaching the termination point $\varepsilon_\psi \approx 0.408$ and period $T \approx 9285$. In (b,c) we additionally plot vertical lines at the v -components of ν_\pm , cf. Figure 4.7. The yaw angle ψ is expressed in radians.

nearby periodic solutions for $0 < \varepsilon_\psi \ll 1$, which continue to the heteroclinic bifurcation at $\varepsilon_\psi \approx 0.408$. Here these solutions appear to terminate in one of the heteroclinic cycles that we found when decreasing ε_ψ from the Hopf bifurcation, i.e., in Figure 4.12 (c) one of the parts with fixed sign of v . Indeed, all the periodic solutions along the branch emerging from the Hopf bifurcations have necessarily winding number zero in the cylinder with periodic ψ . Additionally, the periodic trajectories with ψ_\pm , coming from the pitchfork bifurcations, have winding number one, which is therefore constant on the branch that emanates from these for increasing ε_ψ from zero. In particular, translating this into the yaw angle of the ship, winding number one means that this angle is undergoing a full rotation. We remark that the winding number is a topological invariant along branches, but branches with winding number zero and one can—and apparently do—meet at such a heteroclinic cycle. It appears that this is the way in which the entire region “under” the stability boundary up to the ε_r -axis is organized.

We turn to the resulting ship motions on the Earth-fixed position coordinates $(x, y) \in \mathbb{R}^2$. These coordinates can be conveniently expressed in complex form as $z = x + iy \in \mathbb{C}$, and the relation of $z(t)$ to the ship-fixed (u, v, ψ) -coordinates is given by $\dot{z} = (u + iv)e^{i\psi}$. We have chosen $\psi(0) = 0$ as the reference straight direction, but by symmetry, any other angle ψ_* can be implemented upon multiplication with $e^{i\psi_*}$. Hence, for any initial $z(0)$ the positions can be readily computed by integration, using given ship-fixed coordinates. In particular, the constant (u_0, v_0, r_0) corresponds to straight ($r_0 = 0$) or circular ($r_0 \neq 0$) motion of the ship. For instance, in the 3D system, this constant conforms the reduced equilibrium point ν_\pm (its three first components) at $\varepsilon_\psi = 0$. We display the results for selected solutions in Figures 4.13, 4.14. The physical dimensions of the variables in the plots are $[x] = [y] = \text{m}$ and $[t] = \text{s}$. As expected, periodic solutions near the Hopf bifurcation, for $\varepsilon_\psi \approx 25.6$, closely track the straight motion up to a superposed oscillation, cf. Figure 4.13 (a). Further away from the bifurcation point, e.g., for $\varepsilon_\psi = 1$, the ship still follows the straight motion on average but with much larger oscillations, as illustrated in Figure 4.13 (b). The motion of the vessel between these two solutions behave similarly, in which by decreasing the value of ε_ψ , the amplitude of the oscillations increases. However, decreasing ε_ψ even further, the ship motion is completely altered to a near eight shape as in Figure 4.14 (a), where $\varepsilon_\psi \approx 0.419$.

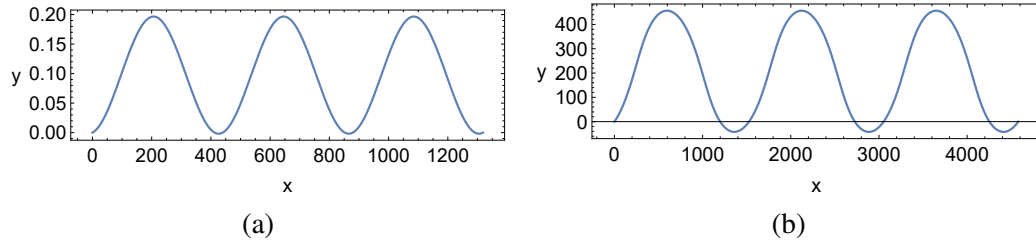


FIGURE 4.13: Earth-fixed coordinate plots of periodic solutions from Figure 4.12, where $\varepsilon_r \approx 10.6$, with $z(0) = 0$, $t \in [0, 3T]$ and T the corresponding period. (a) Small amplitude solution near the Hopf bifurcation with $\varepsilon_\psi \approx 25.6$ and period $T \approx 50.5$. (b) Solution far away from the Hopf bifurcation with $\varepsilon_\psi = 1$ and period $T \approx 311$.

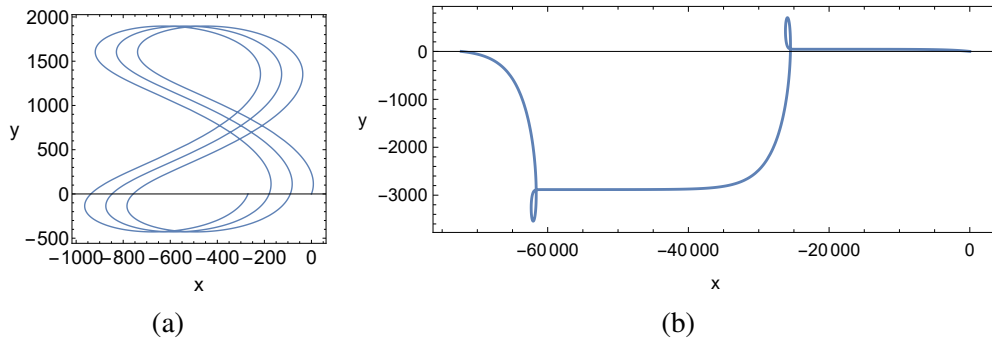


FIGURE 4.14: Earth-fixed coordinate plots of periodic solutions from Figure 4.12, where $\varepsilon_r \approx 10.6$, with $z(0) = 0$. (a) Solution with $\varepsilon_\psi \approx 0.419$, $t \in [0, 3T]$ and period $T \approx 873.4$. (b) Solution close to the heteroclinic orbit with $\varepsilon_\psi \approx 0.408$, $t \in [0, T]$ and period $T \approx 9285$.

In Figure 4.14 (b) we plot the ship track close to the heteroclinic cycle mentioned above for $\varepsilon_\psi \approx 0.408$ over one period of the ship-fixed (u, v, ψ) -coordinates. The ship track consists of two phases that each resemble one of the heteroclinic orbits that are involved in the heteroclinic cycle. These heteroclinic orbits are related by reflection and the motion also appears to be reflection symmetric about the mid-point between the global extrema. In particular, each orbit connects a straight motion with yaw angle $\psi = \pm\pi$ to a straight motion with yaw angle $\psi = \mp\pi$, via a clockwise/counterclockwise rotation, cf. Figure 4.12 (c). The equilibria of the heteroclinic cycle correspond to the straight motion opposite to the reference direction. The ship track closely follows this motion on the nearly horizontal part between the extrema and again towards the right boundary in Figure 4.14 (b). Along the track starting from the right boundary, the ship moves nearly straight along the negative x -axis, and then it makes a clockwise full turn that includes drifting to negative y -values. The vessel continues almost parallel along the negative x -axis and then it turns counterclockwise with a drift back to near $y = 0$. It appears that this motion periodically repeats as time progresses.

We additionally plot the thruster angle η (in radians) of selected solutions in Figure 4.15. As expected, close to the Hopf bifurcation, Figure 4.15 (a), the angle η just mildly oscillates, while further from it, Figure 4.15 (b,c), the thruster angles vary stronger, up to angles of around $0.5 \text{ rad} \approx 28.6^\circ$.

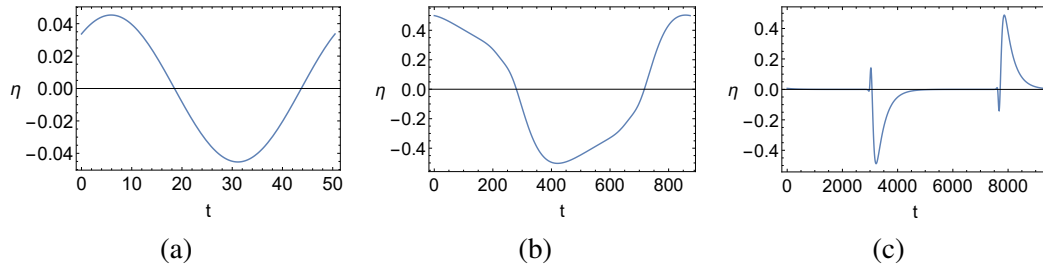


FIGURE 4.15: Thruster angles $\eta = \varepsilon_r r + \varepsilon_\psi \sin(\psi)$ in radians over one period $t \in [0, T]$ of different solutions: (a) solution of Figure 4.13 (a), where $\varepsilon_\psi \approx 25.6$ and $T \approx 50.5$; (b) solution of Figure 4.14 (a), where $\varepsilon_\psi \approx 0.419$ and $T \approx 873.4$; (c) solution of Figure 4.14 (b), where $\varepsilon_\psi \approx 0.408$ and $T \approx 9285$.

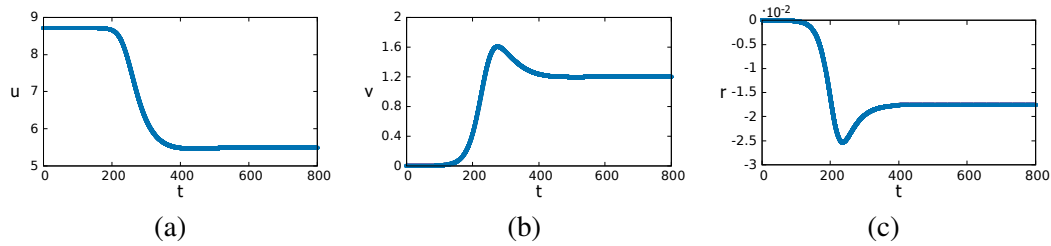


FIGURE 4.16: Time simulation for $\varepsilon_\psi = 0$, $\varepsilon_r \approx 10.6$ from the straight motion; (a) surge (t, u) , (b) sway (t, v) and (c) yaw (t, r) velocities.

Finally, we turn to time simulations of initial value problems in the model for $\varepsilon_r \approx 10.6$. The dimensions of the plots correspond to the unscaled model: $[u] = [v] = \text{m/s}$, $[r] = \text{rad/s}$, and $[t] = \text{s}$. We recall that the analytic prediction of supercritical bifurcations implies stable solutions near the bifurcation, i.e., they possess a basin of attraction so that any solution with initial condition in this basin converges exponentially towards it. Indeed, we found in the numerical continuation that all periodic solutions are stable, i.e., all Floquet exponents have negative real parts, away from the mentioned heteroclinic bifurcations, e.g., for $\varepsilon_\psi \geq 1$.

For $\varepsilon_\psi = 0$, we bring to mind that the ψ -component of the system becomes decoupled. Hence the three first components of ν_\pm are equilibria born from the pitchfork bifurcation, which are stable (all Floquet exponents have negative real parts) in the reduced 3D system, cf. Figure 4.16. These equilibrium points in ship-fixed coordinates correspond to large circular motions in the Earth-fixed coordinates. Moreover, as discussed in §4.2.3.1, for the 4D system these equilibria form exponentially stable periodic orbits. These continue for $\varepsilon_\psi > 0$ to stable periodic orbits. We show an example in Figure 4.17 for $\varepsilon_\psi = 0.2$, $\varepsilon_r \approx 10.6$.

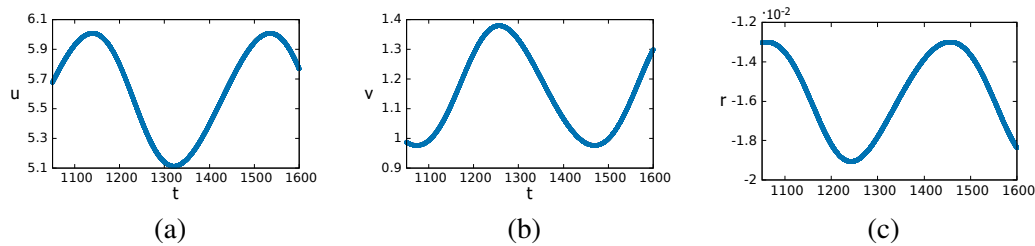


FIGURE 4.17: Time simulation, similar to Figure 4.16, for $\varepsilon_\psi = 0.2$, $\varepsilon_r \approx 10.6$ from $t = 1050$ on.

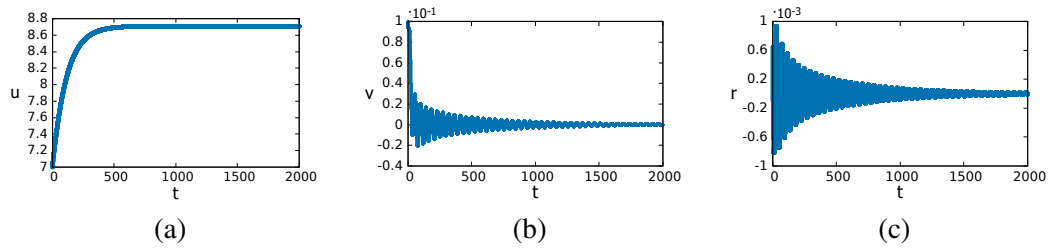


FIGURE 4.18: Time simulation, similar to Figure 4.16, for $\varepsilon_\psi = 30$, $\varepsilon_r \approx 10.6$ from a non-trivially perturbed initial condition. In (b) and (c) the trajectories are oscillatory.

For completeness, and to conclude this chapter, we have computed as well simulations for $(\varepsilon_r, \varepsilon_\psi)$ -values above the stability boundary curve. For instance, for the violet dot in Figure 4.10; see Figure 4.18. Locally, the trajectories converge, as expected, to the stable equilibrium straight motion.

Chapter 5

Conclusions and Outlook

With this last chapter, we summarize the main results of the present thesis and discuss possible directions for further research topics.

5.1 Bifurcation and stability analysis

In Chapter 2 we have analyzed Hopf bifurcations in mildly nonsmooth systems with piecewise smooth nonlinearity for which standard center manifold reduction and normal form computations cannot be used. By averaging and a direct approach we have derived explicit analogues of Lyapunov coefficients and have discussed some codimension-one degeneracies as well as the modified scaling laws. Some of the methods developed have been applied in Chapter 3 to investigate a nonsmooth system undergoing a symmetric Bogdanov–Takens bifurcation. Moreover, in Chapter 4 we have applied the results of Chapter 2 to models for controlled ship maneuvering, where stabilization by P-control induces a Hopf bifurcation.

We believe that the nonsmooth setting considered in this thesis gives an interesting class of equations from a theoretical as well as an applied viewpoint, arising in a variety of models for macroscopic laws with lack of smoothness in the nonlinear part. Among the perspectives, a complete unfolding of homoclinic and heteroclinic bifurcations is noteworthy, which we have started in Chapter 3.

Furthermore, from [9], we find the analysis of the saddle-node Hopf (SNH) bifurcation a stimulating case to investigate in our nonsmooth setting. This codimension-two bifurcation, also called the Gavrilov-Guckenheimer bifurcation, is characterized by the existence of a zero eigenvalue together with a pair of purely imaginary eigenvalues at the equilibrium point. Moreover, in the parameter plane, the curves of saddle-node bifurcations and Hopf bifurcations may intersect tangentially. At this location is where the bifurcation point is expected to be found.

To show briefly some ideas regarding a regular 3D smooth system undergoing a SNH bifurcation, we consider the following normal form in cylindrical coordinates (r, z, ϕ) and

unfolding parameters $\mu, \lambda \in \mathbb{R}$:

$$\begin{cases} \dot{r} = \mu r + \alpha_1 r z + \alpha_2 r^3 + \alpha_3 r z^2 + \mathcal{O}\left((r^2 + z^2)^2\right), \\ \dot{z} = \lambda z + \beta_1 r^2 + \beta_2 z^2 + \beta_3 r^2 z + \beta_4 z^3 + \mathcal{O}\left((r^2 + z^2)^2\right), \\ \dot{\phi} = \omega + \gamma_1 z + \mathcal{O}\left(r^2 + z^2\right). \end{cases}$$

In this case, μ and $\omega \neq 0$ correspond to the real and imaginary part of the complex conjugate pair of eigenvalues, respectively, and λ is the real eigenvalue. At the SNH bifurcation, both μ and λ vanish. We note that the two first equations do not depend on the variable ϕ and thus, truncating the system at cubic terms, we get an equivariant system with respect to rotations about the z -axis. In fact, this truncated normal form determines the dynamic behavior of the system.

For further research, we would start with the already mentioned normal form and modify its form by adding nonsmooth terms. This would imply breaking the radial symmetry and getting back a 3D system. In particular, since the cubic terms would interfere with the dynamics, we would rather replace them with nonsmooth terms, e.g., $r z^2 \mapsto r|z|$. With this setting, we would investigate how the characteristic coefficients differ from the smooth SNH situation in order to analyze the criticality of the system. One expects such quantities to behave differently since they cannot be computed by straightforward expansion. Therefore, the most significant contribution would be as for Chapter 2, in which one would not know a priori how to compute the first Lyapunov coefficient since Taylor expansion cannot be performed due to the lack of differentiability.

For an n -dimensional system with $n > 2$, an additional research direction could be to explore the conditions for the existence of chaos. Notice that if the system is hyperbolic, then there exists a 2-dimensional invariant manifold, which is stable, and hence, no chaos is possible. However, for at least a 3-dimensional system, if the stable manifolds are very different in each quadrant, complicated dynamics could happen.

5.2 Partial differential equations

Going one step further would be to move into partial differential equations (PDEs) and examine models with nonsmooth terms as considered in this thesis.

In fluid dynamics, one can get nonlinear expressions of a similar nature as the second order modulus terms. In particular, drag forces, or specifically bottom friction, in shallow water equations include the form $v|v|$, where $v \in \mathbb{R}^n$. One has here a similar situation as in the previous chapters, in the sense that these kinds of terms are quadratic and with odd reflection symmetry, and thus they enter into the bifurcation equations as terms that scale quadratically. For example, if $v = (v_1, v_2) \in \mathbb{R}^2$, then in the case $v_1 \approx 0$, we have $|v| = \sqrt{v_1^2 + v_2^2} \approx |v_2|$ and therefore $v|v| \approx (v_1|v_2|, v_2|v_2|)$. Indeed, by a change to higher dimensional polar coordinates, we write $v = r\Upsilon$ with Υ being a vector on the unit sphere, i.e., $|\Upsilon| = 1$, and thus $v|v|$ becomes $r|r|\Upsilon = r^2\Upsilon$. Hence, one expects that degenerate pitchfork bifurcations, as well as Hopf bifurcations, can occur.

A natural starting point to tackle a PDE system with such nonsmooth terms could be to make the traveling waves ansatz, i.e., to convert the PDEs with functions of two variables into a system of ODEs with functions of one variable. In this way, rather than having a PDE system with nonsmooth terms, we would have a spatial ODE. Notice that we have already investigated second order nonsmooth ODE systems in §3.3, cf. (3.26).

Potentially one could have reaction-diffusion equations with that form. Although we do not know any explicit model with such terms, it would be nevertheless interesting to ask what could happen and study the effect on stability. To get a first idea on these lines, let us consider

$$u_t = u_{xx} + \mu u + \sigma u|u|^j, \quad (5.1)$$

where $u(t, x) \in \mathbb{C}$ and we choose σ to be either -1 (supercritical bifurcation) or 1 (subcritical bifurcation). Note that for $j = 2$, (5.1) becomes the real Ginzburg–Landau equation (RGLe), and choosing $j = 1$, the nonlinear term becomes of second order modulus type $u|u|$.

We are interested in the impact of this nonsmooth term on the analysis of the previous reaction-diffusion equation. For that, we analyze (5.1) considering general $j \in \mathbb{N}$, and thus, we will be able to observe the differences by setting $j = 1$ and $j = 2$.

To begin with, we study solutions of (5.1) of the form $u(x) = r e^{ikx}$, called wave trains, assuming $r \geq 0$. The equation is then transformed into

$$0 = \left(-k^2 + \mu + \sigma \left| r^j e^{ikxj} \right| \right) r e^{ikx},$$

which for $r \neq 0$ becomes $0 = \mu - k^2 + \sigma r^j$ and therefore $r^j = \frac{k^2 - \mu}{\sigma}$.

As an initial comparison between the nonsmooth case ($j = 1$) with $r_1(k) = \frac{k^2 - \mu}{\sigma}$ and the RGLe ($j = 2$), which is smooth, with $r_2(k) = \sqrt{\frac{k^2 - \mu}{\sigma}}$, we already see a difference in the scaling laws of $r_1(k)$ and $r_2(k)$ close to the crossing points $\pm\sqrt{\mu}$ in the (k, r) -plane. Indeed, in a neighborhood of $\pm\sqrt{\mu}$, the function $r_1(k)$ behaves linear, while $r_2(k)$ as a square root, similar to the pitchfork bifurcation close to the origin, cf. Figure 1.8.

For the stability analysis, we next take polar coordinates $u = \rho e^{i\psi}$, with $\rho = \rho(t, x)$, $\psi = \psi(t, x)$. Computing their partial derivatives and substituting them into (5.1), yield

$$\rho_t + i\rho\psi_t = (\rho_{xx} + 2i\rho_x\psi_x + i\rho\psi_{xx} - \rho\psi_x^2) + \mu\rho + \sigma\rho^{j+1},$$

where we have divided $e^{i\psi}$ out. For $\rho \neq 0$, the previous equation is equivalent to the system

$$\begin{aligned} \rho_t &= \rho_{xx} - \rho\psi_x^2 + \mu\rho + \sigma\rho^{j+1}, \\ \psi_t &= 2(\ln \rho)_x\psi_x + \psi_{xx}, \end{aligned}$$

and its linearization in a wave train with $(\rho, \psi) = (r, kx)$ gives the operator

$$\mathcal{L} = \begin{pmatrix} \partial_{xx} - k^2 + \mu + (j+1)\sigma r^j & -2rk\partial_x \\ 2k\frac{\partial_x}{r} & \partial_{xx} \end{pmatrix}.$$

To study the spectrum of \mathcal{L} , we consider its Fourier transform

$$\hat{\mathcal{L}}(\kappa) = \begin{pmatrix} -\kappa^2 - k^2 + \mu + (j+1)\sigma r^j & -2rk i \kappa \\ 2k \frac{i\kappa}{r} & -\kappa^2 \end{pmatrix},$$

with wavenumber κ , and compute $\det(\hat{\mathcal{L}}(\kappa) - \lambda \text{Id}) = 0$, where Id is the 2×2 identity matrix. This results in the dispersion relation given by

$$d(\lambda, \kappa) := \lambda^2 + (2\kappa^2 + k^2 - \mu - (j+1)\sigma r^j)\lambda + \kappa^2(\kappa^2 - 3k^2 - \mu - (j+1)\sigma r^j) = 0.$$

We recall that $r^j = \frac{k^2 - \mu}{\sigma}$ and substitute it in the dispersion relation, which yields

$$d(\lambda, \kappa) = \lambda^2 + (2\kappa^2 + j\mu - jk^2)\lambda + \kappa^2(\kappa^2 + j\mu - (j+4)k^2) = 0.$$

From this equation we now investigate stability properties of the wave train. Notice that for each given κ , two solutions λ are obtained, from which stability is given by $\text{Re}(\lambda)$. If one of the solutions λ has $\text{Re}(\lambda) > 0$, then the wave train is unstable.

For $\kappa = 0$ we have $d(\lambda, 0) = \lambda^2 + j(\mu - k^2)\lambda = 0$, and thus the solutions are given by $\lambda = 0$ and $\lambda = j(k^2 - \mu)$. In this case, for $\mu \neq k^2$, the solution $\lambda = 0$ is isolated and, by the implicit function theorem, the nearby solutions come as a curve $\lambda(\kappa)$ with $\lambda(0) = 0$, and $\lambda'(0) = 0$ since $d(\lambda(\kappa^2), \kappa^2) = 0$. Hence, if $\text{Re}(\lambda''(0)) > 0$, then the wave train is unstable. For this reason, we consider $\text{Re}(\lambda'') \leq 0$ as a necessary condition for stability.

Computing λ'' from the dispersion relation gives

$$\lambda'' = -\frac{\partial_{\kappa}^2 d}{\partial_{\lambda} d} = -\frac{2(j\mu - (j+4)k^2)}{j(\mu - k^2)},$$

which is real, $\lambda'' \in \mathbb{R}$. Next, assuming the supercritical case for $\sigma = -1$, we have $r^j = \mu - k^2$, and for non-trivial solutions, $\mu - k^2 > 0$ must hold. Therefore, $\lambda'' \leq 0$ is equivalent to

$$j\mu - (j+4)k^2 \geq 0.$$

Notice that this condition actually scales differently between the cases $j = 1$ and $j = 2$. Indeed, for the nonsmooth case with $j = 1$ the inequality becomes $\mu - 5k^2 \geq 0$, while for the RGLe with $j = 2$, we have $\mu - 3k^2 \geq 0$ after dividing out a factor 2. In particular, $\mu - 3k^2 = 0$ is called the Eckhaus boundary, and ‘‘above’’ it, for the inequality, it is where the wave train is Eckhaus stable. This means that the stability region for $j = 2$ is larger than in the nonsmooth case.

5.3 Analysis for marine craft models

In Chapter 4 we have presented an accurate analysis of stabilizing the straight motion in a 3 DOF ship model with P-control. We have identified the location and geometry of the stability region in the control parameter space, which has been, essentially, independent of the propeller diameter, as well as its frequency, but it has strongly depended on the thruster—or rudder—position. In the Hamburg Test Case, the stability region has shrunk and even disappeared when moving the thruster location further to the fore of the ship. On the nonlinear level, the second order modulus nonlinearities require a non-standard approach which we have applied to the current setting in detail. In this manner, we have confirmed that the linearly stabilizing control produces also a “safe” nonlinear system. By numerical continuation we have corroborated these analytical results and, moreover, presented the arrangement of periodic solutions and equilibria in ship-fixed coordinates globally in the control parameter space. Finally, we have illustrated the resulting ship tracks in Earth-fixed coordinates.

While the details of the analysis depend on the specific choice of some parameters, such as the thruster position, the approach can be in principle adapted to any other design parameter of the ship model and even to related ones. A first approach could be to do different numerical simulations for other parameter sets.

A number of questions and further lines of research arise from this report. On the one hand, a natural next step would be to perform the same study for the full “rudder model” and explore whether again only “safe” bifurcations occur. For instance, in this setting, it is not obvious that the steady state is unique and, in addition, one would analyze how the eigenvalues differ from the thruster model.

An extension would include turning circle maneuvers and optimality conditions, possibly multi-objective control. On the other hand, it would be interesting to complete the analytical unfolding of the double zero eigenvalue in this cylindrical geometry and nonsmooth setting, and relate it to Bogdanov–Takens points with symmetry. One could start approximating numerically the homoclinic or heteroclinic curves for this nonsmooth model and, from the outcome, perform a similar analysis as in Chapter 3.

Furthermore and beyond the ship-fixed equilibrium maneuvers, numerical continuation can be used as well to effectively investigate diverse planned movements, for instance, zig-zag maneuvers. Notice that for the zig-zag maneuver delays on the trajectory could be expected due to the time lag while switching the rudder. However, if the motion is instantaneous, then one would talk about bang-bang control.

Moreover, a further research direction could be to add more DOF to the system. As an example, a usual 4 DOF model would include the roll motion to the horizontal plane model (surge, sway and yaw). In this case, possible control methods would consider fin stabilizers and rudders. Clearly, distinct motions could be added to the model until reaching the system with 6 DOF, i.e., with the maximum number of degrees of freedom.

5.4 Further applications

In this thesis, we have observed that continuous nonsmooth terms are entailed in standard marine craft systems (Chapter 4) as well as in models for a shimmying wheel (Chapter 2). Therefore, an expected direction of research would be to investigate other possible vehicles with such a nonsmooth setting. For instance, it would be interesting to apply our bifurcation analysis approach to a two-vessel motion in a tandem offloading system [36], with similar nonsmoothnesses.

Last but not least, a new perspective could be to shift into aircraft models, since the equations of motion of a marine craft can be adapted to describe aircraft, cf. [19]. Without going into detail, we mention here some similarities as well as differences between both types of craft.

As a first comparison, we note that the vector of states for the rigid-body dynamics of a plane is composed, in general, by the longitudinal (forward) U , lateral (transverse) V and vertical W velocities, and the roll P , pitch Q and yaw R rates, similarly as for ship models. The Earth-fixed coordinates for the position are $(x, y, z) \in \mathbb{R}^3$, where the altitude z is more relevant in this case. Besides the roll, pitch and yaw angles, we find the so-called angle of attack α and the sideslip angle β , defined as $\tan(\alpha) := W/U$ and $\sin(\beta) := V/V_T$, respectively, where $V_T = \sqrt{U^2 + V^2 + W^2}$ is the speed of the craft. We remark that for an underwater vehicle these two angles would also be of interest. Moreover, it is common to use β and α as states of the system under the assumption that they are small. Specifically, after applying some transformations to the system, we obtain $U = V_T$, and β, α can be expressed as $\beta = V/V_T$, $\alpha = W/V_T$. In practice, the variables β and α basically replace the previous lateral and vertical velocities in the system.

Before finishing this very short link between aircraft and watercraft, we turn our attention to their physical structure. Although both craft require a thruster (or thrusters) to move forward, the architecture of a plane considers the propulsion mechanism not at the end of the vehicle, as happens for sea vessels, but usually at the laterals or front of the craft. Hence, it would be intriguing to see how the (extensive) study of the impact of x_T , the longitudinal position of the thruster, modifies the stability analysis of §4.2.2.2.

Appendix A

Detailed Calculations for Chapter 2

A.1 Averaging

Near-identity transformation

For completeness, we provide details for the essentially standard normal form transformation used in the proof of Theorem 2.8. We set

$$f(x, \varphi, \epsilon) := \frac{m}{\omega}x + \frac{\chi_2}{\omega}x^2 + \epsilon \left(\frac{\chi_3}{\omega} - \frac{\chi_2\Omega_1}{\omega^2} \right) x^3,$$

which is the leading part of the right-hand side of (2.26) up to a factor of ϵ . We write f as the sum of its mean, \bar{f} , and its oscillating part, \tilde{f} ,

$$\begin{aligned} \bar{f}(x) &= \frac{1}{2\pi} \int_0^{2\pi} f(x, \varphi, 0) d\varphi = \frac{m}{\omega}x + \frac{2}{3\pi\omega}\sigma_{\#}x^2, \\ \tilde{f}(x, \varphi, \epsilon) &= f(x, \varphi, \epsilon) - \bar{f}(x) = \left(\frac{\chi_2}{\omega} - \frac{2}{3\pi\omega}\sigma_{\#} \right) x^2 + \epsilon \left(\frac{\chi_3}{\omega} - \frac{\chi_2\Omega_1}{\omega^2} \right) x^3. \end{aligned} \quad (\text{A.1})$$

Hence, $f(x, \varphi, \epsilon) = \bar{f}(x) + \tilde{f}(x, \varphi, \epsilon)$ and (2.26) reads

$$x' = \epsilon(\bar{f}(x) + \tilde{f}(x, \varphi, \epsilon)) + \epsilon^2 \mathcal{O}(\epsilon x^4 + |m|x^2). \quad (\text{A.2})$$

The near-identity transformation which we will use has smooth coefficients w_1, w_2 and is of the form

$$x = y + \epsilon w_1(y, \varphi, \epsilon) + \epsilon^2 w_2(y, \varphi, \epsilon).$$

Differentiating this equation with respect to φ , using the right-hand side of (A.2) for x' , and rearranging terms give

$$y' = \epsilon(\bar{f}(x) + \tilde{f}(x, \varphi, \epsilon)) + \epsilon^2 \mathcal{O}(\epsilon x^4 + |m|x^2) - \epsilon \left(\frac{\partial w_1}{\partial \varphi} + D_y w_1 y' \right) - \epsilon^2 \left(\frac{\partial w_2}{\partial \varphi} + D_y w_2 y' \right).$$

Further rearrangements yield

$$(1 + \epsilon D_y w_1 + \epsilon^2 D_y w_2) y' = \epsilon(\bar{f}(x) + \tilde{f}(x, \varphi, \epsilon)) + \epsilon^2 \mathcal{O}(\epsilon x^4 + |m|x^2) - \epsilon \frac{\partial w_1}{\partial \varphi} - \epsilon^2 \frac{\partial w_2}{\partial \varphi},$$

and inverting the first factor on the left and expanding in terms of ϵ we obtain

$$y' = \left(1 - \epsilon D_y w_1 + \mathcal{O}(\epsilon^2)\right) \epsilon \left(\bar{f}(x) + \tilde{f}(x, \varphi, \epsilon) - \frac{\partial w_1}{\partial \varphi} - \epsilon \frac{\partial w_2}{\partial \varphi} \right) + \epsilon^2 \mathcal{O}(\epsilon x^4 + |m|x^2). \quad (\text{A.3})$$

Concerning f and the error term, directly using the transformation to y we expand

$$\begin{aligned} \bar{f}(x) &= \bar{f}(y) + D_y \bar{f}(y) \epsilon w_1 + \mathcal{O}(\epsilon^2), \\ \tilde{f}(x, \varphi, \epsilon) &= \tilde{f}(y, \varphi, 0) + D_y \tilde{f}(y, \varphi, 0) \epsilon w_1 + \frac{\partial \tilde{f}}{\partial \epsilon}(y, \varphi, 0) \epsilon + \mathcal{O}(\epsilon^2), \end{aligned}$$

and note that $\epsilon^2 \mathcal{O}(\epsilon x^4 + |m|x^2) = \mathcal{O}(\epsilon^3 + \epsilon^2 |m| y^2)$. Substituting into (A.3) gives

$$\begin{aligned} y' &= \left(1 - \epsilon D_y w_1\right) \epsilon \left(\bar{f}(y + \epsilon w_1 + \epsilon^2 w_2) + \tilde{f}(y + \epsilon w_1 + \epsilon^2 w_2, \varphi, \epsilon) - \frac{\partial w_1}{\partial \varphi} - \epsilon \frac{\partial w_2}{\partial \varphi} \right) \\ &\quad + \mathcal{O}(\epsilon^3 + \epsilon^3 y^4 + \epsilon^2 |m| y^2) \\ &= \epsilon \left(\bar{f}(y) + \tilde{f}(y, \varphi, 0) - \frac{\partial w_1}{\partial \varphi} \right) + \epsilon^2 \left(D_y f(y, \varphi, 0) w_1(y, \varphi, 0) + \frac{\partial \tilde{f}}{\partial \epsilon}(y, \varphi, 0) - \frac{\partial w_2}{\partial \varphi} \right) \\ &\quad - \epsilon^2 D_y w_1(y, \varphi, 0) \left(\bar{f}(y) + \tilde{f}(y, \varphi, 0) - \frac{\partial w_1}{\partial \varphi} \right) + \mathcal{O}(\epsilon^3). \end{aligned}$$

In order to cancel φ -dependent terms and obtain (2.27), we choose periodic $w_1(y, \varphi, \epsilon)$ and $w_2(y, \varphi, \epsilon)$ as follows. Firstly, since we have

$$\begin{aligned} \int_0^{2\pi} \tilde{f}(y, \varphi, 0) d\varphi &= \int_0^{2\pi} \left(\frac{\chi_2(\varphi)}{\omega} - \frac{2}{3\pi\omega} \sigma_{\#} \right) y^2 d\varphi \\ &= \left(\frac{1}{\omega} \int_0^{2\pi} \chi_2(\varphi) d\varphi - \frac{4}{3\omega} \sigma_{\#} \right) y^2 = 0, \end{aligned}$$

the function w_1 can be defined via

$$\frac{\partial w_1}{\partial \varphi} = \tilde{f}(y, \varphi, 0).$$

Regarding w_2 , we take the ansatz

$$\frac{\partial w_2}{\partial \varphi} = D_y f(y, \varphi, 0) w_1(y, \varphi, 0) + \frac{\partial \tilde{f}}{\partial \epsilon}(y, \varphi, 0) - D_y w_1(y, \varphi, 0) \bar{f}(y) - \bar{f}_2(y), \quad (\text{A.4})$$

where $\bar{f}_2(y)$ is to be determined such that $\int_0^{2\pi} \frac{\partial w_2}{\partial \varphi} d\varphi = 0$ holds, i.e., in order for w_2 to be periodic. To simplify the notation, we define

$$A(s) := \frac{\chi_2(s)}{\omega} - \frac{2\sigma_{\#}}{3\pi\omega},$$

and the expressions from the right-hand side of (A.4) can be then written as

$$\begin{aligned} D_y f(y, \varphi, 0) w_1(y, \varphi, 0) &= \frac{m}{\omega} \int_0^\varphi A(s) ds y^2 + \frac{2\chi_2(\varphi)}{\omega} \int_0^\varphi A(s) ds y^3, \\ \frac{\partial \tilde{f}}{\partial \epsilon}(y, \varphi, 0) &= \left(\frac{\chi_3(\varphi)}{\omega} - \frac{\chi_2(\varphi)\Omega_1(\varphi)}{\omega^2} \right) y^3, \\ D_y w_1(y, \varphi, 0) \bar{f}(y) &= \frac{2m}{\omega} \int_0^\varphi A(s) ds y^2 + \frac{4\sigma_\#}{3\pi\omega} \int_0^\varphi A(s) ds y^3. \end{aligned}$$

Next, arranging the coefficients for y^2 and y^3 , the integral of $\bar{f}_2(y)$ reads

$$\begin{aligned} \int_0^{2\pi} \bar{f}_2(y) d\varphi &= \int_0^{2\pi} \left(D_y f(y, \varphi, 0) w_1(y, \varphi, 0) + \frac{\partial \tilde{f}}{\partial \epsilon}(y, \varphi, 0) - D_y w_1(y, \varphi, 0) \bar{f}(y) \right) d\varphi \\ &= -\frac{m}{\omega} \int_0^{2\pi} \int_0^\varphi A(s) ds d\varphi y^2 \\ &\quad + \left[\frac{2}{\omega} \int_0^{2\pi} \chi_2(\varphi) \int_0^\varphi A(s) ds d\varphi + \frac{1}{\omega} \int_0^{2\pi} \chi_3(\varphi) d\varphi \right. \\ &\quad \left. - \frac{1}{\omega^2} \int_0^{2\pi} \chi_2(\varphi)\Omega_1(\varphi) d\varphi - \frac{4\sigma_\#}{3\pi\omega} \int_0^{2\pi} \int_0^\varphi A(s) ds d\varphi \right] y^3, \end{aligned}$$

where the expression with m gives a term of order $\mathcal{O}(|m|y^2)$. Substituting the expression for $A(s)$ and then collecting the $\sigma_\#$ terms yield

$$\begin{aligned} \int_0^{2\pi} \bar{f}_2(y) d\varphi &= \left[\frac{2}{\omega^2} \int_0^{2\pi} \chi_2(\varphi) \int_0^\varphi \left(\chi_2(s) - \frac{2\sigma_\#}{3\pi} \right) ds d\varphi \right. \\ &\quad + \frac{1}{\omega} \int_0^{2\pi} \chi_3(\varphi) d\varphi - \frac{1}{\omega^2} \int_0^{2\pi} \chi_2(\varphi)\Omega_1(\varphi) d\varphi \\ &\quad \left. - \frac{4\sigma_\#}{3\pi\omega^2} \int_0^{2\pi} \int_0^\varphi \left(\chi_2(s) - \frac{2\sigma_\#}{3\pi} \right) ds d\varphi \right] y^3 + \mathcal{O}(|m|y^2) \\ &= \frac{1}{\omega^2} \left[2 \int_0^{2\pi} \chi_2(\varphi) \int_0^\varphi \chi_2(s) ds d\varphi + \omega \int_0^{2\pi} \chi_3(\varphi) d\varphi - \int_0^{2\pi} \chi_2(\varphi)\Omega_1(\varphi) d\varphi \right. \\ &\quad \left. - \frac{4\sigma_\#}{3\pi} \left(\int_0^{2\pi} \chi_2(\varphi)\varphi d\varphi + \int_0^{2\pi} \int_0^\varphi \chi_2(\varphi) ds d\varphi - \frac{4\pi\sigma_\#}{3} \right) \right] y^3 + \mathcal{O}(|m|y^2) \\ &= \left(\frac{\pi}{4\omega} S_c + \frac{\pi}{4\omega^2} S_q + \frac{1}{\omega^2} \sigma_2 \right) y^3 + \mathcal{O}(\sigma_\# y^3 + |m|y^2), \end{aligned} \tag{A.5}$$

with S_q, S_c from (2.21). Notice that, although the terms with $\sigma_\#$ are not relevant for our analysis, since they contribute to $\mathcal{O}(\sigma_\# y^3)$, we have shown the detailed computations for completeness. All these lead to $\bar{f}_2(y)$ to be defined as

$$\bar{f}_2(y) = \left(\frac{1}{8\omega} S_c + \frac{1}{8\omega^2} S_q + \frac{1}{2\pi\omega^2} \sigma_2 \right) y^3 + \mathcal{O}(\sigma_\# y^3 + |m|y^2),$$

which gives (2.27).

Integration of some periodic functions with absolute values

Here we explain the computations of the integrals which yield $\bar{f}(y)$, $\bar{f}_2(y)$ in (2.28).

We show $\int_0^{2\pi} \chi_2(\varphi) d\varphi = \frac{4}{3}\sigma_{\#}$ in order to prove the resulting expression of \bar{f} in (A.1). On the one hand, the smooth terms of $\chi_2(\varphi)$ have clearly zero integral over 2π due to symmetry. On the other hand, all nonsmooth terms have the following feature: a_{ij} and b_{ij} are always multiplied by c and s , respectively, times a common symmetric odd or even function, which implies that only one of the coefficients for each pair of (i, j) will be nonzero after integrating over 2π . For instance,

$$\int_0^{2\pi} c|c|(a_{11}c + b_{11}s)d\varphi = \frac{8a_{11}}{3} \quad \text{and} \quad \int_0^{2\pi} s|c|(a_{21}c + b_{21}s)d\varphi = \frac{4b_{21}}{3}.$$

Finally, the factor 2 for a_{11} and b_{22} is due to the product of purely c or s :

$$\int_0^{2\pi} c^2|c|d\varphi = \int_0^{2\pi} s^2|s|d\varphi = 2 \int_0^{2\pi} c^2|s|d\varphi = 2 \int_0^{2\pi} s^2|c|d\varphi.$$

The computations in (A.5), which give the second expression in (2.28), are much more involved. However, for the integral of $\chi_3(\varphi)$ over 2π one proceeds similarly as before. Indeed, this yields $\frac{\pi}{4}S_c$ since the integral of the arising mixed products between c and s vanishes. Furthermore, different prefactors compared with $\sigma_{\#}$ occur due to the fact that the power of c and s is distinct as well:

$$\int_0^{2\pi} c^4 d\varphi = \frac{3}{4} \int_0^{2\pi} c^2 d\varphi = \frac{3}{4} \int_0^{2\pi} s^2 d\varphi.$$

Moreover,

$$2 \int_0^{2\pi} \chi_2(\varphi) \int_0^{\varphi} \chi_2(s) ds d\varphi - \int_0^{2\pi} \chi_2(\varphi) \Omega_1(\varphi) d\varphi = \frac{\pi}{4}S_q + \sigma_2,$$

where S_q comes from integrating the smooth terms and σ_2 from integrating the others, which give the products between a_i , b_j , and a_{ij} , b_{kl} , respectively.

A.2 Poincaré map

To prove stability of the periodic orbit we make use of the monotonicity of the Poincaré map (also called the first recurrence map), as in the proof of Proposition 2.15. In particular, on the one hand, if the map is monotonically increasing inside the limit cycle, then the fixed point is unstable while the periodic orbit is stable. On the other hand, if it is monotonically decreasing, then the stabilities of the equilibrium and the periodic orbit switch.

Considering (2.8) with (2.9), we define the Poincaré section as $S = \{(v, 0) \mid v \in \mathbb{R}_+\}$, which is transversal to the flow, and choose the initial condition $(\varphi, r) = (0, r_1)$ for the system in polar coordinates, (2.29).

To compute the Poincaré map in our nonsmooth setting, we start calculating

$$\tilde{r}_i(\varphi; r_i) = \alpha_{1,i}(\varphi)r_i + \alpha_{2,i}(\varphi)r_i^2 + \mathcal{O}(r_i^3) \quad (\text{A.6})$$

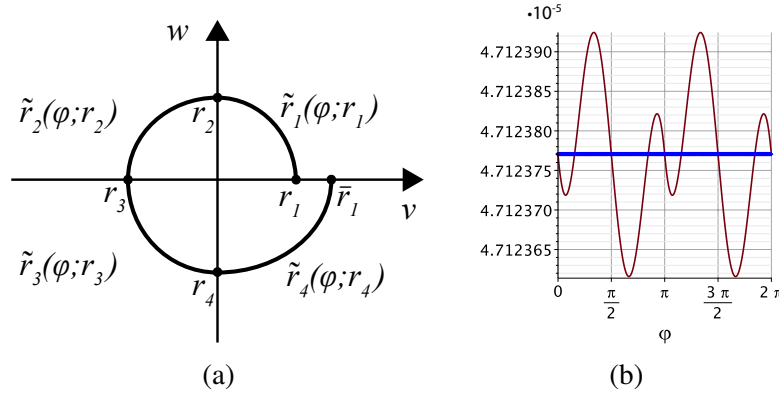


FIGURE A.1: (a) Composition of the Poincaré map by quadrants. (b) Glued functions $\tilde{r}_i(\varphi; r_i)$ for a complete period. The horizontal blue line marks the leading order amplitude r_* .

for each quadrant in order to avoid the nonsmoothnesses of the system. In Figure A.1 (a), a schematic idea of the procedure can be observed. We compose these expressions to get the Poincaré map, $\tilde{r}_4(2\pi; r_1)$, i.e., the function on the fourth quadrant composed with the previous ones after a period of 2π .

Indeed, for the initial condition $(0, r_1)$, one starts computing $\tilde{r}_1(\varphi; r_1)$ in the first quadrant. Next, the function for the second quadrant is $\tilde{r}_2(\varphi; r_2)$ with starting condition the end point of the previous function, i.e., $r_2 = \tilde{r}_1(\pi/2; r_1)$. In this way, we compute further the function in the third quadrant, $\tilde{r}_3(\varphi; r_3)$ with $r_3 = \tilde{r}_2(\pi; r_2)$; and finally the function in the fourth quadrant, $\tilde{r}_4(\varphi; r_4)$ with $r_4 = \tilde{r}_3(3\pi/2; r_3)$.

With the corresponding initial conditions, one computes $\alpha_{1,i}(\varphi)$, $\alpha_{2,i}(\varphi)$ as in the proof of Proposition 2.15. Subsequently, “gluing” all functions correspondingly, one can write \tilde{r}_4 in terms of r_1 , so that the following “iteration” is given by $\tilde{r}_4(2\pi; r_1) = \tilde{r}_1(0; r_1)$. Hence, the periodic orbit of the original system corresponds to the smallest (due to the leading order term) positive solution of $r_* = \tilde{r}_4(2\pi; r_*)$.

For comparison, computing numerically $r_* = \tilde{r}_4(2\pi; r_*)$ and using the expression r_0 of (2.23), we observe that the difference between them is merely of order (around) 10^{-9} . For instance, choosing $a_{12} = 1$ and all other a_{ij}, b_{ij} zero, such that $\sigma_{\#} = 1$, together with $\mu = -10^{-5}$, give $r_* = 4.712377012 \cdot 10^{-5}$ and $r_0 = 4.712388981 \cdot 10^{-5}$.

We note that the radial amplitudes $\tilde{r}_i(\varphi; r_i)$ depend on φ , and therefore, in general, $\tilde{r}_i(\varphi; r_i) \equiv r_{i+1}$ is not true for all φ . Hence, strictly speaking, r_* is the leading order amplitude of the oscillation, as should be thought r_0 as well. We display an example in Figure A.1 (b), showing the variation of the amplitude for $\varphi \in [0, 2\pi]$.

Finally, the corresponding Poincaré map for the case $\sigma_{\#} = 0$ can also be computed in a similar way. For that, one expands (A.6) up to third order, as for Theorem 2.19, and proceed as above. However, in this situation, the variation of results between the numerical value r_* and the analytical expression (2.38) is larger. Numerically, a disparity of order 10^{-3} is observed in general.

A.3 3D system

A.3.1 Computation of γ_{ij} , δ_{ij} of system (2.57)

In this subsection we present the functions γ_{ij} , δ_{ij} of system (2.57), used for the proof of Theorem 2.21.

We first note that (2.56a) simplifies since $\Psi_u(0, 0, \varphi) = \partial_r \Psi_u(0, 0, \varphi) = 0$, and to ease the notation we define

$$\begin{aligned} p_1 &:= \partial_u \Psi_u(0, 0, \varphi) = \frac{c_1}{\omega}, \\ p_2(\varphi) &:= \frac{1}{2} \partial_u^2 \Psi_u(0, 0, \varphi) = \frac{c_2 \omega - c_1 \Omega_0(\varphi)}{\omega^2}, \\ p_3(\varphi) &:= \frac{1}{2} \partial_r^2 \Psi_u(0, 0, \varphi) = \frac{\Upsilon(\varphi)}{\omega}, \\ p_4(\varphi) &:= \partial_{ur}^2 \Psi_u(0, 0, \varphi) = \frac{\cos(\varphi)c_3 + \sin(\varphi)c_4}{\omega} - \frac{c_1 \Omega_1(\varphi)}{\omega^2}. \end{aligned}$$

Similarly, in (2.56b) we have $\Psi_r(0, 0, \varphi) = \partial_u \Psi_r(0, 0, \varphi) = \frac{1}{2} \partial_u^2 \Psi_r(0, 0, \varphi) = 0$, and we define

$$\begin{aligned} k_1 &:= \partial_r \Psi_r(0, 0, \varphi) = \frac{\mu}{\omega}, \quad k_2(\varphi) := \frac{1}{2} \partial_r^2 \Psi_r(0, 0, \varphi) = \frac{\chi_2(\varphi)\omega - \mu \Omega_1(\varphi)}{\omega^2}, \\ k_3(\varphi) &:= \partial_{ur}^2 \Psi_r(0, 0, \varphi) = \frac{\chi_1(\varphi)\omega - \mu \Omega_0(\varphi)}{\omega^2}. \end{aligned}$$

The expressions for γ_{ij} and δ_{ij} follow from solving the ODEs that arise upon substituting (2.57) into (2.56a) and (2.56b), and matching the coefficients of the powers of u_0 and r_0 . We start with the equations and initial conditions to obtain γ_{01} , γ_{10} , δ_{01} , δ_{10} :

$$\begin{aligned} \gamma'_{01} &= p_1 \gamma_{01}, \quad \gamma_{01}(0) = 0 \Rightarrow \gamma_{01} \equiv 0, & \delta'_{01} &= k_1 \delta_{01}, \quad \delta_{01}(0) = 1 \Rightarrow \delta_{01}(\varphi) = e^{k_1 \varphi}, \\ \gamma'_{10} &= p_1 \gamma_{10}, \quad \gamma_{10}(0) = 1 \Rightarrow \gamma_{10}(\varphi) = e^{p_1 \varphi}, & \delta'_{10} &= k_1 \delta_{10}, \quad \delta_{10}(0) = 0 \Rightarrow \delta_{10} \equiv 0. \end{aligned}$$

Using these, we solve the corresponding equations for the remaining coefficients as follows:

$$\begin{aligned} \gamma'_{20} &= p_1 \gamma_{20} + p_2(\varphi) \gamma_{10}^2, \quad \gamma_{20}(0) = 0 \Rightarrow \gamma_{20} = \int_0^\varphi e^{p_1(\varphi+s)} p_2(s) ds, \\ \gamma'_{02} &= p_1 \gamma_{02} + p_3(\varphi) \delta_{01}^2, \quad \gamma_{02}(0) = 0 \Rightarrow \gamma_{02}(\varphi) = \int_0^\varphi e^{p_1(\varphi-s)+2k_1 s} p_3(s) ds, \\ \gamma'_{11} &= p_1 \gamma_{11} + p_4(\varphi) \gamma_{10} \delta_{01}, \quad \gamma_{11}(0) = 0 \Rightarrow \gamma_{11}(\varphi) = \int_0^\varphi e^{p_1 \varphi + k_1 s} p_4(s) ds, \\ \delta'_{20} &= k_1 \delta_{20}, \quad \delta_{20}(0) = 0 \Rightarrow \delta_{20} \equiv 0, \\ \delta'_{02} &= k_1 \delta_{02} + k_2(\varphi) \delta_{01}^2, \quad \delta_{02}(0) = 0 \Rightarrow \delta_{02}(\varphi) = \int_0^\varphi e^{k_1(\varphi+s)} k_2(s) ds, \\ \delta'_{11} &= k_1 \delta_{11} + k_3(\varphi) \gamma_{10} \delta_{01}, \quad \delta_{11}(0) = 0 \Rightarrow \delta_{11}(\varphi) = \int_0^\varphi e^{k_1 \varphi + p_1 s} k_3(s) ds. \end{aligned}$$

Since we aim to solve the boundary value problem $0 = u(2\pi) - u(0)$, $0 = r(2\pi) - r(0)$, we write $\bar{\gamma}_{ij} := \gamma_{ij}(2\pi) - \gamma_{ij}(0)$, $\bar{\delta}_{ij} := \delta_{ij}(2\pi) - \delta_{ij}(0) \forall i, j \geq 0$. Direct computation

of $\bar{\gamma}_{10}$ and $\bar{\gamma}_{20}$ gives the expressions in (2.51). For the other functions, we consider the corresponding integrals and Taylor expand in $\mu = 0$, which results in $\bar{\gamma}_{11}$, $\bar{\delta}_{01}$, $\bar{\delta}_{02}$, and $\bar{\delta}_{11}$ shown in (2.51). For illustration of details omitted, we next present the full derivation for the explicit form of $\bar{\gamma}_{02}$. Taylor expansion of $e^{s\frac{2\mu}{\omega}}$ in $\mu = 0$ and rearranging the terms in the integral of γ_{02} give

$$\bar{\gamma}_{02} = \frac{1}{\omega} e^{\frac{2\pi c_1}{\omega}} \int_0^{2\pi} e^{-s\frac{c_1}{\omega}} \Upsilon(s) ds + \frac{2\mu}{\omega^2} e^{\frac{2\pi c_1}{\omega}} \int_0^{2\pi} s e^{-s\frac{c_1}{\omega}} \Upsilon(s) ds + \mathcal{O}(\mu^2). \quad (\text{A.7})$$

We compute the two integrals in (A.7) separately. The first one readily expands in $c_1 = 0$ as

$$\begin{aligned} \frac{1}{\omega} e^{\frac{2\pi c_1}{\omega}} \int_0^{2\pi} e^{-s\frac{c_1}{\omega}} \Upsilon(s) ds &= \frac{\omega}{c_1(c_1^2 + 4\omega^2)} \left[2 \left(e^{\frac{3\pi}{2\omega} c_1} - e^{\frac{\pi}{2\omega} c_1} \right) (c_1 h_{21} - 2h_{11}\omega) \right. \\ &\quad + \left(e^{\frac{2\pi}{\omega} c_1} - 2e^{\frac{\pi}{\omega} c_1} + 1 \right) (c_1 h_{12} + 2h_{22}\omega) \\ &\quad \left. + \left(e^{\frac{2\pi}{\omega} c_1} - 1 \right) \left(c_1 h_{21} + c_1 c_5 + \frac{c_1^2 h_{11}}{\omega} + 2h_{11}\omega \right) \right] \\ &= \frac{1}{c_1^2 + 4\omega^2} \left[2\pi (c_1 h_{21} - 2h_{11}\omega) \right. \\ &\quad \left. + 2\pi \left(c_1 h_{21} + c_1 c_5 + \frac{c_1^2 h_{11}}{\omega} + 2h_{11}\omega \right) \right] + \mathcal{O}(c_1^2). \end{aligned}$$

In particular, it vanishes for $c_1 = 0$.

For the second integral of (A.7) we proceed similarly. Its explicit expression reads

$$\begin{aligned} \frac{2\mu}{\omega^2} e^{\frac{2\pi c_1}{\omega}} \int_0^{2\pi} s e^{-s\frac{c_1}{\omega}} \Upsilon(s) ds &= -\frac{4\mu}{\omega c_1^2 (c_1^2 + 4\omega^2)^2} \left[\omega^2 c_1^3 (6h_{11}\pi - h_{12}) + \omega c_1^4 \pi (c_5 + h_{21}) + c_1^5 h_{11} \pi \right. \\ &\quad + \frac{\omega}{2} \left\{ (-16h_{11}\omega^4 - 12c_1^2 h_{11}\omega^2 + 4c_1^3 h_{21}\omega) \left(e^{\frac{\pi}{2\omega} c_1} - e^{\frac{3\pi}{2\omega} c_1} \right) \right. \\ &\quad \left. + \pi (-8c_1 h_{11}\omega^3 + 4c_1^2 h_{21}\omega^3 + c_1^4 h_{21} - 2h_{11} c_1^3 \omega) \left(3e^{\frac{\pi}{2\omega} c_1} - e^{\frac{3\pi}{2\omega} c_1} \right) \right\} \\ &\quad + \omega \left\{ (3c_1^2 h_{22}\omega^2 + c_1^3 h_{12}\omega + 4h_{22}\omega^4) \left(-e^{\frac{2\pi}{\omega} c_1} + 2e^{\frac{\pi}{\omega} c_1} \right) \right. \\ &\quad \left. + \left(\omega^4 4h_{11} + \omega^2 c_1^2 h_{11} + \omega c_1^3 (h_{21} + c_5) + \frac{1}{2} c_1^4 h_{11} \right) \left(-e^{\frac{2\pi}{\omega} c_1} + 1 \right) \right\} \\ &\quad + (\omega^4 4\pi c_1 h_{22} + \omega^3 4\pi c_1^2 h_{12} + \omega^2 2\pi c_1^3 h_{22} + \omega \pi c_1^4 h_{12}) \left(e^{\frac{\pi}{\omega} c_1} - 1 \right) \\ &\quad \left. - 4\omega^5 h_{22} + \omega^4 8c_1 h_{11}\pi + \omega^3 c_1^2 (4\pi (c_5 + h_{21} c_1) - 3h_{22}) \right]. \end{aligned}$$

Expanding again the exponential functions in $c_1 = 0$ and simplifying coefficients, at $c_1 = 0$ we obtain

$$\frac{2\mu}{\omega^2} e^{\frac{2\pi c_1}{\omega}} \int_0^{2\pi} s e^{-s\frac{c_1}{\omega}} \Upsilon(s) ds = -\mu \frac{\pi}{\omega^2} (2h_{21} + c_5 + \pi h_{22}).$$

A.3.2 Computation of δ_{03} of system (2.65)

Similar to the previous subsection, we present the function δ_{03} of system (2.65), used in the proof of Corollary 2.23.

Taylor expanding the right-hand sides of (2.55) in $(u, r) = (0, 0)$ up to fourth order gives the following; we omit the dependence of Ψ_u and Ψ_r on (u, r, φ) at $(0, 0, \varphi)$ to simplify the notation:

$$\begin{aligned} u' &= \Psi_u + \partial_u \Psi_u u + \partial_r \Psi_u r + \frac{1}{2} \partial_u^2 \Psi_u u^2 + \frac{1}{2} \partial_r^2 \Psi_u r^2 + \partial_{ur}^2 \Psi_u ur \\ &\quad + \frac{1}{3!} \partial_u^3 \Psi_u u^3 + \frac{1}{3!} \partial_r^3 \Psi_u r^3 + \frac{1}{2} \partial_{u^2 r}^3 \Psi_u u^2 r + \frac{1}{2} \partial_{ur^2}^3 \Psi_u ur^2 + \mathcal{O}(4), \end{aligned} \quad (\text{A.8a})$$

$$\begin{aligned} r' &= \Psi_r + \partial_u \Psi_r u + \partial_r \Psi_r r + \frac{1}{2} \partial_u^2 \Psi_r u^2 + \frac{1}{2} \partial_r^2 \Psi_r r^2 + \partial_{ur}^2 \Psi_r ur \\ &\quad + \frac{1}{3!} \partial_u^3 \Psi_r u^3 + \frac{1}{3!} \partial_r^3 \Psi_r r^3 + \frac{1}{2} \partial_{u^2 r}^3 \Psi_r u^2 r + \frac{1}{2} \partial_{ur^2}^3 \Psi_r ur^2 + \mathcal{O}(4), \end{aligned} \quad (\text{A.8b})$$

where $\frac{1}{3!} \partial_u^3 \Psi_r = 0$. We also set $k_4(\varphi) := \frac{1}{3!} \partial_r^3 \Psi_r = \frac{-\omega\chi_2(\varphi)\Omega_1(\varphi) + \mu\Omega_1(\varphi)^2}{\omega^3}$.

Substituting (2.65) into (A.8a) and (A.8b), and matching the coefficients of the powers of u_0 and r_0 we get to solve a set of ODEs in order to obtain the expressions for γ_{ij} , δ_{ij} for i, j such that $i + j = 3$, which are rather lengthy. We show δ_{03} , which is the only one required for the leading order analysis in the degenerate case $\sigma_{\#} = 0$, $c_1 \neq 0$ in Corollary 2.23:

$$\begin{aligned} \delta'_{03} &= k_4 \delta_{01}^3 + 2k_2 \delta_{01} \delta_{02} + k_3 \delta_{01} \gamma_{02} + k_1 \delta_{03}, \quad \delta_{03}(0) = 0 \Rightarrow \\ \delta_{03}(\varphi) &= e^{k_1 \varphi} \int_0^\varphi e^{-k_1 s} \delta_{01}(s) [2k_2(s) \delta_{02}(s) + k_3(s) \gamma_{02}(s) + k_4(s) \delta_{01}(s)^2] ds. \end{aligned} \quad (\text{A.9})$$

Appendix B

Ship Characteristics

B.1 HTC Characteristics

The parameter values listed here are taken from [57].

Hull forces			
Coefficient	Value	Coefficient	Value
\bar{m}	0.2328	\bar{m}_{uu}	0.0247
\bar{I}_z	0.0134	\bar{m}_{vv}	0.2286
		\bar{m}_{rr}	0.0150
		\bar{m}_{vr}	0.0074
		\bar{m}_{rv}	0.0074

TABLE B.1: Rescaled rigid-body's mass, added mass coefficients and moment of inertia in yawing, (4.5).

Hull forces			
Coefficient	Value	Coefficient	Value
$X_{u u }$	-0.0141		
Y_β	-0.1735	N_β	-0.1442
Y_γ	0.0338	N_γ	-0.0276
$Y_{\beta \beta }$	-1.1378	$N_{\beta \beta }$	-0.0375
$Y_{\gamma \gamma }$	0.0123	$N_{\gamma \gamma }$	-0.0386
$Y_{\beta \gamma }$	-0.0537		
$Y_{ \beta \gamma}$	0.1251		
a_y	3	a_n	1
b_y	2	b_n	3
		c_n	2

TABLE B.2: Hydrodynamic bare hull coefficients for (4.2). To obtain the rescaled values for (4.5), multiply each force with L_{pp}^{-1} .

Propeller characteristics			
Coefficient	Value	Coefficient	Value
D_p	6.105	K_{T0}	0.366897
n_p	2	K_{T1}	-0.345036
		K_{T2}	0.068841
		K_{T3}	-0.710991
		K_{T4}	0.948559
		K_{T5}	-0.428915

TABLE B.3: Propeller characteristics with propeller diameter $[D_p] = \text{m}$ and non-dimensional coefficients K_{T_i} of the propeller thrust T_p , corresponding to the model No. 5286. Although the frequency $[n_p] = 1/\text{s}$ is not a particular of the HTC propeller, we list it here for completeness.

Coefficient	Value	Coefficient	Value
L_{pp}	153.70	t	0.22
T	10.30	w	0.38
ρ	1025		

TABLE B.4: Further parameters: length between perpendiculars of the vessel $[L_{pp}] = \text{m}$, mean draft $[T] = \text{m}$, water density $[\rho] = \text{kg}/\text{m}^3$, and non-dimensional thrust deduction fraction t and wake fraction w .

B.2 Rudder forces

The rudder forces for forward speed are given by

$$\begin{aligned}
X_R &= -\frac{1}{2}\rho V_{rr}^{-1} A_R C_L (u_r \sin \eta - v_r \cos \eta) \\
&\quad \cdot \left(\frac{C_L u_r}{\pi \Lambda} (u_r \sin \eta - v_r \cos \eta) + v_r (u_r \cos \eta + v_r \sin \eta) \right), \\
Y_R &= \frac{1}{2}(1 + a_H)\rho V_{rr}^{-1} A_R C_L (u_r \sin \eta - v_r \cos \eta) \\
&\quad \cdot \left(u_r (u_r \cos \eta + v_r \sin \eta) - \frac{C_L v_r}{\pi \Lambda} (u_r \sin \eta - v_r \cos \eta) \right), \\
N_R &= Y_R x_T - X_R y_T,
\end{aligned}$$

where u_r is the velocity at the rudder position and v_r is the transverse velocity component,

$$\begin{aligned}
u_r &= u_p + C_{rue} \left(\sqrt{u_p^2 + \frac{8T_p(u)}{\rho \pi D_p^2}} - u_p \right), \quad \text{with } u_p = (1 - w)u; \\
v_r &= C_{db}v + C_{dr}x_{Tr},
\end{aligned}$$

respectively. The velocity at the rudder is then computed as

$$V_{rr} = \sqrt{u_r^2 + v_r^2}.$$

Furthermore, x_T and y_T are the longitudinal and transverse position of the rudder, respectively; A_R is the rudder area, Λ the rudder aspect ratio, C_{rue} the propeller-rudder interaction coefficient, C_{db} and C_{dr} the flow straightening factor for drift and yaw motion, respectively, and C_L the lift coefficient. For a detailed description of these expressions and coefficients, we refer to [57].

Note that the rudder forces introduce additional complications to the bifurcation analysis of the model due to, for instance, the non-polynomial dependence of the variables u, v . In addition, in this manuscript, the focus falls on the influence of the hull forces on the ship maneuvering, and thus, the simplified thruster model is considered.

Appendix C

Implementations of Simulations

The simulations developed in this thesis have been implemented with the software `AUTO`, which is a Fortran based open source, as well as with `MAPLE` (version 2017), a mathematics-based software from the company Maplesoft. In addition, simulations have been checked using the commercial software `WOLFRAM MATHEMATICA` (version 10). For plotting purposes, the program `GNUPLOT` has been mainly employed.

In particular, for the implementation of the ship model in `AUTO`, several files have been used. Firstly, the specific values of the model parameters are collected in the file `ship.f90`, including the HTC characteristics from B.1. Additional constants are contained in `constant.f90`, as for example a conversion factor to change the angles from degrees to radians, and inversely.

The file called `c.man` consists of a list with all `AUTO` constants for the problem type to work with, as the tolerances and the continuation steps, among others.

The right-hand side of the system to implement, cf. (4.8), is fully contained in `man.f90`, with all corresponding variables, functions, continuation parameters, initialization values, etc.

Finally, the specific command lines in order to perform the numerical continuation are saved in `man.script`. For instance, one may start running the file `man.f90` and locate the Hopf bifurcation when modifying the values of ε_ψ giving a starting point. Then, the Hopf bifurcation can be traced out in the $(\varepsilon_r, \varepsilon_\psi)$ -plane, giving the stability boundary curve shown in Figure 4.10.

Additionally, when saving the output data from `AUTO`, three files are obtained: a solution file `s.name`, a bifurcation file `b.name`, and a diagnostic file `d.name`. With these, one can employ a different program to plot the wished data conveniently, as done for Figure 4.12, for instance, where `MATHEMATICA` has been used.

For a detailed explanation of the software `AUTO`, we refer to [18].

By request, the specific codes can be provided.

Afterword

Lastly, I would like to close this thesis by briefly presenting my very first outcome during my PhD period, namely, the logo of the Applied Analysis group, from the University of Bremen, which is shown in Figure 0.

This vignette combines diverse features which characterize the research directions of the members of our working group. For instance, on the top, one can appreciate a couple of Lorenz attractors whose shape reminds butterflies. Moreover, there is also the popular saying that a butterfly flapping its wings in Brazil could trigger a tornado in Texas, meaning that the Lorenz system, which consists of equations modeling weather behavior, is extremely sensitive to initial conditions. Obviously, this saying must not be taken literally.

Furthermore, in our research group, fluid dynamics and waves equations are studied, having their representation by some waves on the picture, for which the silver ratio has been used. In addition, trajectories are depicted between fixed points.

Finally, on the bottom, some Rayleigh-Bénard convection cells are sketched, encircling the explicit formulation of the topics spectral theory, pattern formation, and dynamical systems.

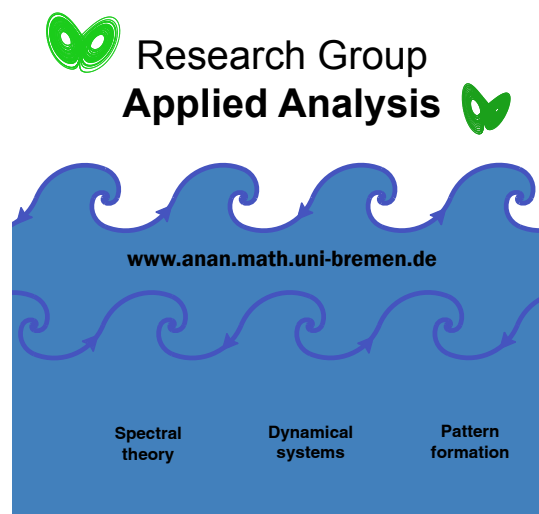


FIGURE 0: Applied analysis logo.

Bibliography

- [1] S.-I. AMARI, *Dynamics of pattern formation in lateral-inhibition type neural fields*, Biological Cybernetics, 27 (1977), pp. 77–87, <https://doi.org/10.1007/BF00337259>.
- [2] AMERICAN BUREAU OF SHIPPING, *Guide for Vessel Maneuverability*, ABS Plaza, 16855 Northchase Drive, Houston, TX 77060 USA, 2006. Updated February 2017.
- [3] M. APRI, N. BANAGAAYA, J. V. D. BERG, R. BRUSSEE, D. BOURNE, T. FATIMA, F. IRZAL, J. D. M. RADEMACHER, B. RINK, F. VEERMAN, AND S. VERPOORT, *Analysis of a model for ship manoeuvring*, in Proceedings of the Seventy-ninth European Study Group Mathematics with Industry, R. Planque, S. Bhulai, J. Hulshof, W. Kager, and R. T.O., eds., Vrije Universiteit Uitgeverij, 2012, pp. 83–116.
- [4] B. AULBACH AND T. WANNER, *Integral manifolds for Carathéodory type differential equations in Banach spaces*, in Six lectures on dynamical systems, World Sci. Publ., River Edge, NJ, 1996, pp. 45–119.
- [5] S. BEREGI, D. TAKÁCS, AND C. HŐS, *Nonlinear analysis of a shimmying wheel with contact-force characteristics featuring higher-order discontinuities*, Nonlinear Dynamics, 90 (2017), pp. 877–888, <https://doi.org/10.1007/s11071-017-3699-3>.
- [6] C. A. BUZZI, J. C. MEDRADO, AND J. TORREGROSA, *Limit cycles in 4-star-symmetric planar piecewise linear systems*, Journal of Differential Equations, 268 (2020), pp. 2414–2434, <https://doi.org/10.1016/j.jde.2019.09.008>.
- [7] C. CANUDAS DE WIT, H. OLSSON, K. ASTROM, AND P. LISCHINSKY, *A new model for control of systems with friction*, IEEE Transactions on Automatic Control, 40 (1995), pp. 419–425, <https://doi.org/10.1109/9.376053>.
- [8] J. CARR, *Applications of centre manifold theory*, vol. 35 of Applied Mathematical Sciences, Springer-Verlag, New York-Berlin, 1981.
- [9] A. R. CHAMPNEYS AND V. KIRK, *The entwined wiggling of homoclinic curves emerging from saddle-node/Hopf instabilities*, Phys. D, 195 (2004), pp. 77–105, <https://doi.org/10.1016/j.physd.2004.03.004>.
- [10] M. CHIRILUS-BRUCKNER, P. VAN HEIJSTER, H. IKEDA, AND J. D. M. RADEMACHER, *Unfolding symmetric Bogdanov–Takens bifurcations for front dynamics in a reaction–diffusion system*, Journal of Nonlinear Science, 29 (2019), pp. 2911–2953, <https://doi.org/10.1007/s00332-019-09563-2>.
- [11] S.-N. CHOW AND J. K. HALE, *Methods of bifurcation theory*, vol. 251 of Grundlehren der Mathematischen Wissenschaften [Fundamental Principles of Mathematical Science], Springer-Verlag, New York, 1982.
- [12] E. A. CODDINGTON AND N. LEVINSON, *Theory of ordinary differential equations*, McGraw-Hill Book Company, 1955.

- [13] B. COLL, A. GASULL, AND R. PROHENS, *Degenerate Hopf bifurcations in discontinuous planar systems*, *Journal of Mathematical Analysis and Applications*, 253 (2001), pp. 671–690, <https://doi.org/10.1006/jmaa.2000.7188>.
- [14] S. COOMBES, *Waves, bumps, and patterns in neural field theories*, *Biological Cybernetics*, 93 (2005), pp. 91–108, <https://doi.org/10.1007/s00422-005-0574-y>.
- [15] H. DANKOWICZ AND A. B. NORDMARK, *On the origin and bifurcations of stick-slip oscillations*, *Phys. D*, 136 (2000), pp. 280–302, [https://doi.org/10.1016/S0167-2789\(99\)00161-X](https://doi.org/10.1016/S0167-2789(99)00161-X), [https://doi.org/10.1016/S0167-2789\(99\)00161-X](https://doi.org/10.1016/S0167-2789(99)00161-X).
- [16] M. DI BERNARDO, C. J. BUDD, A. R. CHAMPNEYS, AND P. KOWALCZYK, *Piecewise-smooth dynamical systems*, vol. 163 of Applied Mathematical Sciences, Springer-Verlag London, 2008.
- [17] M. DI BERNARDO, C. J. BUDD, A. R. CHAMPNEYS, P. KOWALCZYK, A. B. NORDMARK, G. OLIVAR TOST, AND P. T. PIROINEN, *Bifurcations in nonsmooth dynamical systems*, *SIAM Review*, 50 (2008), pp. 629–701, <https://doi.org/10.1137/050625060>.
- [18] E. J. DOEDEL, A. R. CHAMPNEYS, T. F. FAIRGRIEVE, Y. A. KUZNETSOV, B. SANDSTED, AND X. J. WANG, *Auto97 : Software for continuation and bifurcation problems in ordinary differential equations*, Technical report, California Institute of Technology, Pasadena CA 91125, (1998), <http://indy.cs.concordia.ca/auto>.
- [19] B. ETKIN AND L. D. REID, *Dynamics of Flight: Stability and Control*, John Wiley & Sons, Ltd., third ed., 1996.
- [20] A. FILIPPOV, *Differential Equations with Discontinuous Righthand Sides*, vol. 18, Springer Netherlands, 1988, <https://doi.org/10.1007/978-94-015-7793-9>.
- [21] T. I. FOSSEN, *Handbook of marine craft hydrodynamics and motion control*, John Wiley & Sons, Ltd., 2011.
- [22] F. R. GANTMACHER, *The Theory of Matrices*, vol. 1, Chelsea Publishing Company, 1960.
- [23] A. GASULL AND J. TORREGROSA, *Center-focus problem for discontinuous planar differential equations*, *International Journal of Bifurcation and Chaos in Applied Sciences and Engineering*, 13 (2003), pp. 1755–1765, <https://doi.org/10.1142/S0218127403007618>.
- [24] B. GOLDING, A. ROSS, AND T. I. FOSSEN, *Identification of nonlinear viscous damping for marine vessels*, 14th IFAC Symposium on System Identification, Newcastle, Australia, (2006).
- [25] J. GUCKENHEIMER AND P. HOLMES, *Nonlinear oscillations, dynamical systems, and bifurcations of vector fields*, vol. 42 of Applied Mathematical Sciences, Springer-Verlag, New York, 1983, <https://doi.org/10.1007/978-1-4612-1140-2>.
- [26] D. HAESSIG AND B. FRIEDLAND, *On the modeling and simulation of friction*, *Proceedings of SPIE - The International Society for Optical Engineering*, 1482 (1990), pp. 1256–1261, <https://doi.org/10.1115/1.2896418>.
- [27] J. HARRIS AND B. ERMENTROUT, *Bifurcations in the Wilson-Cowan equations with nonsmooth firing rate*, *SIAM Journal on Applied Dynamical Systems*, 14 (2015), pp. 43–72, <https://doi.org/10.1137/140977953>.
- [28] P. HARTMAN, *Ordinary differential equations*, vol. 38 of Classics in Applied Mathematics, Society for Industrial and Applied Mathematics, Philadelphia, PA, 2002, <https://doi.org/10.1137/1.9780898719222>.

- [29] H. KAPER AND H. ENGLER, *Mathematics & climate*, Society for Industrial and Applied Mathematics, Philadelphia, PA, 2013, <https://doi.org/10.1137/1.9781611972610>, <https://doi.org/10.1137/1.9781611972610>.
- [30] P. E. KLOEDEN AND M. RASMUSSEN, *Nonautonomous dynamical systems*, vol. 176 of Mathematical Surveys and Monographs, American Mathematical Society, 2011, <https://doi.org/10.1090/surv/176>.
- [31] M. KUNZE, *Non-Smooth Dynamical Systems*, vol. 1744 of Lecture Notes in Mathematics, Springer-Verlag, Berlin Heidelberg, 2000.
- [32] T. KÜPPER, H. HOSHAM, AND D. WEISS, *Bifurcation for Non-smooth Dynamical Systems via Reduction Methods*, vol. 35, Springer Basel, 2013, pp. 79–105, https://doi.org/10.1007/978-3-0348-0451-6_5.
- [33] T. KÜPPER AND H. A. HOSHAM, *Reduction to invariant cones for non-smooth systems*, Mathematics and Computers in Simulation, 81 (2011), pp. 980–995, <https://doi.org/10.1016/j.matcom.2010.10.004>.
- [34] T. KÜPPER AND S. MORITZ, *Generalized Hopf bifurcation for non-smooth planar systems*, Philos. Trans. R. Soc. Lond. Ser. A Math. Phys. Eng. Sci., 359 (2001), pp. 2483–2496, <https://doi.org/10.1098/rsta.2001.0905>.
- [35] Y. A. KUZNETSOV, *Elements of applied bifurcation theory*, vol. 112 of Applied Mathematical Sciences, Springer-Verlag, New York, second ed., 1998.
- [36] D. H. LEE AND H. S. CHOI, *A stability analysis of tandem offloading systems at sea*, Journal of Marine Science and Technology, 10 (2005), pp. 53–60.
- [37] R. I. LEINE, *Bifurcations of equilibria in non-smooth continuous systems*, Physica D: Nonlinear Phenomena, 223 (2006), pp. 121–137, <https://doi.org/10.1016/j.physd.2006.08.021>.
- [38] J. LLIBRE, D. D. NOVAES, AND C. A. RODRIGUES, *Averaging theory at any order for computing limit cycles of discontinuous piecewise differential systems with many zones*, Physica D: Nonlinear Phenomena, 353–354 (2017), pp. 01–10, <https://doi.org/10.1016/j.physd.2017.05.003>.
- [39] J. LLIBRE, M. ORDÓÑEZ, AND E. PONCE, *On the existence and uniqueness of limit cycles in planar continuous piecewise linear systems without symmetry*, Nonlinear Anal. Real World Appl., 14 (2013), pp. 2002–2012, <https://doi.org/10.1016/j.nonrwa.2013.02.004>.
- [40] O. MAKARENKO AND J. S. W. LAMB, *Dynamics and bifurcations of nonsmooth systems: A survey*, Physica D. Nonlinear Phenomena, 241 (2012), pp. 1826–1844, <https://doi.org/10.1016/j.physd.2012.08.002>.
- [41] J. E. MARSDEN AND M. McCRACKEN, *The Hopf bifurcation and its applications*, Applied Mathematical Sciences, Springer-Verlag New York, 1976.
- [42] F. C. MOON AND P. J. HOLMES, *A magnetoelastic strange attractor*, Journal of Sound and Vibration, 65 (1979), pp. 275–296.
- [43] P. OLTMANN AND S. D. SHARMA, *Simulation of combined engine and rudder maneuvers using an improved model of hull-propeller-rudder interactions*, 1984. Technische Universität Hamburg-Harburg, Schriftenreihe Schiffbau.
- [44] F. A. PAPOULIAS, C. A. BATEMAN, AND S. ORNEK, *Dynamic loss of stability in depth control of submersible vehicles*, Applied Ocean Research, 17 (1995), pp. 205–216, [https://doi.org/10.1016/0141-1187\(95\)00009-7](https://doi.org/10.1016/0141-1187(95)00009-7).

- [45] F. A. PAPOULIAS AND Z. O. ORAL, *Hopf bifurcations and nonlinear studies of gain margins in path control of marine vehicles*, Applied Ocean Research, 17 (1994), pp. 21–32, [https://doi.org/10.1016/0141-1187\(94\)00016-G](https://doi.org/10.1016/0141-1187(94)00016-G).
- [46] A. ROBERTS AND R. SAHA, *Relaxation oscillations in an idealized ocean circulation model*, Climate Dynamics, 48 (2017), pp. 2123–2134, <https://doi.org/10.1007/s00382-016-3195-3>, <https://doi.org/10.1007/s00382-016-3195-3>.
- [47] R. C. ROBINSON, *An Introduction to Dynamical Systems: Continuous and Discrete*, American Mathematical Society, Providence, Rhode Island, second ed., 2012.
- [48] J. A. SANDERS, F. VERHULST, AND J. MURDOCK, *Averaging methods in nonlinear dynamical systems*, vol. 59 of Applied Mathematical Sciences, Springer-Verlag, New York, second ed., 2007, <https://doi.org/10.1007/978-0-387-48918-6>.
- [49] D. J. W. SIMPSON, *Twenty Hopf-like bifurcations in piecewise-smooth dynamical systems*, arXiv Preprint, arXiv:1905.01329 (2019).
- [50] K. J. SPYROU AND J. M. T. THOMPSON, *The nonlinear dynamics of ship motions: a field overview and some recent developments*, The Royal Society, 358 (2000), pp. 1735–1760, <https://doi.org/10.1098/rsta.2000.0613>.
- [51] M. STEINHERR ZAZO AND J. D. RADEMACHER, *Lyapunov coefficients for Hopf bifurcations in systems with piecewise smooth nonlinearity*, SIAM J. Appl. Dyn. Syst., 19 (2020), pp. 2847–2886, <https://doi.org/10.1137/20M1343129>.
- [52] M. STEINHERR ZAZO AND J. D. RADEMACHER, *Nonlinear effects of stabilization in ship models with non-smooth nonlinearities using P-control*, 2021, <https://arxiv.org/abs/2104.10663>. (The title may change after revision).
- [53] H. STOMMEL, *Thermohaline convection with two stable regimes of flow*, Tellus, 13 (1961), pp. 224–230, <https://doi.org/10.1111/j.2153-3490.1961.tb00079.x>, <https://doi.org/10.1111/j.2153-3490.1961.tb00079.x>.
- [54] M. TEMMEN, *Analyse der Stabilität und Steuerung eines 3DOF-Schiffskörpers*, master’s thesis, Universität Bremen, March 2019.
- [55] Y. TIAN, *Bifurcation of limit cycles in smooth and non-smooth dynamical systems with normal form computation*, PhD thesis, The University of Western Ontario, Canada, 2014.
- [56] S. TOXOPEUS, *Deriving mathematical manoeuvring models for bare ship hulls using viscous flow calculations*, Journal of Marine Science and Technology, 14 (2009), pp. 30–38, <https://doi.org/10.1007/s00773-008-0002-9>.
- [57] S. TOXOPEUS, *Practical Application of Viscous-flow Calculations for the Simulation of Manoeuvring Ships*, PhD thesis, Maritime Research Institute Netherlands (MARIN), May 2011.
- [58] P.-F. VERHULST, *Notice sur la loi que la population suit dans son accroissement*, in Correspondance Mathématique et Physique, vol. 10, L’Observatoire de Bruxelles, 1838, pp. 113–121.
- [59] M. VIALON, S. SUTULO, AND C. GUEDES SOARES, *On the order of polynomial regression models for manoeuvring forces*, IFAC Proceedings Volumes, 45 (2012), pp. 13–18, <https://doi.org/10.3182/20120919-3-IT-2046.00003>.
- [60] D. WEISS, T. KÜPPER, AND H. HOSHAM, *Invariant manifolds for nonsmooth systems*, Physica D: Nonlinear Phenomena, 241 (2012), pp. 1895–1902, <https://doi.org/10.1016/j.physd.2011.07.012>.

-
- [61] K. WOLFF, *Ermittlung der Manövriereigenschaften fünf repräsentativer Schiffstypen mit Hilfe von CPMC-Modellversuchen*, Institut für Schiffbau der Universität Hamburg, 1981. Schriftenreihe Schiffbau.
- [62] Y. ZOU AND T. KÜPPER, *Generalized Hopf bifurcation emanated from a corner for piecewise smooth planar systems*, *Nonlinear Analysis: Theory, Methods & Applications*, 62 (2005), pp. 1–17, <https://doi.org/10.1016/j.na.2004.06.004>.
- [63] Y. ZOU, T. KÜPPER, AND W.-J. BEYN, *Generalized Hopf bifurcation for planar filippov systems continuous at the origin*, *Journal of Nonlinear Science*, 16 (2006), pp. 159–177, <https://doi.org/10.1007/s00332-005-0606-8>.